

Spectroscopic Investigations of the \tilde{X} and \tilde{A} State
Dynamics of $^{13}\text{C}_2\text{H}_2$

by

Michelle Lee Silva

Submitted to the Department of Chemistry
in partial fulfillment of the requirements for the degree of

Doctor of Philosophy

at the

MASSACHUSETTS INSTITUTE OF TECHNOLOGY

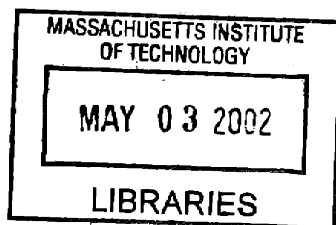
February 2002

© Massachusetts Institute of Technology 2002. All rights reserved.

Author
Department of Chemistry
October 24, 2001

Certified by
Robert W. Field
Haslam and Dewey Professor of Chemistry
Thesis Supervisor

Accepted by
Robert W. Field
Chairman, Departmental Committee on Graduate Students



ARCHIVES

This doctoral thesis has been examined by a Committee of the Department of Chemistry that included

Professor Robert J. Silbey _____
(Chairperson)

Professor Sylvia T. Ceyer _____

Professor Robert W. Field _____
(Thesis Supervisor)

Spectroscopic Investigations of the \tilde{X} and \tilde{A} State Dynamics of $^{13}\text{C}_2\text{H}_2$

by

Michelle Lee Silva

Submitted to the Department of Chemistry
on October 24, 2001, in partial fulfillment of the
requirements for the degree of
Doctor of Philosophy

Abstract

The objective of the experiments described in this thesis is to perform a detailed spectroscopic study of the dynamics on the \tilde{A} and \tilde{X} state surfaces of $^{13}\text{C}_2\text{H}_2$ in order to further understand the acetylene \leftrightarrow vinylidene isomerization process in the ground electronic state. Acetylene exemplifies one of the simplest bond-breaking isomerization systems and it has served as a prototype for studies of large amplitude vibrational motion in molecules. The short-time, large amplitude, vibrational dynamics of acetylene are well understood up to the acetylene \leftrightarrow vinylidene isomerization barrier. However, direct observation of acetylene \leftrightarrow vinylidene isomerization remains elusive. To this end, five experimental techniques, Laser Induced Fluorescence (LIF), Dispersed Fluorescence (DF), Cavity Ring-Down Spectroscopy (CRDS), Noise Immune Cavity Enhanced Optical Heterodyne Molecular Spectroscopy (NICE-OHMS) and Stimulated Emission Pumping (SEP) are employed to study the spectroscopy and dynamics of acetylene. All of these experiments focus on $^{13}\text{C}_2\text{H}_2$ instead of $^{12}\text{C}_2\text{H}_2$, except for the Cavity Ring-Down measurements. These experiments concentrate on $^{13}\text{C}_2\text{H}_2$ because of the possibility of observing nuclear permutation tunneling splittings which are indicative of acetylene \leftrightarrow vinylidene isomerization.

The experiments described here provide the necessary foundation for observing nuclear permutation tunneling splittings. Attempts were made to observe nuclear permutation tunneling splittings in $^{13}\text{C}_2\text{H}_2$ using NICE-OHMS and SEP. Although permutation splittings were not observed, these experiments enhanced our knowledge of the dynamics and spectroscopy of the \tilde{A} and \tilde{X} states of $^{13}\text{C}_2\text{H}_2$. Moreover, these experiments have led to a better understanding of how to design and focus future studies in order to successfully observe nuclear permutation tunneling splittings in $^{13}\text{C}_2\text{H}_2$ as a means for directly observing acetylene \leftrightarrow vinylidene isomerization.

Thesis Supervisor: Robert W. Field

Title: Haslam and Dewey Professor of Chemistry

Acknowledgments

There are many people who have supported me on this journey and I would like to express my gratitude to them all.

First and foremost, I would like to thank my advisor Robert W. Field. He has given me unprecedented intellectual freedom to follow the path I have chosen and his enthusiasm and love of spectroscopy has been a constant source of inspiration.

I also would like to thank several others mentors and collaborators that I have had the privilege of working with:

- John Hall, Long-Sheng Ma, and Jun Ye at JILA/NIST for their unwavering support, patience encouragement and the chance to prove that a chemist can do physics.
- Kevin Lehmann and Giacinto Scoles at Princeton for their insight and enthusiasm and the opportunity to learn from them.
- Peter Weber for his guidance and encouragement.

Additionally, I would like to thank all the teachers I have had over the years, specifically, my high school physics teacher E. Sheldon Smith who started me on this incredible journey, and Michael Lewandowski who introduced me to chemistry.

I owe a great deal of thanks to past and present members of the Field group, whom I have worked with, including Selen Altunata, Leah Ruslen, Kevin Cunningham, Sergey Panov, Scott Witonsky, Ryan Thom, Xing Jiang, and Serhan Altunata. I have learned a great deal from all them. Specifically, I would like to acknowledge:

- Matthew Jacobson, who taught me everything about acetylene and has set the standard for intellectual pursuits in our group.
- Jason Clevenger, whose constant support and friendship has aided me during every step of this journey, and whose ability to persevere and accomplish brilliant science has been inspirational.

- Zicheng Duan, who spent many hours in lab with me and taught me about being a good person not just a good scientist.

I would also like to thank everyone at JILA for their unparalleled support during my time in Colorado. Specifically, I would like to acknowledge David Jones and Scott Diddams for their help. Thank you to Matt, Brad, Julie, Nikki, Elizabeth and Penny, for your friendship and all that I have learned from you.

I would like to thank my former roommates, Heidi Burch, Karen Shafer, and Mara Landers, for their friendship and constant support over the past 5 years.

I would like to thank Ryan Clark for his friendship and the wonderful sense of balance he has given to my life during the conclusion of this research.

Finally, I would like to thank my family. Without the unwavering support and friendship of my parents and sister this work would have never been completed. They have put the world at my feet and for that, I will be forever grateful.

For Kelly

"For there is no friend like a sister in calm or stormy weather..."

-Christina Georgina Rossetti

Contents

1	Introduction	21
1.1	Objective	21
1.2	Spectroscopy of the \tilde{X} state	22
1.2.1	CNPI-MS Group Theory: Permutation Tunneling Splittings in $^{13}\text{C}_2\text{H}_2$	24
1.2.2	Attempts to Observe Nuclear Permutation Tunneling Doublets in Overtone Spectra	28
1.3	Spectroscopy of \tilde{A} state	29
2	Laser Induced Fluorescence Studies of the \tilde{A}-State of $^{13}\text{C}_2\text{H}_2$	31
2.1	Introduction	31
2.2	LIF Experimental Details	33
2.3	Results and Analysis of LIF Spectra	34
2.4	Conclusion	40
2.5	Appendix	41
3	Laser Induced Fluorescence Spectra of the V_0^3K_0^1 and V_0^4K_0^1 Rovibronic Bands in $^{13}\text{C}_2\text{H}_2$	43
3.1	Introduction	43
3.2	Experimental Details	46
3.3	V_0^4K_0^1 Band LIF Spectra	46
3.4	V_0^3K_0^1 LIF Spectra	53
3.5	Conclusion	57

4	$\tilde{A}^1A_u-\tilde{X}^1\Sigma_g^+$ Dispersed Fluorescence Spectra of $^{13}\text{C}_2\text{H}_2$	59
4.1	Introduction	60
4.2	Experimental Details	61
4.3	Results	65
4.3.1	V_0^4 band	72
4.4	Effective Hamiltonian Models	74
4.4.1	Normal-Mode Fitting	74
4.4.2	Local-Mode Fitting	79
4.5	Conclusion	82
5	Cavity Ring-Down Spectroscopy of $\tilde{A}^1A_u-\tilde{X}^1\Sigma_g^+$ Transition of $^{12}\text{C}_2\text{H}_2$: Determination of Absorption Cross Sections	84
5.1	Introduction	84
5.2	History of CRDS	87
5.3	Theoretical Background: Two Distinct Viewpoints	90
5.4	Brief Note on Cavity Design	94
5.5	CRDS Experimental Details	98
5.6	CRDS Results	101
5.7	Determination of Oscillator Strengths	114
5.8	Conclusion	119
6	Noise Immune Cavity Enhanced Optical Heterodyne Molecular Spec- troscopy of $^{13}\text{C}_2\text{H}_2$ and H_2O	125
6.1	Introduction	125
6.2	Experimental Setup: Initial One-Photon Experiments on H_2O and $^{13}\text{C}_2\text{H}_2$	129
6.2.1	Comparison of NICE-OHMS Signal for Different Demodulation Schemes	136
6.3	One Photon H_2O Results	141
6.4	Double Resonance NICE-OHMS of Acetylene	150
6.5	Double Resonance NICE-OHMS Experimental Details	151

6.6	Double Resonance NICE-OHMS of Acetylene Results and Discussion	157
6.7	Conclusion	160
7	Conclusion	163
7.1	Stimulated Emission Pumping Experiments	164
7.1.1	Results of Preliminary Stimulated Emission Pumping Experiments	166
7.2	Current Work: Hot-band Experiments	167

List of Figures

1-1	Vibrational modes of the \tilde{X} and \tilde{A} states. The vibronic symmetry of each level is noted.	23
1-2	Energy level diagram for a totally symmetric vibrational levels in vinylidene and linear acetylene for $^{12}\text{C}_2\text{H}_2$. The nuclear statistical weights are given in parentheses.	25
1-3	Energy level diagram for a totally symmetric vibrational level in vinylidene and linear acetylene for $^{13}\text{C}_2\text{H}_2$. The nuclear statistical weights are given in parentheses.	27
2-1	Laser Induced Fluorescence Spectrum of the $2_0^1V_0^0K_0^1$ band. Nuclear spin statistics predict a 10:6 intensity alteration for even:odd J''	34
3-1	Laser Induced Fluorescence of the $V_0^4K_0^1$ Band. Nuclear spin statistics predict a 10:6 intensity alternation for even:odd J . In the inset, doublings of several lines in the P branch, that are the result of a B-type Coriolis perturbation, are clearly evident.	49
3-2	Off-diagonal matrix elements that couple the e-parity levels $J = 8-11$ of the V^4K^1 level to a nearby perturbing state. Note that the matrix elements scale roughly as $\sqrt{J(J+1)}$. The straight line is a fit of the data to $\sqrt{J(J+1)}$	50
3-3	The zero-order energies of the perturbing state, observed in transitions that terminate on the e-parity levels of V^4K^1 , are plotted versus $J(J+1)$ in order to determine T_0 and an effective rotational constant, B . The fitted line is also shown.	51

3-4	Laser Induced Fluorescence of the $V_0^3K_0^1$ band. The spectrum exhibits many perturbations. The lines Q(1) - Q(3), in particular, are extremely fractionated and it is difficult to assign them without performing a lifetime study or obtaining information from other vibrational bands.	54
3-5	Dispersed fluorescence patterns originating from lines in the R branch region of the $V_0^3K_0^1$ band. It is easy to determine which transitions in the LIF spectrum originate from the same vibronic band. The solid curves correspond to DF spectra originating from rotational levels of the $V_0^3K_0^1$ band. The dotted lines are DF spectra originating from unknown rotational lines which do not belong to the $V_0^3K_0^1$ band.	58
4-1	Panel (a) shows the unscaled raw spectra. Panel (b) is the recursion map of the overlapping portions of the frequency calibrated segments, where the intensity of one segment is plotted versus the intensity of the second. The intensity ratio of the segments is given by the slope of the line in the recursion map. Panel (c) depicts the intensity-scaled segments	64
4-2	In the upper panel, 7 consecutive dispersed fluorescence segments are shown. Each segment overlaps with more than half of the adjacent segment. The bottom panel illustrates the result of the concatenation of the above segments.	66
4-3	DF spectra excited via the $V_0^2K_0^1$, $2_0^1V_0^1K_0^1$, $2_0^1V_0^2K_0^1$, and $V_0^4K_0^1$ bands, which extend from 0 to 22,000 cm^{-1} of internal energy.	67
4-4	Comparison of the $^{12}\text{C}_2\text{H}_2$ versus $^{13}\text{C}_2\text{H}_2$ DF spectra at low and high energy. At low internal energy the spectra are quite similar but at high internal energy the $^{13}\text{C}_2\text{H}_2$ spectrum becomes obviously simpler.	68

4-5	A sample of the extracted polyad patterns for $^{13}\text{C}_2\text{H}_2$ assembled into an IVR map. More than 50 distinct patterns have been extracted and identified. Here we show 24 of those patterns arranged according to the number of quanta of <i>trans</i> -bend, v_4 , and the number of quanta of CC-stretch, v_2	70
4-6	Classical mechanical zero-order frequency detuning for the (3,245) resonance in $^{13}\text{C}_2\text{H}_2$ and $^{12}\text{C}_2\text{H}_2$ calculated from our effective Hamiltonian model. $^{12}\text{C}_2\text{H}_2$ should be strongly influenced by the (3,245) resonance while $^{13}\text{C}_2\text{H}_2$ is not.	71
4-7	Extracted fractionation patterns above and below the lowest predicted zero-point dressed energy of the isomerization barrier. The polyads [20,0], [23,1], and [22,0] beneath the dashed line lie below the isomerization energy but the other 5 patterns above the dashed line lie above the isomerization barrier. Note the similarity in the fractionation patterns of the polyads. The spurious peak denoted with an asterisk in polyad [25,1] is attributed to a different polyad, but we were unable to disentangle the two polyads.	73
4-8	Comparison of the DF spectrum excited via the $V_0^4K_0^1$ band with the pure bending bright state fractionation patterns extracted from the $2_0^1V_0^1K_0^1$, $V_0^2K_0^1$, and $2_0^1V_0^2K_0^1$ vibrational band DF spectra. There is strong evidence for contributions from two classes of bright states in the figure. The usual bright state expected in the DF spectrum is $(0, v_2, 0, v_4, 0)$. Instead, states of the type $(0, v_2, 0, v_4 - 2, 2)$ appear in the $V_0^4K_0^1$ DF spectra to have their own intrinsic intensity. This intensity in the $(0, v_2, 0, v_4 - 2, 2)$ bright state is present because of an anharmonic perturbation in the \tilde{A} state.	75

4-9	Panels (a) and (b) illustrate the results of the normal-mode fit for pure bend polyad fractionation patterns [12,0] and [24,0]. The fractionation patterns in the pure bend polyads were fit to an RMS error of $\pm 1.33 \text{ cm}^{-1}$. Panels (c) and (d) illustrate the results of the local-mode fit, and, in this case, the pure bend bright state fractionation patterns were fit to an RMS error of $\pm 1.22 \text{ cm}^{-1}$	81
5-1	Mode structure of a resonator.	92
5-2	Symmetric Resonator where $R_1 = R_2 = R \geq L/2$	95
5-3	Stability diagram for various types of resonators.	95
5-4	Ring-Down decays for a mode matched and incorrectly mode matched cavity. In the case of the mode matched cavity ($L=1.5R$), the pattern of 3 stationary exit spots results in 3 families of exponential decays with the same decay constant. For the case of the mismatched cavity the intensity pattern appears random and is a result of mode-beating.	97
5-5	CRD spectrometer	98
5-6	Raw CRD spectrum. Ring-Down time, versus frequency.	102
5-7	Absorption Spectrum of the Origin band. Pressure = 8.6 Torr	103
5-8	Absorption Spectrum of the $V_0^1 K_0^1$ transition. The pressure in the cell was 7 Torr.	105
5-9	Absorption Spectrum of the $2_0^1 V_0^0 K_0^1$ transition recorded at 7 Torr.	111
5-10	CRD spectrum of Rovibrational Transitions in the region of $43020 - 43076 \text{ cm}^{-1}$	112
5-11	Absorption Spectrum of the $V_1^0 K_1^0$ transition.	113
5-12	Absorption Spectrum of the $V_0^1 K_0^1$ transition near Q(8). For the high resolution scans the change in ring-down time for a particular absorption feature is much larger than the change in ring-down times observed for the low resolution scans. Consequently, the measured absorption cross section for the high resolution scans is larger.	121

5-13	Absorption Spectrum of the $V_0^1 K_0^1$ transition near Q(1), Q(2), and Q(3). For the high resolution scans the change in ring-down time for a particular absorption feature is much larger than the change in ring-down times observed for the low resolution scans. Consequently, the measured absorption cross section for the high resolution scans is larger.	122
6-1	Trace amount of water vapor detected in 1 Torr of $^{13}\text{C}_2\text{H}_2$. The dispersion line shape maps out the Doppler profile of the transition centered at $12,074.5689 \text{ cm}^{-1}$. The signal from the sweep wave applied to the voltage driver of the PZT serves to roughly calibrate the scan, where the peak to peak range of the sweep wave corresponds to tuning the laser frequency a distance of 2.3981 GHz.	128
6-2	Experimental setup of the NICE-OHMS Spectrometer.	130
6-3	Measurement of finesse of the NICE-OHMS spectrometer using the cavity Ring-Down method. Ring-Down decays are evident for the center laser frequency, ω_0 , and the 4 MHz rf sidebands, $\omega_0 \pm \text{rf}$, which were imposed on the carrier frequency for Pound-Drever-Hall locking of the laser to the high finesse cavity.	132
6-4	VCXO servo used for tracking the 421 MHz sidebands to the free spectral range of the cavity.	133
6-5	The error signal produced for tracking the FM sidebands Δ to the cavity FSR as the laser is scanned over a rovibrational transition in water is shown in the left panel. Shown on the right, is the saturated absorption NICE-OHMS signal for a transition in water observed at 817.9223 nm.	134
6-6	VCXO frequency. The cavity is scanned approximately 70 MHz, and the rms noise is 125 Hz. Note that a frequency offset of 150MHz has been subtracted.	134

6-7	FM modulation of the incident laser beam. Modulation at $\delta = 4\text{MHz}$ is used to lock the laser frequency to the high finesse cavity. Modulation at $\Delta = 421\text{ MHz}$ is used to generate the NICE-OHMS signal, and modulation at $\omega = 51\text{ kHz}$ is used to actively lock Δ to the FSR of the cavity.	135
6-8	Comparison of saturated absorption NICE-OHMS lineshapes for a H_2O absorption at $12,226.1\text{ cm}^{-1}$ at 14 mTorr . Solid curve shows the signal for a 2.2 MHz dither amplitude on the cavity PZT and the dotted curve shows the signal for a 1 MHz dither amplitude.	137
6-9	Panel a) is the result for demodulation at 417 MHz in reflection. Panel b) is the result for demodulation at 421 MHz in reflection. Panel c) is the NICE-OHMS signal obtained in transmission for demodulation at 421MHz and panel d) is the dc transmission. The insets in each panel are an expanded view of the noise level.	139
6-10	$J''_{K_a, K_c} \leftarrow J''_{K_a, K_c} = 4_{0,4} \leftarrow 3_{0,3}$ transition at 12226.1 cm^{-1} . Solid line: NICE-OHMS signal at 10 mTorr . Dotted line: DC detection.	142
6-11	Frequency scan of the H_2O resonance at 817.922 nm and the theoretical fit based on Wahlquist's modulation broadening formalism. Fit residuals are shown in the lower curve.	148
6-12	Pressure study of the absorption line at $12,226.101\text{ cm}^{-1}$. The pressure broadening rate is determined to be 12 MHz/Torr	149
6-13	A diode laser at $1.5\ \mu\text{m}$ is used to excite the $(1,1,0,1^{+1},1^{-1})$ overtone which is resonant with $(1,0,1,0,0)$ level. A Ti:Sapphire laser is used to access rotational levels in either the $(2,1,3,1^{+1},1^{-1})$ or $(4,1,1,1^{+1},1^{-1})$ vibrational levels.	150
6-14	Wavelength measurement of DFB diode laser from Ortel.	153

6-15	Beat note between the frequency doubled output of the DFB diode laser and the Ti:Sapphire laser at 769.41 nm. The signals at 80 and 160 MHz are due to the acousto-optic modulation of the Ti:Sapphire laser beam. The signal at 400 MHz is 200 MHz wide and is due to the drift of the DFB diode laser, which has an instantaneous linewidth of 3 MHz.	154
6-16	Comparison of NICE-OHMS and DC absorption signals using a cavity with a finesse of 32,000. Left: One photon NICE-OHMS signal of $^{13}\text{C}_2\text{H}_2$ at 793.3677nm. Right: DC signal	158
7-1	SEP experimental setup.	164
7-2	Portion of the SEP spectrum of $^{13}\text{C}_2\text{H}_2$ near $E_{vib} = 21,400 \text{ cm}^{-1}$. The $J' = 1$ of the V^2K^1 level was used as an intermediate state. No nuclear permutation tunneling doublets were observed.	166
7-3	Preliminary results of hot-band Experiments implementing eXtended Cross Correlation to disentangle hot-band transitions from cold band transitions. Spectra taken at simultaneously at two different temperatures are shown in the upper panel. The middle diagram is a recursion map used for disentangling the spectra. The disentangled hot-band and cold-band spectra are shown in the bottom panel. Courtesy of Zicheng Duan.	169

List of Tables

1.1	Complete Nuclear Permutation Inversion Group for Acetylene	25
2.1	Assignment of Observed Rovibrational Transitions of the $V_0^0K_0^1$ and $V_0^1K_0^1$ Bands. Transitions are reported in cm^{-1} . The residuals reported are observed minus calculated values based on the least square fit to equations 2.3 and 2.4. The residuals are also reported in cm^{-1} . Transitions denoted with an * had a large residual indicative of a perturbation, and consequently, those transitions were excluded from the fit that determined rotational constants.	36
2.2	Assignment of Observed Rovibrational Transitions of the $2_0^1V_0^0K_0^1$ and $V_0^2K_0^1$ Bands. Transitions are reported in cm^{-1} . The residuals reported are observed minus calculated values based on the least square fit to equations 2.3 and 2.4. The residuals are also reported in cm^{-1} . Transitions denoted with an * had a large residual indicative of a perturbation, and consequently, those transitions were excluded from the fit that determined rotational constants.	37
2.3	Assignment of Observed Rovibrational Transitions of the $2_0^1V_0^1K_0^1$ and $2_0^1V_0^2K_0^1$ Bands. Transitions are reported in cm^{-1} . The residuals reported are observed minus calculated values based on the least square fit to equations 2.3 and 2.4. The residuals are also reported in cm^{-1} . Transitions denoted with an * had a large residual indicative of a perturbation, and consequently, those transitions were excluded from the fit that determined rotational constants.	39

2.4	Rotational Constants Determined from Least Squares Fit to the Data in Tables 2.1, 2.2, and 2.3. Values in parenthesis are 1 sigma errors. Note that the D_{jj} constants are not well determined.	41
2.5	Axis Switching Transitions identified in the $V_0^2K_0^0$ and $2_0^1V_0^1K_0^0$ bands of $^{13}\text{C}_2\text{H}_2$	42
3.1	Coriolis Interactions of Vibrational Levels, C_{2h} point group.	44
3.2	Assignments of observed rovibrational transitions in the $V_0^4K_0^1$ Band. Transitions are reported in cm^{-1} . The residuals reported are observed minus calculated values based on the least squares fit to equations 2.3 and 2.4. The residuals are also reported in cm^{-1} . Transitions denoted with an * were not included in the fit used to determine rotational constants.	47
3.3	Term values for observed perturbed transitions in the $V_0^4K_0^1$ band, which terminate on e-parity levels. The intensity information is used to determine the locations of the bright and dark states. The off-diagonal matrix elements between the two interacting states are also reported. All values are reported in cm^{-1}	50
3.4	Rotational constants determined from least squares fit to the data in table 3.3. Listed in parenthesis are the 1σ uncertainties in the last digits reported. All values are reported in cm^{-1}	51
3.5	Assignment of Observed Rovibrational Transitions of the $V_0^3K_0^1$ band. Transitions are reported in cm^{-1} . The residuals reported are observed minus calculated values based on the least square fit to equations 2.3 and 2.4. The residuals are also reported in cm^{-1} . Transitions denoted with an * were not included in the fit to determine rotational constants.	56

4.1	Data included in the effective Hamiltonian fit. The vibrational energies in the lower section of the table are for the 31 pure-bending vibrational levels, observed by absorption spectroscopy, that were previously reported by Herman and coworkers[1]. The upper section of the table lists 30 pure-bending vibrational levels that were assigned by applying numerical pattern-recognition to our dispersed fluorescence data set. The columns N_b , l , and g/u specify the polyad and symmetry assignments of the vibrational levels included in the fit. For the $l = 0$ polyads, the parity of the vibrational wavefunctions is specified as a superscript; that is, “+” specifies a vibrational wavefunction of $\Sigma_{g/u}^+$ symmetry species, and “-” specifies $\Sigma_{g/u}^-$. The notations $E_{\mathcal{N}}^{calc}$ and $E_{\mathcal{L}}^{calc}$ refer to the normal-mode and local-mode fits respectively and $0^+/2$ designates an unresolved pair of $l = 0/l = 2$ eigenstates, the calculated energies of which were averaged.	77
4.2	Parameters determined from a least-squares fit of the pure bending effective Hamiltonian, expressed in the <i>normal-mode basis set</i> , to the data set described in the text. Numbers in parentheses are 1σ uncertainties in the last digit (estimates obtained from diagonal elements of the covariance matrix). All parameters are in units of cm^{-1}	80
4.3	Parameters determined from a least-squares fit of the pure-bending effective Hamiltonian, expressed in the <i>local-mode basis set</i> , to the to the data set described in the text. Numbers in parentheses are 1σ uncertainties in the last digit (estimates obtained from diagonal elements of the covariance matrix). All parameters are in units of cm^{-1}	82
5.1	Assignment of observed Rovibrational Transitions of $V_0^0K_0^1$ at 8.6 Torr. The peak intensities, $\alpha(\omega)$, are reported in cm^{-1} and the absolute intensities of each line, $\sigma(\omega)$, are given in cm^2/mol . Transitions that are blended are indicated with an *.	104

5.2	Assignment of observed Rovibrational Transitions of $V_0^1 K_0^1$ band. The peak intensities, $\alpha(\omega)$, are reported in cm^{-1} and the absolute intensities of each line, $\sigma(\omega)$, are given in cm^2/mol . The spectra were recorded with 7 Torr of acetylene.	106
5.3	Assignment of observed Rovibrational Transitions of $2_0^1 V_0^0 K_0^1$ band recorded at 7 Torr. Several other vibrational bands observed in this spectral region are also listed. The peak intensities, $\alpha(\omega)$, are reported in cm^{-1} and the absolute intensities of each line, $\sigma(\omega)$, are given in cm^2/mol	106
5.4	Assignment of the observed Rovibrational Transitions in the region of 43020 - 43076 cm^{-1} . The peak intensities, $\alpha(\omega)$, are reported in cm^{-1} and the absolute intensities of each line, $\sigma(\omega)$, are given in cm^2/mol . Overlapped lines are denoted by an * and the same peak intensity is reported for each line.	108
5.5	Assignment of the observed Rovibrational Transitions of the $V_1^0 K_1^0$ transition. Other rovibrational transitions observed in this region are also reported. The peak intensities, $\alpha(\omega)$, are reported in cm^{-1} and the absolute intensities of each line, $\sigma(\omega)$, are given in cm^2/mol . Overlapped lines are denoted by an * and the same peak intensity is reported for each line.	113
5.6	Absorption strength, $\alpha(\omega)$, and Band oscillator strengths, f_v , for several rotational lines of the $V_0^1 K_0^1$ transition measured at low and high resolution.	121
6.1	Transitions observed in the NICE-OHMS experiment. The differences between our measurements and those of Toth [2] are listed in column 4.	145

Chapter 1

Introduction

1.1 Objective

The main objective of the projects described in this thesis is to perform a detailed spectroscopic study of the dynamics on the \tilde{A} and \tilde{X} state surfaces of $^{13}\text{C}_2\text{H}_2$ in order to further understand the acetylene \leftrightarrow vinylidene isomerization process in the ground electronic state. The experiments presented in this thesis provide the necessary groundwork for observing nuclear permutation tunneling splittings, which are indicative of acetylene \leftrightarrow vinylidene isomerization. Furthermore, several attempts were made to observe nuclear permutation tunneling splittings in $^{13}\text{C}_2\text{H}_2$ using different experimental methodologies. Although no permutation splittings were observed, those experiments enhanced our knowledge of the dynamics and spectroscopy of the \tilde{A} and \tilde{X} states of $^{13}\text{C}_2\text{H}_2$ and have led to a better understanding of how future experiments should be designed in order to successfully observe nuclear permutation tunneling splittings in $^{13}\text{C}_2\text{H}_2$ as a means for directly observing acetylene \leftrightarrow vinylidene isomerization. To this end, 5 different experimental techniques, Laser Induced Fluorescence (LIF), Dispersed Fluorescence (DF), Cavity Ring-Down Spectroscopy (CRDS), Noise Immune Cavity Enhanced Optical Heterodyne Molecular Spectroscopy (NICE-OHMS), and Stimulated Emission Pumping (SEP) are used to study the spectroscopy and dynamics of acetylene and the results are presented in this thesis.

1.2 Spectroscopy of the \tilde{X} state

Since the pioneering works of Ingold and King [3] and Innes [4], the spectroscopy of the acetylene molecule has proven to be intriguing. The ground electronic state of acetylene is linear and has $D_{\infty h}$ symmetry. The first excited singlet state is *trans*-bent and has C_{2h} symmetry. The normal mode vibrations for the \tilde{X} and \tilde{A} states are shown in Figure 1-1. The ground state and the first excited singlet state exhibit numerous perturbations, which result in quite complex spectra. More importantly, information about dynamical processes are encoded in these spectra. For example it is well established that dynamical processes such as Intramolecular Vibrational Redistribution, IVR, in acetylene can be studied by examining frequency domain spectra [5, 6, 7, 8, 9, 10, 11, 12, 13, 1, 14]. This is the fundamental premise of this body of work. Frequency domain spectra encode unimolecular dynamics. The original purpose of this thesis was to observe nuclear permutation tunneling splittings in $^{13}\text{C}_2\text{H}_2$, which would be a direct spectroscopic signature of acetylene \leftrightarrow vinylidene isomerization. Nuclear spin statistics prohibit the observation of such splittings in $^{12}\text{C}_2\text{H}_2$, as will be explained later in this chapter. The search for tunneling splittings has proven thus far to be unsuccessful. It has, however, led to an understanding of the necessary conditions essential to spectroscopically observing acetylene \leftrightarrow vinylidene isomerization in the frequency domain.

Many experiments characterizing the \tilde{X} and \tilde{A} states of $^{13}\text{C}_2\text{H}_2$ needed to be performed before proceeding with experiments aimed at observing tunneling splittings. It was absolutely necessary to be able to predict the location of certain energy levels or polyads in the ground state potential of $^{13}\text{C}_2\text{H}_2$ and to completely understand intramolecular vibrational redistribution in $^{13}\text{C}_2\text{H}_2$. Note that all of this has been well established for the $^{12}\text{C}_2\text{H}_2$ isotopomer and the spectra and dynamics of $^{12}\text{C}_2\text{H}_2$ are well understood up to $\sim 15,000\text{ cm}^{-1}$. This is not the case for the $^{13}\text{C}_2\text{H}_2$ isotopomer and much work needed to be done in order to characterize the \tilde{X} and \tilde{A} states. The first step in this process was to perform a series of Laser Induced Fluorescence experiments to locate energy levels in the \tilde{A} state from which Dispersed Fluorescence spectra

Vibrational Modes and Vibronic Symmetry

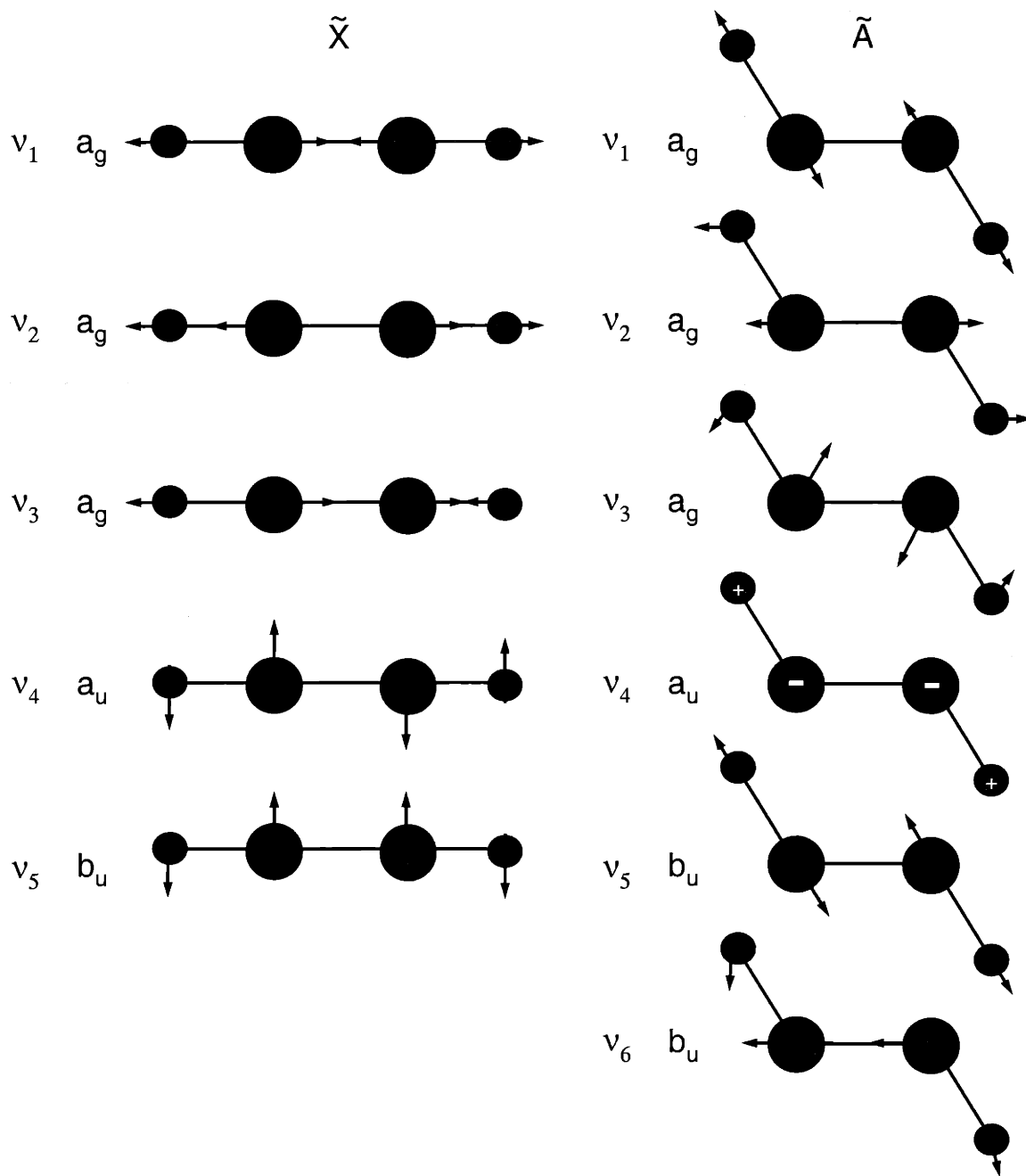


Figure 1-1: Vibrational modes of the \tilde{X} and \tilde{A} states. The vibronic symmetry of each level is noted.

could be recorded. Once that was accomplished, Dispersed Fluorescence spectra were obtained from several different rovibrational levels in the \tilde{A} state. From these spectra we were able to gain an understanding of IVR in the ground state. The analysis of the DF spectra allowed us to predict the locations of energy levels in the \tilde{X} state which were to be the target of overtone experiments or Stimulated Emission Pumping experiments aimed at observing nuclear permutation tunneling splittings.

1.2.1 CNPI-MS Group Theory: Permutation Tunneling Splittings in $^{13}\text{C}_2\text{H}_2$

The ground electronic state potential surface (as well as several other excited electronic states) of acetylene exhibit several potential minima, which correspond to different geometric isomers. The most stable minimum corresponds to the linear $D_{\infty h}$ configuration, but other structures such as the *cis*-bent and vinylidene C_{2v} isomers as well as non-planar C_2 symmetry isomers are possible [15, 16, 17, 18]. The point group treatment for acetylene is of limited utility in that it involves rotations and reflections around a molecule fixed axis and these symmetry operations are not necessarily common to each of the point groups representing all the stable structures of acetylene [18]. In order to establish a unified framework for discussing the rotations and vibrations for all of the structural conformers of acetylene, it is necessary to use the more general symmetry classifications based on Complete Nuclear Permutation Inversion-Molecular Symmetry (CNPI-MS) group theory. For a complete treatment of all the acetylene isomers using CNPI-MS group theory, see the work of Lundberg [19, 18]. Some of the more salient aspects of the CNPI-MS group theory treatment for acetylene will be reviewed briefly here. The CNPI-MS classification for acetylene is G_8 . There are 8 'true symmetry' operations which are common to all isomeric forms of acetylene. Shown in Table 1.2.1 are all the possible operations. The notation (12) refers to permutation of the two carbon nuclei, (ab) refers to permutation of the two hydrogen nuclei, and E is the identity operator. An * after an operation refers to inversion of the x, y and z axes (e.g. $x \rightarrow -x$, $y \rightarrow -y$ and $z \rightarrow -z$).

Table 1.1: Complete Nuclear Permutation Inversion Group for Acetylene

G_8	E	(12)(ab)	E^*	(12)(ab)*	(12)	(ab)	(12)*	(ab)*
Ss+	1	1	1	1	1	1	1	1
Ss-	1	1	-1	-1	1	1	-1	-1
As-	1	-1	-1	1	1	-1	-1	1
As+	1	-1	1	-1	1	-1	1	-1
Aa+	1	1	1	1	-1	-1	-1	-1
Aa-	1	1	-1	-1	-1	-1	1	1
Sa-	1	-1	-1	1	-1	1	1	-1
Sa+	1	-1	1	-1	-1	1	-1	1

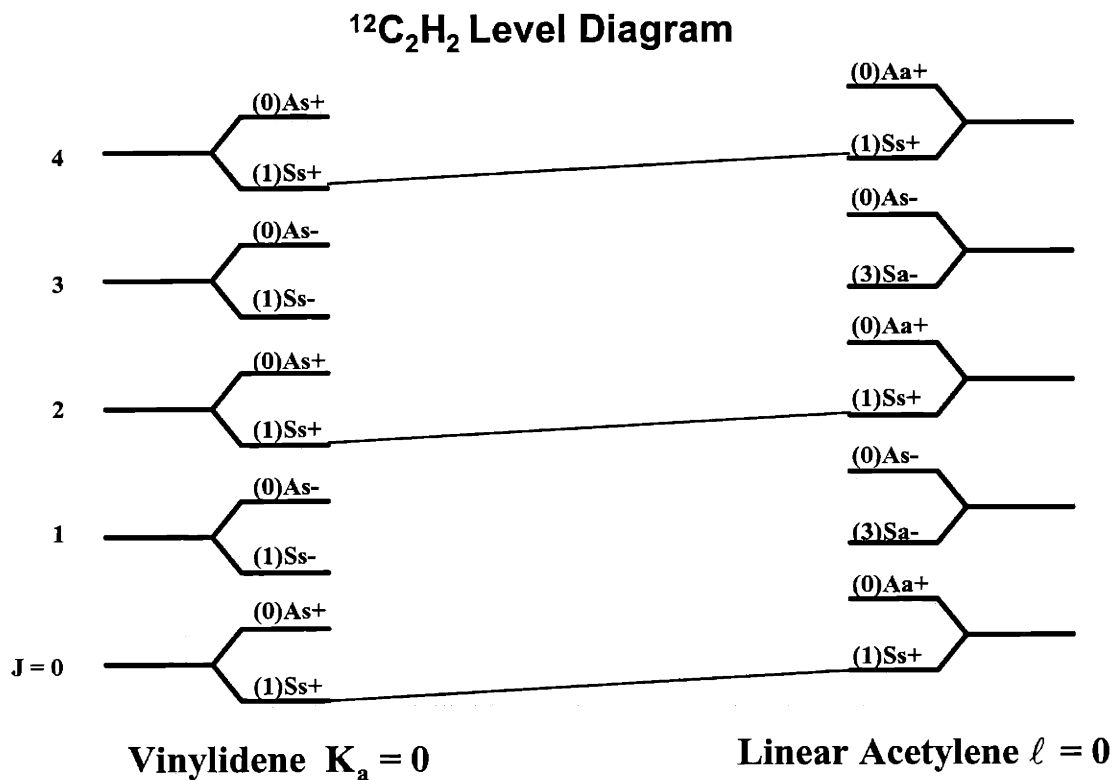


Figure 1-2: Energy level diagram for a totally symmetric vibrational levels in vinylidene and linear acetylene for $^{12}\text{C}_2\text{H}_2$. The nuclear statistical weights are given in parentheses.

Instead of the usual point group symmetry notation, $A_{u/g}$ and $B_{u/g}$, the labels $S_{s\pm}$, $A_{a\pm}$, $A_{s\pm}$, $S_{a\pm}$ are used. The wavefunctions (rotational, nuclear, vibrational) are labelled according to parity, which is denoted by '+' or '-', 'S' or 'A' which refer to symmetric or antisymmetric with respect to permutation of the Carbon nuclei, and 's' or 'a' which refer to symmetric or antisymmetric with respect to permutation of the Hydrogen nuclei.

Using this notation, which applies to all isomers, we can classify the energy levels of different vibronic states. Shown in Figure 1-2 is the correlation diagram for $^{12}\text{C}_2\text{H}_2$ in the linear configuration and vinylidene. For each J, there are two degenerate levels. The statistical weight of each level is given in parentheses. From this it is easy to see, based on symmetry considerations, that only one member of the even-J levels of linear acetylene for a symmetric vibration can interact with a nearby vinylidene states. All other levels either have 0 nuclear spin weight or have the wrong symmetry to interact with vinylidene levels. In the case of $^{13}\text{C}_2\text{H}_2$, shown in Figure 1-3, all of the levels now have nonzero nuclear spin weights. As a result, for each J, one member has the correct symmetry to interact with a vinylidene level. The degeneracy is broken due to the interaction with vinylidene and one member will shift either higher or lower in energy with respect to the unperturbed line (the location of the unperturbed level indicates the zero-order position).

Nuclear permutation tunneling doublets will have an intensity ratio of 1:9 for even-J and 3:3 for odd-J rovibrational lines in $^{13}\text{C}_2\text{H}_2$. In the case of $^{12}\text{C}_2\text{H}_2$, one member of each permutation doublet cannot exist due to nuclear spin statistics. The level that can interact with a nearby vinylidene state may shift slightly either higher or lower in energy depending on the position of the vinylidene state. However, this shift is likely to be small and the magnitude of this shift for levels in $^{12}\text{C}_2\text{H}_2$ is impossible to determine without effective Hamiltonian models that predict the positions of rovibrational levels to within a few hundredths of a wavenumber.

This problem does not exist in the case of $^{13}\text{C}_2\text{H}_2$. Both members of each doublet have nonzero nuclear spin weights and only one member of each doublet interacts with a nearby vinylidene level. Consequently, the energy difference between the two

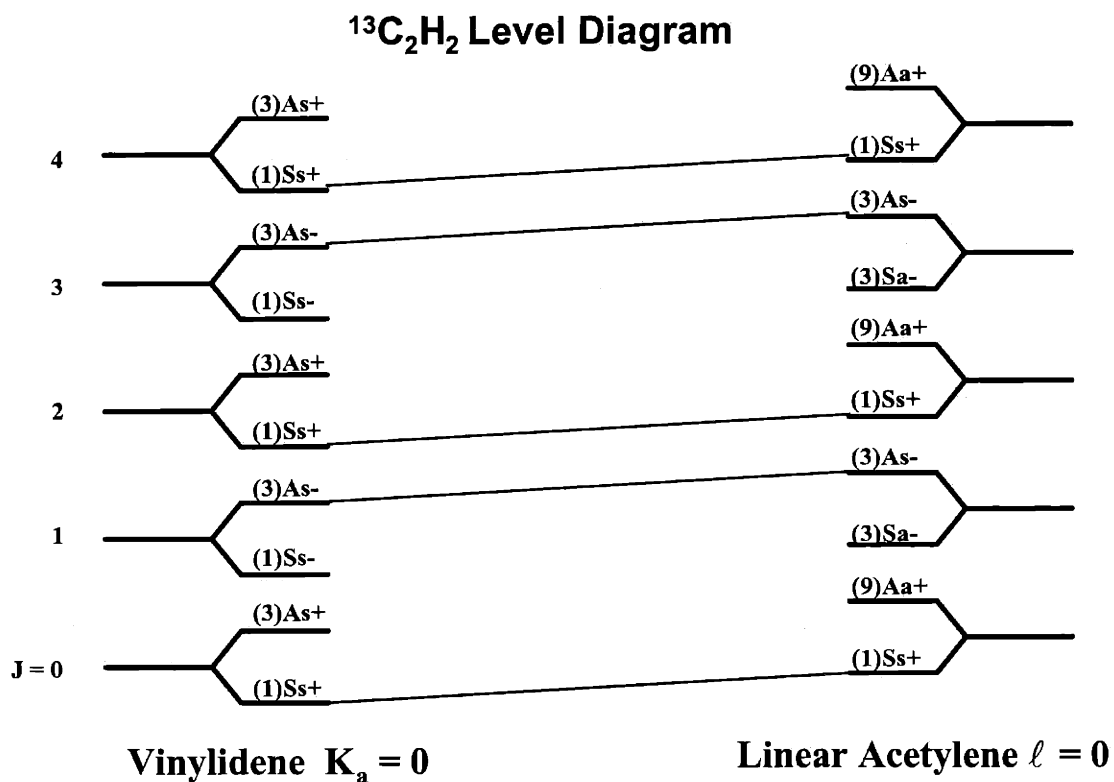


Figure 1-3: Energy level diagram for a totally symmetric vibrational level in vinylidene and linear acetylene for $^{13}\text{C}_2\text{H}_2$. The nuclear statistical weights are given in parentheses.

split levels is a direct sample of the position of the nearby vinylidene state. For this reason, our efforts to study acetylene \leftrightarrow vinylidene isomerization now focus on the $^{13}\text{C}_2\text{H}_2$ isotopomer rather than $^{12}\text{C}_2\text{H}_2$.

1.2.2 Attempts to Observe Nuclear Permutation Tunneling Doublets in Overtone Spectra

In order to observe nuclear permutation tunneling doublets, several different experimental methodologies are relevant. One possibility is the use of Stimulated Emission Pumping, which exploits the geometry of the \tilde{A} state to gain Franck-Condon access to vibrational levels of the \tilde{X} that are not only energetically capable of isomerization (e.g. vibrational levels near the isomerization barrier) but are also strongly coupled into the isomerization coordinate. However, SEP experiments have a resolution limited by the bandwidth of the laser and, in the case of experiments performed at MIT, this corresponds to 0.03 cm^{-1} .¹ Consequently, nuclear permutations tunneling splittings cannot be resolved by SEP unless the splitting is larger than 0.03 cm^{-1} .

It is possible that nuclear permutation tunneling doublets may be observable in overtone spectroscopy of highly vibrationally excited levels in the \tilde{X} state. Overtone experiments on acetylene typically excite CH stretch vibrational modes. Due to IVR on the ground electronic state, vibrational levels with 1-2 quanta of CC stretch as well as *cis*- and *trans*-bending motions borrow intensity from CH stretch vibrational levels. In order to observe nuclear permutation tunneling splittings in overtone experiments, high sensitivity is needed to access highly excited vibrational levels and high resolution is needed to be able to resolve the doublets. Noise Immune Cavity Enhanced Optical Heterodyne Molecular Spectroscopy experiments, in collaboration with John Hall and Jun Ye at NIST, attempting a double resonance scheme to excite rovibrational levels near $E_{vib} \sim 18,600\text{ cm}^{-1}$, will be described in Chapter 6 of this thesis.

A second collaboration with Professors Giacinto Scoles and Kevin Lehmann at

¹The resolution in the visible region for a standard FL3002 Lambda Physik dye laser is 0.03 cm^{-1} . However this resolution is degraded to 0.06 cm^{-1} when the laser output is frequency doubled.

Princeton University, employed a two-photon double resonance technique with a resolution of 15 MHz [20] to study highly excited vibrational levels in $^{13}\text{C}_2\text{H}_2$. Four rotational levels ($J = 1-4$) of the $(v'_1, v'_2, v'_3, v'_4, v'_5) = (2, 1, 3, 1^{+1}, 1^{-1})$ level were observed. Three of the 4 rotational lines were observed to be split. However, these lines did not exhibit the predicted intensity ratios for members of nuclear permutation tunneling doublets. Additionally, spectra of the corresponding band in $^{12}\text{C}_2\text{H}_2$ exhibited similar perturbations. Based on these two results, it was concluded that the splitting was not due to nuclear permutation tunneling doublets resulting from acetylene \leftrightarrow vinylidene isomerization. Furthermore, an upper limit of 15 MHz can be placed on the tunneling splittings. This corresponds to a tunneling time of 30 ns. However, tunneling rates based on RRKM theory predict a rate on the order of 1 ps [20]. This discrepancy between the statistical rate calculated using RRKM and the observed rate is not surprising. There are many instances where state-specific unimolecular dynamics results in a nonstatistical rate [21, 20]. The results indicate that there is a strong bottleneck separating the phase space which can classically isomerize from the rest of phase space which cannot isomerize [20]. This is entirely consistent with the current understanding of acetylene \leftrightarrow vinylidene isomerization dynamics which postulates that local bender states, with excitation exclusively along the isomerization coordinate, are decoupled from other degrees of freedom [8, 7, 14].

1.3 Spectroscopy of \tilde{A} state

Spectroscopic studies of the dynamics of the \tilde{A} state are instrumental in observing direct spectroscopic evidence of acetylene \leftrightarrow vinylidene isomerization on the \tilde{X} state potential surface. In order to find a eigenstate that will serve as a "local-bender-pluck" for high overtones of the local-bend near the acetylene \leftrightarrow vinylidene transition in the \tilde{X} state, it is necessary to understand the anharmonic and Coriolis interactions between the torsional (v'_4) and antisymmetric in-plane bending (v'_6) normal modes of the \tilde{A} state.

Progressions of pure-bender polyads that extend to E_{vib} more than 4,000 cm^{-1}

above the zero-point-energy-dressed acetylene \leftrightarrow vinylidene barrier are observed in DF spectra, however, transitions into local-bender eigenstates which are strongly coupled into the isomerization coordinate are too weak to be observed in DF spectra recorded from the typical Franck-Condon accessible CC-stretch and *trans*-bend combination and overtone vibrational levels of the \tilde{A} state. Consequently, a form of transition state spectroscopy must be employed. It is known that the $3\nu'_3$ [22] and $4\nu'_3$ levels of the \tilde{A} state are perturbed by members of a $4\nu'_{bend}$ polyad based on a normal mode assignment proposed by Crim et al [23]. The $4\nu'_{bend}$ polyad is described further in Chapter 3. The DF spectra recorded from the $4\nu'_{bend}$ perturbing levels exhibit pure-bender polyads suggestive of a 'local bender pluck' of the \tilde{X} state. By exploiting similar $4\nu'_{bend}$ perturbing levels in the \tilde{A} state of $^{13}\text{C}_2\text{H}_2$ it will be possible to excite local-bender vibrational modes in the \tilde{X} state that are coupled strongly to the acetylene \leftrightarrow vinylidene isomerization coordinate (as opposed to the primarily CH stretch modes seen in direct absorption experiments) which would exhibit resolvable nuclear permutation tunneling splittings.

It is essential to map out the level diagrams of both the \tilde{X} and \tilde{A} states of $^{13}\text{C}_2\text{H}_2$ in order to decipher how the large amplitude vibrational motions, which lead to dynamically relevant processes such as a bond breaking isomerization, are encoded in frequency domain spectra.

Chapter 2

Laser Induced Fluorescence

Studies of the \tilde{A} -State of $^{13}\text{C}_2\text{H}_2$

2.1 Introduction

This chapter focuses on Laser Induced Fluorescence spectra recorded from several bands of the $\tilde{A} \ ^1A_u$ - $\tilde{X} \ ^1\Sigma_g^+$ state of $^{13}\text{C}_2\text{H}_2$. The \tilde{A} state of acetylene has been the subject of numerous investigations starting with the pioneering works of Ingold and King [3] and Innes [4]. However, to our knowledge no extensive information concerning the \tilde{A} -state of the $^{13}\text{C}_2$ isotopomer of acetylene has been published. Our investigation of this isotopomer is motivated primarily by the possibility of directly observing spectroscopic signatures of acetylene \leftrightarrow vinylidene isomerization on the electronic ground state potential surface through experiments which exploit the \tilde{A} state geometry as well as anharmonic perturbations in the \tilde{A} to enhance Franck-Condon overlap with the isomerization coordinate. These signatures should be manifest as nuclear permutation tunneling splittings in the \tilde{X} -State of $^{13}\text{C}_2\text{H}_2$, which do not exist in $^{12}\text{C}_2\text{H}_2$ due to nuclear spin statistics.

It has been postulated that the isomerization coordinate is highly localized in a local mode CCH bend and does not couple readily into other vibrational modes of the molecule [14, 7, 24]. As a result, one would expect that ordinary absorption experiments, which primarily excite CH stretching motions in the ground state, would

not prove fruitful and more clever schemes are needed. To this end, we have begun by recording Laser Induced Fluorescence Spectra of several vibrational bands of the \tilde{A} - \tilde{X} transition in order to identify rotation-vibration levels in the \tilde{A} state that may be used in either Dispersed Fluorescence studies or as the upper state of the pump transition in future Stimulated Emission Pumping experiments. We have recorded LIF spectra via the $V_0^0K_0^1$, $2_0^1V_0^0K_0^1$, $V_0^1K_0^1$, $2_0^1V_0^1K_0^1$, $V_0^2K_0^1$, $V_0^3K_0^1$, $V_0^4K_0^1$, and $2_0^1V_0^2K_0^1$ bands. The symbol V_n^m represents transitions from n quanta of the *trans* bending mode, V_4' , in the \tilde{X} state to m quanta of the *trans* bending mode V_3'' , in the \tilde{A} state. Similarly the symbol 2_n^m represents the change of number of quanta of CC stretch, and K_n^m is the unsigned body-fixed projection of the total angular momentum. For the zero-point level of the linear ground electronic state, $K \equiv l = 0$.

Since the original purpose of these LIF studies was to identify rovibrational levels in the \tilde{A} state to use in subsequent dispersed fluorescence spectra, only the cold bands were studied and, for the most part, hot-bands and axis-switching transitions are ignored in this analysis. In the Appendix, a list of identified axis switching transitions are included. For the purpose of this chapter, only unperturbed transitions which originate from the vibrationless ground state and terminate on upper state vibrational levels involving excitation in either the CC stretch or the *trans* bending mode will be discussed. These bands are well understood in $^{12}\text{C}_2\text{H}_2$ and are easily assigned here for the $^{13}\text{C}_2\text{H}_2$ isotopomer, except for a few rotational transitions in the $V_0^3K_0^1$ and $V_0^4K_0^1$ bands. It is well known that the LIF spectrum of $V_0^3K_0^1$ and $V_0^4K_0^1$ bands of $^{12}\text{C}_2\text{H}_2$ are highly perturbed by near degenerate singlet and triplet states [25, 26, 27, 23, 28]. Similarly, LIF spectra of the $V_0^3K_0^1$ and $V_0^4K_0^1$ bands of $^{13}\text{C}_2\text{H}_2$ are perturbed. For example in $V_0^4K_0^1$ of $^{12}\text{C}_2\text{H}_2$ we have identified a Coriolis perturbation. Work is ongoing in our group to identify the exact character of the triplet and singlet perturbers in both the $V_0^3K_0^1$ and $V_0^4K_0^1$ bands. The perturbations in the $V_0^3K_0^1$, $V_0^4K_0^1$ LIF spectra of $^{13}\text{C}_2\text{H}_2$ deserve special consideration and will be discussed in the next chapter.

2.2 LIF Experimental Details

The experimental details are fairly straightforward and will be briefly reviewed here. A XeCl excimer laser (Lambda-Physik LPX-210icc) operating at 20 Hz and 275 mJ/pulse is used to pump a Lambda-Physik FL2002 dye laser, equipped with an intracavity etalon. The dye laser, operated with Coumarin 440 or 450 dye, with 10 mJ/pulse, was pressure tuned over a range of $\approx 10 \text{ cm}^{-1}$ by varying the pressure of N_2 from vacuum to 1 atm. The radiation from the dye laser is subsequently frequency doubled using a β -BBO crystal. Approximately 1 mJ of tunable UV radiation (215–240 nm) was produced with a spectral width $\leq 0.05 \text{ cm}^{-1}$. The doubled output is separated from the fundamental frequency using two 60° S1-UV fused silica prisms.

Frequency calibration was performed using the fundamental radiation from the dye laser which was sent through a quartz $^{130}\text{Te}_2$ cell. The $^{130}\text{Te}_2$ cell was placed in an oven and heated to either ($\sim 500 \text{ }^\circ\text{C}$) or ($\sim 650 \text{ }^\circ\text{C}$). Absorption spectra of the $^{130}\text{Te}_2$ were recorded using a photodiode. The photodiode output was sent to a boxcar integrator (Stanford Research Systems SRS 250) and averaged over 30 shots. Spectra were calibrated to an accuracy of 0.02 cm^{-1} .

The Laser Induced Fluorescence studies were performed in a static gas cell containing 250 mTorr of $^{13}\text{C}_2\text{H}_2$ (MSD Isotopes, 98% pure). The $^{13}\text{C}_2\text{H}_2$ was subject to several freeze-pump-thaw cycles for purification before it was distilled into the stainless steel sample cell using a pentane-liquid N_2 slurry ($-129.7 \text{ }^\circ\text{C}$). The doubled radiation was passed through the sample cell. Fluorescence in the cell is detected perpendicular to the direction of the laser propagation using a Hamamatsu R331 photomultiplier tube. A Schott filter (UG11) is placed in front of the photomultiplier to reduce scattered light from the laser. The signal from the photomultiplier was sent to a boxcar integrator (Stanford Research Systems SRS 250) with a 100 ns gate and averaged over 30 shots. The outputs of both boxcars were digitized and recorded using LabVIEW data acquisition software.

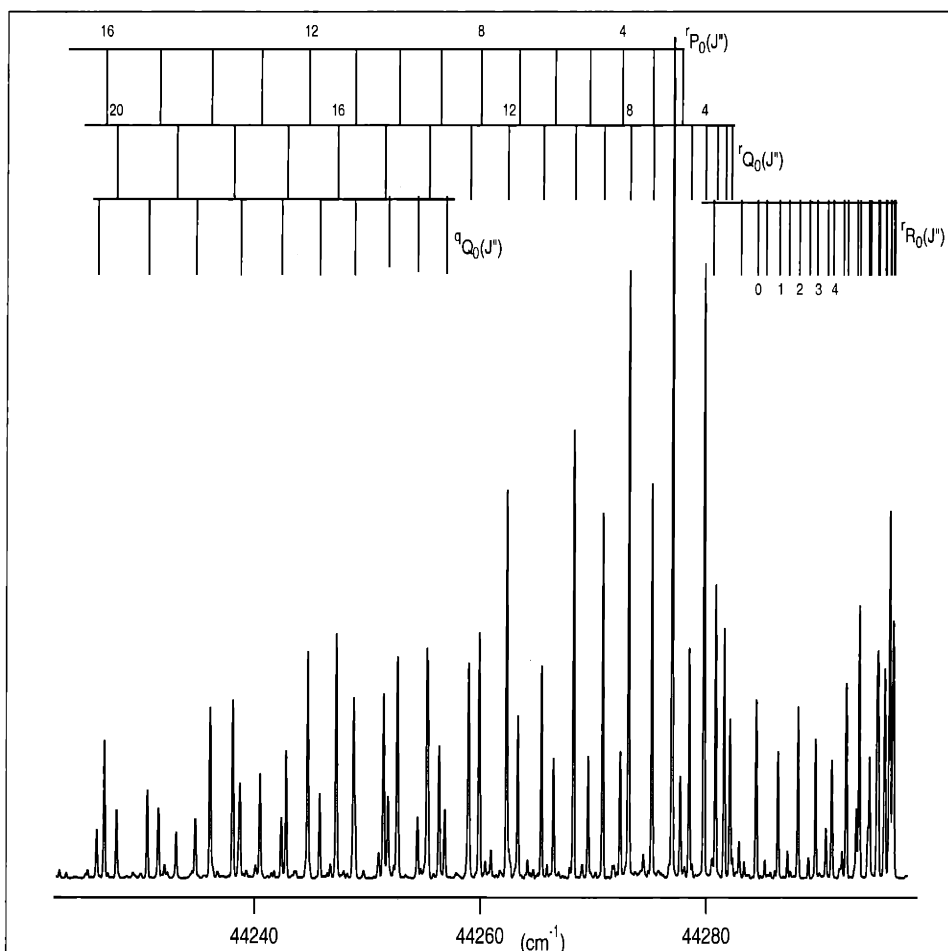


Figure 2-1: Laser Induced Fluorescence Spectrum of the $2_0^1V_0^0K_0^1$ band. Nuclear spin statistics predict a 10:6 intensity alteration for even:odd J'' .

2.3 Results and Analysis of LIF Spectra

Laser Induced Fluorescence spectra were recorded for several ro-vibrational bands up to $J \approx 25$. Shown in Figure 2-1 is a portion of the spectrum recorded for the $2_0^1V_0^0K_0^1$ band. As expected, due to nuclear spin statistics for $^{13}\text{C}_2\text{H}_2$ there is a 10:6 intensity alternation between even and odd J'' in contrast to $^{12}\text{C}_2\text{H}_2$ wherein the intensities instead follow a 1:3 intensity pattern instead).

The \tilde{A} -State of acetylene is known to be a near prolate top [3, 4]. The transitions reported here, $V_0^0K_0^1$, $2_0^1V_0^0K_0^1$, $V_0^1K_0^1$, $2_0^1V_0^1K_0^1$, $V_0^2K_0^1$, $V_0^3K_0^1$, $V_0^4K_0^1$, and $2_0^1V_0^2K_0^1$ originate from the vibrationless level in the ground electronic state and terminate on

rovibrational levels involving the CC stretch or *trans* bending mode in the \tilde{A} state. The rotational selection rules for a c type transition require that $\Delta K_a = \pm 1$. However, Hougen and Watson [29] demonstrated that axis switching transitions exist in acetylene. These give rise to $\Delta K_a = \pm 0, 2$ transitions which, have been observed in the $\tilde{A} - \tilde{X}$ band system [29].

For the energy levels of a near prolate top, the diagonal matrix elements of the rotational Hamiltonian are given by:

$$H_{i,i} = T_v + \frac{1}{2}(B+C)(J(J+1) - K^2) + AK^2 - D_{JJ}J^2(J+1)^2 - D_{JK}J(J+1)K^2 - D_{KK}K^4 \quad (2.1)$$

and the off-diagonal matrix elements are given by:

$$H_{i,i\mp 2} = T_v + \frac{1}{4}(B - C)(\sqrt{(J^2 - (K \pm 1)^2)((J + 1)^2 - (K \pm 1)^2)}). \quad (2.2)$$

In some of the spectra of the bands reported, the K_0^0 axis switching bands are observed, however their absolute rotational assignment is still uncertain. As a result, in this section, the A rotational constants are not determined nor are the D_{KK} or D_{JK} centrifugal distortion constants. In the appendix, the axis switching transitions are identified when possible.

For P,R branch transitions which terminate on the e-parity $\Delta K_a = 0$ energy levels of the \tilde{A} state, the rovibrational energy levels are approximately given by:

$$E = T_e + J(J + 1)\left(\frac{1}{2}(B + C) - \frac{1}{4}(B - C) - D_{JJ}J(J + 1)\right). \quad (2.3)$$

For a Q branch transition, which terminates on the f-parity energy levels of the \tilde{A} state, the upper state rovibrational energy levels are approximated by

$$E = T_e + J(J + 1)\left(\frac{1}{2}(B + C) + \frac{1}{4}(B - C) - D_{JJ}J(J + 1)\right). \quad (2.4)$$

The observed transitions are listed in 2.1, 2.2, and 2.3 list and their corresponding assignments. In some cases the observed minus calculated values were quite large and

the corresponding rotational lines were not included in the rotational fit. Those lines are denoted by an * in the tables.

Table 2.1: Assignment of Observed Rovibrational Transitions of the $V_0^0K_0^1$ and $V_0^1K_0^1$ Bands. Transitions are reported in cm^{-1} . The residuals reported are observed minus calculated values based on the least square fit to equations 2.3 and 2.4. The residuals are also reported in cm^{-1} . Transitions denoted with an * had a large residual indicative of a perturbation, and consequently, those transitions were excluded from the fit that determined rotational constants.

$V_0^0K_0^1$				$V_0^1K_0^1$			
J'	J''	Transition	Residual	J'	J''	Transition	Residual
13	13	42203.6	0.0077	13	13	43239.71	0.034
7	8	42203.79	0.0083	7	8	43240.29	0.031
12	12	42206.88	0.023	12	12	43243.00	0.00011
6	7	42207.18	0.0087	6	7	43243.70	0.053
11	11	42209.85	-0.014	11	11	43246.04	-0.01
5	6	42210.41	0.023	5	6	43246.86	-0.012
10	10	42212.65	0.036	10	10	43248.83	-0.019
4	5	42213.43	-0.007	4	5	43259.96	0.03
9	9	42215.05	-0.05	9	9	43251.38	-0.0019
3	4	42216.33	0.00037	3	4	43252.81	-0.0034
8	8	42217.33	-0.011	8	8	43253.64	-0.026
2	3	42219.07	0.011	2	3	43255.57	0.028
7	7	42219.31	-0.023	7	7	43255.71	0.02
6	6	42221.03	-0.033	6	6	43257.44	-0.014
1	2	42221.59	0.031	1	2	43258.07	-0.037
5	5	42222.57	0.012	5	5	43258.95	-0.025
4	4	42223.88 *	0.085	4	4	43260.20	-0.032
3	3	42224.82	0.045	3	3	43261.23	-0.0073
2	2	42225.52	0.0026	2	2	43262.03	0.033
1	1	42226	-0.01	1	1	43262.51	0.012
25	24	42226.6	-0.048	1	0	43264.80	-0.03
1	0	42228.33	-0.0062	2	1	43266.73	-0.0085
24	23	42228.89	0.0044	3	2	43268.50	0.0038
2	1	42230.29	0.034	4	3	43270.05	-0.032
23	22	42230.97	0.058	5	4	43271.47	-0.028
3	2	42232	-0.0085	20	19	43272.35	-0.026
22	21	42232.71	-0.019	6	5	43272.78	0.027
4	3	42233.57	-0.025	19	18	43273.62	0.06
21	20	42234.37	0.02	7	6	43273.90	0.05
5	4	42235.03	0.015	18	17	43274.59	0.026
20	19	42235.89 *	0.12	8	7	43274.78	0.0092

continued on next page

<i>continued from previous page</i>							
$V_0^0K_0^1$				$V_0^1K_0^1$			
J'	J''	Transition	Residual	J'	J''	Transition	Residual
6	5	42236.34	0.068	17	16	43275.30	-0.084
19	18	42237.02	0.032	9	8	43275.53	-7.9e-05
7	6	42237.36	-0.008	10	9	43276.10	-0.023
18	17	42238.01	-0.009				
8	7	42238.26	-0.034				
17	16	42238.84	-0.017				
9	8	42239.01	-0.038				
10	9	42239.59	-0.046				

Table 2.2: Assignment of Observed Rovibrational Transitions of the $2_0^1V_0^0K_0^1$ and $V_0^2K_0^1$ Bands. Transitions are reported in cm^{-1} . The residuals reported are observed minus calculated values based on the least square fit to equations 2.3 and 2.4. The residuals are also reported in cm^{-1} . Transitions denoted with an * had a large residual indicative of a perturbation, and consequently, those transitions were excluded from the fit that determined rotational constants.

$2_0^1V_0^0K_0^1$				$V_0^2K_0^1$			
J'	J''	Transition	Residual	J'	J''	Transition	Residual
16	17	43500.33	-0.0023	24	25	44175.61	-0.0035
15	16	43505.55	0.026	23	24	44182.08	-0.0041
20	20	43507.21	0.067	22	23	44188.35	-0.0091
14	15	43510.53	0.011	21	22	44194.44	0.019
19	19	43512.61	0.049	17	18	44216.75	0.00077
13	14	43515.31	-0.013	16	17	44221.85	-0.0094
18	18	43517.71	0.014	21	21	4222.289 *	0.13
12	13	43519.96	0.027	15	16	44226.78	-0.0015
17	17	43522.53	-0.019	20	20	44227.85 *	0.11
11	12	43524.36	0.015	14	15	44231.54	0.0072
16	16	43527.09	-0.025	19	19	44233.11	0.061
10	11	43528.58	0.00096	13	14	44236.1	0.0057
15	15	43531.35	-0.041	18	18	44238.09	0.024
9	10	43532.63	0.0031	12	13	44240.49	0.0047
14	14	43535.39	-0.0061	17	17	44242.8	-0.0029
8	9	43536.54	0.055	11	12	44244.7	-0.0035
13	13	43539.08	-0.043	16	16	44247.23	-0.021
7	8	43540.17	0.0019	10	11	44248.76	0.0037
12	12	43542.54	-0.03	15	15	44251.42	-0.012
6	7	43543.66	-0.0034	9	10	44252.64	0.011
11	11	43545.72	-0.032	14	14	44255.29	-0.045
5	6	43546.98	0.0028	8	9	44256.34	-0.00066

continued on next page

<i>continued from previous page</i>							
$2_0^1V_0^0K_0^1$				$V_0^2K_0^1$			
J'	J''	Transition	Residual	J'	J''	Transition	Residual
10	10	43548.62	-0.031	13	13	44258.96	-0.0088
4	5	43550.11	-0.0056	7	8	44259.85	-0.029
9	9	43551.26	-0.031	12	12	44262.32	-0.017
3	4	43553.08	0.011	6	7	44263.31	0.047
8	8	43553.64	-0.023	11	11	44265.41	-0.026
7	7	43555.74	-0.026	5	6	44266.48	0.005
2	3	43555.74 *	0	10	10	44268.25	-0.021
6	6	43557.58	-0.015	4	5	44269.54	0.018
1	2	43558.43 *	0.0063	9	9	44270.83	-0.002
5	5	43559.16	-0.015	3	4	44272.39	-0.019
4	4	43560.43	-0.045	8	8	44273.12	-0.02
3	3	43561.53	0.0005	7	7	44275.18	-0.0067
2	2	43562.34	0.032	2	3	44275.18 *	0
1	1	43562.84	0.008	6	6	44276.98	-0.0043
23	22	43563.36	-0.015	1	2	44277.7	0.0084
1	0	43565.16	0.0063	5	5	44278.49	-0.024
22	21	43565.54	-0.022	4	4	44279.79	-1.5e-05
2	1	43567.08	0.043	26	25	44280.53	0.03
21	20	43567.52	0.0042	3	3	44280.81	0.0097
3	2	43568.73	-0.012	2	2	44281.58	0.014
20	19	43569.21	-0.059	1	1	44282.1	0.019
19	18	43570.81	0.0062	25	24	44282.9	-0.045
5	4	43571.63	0.024	1	0	44284.41	0.0052
18	17	43572.16	0.025	24	23	44285.17	-0.0023
6	5	43572.8	0.026	2	1	44286.34	0.016
17	16	43573.26	0.0084	23	22	44287.17	-0.015
7	6	43573.74	-0.015	3	2	44288.1	0.022
8	7	43574.48	-0.075	22	21	44289.01	0.017
15	14	43574.88	-0.015	4	3	44289.64	-0.029
9	8	43575.19	0.028	21	20	44290.56	-0.043
14	13	43575.46	0.034	5	4	44291.08	-0.025
10	9	43575.65	0.051	6	5	44292.36	-0.0092
11	10	43575.88	0.038	19	18	44293.25	0.03
				7	6	44293.5	0.03
				18	17	44294.28	0.043
				8	7	44294.41	0.0057

Table 2.3: Assignment of Observed Rovibrational Transitions of the $2_0^1V_0^1K_0^1$ and $2_0^1V_0^2K_0^1$ Bands. Transitions are reported in cm^{-1} . The residuals reported are observed minus calculated values based on the least square fit to equations 2.3 and 2.4. The residuals are also reported in cm^{-1} . Transitions denoted with an * had a large residual indicative of a perturbation, and consequently, those transitions were excluded from the fit that determined rotational constants.

$2_0^1V_0^1K_0^1$				$2_0^1V_0^2K_0^1$			
J'	J''	Transition	Residual	J'	J''	Transition	Residual
16	17	44536.8	0.068	21	22	45525.69	-0.024
21	21	44536.8 *	0.12	20	21	45532.05	-0.013
15	16	44541.92	-0.0057	19	20	45538.19	-0.0036
20	20	44542.57	0.063	18	19	45544.09	-0.0076
14	15	44546.93	0.011	17	18	45549.8	0.025
19	19	44548.08	0.049	16	17	45555.27	0.014
13	14	44551.72	-0.0018	14	15	45565.59	0.012
18	18	44553.29	0.025	13	14	45570.45	0.01
12	13	44556.33	0.00068	18	18	45571.17	-0.017
17	17	44558.18	-0.017	12	13	45575.09	-0.0092
11	12	44560.75	-0.0042	17	17	45576.34	0.074
16	16	44562.8	-0.041	11	12	45579.57	0.0073
10	11	44564.99	0.0021	16	16	45581.07	0.034
15	15	44567.18	-0.024	10	11	45583.84	0.0098
9	10	44569.04	0.015	15	15	45585.5	-0.012
14	14	44571.24	-0.039	9	10	45587.92	0.013
8	9	44572.91	0.018	14	14	45589.69	0.0031
13	13	44575.03	-0.045	8	9	45591.8	0.0023
7	8	44576.55	-0.017	13	13	45593.55	-0.02
12	12	44578.58	-0.0094	7	8	45595.44	-0.049
6	7	44580.06	-0.0053	12	12	45597.13	-0.035
11	11	44581.77	-0.052	6	7	45599	-0.0026
5	6	44583.38	0.0046	11	11	45600.38 *	-0.094
10	10	44584.77	-0.017	5	6	45602.32	-0.01
4	5	44586.49	-0.021	10	10	45603.47	-0.029
9	9	44587.43	-0.036	4	5	45605.47	-0.0071
3	4	44589.48	0.015	9	9	45606.17	-0.068
8	8	44589.88	-0.001	3	4	45608.48	0.034
7	7	44591.99	-0.03	8	8	45608.67	-0.028
2	3	44592.23	-0.0077	7	7	45610.84	-0.045
6	6	44593.86	-0.032	2	3	45611.21	-0.015
1	2	44594.85	0.02	6	6	45612.73	-0.059
5	5	44595.52	0.026	5	5	45614.43	0.011
4	4	44596.87	0.044	4	4	45615.82	0.041
24	23	44597.35	-0.02	3	3	45616.88	0.018

continued on next page

<i>continued from previous page</i>							
$2_0^1V_0^1K_0^1$				$2_0^1V_0^2K_0^1$			
J'	J''	Transition	Residual	J'	J''	Transition	Residual
3	3	44597.92	0.023	2	2	45617.68	0.0076
2	2	44598.7	0.0086	1	1	45618.24	0.029
1	1	44599.21	-0.0097	22	21	45619.79	0.0067
23	22	44599.73	-0.042	1	0	45620.56	0.018
1	0	44601.56	0.013	21	20	45621.89	-0.0081
22	21	44601.96	0.007	2	1	45622.44	0.015
2	1	44603.43	0.0016	3	2	45624.11	-0.0053
21	20	44603.91	-0.0082	19	18	45625.44	0.0016
3	2	44605.14	0.0058	4	3	45625.64	0.0049
4	3	44606.67	0.0084	5	4	45626.96	-0.0037
19	18	44607.22	0.014	6	5	45628.1	-0.011
5	4	44608.01	0.0043	7	6	45629.11	0.032
18	17	44608.55	0.012	8	7	45629.9	0.049
6	5	44609.17	0.0021	9	8	45630.46	0.016
17	16	44609.67	0.0083	10	9	45630.84	-0.005
7	6	44610.15	-0.00088				
16	15	44610.59	0.0047				
8	7	44610.96	0.0035				
9	8	44611.57	0.0018				
14	13	44611.83	0.00096				
10	9	44612.01	0.008				

The rotational constants derived by fitting the observed transitions to equations 2.3 and 2.4 are listed in Table 2.3. In this analysis, the A rotational constant could not be determined and the vibrational term values listed in the table are actually $T_0 + A$. We were able to reproduce the experimental measurements to within 0.05 cm^{-1} using the constants listed here. Note that the ground state constants were held fixed at $B = 1.119574687$ and $D = 1.487382\text{e-}6$, determined by G. Di Lonardo and coworkers [30].

2.4 Conclusion

In this chapter LIF spectra of $V_0^0K_0^1$, $2_0^1V_0^0K_0^1$, $V_0^1K_0^1$, $2_0^1V_0^1K_0^1$, $V_0^2K_0^1$, and $2_0^1V_0^2K_0^1$ in the $\tilde{A} \ ^1A_u$ state of $^{13}\text{C}_2\text{H}_2$ are reported. Assignments are made for the $\Delta K = \pm 1$ transitions. Additionally rotational constants for these bands are reported. In some

Table 2.4: Rotational Constants Determined from Least Squares Fit to the Data in Tables 2.1, 2.2, and 2.3. Values in parenthesis are 1 sigma errors. Note that the D_{jj} constants are not well determined.

	$V_0^0 K_0^1$	$V_0^1 K_0^1$	$2_0^1 V_0^0 K_0^1$
T_e	42226.26(27)	43262.75(29)	43563.09(27)
B	1.059(05)	1.060(10)	1.051(04)
C	0.975(05)	0.972(06)	0.968(03)
D_{jj}	$8 \times 10^{-06}(7)$	$6 \times 10^{-06}(20)$	$8 \times 10^{-06}(6)$
	$V_0^2 K_0^1$	$2_0^1 V_0^1 K_0^1$	$2_0^1 V_0^2 K_0^1$
T_e	44282.33(24)	44599.49(24)	45618.48 (26)
B	1.062(03)	1.052(03)	1.052(05)
C	0.969(03)	0.964(03)	0.962(04)
D_{jj}	$8 \times 10^{-06}(4)$	$8 \times 10^{-06}(6)$	$10 \times 10^{-06}(9)$

cases axis switching transitions were observed are reported in the appendix 2.5. The LIF spectra of $V_0^3 K_0^1$, $V_0^4 K_0^1$ were also recorded but are highly perturbed. The analysis of those LIF spectra will be discussed in the next chapter.

2.5 Appendix

Hougen and Watson [29] demonstrated that $\Delta K_a = \pm 0,2$ transitions are possible in the $\tilde{A} - \tilde{X}$ band system of acetylene. Similarly, axis switching transitions which terminate on $K = 0$ levels of the \tilde{A} state have been identified in LIF spectra of $^{13}\text{C}_2\text{H}_2$. Note that these are preliminary assignments and in order to confirm the assignments listed in Table 2.5 additional hot-band spectra are needed. The axis switching transitions have been tentatively assigned based on the rotational constants listed in Section 2-1.

Table 2.5: Axis Switching Transitions identified in the $V_0^2K_0^0$ and $2_0^1V_0^1K_0^0$ bands of $^{13}\text{C}_2\text{H}_2$.

Band	J'	J''	Transition (cm^{-1})
$V_0^2K_0^0$	18	18	44221.33
$V_0^2K_0^0$	17	17	44226.11
$V_0^2K_0^0$	16	16	44230.56
$V_0^2K_0^0$	15	15	44234.79
$V_0^2K_0^0$	14	14	44238.70
$V_0^2K_0^0$	13	13	44242.37
$V_0^2K_0^0$	12	12	44245.77
$2_0^1V_0^1K_0^0$	16	16	44546.67
$2_0^1V_0^1K_0^0$	15	15	44551.11
$2_0^1V_0^1K_0^0$	14	14	44555.27
$2_0^1V_0^1K_0^0$	13	13	44559.13

Chapter 3

Laser Induced Fluorescence

Spectra of the $V_0^3K_0^1$ and $V_0^4K_0^1$

Rovibronic Bands in $^{13}\text{C}_2\text{H}_2$

3.1 Introduction

It is well known that the V^3K^1 and V^4K^1 levels of the $^{12}\text{C}_2\text{H}_2$ \tilde{A} -state are heavily perturbed by both singlet and triplet states. One or more "doorway" triplet states are strongly coupled to $3\nu_3'$. This special triplet level is further mixed with other triplet levels thereby facilitating intersystem crossing between the S_1 and T_n ($n=1,2,3$) electronic states [25, 26, 31, 32, 33, 28]. It is believed that the T_3 state, has a low vibrational density of states and serves as "doorway" state. The T_3 state in turn is coupled to T_1 and T_2 states, which have a high density of vibrational levels [25, 26].

Scherer and coworkers [22] were among the first to identify and assign the singlet perturber in $3\nu_3'$. Although their assignment was later shown to be incorrect, it is worth discussing their characterization of the perturbing level. This perturbation could be due to one of two possible types of interactions: an anharmonic perturbation, involving only anharmonic coupling between vibrational levels, or a Coriolis perturbation, in which vibration-rotation interactions occur. The singlet perturber

of $3\nu'_3$ in $^{12}\text{C}_2\text{H}_2$ appeared in both the e and f parity components of $K_a = 1$ levels indicating that the perturber has $K_a > 0$. Also, $J=1$ was perturbed, indicating that the perturber is a $K_a = 1$ level. Therefore $\Delta K_a = 0$. As a result, the perturbation must be due to an A-type Coriolis interaction or an anharmonic interaction, both of which have the selection rule $\Delta K_a = 0$. Note that B-type Coriolis interactions must satisfy the selection rule $\Delta K_a = \pm 1$ and C-type Coriolis interactions are not possible in the *trans*-bent \tilde{A} state of acetylene [23].

Listed in Table 3.1 are the possible interactions for A, B, and C -type Coriolis coupling mechanisms for vibrational levels of the \tilde{A} state of acetylene, which have a_g , a_u , b_g , and b_u symmetry. For example, 2 vibrational levels of a_g symmetry can interact via a C-type Coriolis mechanism.

Table 3.1: Coriolis Interactions of Vibrational Levels, C_{2h} point group.

Operator	Vibrational Level Symmetry
	$\Psi_1 \Psi_2$
J_c	$a_g a_g$
	$b_g b_g$
	$a_u a_u$
	$b_u b_u$
$J_{a,b}$	$b_g a_g$
	$b_u a_u$

Electric dipole rules require that only *gerade* vibrational levels of the $\tilde{A} \ ^1A_u$ electronic state may be accessed by a 1-photon transition that originates from the vibrationless level of the \tilde{X} state. Consequently, the perturbers must be of a_g vibrational symmetry if the interaction mechanism with $a_g \ 3\nu'_3$ is anharmonic, or the perturber must have b_g symmetry if it is an A-type Coriolis perturber of $A_g \ 3\nu'_3$. At the time of Scherer's [22] analysis, the vibrational frequencies for the normal modes in the \tilde{A} state were not well known. Scherer et al [22] had to rely on *ab initio* harmonic vibrational frequencies for their assignment. No levels of b_g symmetry were found to lie in the vicinity of $3\nu'_3$ and the a_g level closest to $3\nu'_3$ was predicted to be $\nu'_2 + 2\nu'_4$. Therefore, they assigned the perturbing level to $\nu'_2 + 2\nu'_4$. Moreover, rotational anal-

ysis of the perturbing band led to the identification of yet another perturber. The B and C rotational constants determined for the perturbing $\nu'_2 + 2\nu'_4$ level (and the difference between them) were found to be unphysically large, leading the authors to conclude that yet another perturbation was involved. In order to account for an unphysically large asymmetry splitting, the perturber of $\nu'_2 + 2\nu'_4$ had to have $K_a = 0$ and b_g symmetry. The main perturber of $3\nu'_3$, $\nu'_2 + 2\nu'_4$ was postulated to interact with yet a second level, via a B-type Coriolis interaction and this state was assigned as $3\nu'_4 + \nu'_6$.

Double resonance IR-UV experiments performed several years later by Utz and coworkers [23] reassigned this perturbation. The double resonance IR-UV experiments allowed access to *ungerade* vibrational levels. In this manner, the vibrational frequencies for the fundamentals of *ungerade* vibrational modes, ν'_4 (torsion), and ν'_6 (antisymmetric in-plane bend) were determined. A strong Coriolis interaction between ν'_4 and ν'_6 was found. Based on the experimentally determined vibrational frequencies, Utz et al [23] showed that the putative $\nu'_2 + 2\nu'_4$ perturbing level was actually 170 cm^{-1} distant from $3\nu'_3$. The singlet perturber was reassigned as one of the a_g members of the $4\nu'_b$ pentad. The $4\nu_b$ pentad consists of the following levels: $4\nu'_4$, $2\nu'_4 + 2\nu'_6$, $4\nu'_6$, $\nu'_4 + 3\nu'_6$ and $3\nu'_4 + \nu'_6$. These interact with one another via both anharmonic and Coriolis mechanisms. Note that the first 3 levels listed are of a_g vibrational symmetry (A_u vibronic symmetry) and the last two are of b_g vibrational symmetry (B_u vibronic symmetry). Furthermore since each a_g level of $4\nu'_b$ interacts with 2 $K_a=0$ b-axis Coriolis partners, one of these two $K_a=0$ b_g levels is actually the second perturber of $3\nu'_3$.

In the case of the $4\nu'_3$ level, Watson and co-workers [34, 29, 35] were the first to report several perturbations. However, no attempt was made to assign the states responsible for these perturbations. Again the work of Utz et al. [23] sheds light on the nature of the perturber. They propose that the perturber of $4\nu'_3$ is actually $\nu'_3 + 4\nu'_6$.

Since the G matrices for $^{12}\text{C}_2\text{H}_2$ and $^{13}\text{C}_2\text{H}_2$ are almost identical, one would expect similar perturbations to appear in the $V_0^3K_0^1$ and $V_0^4K_0^1$ rovibronic bands of $^{12}\text{C}_2\text{H}_2$

and $^{13}\text{C}_2\text{H}_2$. As stated earlier, very little information exists about the \tilde{A} state of $^{13}\text{C}_2\text{H}_2$. The discussion will focus on the LIF spectra of the $V_0^3K_0^1$ and $V_0^4K_0^1$ bands and the perturbations observed. In the case of $V_0^4K_0^1$, assignments are made for all of the rotational transitions up to $J \sim 25$. A perturbation in the P and R branches, beginning at $J \approx 7$, is evident and we were able to perform a deperturbation analysis to determine the rotational constants and vibrational term value for the perturbing state. For the case of the $V_0^3K_0^1$ band, assignments are made for all of the lines observed in the P and R branches and these assignments are confirmed using combination-differences. The higher-J Q branch lines are also assigned. The lines at low-J in the Q branch are strongly and multiply perturbed and definite assignments cannot be made without additional spectroscopic data e.g. (hot-bands from $l'' = 1$).

3.2 Experimental Details

The LIF spectra were recorded in exactly the same manner as the LIF spectra discussed in Section 2-1. Additionally, since it was thought that the perturber of $3\nu_3'$ would prove quite useful for the pump step in SEP experiments to observe nuclear permutation tunneling splittings in $^{13}\text{C}_2\text{H}_2$, Dispersed Fluorescence spectra were recorded via several lines in the R branch of the $V_0^3K_0^1$ band. An unexpected benefit was that the DF spectra aided in assignment of many of the lines in the very congested $3\nu_3'$ LIF spectrum. Details of the conditions for recording DF spectra can be found in Chapter 4 and will not be repeated here.

3.3 $V_0^4K_0^1$ Band LIF Spectra

Figure 3-1 shows a portion of the LIF spectrum recorded for the $V_0^4K_0^1$ band. The intensities follow the expected nuclear spin statistical weights, which predicts a 10:6 intensity alternation for even:odd J lines. The inset is an expanded view of the perturbed lines. A doubling in the P branch is observed for $J = 7-13$. Unfortunately, this doubling can only be followed for a few J lines in the R branch. In the R

branch the perturbation occurs near the R head and this region of the spectrum is too congested to permit the perturbation to be followed for higher-J lines.

The unperturbed lines were fit to Equations 2.3 and 2.4 in Chapter 2-1 in order to determine the rotational constants for this band. The observed transitions and their assignments are listed in Table 3.2. The e parity $J'' = 6-13$ perturbed lines were not included in this fit in order to determine the constants of the V^4K^1 bright state. Additionally, it was found that several lines in the Q branch are perturbed, as evident from the residuals and hence were removed from the fitting procedure. The lines not included in the least squares fit are denoted by an asterisk in Table 3.2. The results of the fit are listed in Table 5.7. The origin of the $V_0^4K_0^1$ vibrational band lies at 46260.24 cm^{-1} . The V^4K^1 level has effective B and C values of 1.06 and 0.96 cm^{-1} and the diagonal centrifugal distortion term D_{JJ} was determined to be $7.65 \times 10^{-6} \text{ cm}^{-1}$.

Table 3.2: Assignments of observed rovibrational transitions in the $V_0^4K_0^1$ Band. Transitions are reported in cm^{-1} . The residuals reported are observed minus calculated values based on the least squares fit to equations 2.3 and 2.4. The residuals are also reported in cm^{-1} . Transitions denoted with an * were not included in the fit used to determine rotational constants.

$V_0^4K_0^1$							
J'	J''	Transition	Residual	J'	J''	Transition	Residual
25	26	46146.55	-0.0081	5	6	46244.31	-0.041
24	25	46153.24	-0.006	10	10	46245.73	-0.05
21	22	46172.09	0.012	4	5	46247.41	0.0007
20	21	46177.94	-0.022	3	4	46250.31	0.0025
19	20	46183.63	-0.025	8	8	46250.72	-0.07
18	19	46189.15	-0.0025	7	7	46252.95	0.055
22	22	46192.71 *	0.22	2	3	46252.97	-0.062
17	18	46194.48	0.018	6	6	46254.65	-0.084
21	21	46198.62 *	0.11	1	2	46255.58	-0.021
16	17	46199.59	0.006	5	5	46256.25	-0.057
20	20	46204.48 *	0.26	4	4	46257.65	0.034
14	15	46209.32	0.032	26	25	46258.12	0.0075
19	19	46209.69	0.032	3	3	46258.73	0.064
13	14	46213.87	-0.0019	2	2	46259.45	-0.0061
18	18	46214.8	0.0038	1	1	46259.98	0.0024
12	13	46218.4 *	0.12	25	24	46260.52	-0.036

continued on next page

<i>continued from previous page</i>							
$V_0^4K_0^1$							
J'	J''	Transition	Residual	J'	J''	Transition	Residual
17	17	46219.64	-0.0062	1	0	46262.37	0.056
11	12	46222.5 *	-0.018	24	23	46262.79	0.0022
16	16	46224.21	0.0005	2	1	46264.26	0.03
10	11	46226.4 *	-0.18	23	22	46264.83	0.014
15	15	46228.54	0.046	3	2	46266.01	0.029
9	10	46230.39 *	-0.078	22	21	46266.65	0.016
14	14	46232.52	0.018	4	3	46267.57	0.009
8	9	46234.13 *	-0.066	21	20	46268.3	0.053
13	13	46236.2	-0.037	5	4	46269.07	0.089
7	8	46237.85 *	0.1	20	19	46269.67	0.0026
12	12	46239.63	-0.055	19	18	46270.84	-0.053
6	7	46241.23 *	0.089	18	17	46271.93	0.0076

In order to determine the locations of the unperturbed levels for $J = 8-11$, both frequency and intensity information were used. The zero-order deperturbed positions of the main levels were determined by taking the intensity weighted average of the term values of the 2 lines observed for each J . The deperturbed position of the perturbing level is then easily calculable. It is simply the sum of the energies of the eigenstates minus that of the zero-order bright state. The off-diagonal matrix elements coupling the 2 levels were also easy to determine. They are simply:

$$H_{i,j} = \sqrt{E_{Bri} * E_{Pert} - E_{Eigen1} * E_{Eigen2}} \quad (3.1)$$

The term values for each of the eigenstates as well as the energies of the basis states and the values of the off-diagonal coupling matrix elements are listed in Table 3.3. It is interesting to note that the coupling matrix elements listed appear to scale with J slightly faster than $\sqrt{J'(J' + 1)}$. When taking into account that the spectra were calibrated to within 0.02 cm^{-1} , it is reasonable to conclude that the off-diagonal matrix elements scale as $\sqrt{J'(J' + 1)}$. This suggests that the perturbation is a B-type Coriolis interaction rather than an anharmonic resonance. Figure 3-2 illustrates the dependence of the coupling matrix elements on $\sqrt{J'(J' + 1)}$.

Table 3.3 lists the rotational constants determined for the V^4K^1 band as well as for

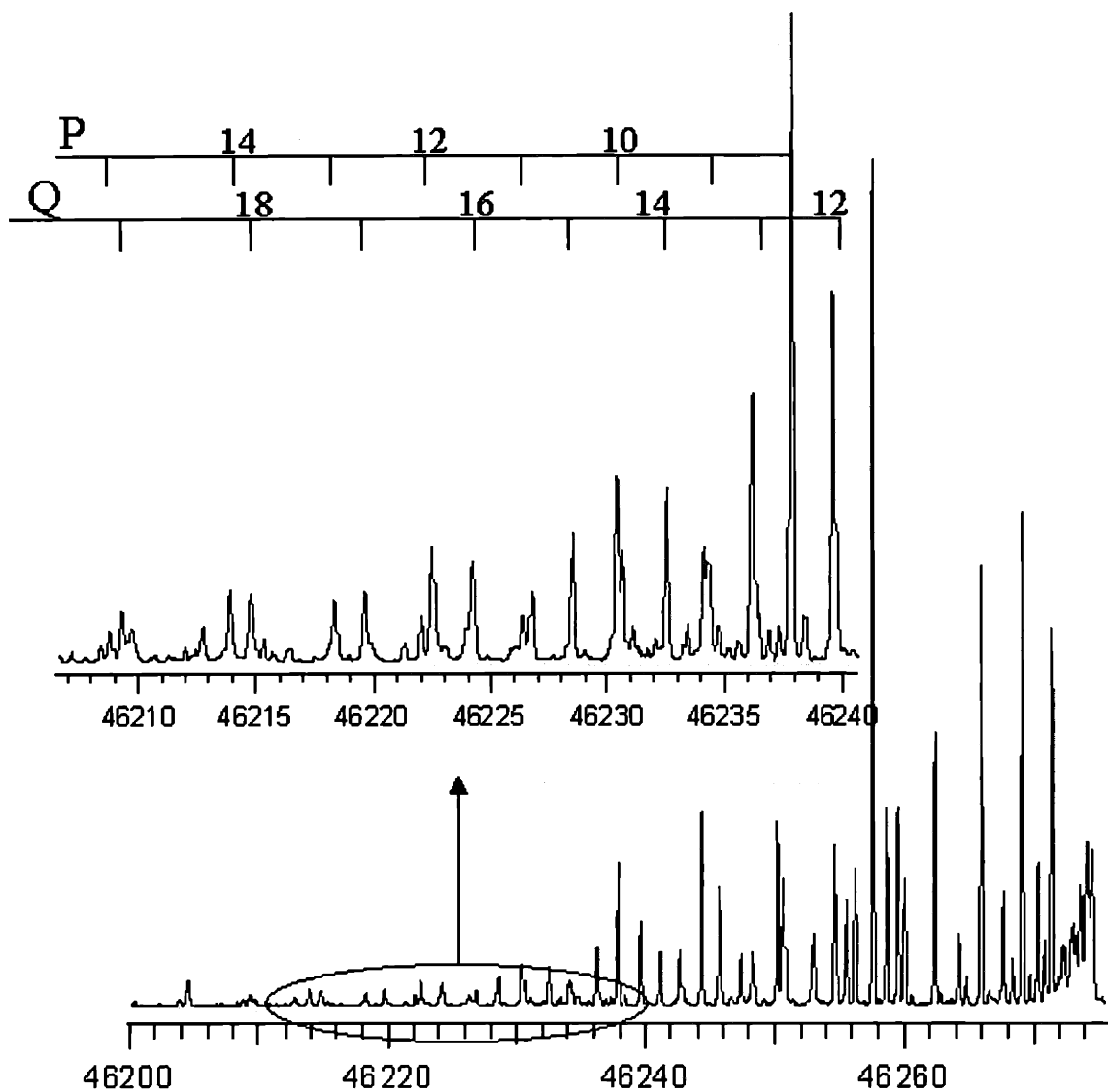


Figure 3-1: Laser Induced Fluorescence of the $V_0^4K_0^1$ Band. Nuclear spin statistics predict a 10:6 intensity alternation for even:odd J . In the inset, doublings of several lines in the P branch, that are the result of a B-type Coriolis perturbation, are clearly evident.

Table 3.3: Term values for observed perturbed transitions in the $V_0^4K_0^1$ band, which terminate on e-parity levels. The intensity information is used to determine the locations of the bright and dark states. The off-diagonal matrix elements between the two interacting states are also reported. All values are reported in cm^{-1} .

J'	J''	Term Value 1	Term Value 2	Intensity Ratio	Bright State	Perturbing State	Coupling
8	9	46334.89	46335.05	10:9	46334.98	46334.97	0.081
9	10	46353.54	46353.81	2:1	46353.71	46353.64	0.13
10	11	46374.17	46374.53	5:8	46374.31	46374.39	0.18
11	12	46396.68	46397.16	10:7	46396.96	46396.87	0.24

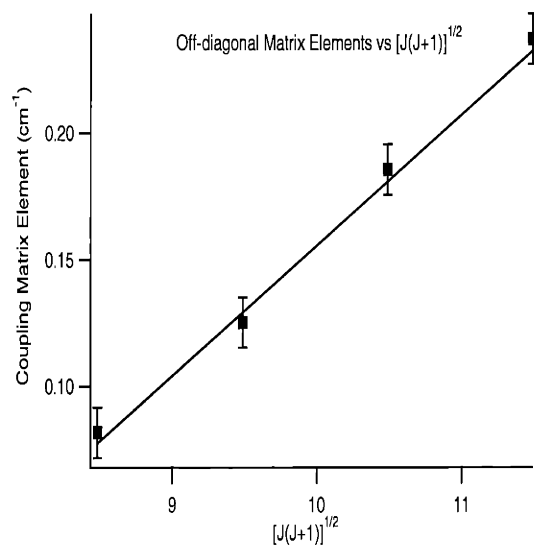


Figure 3-2: Off-diagonal matrix elements that couple the e-parity levels $J = 8-11$ of the V^4K^1 level to a nearby perturbing state. Note that the matrix elements scale roughly as $\sqrt{J(J+1)}$. The straight line is a fit of the data to $\sqrt{J(J+1)}$

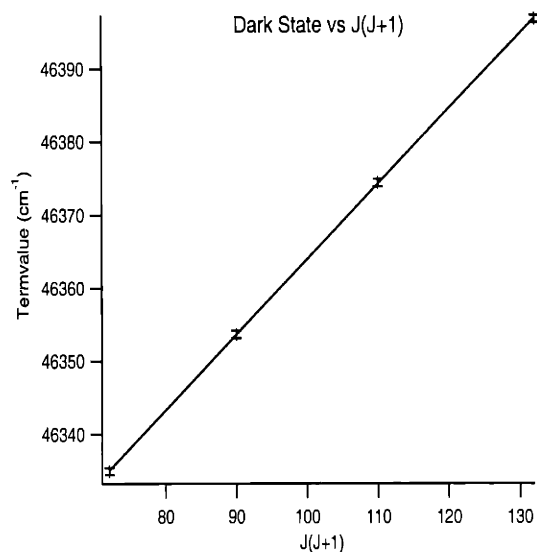


Figure 3-3: The zero-order energies of the perturbing state, observed in transitions that terminate on the e-parity levels of V^4K^1 , are plotted versus $J(J+1)$ in order to determine T_0 and an effective rotational constant, B . The fitted line is also shown.

the perturbing level observed in the P,R branch for $J=8-11$. A plot of the energy of the perturbing state versus $J'(J'+1)$ should be approximately a straight line and the vibrational band origin and effective B constant for the perturber can be determined from such a graph. The vibrational term value of the perturbing level, 46260.72cm^{-1} , lies approximately 0.5cm^{-1} higher than that of the V^4K^1 level and has an effective B rotational constant of 1.03cm^{-1} .

Table 3.4: Rotational constants determined from least squares fit to the data in table 3.3. Listed in parenthesis are the 1σ uncertainties in the last digits reported. All values are reported in cm^{-1} .

Parameter	$V_0^4K_0^1$	Perturber
T_0	46260.24(25)	46260.71(31)
B	1.063(03)	1.033(03)
C	0.964(03)	-
D_{JJ}	$8 \times 10^{-6}(4)$	-

The vibrational identity of the perturber is still ambiguous. Based on the spectra

of $^{12}\text{C}_2\text{H}_2$, it is likely that the perturber is a member of the $\nu'_3 + 4\nu'_6$ pentad. In the case of $^{12}\text{C}_2\text{H}_2$, Utz and coworkers [23] identified the singlet perturber of V^4K^1 as $\nu'_3 + 4\nu'_6$. The perturbation observed here in the $^{13}\text{C}_2\text{H}_2$ $V_0^4K_0^1$ band LIF spectrum appears only in the P,R branch transitions for $J=7-13$ and not in the Q branch transitions. Recall that the P and R branch transitions for $K'_a = 1 \leftarrow l'' = 0$ transitions for a symmetric vibration of a near prolate top terminate on e -parity states. Consequently, the perturbing state must have $K = 0$. Levels of $K = 0$ have only one parity and therefore may only interact with one of the two parity components of $K' = 1$ levels. If the perturber had been found to interact with both parity components then it must have $K' > 0$. As a result, this perturber is unambiguously determined to have $K'=0$ and e -parity. Furthermore, from this we can conclude that the interaction of the perturber with $V_0^4K_0^1$ occurs via a B -type Coriolis mechanism based on selection rules that require $\Delta K_a = \pm 1$ and $\Delta K_c = \text{odd}$. For a Coriolis interaction between vibrational levels Ψ_1 and Ψ_2 ,

$$\Gamma^{\Psi_2} \otimes \Gamma^R \otimes \Gamma^{\Psi_1} \quad (3.2)$$

must contain the totally symmetric irreducible representation. Note that $R = R_x, R_y, R_z$ since the Coriolis terms transform as rotations. For a B -type Coriolis interaction, Γ^R has b_g rovibrational symmetry in the C_{2h} point group. The vibrational level $4\nu'_3$ has a_g rovibrational symmetry. In order for Equation 3.2 to be satisfied, the perturber, Ψ_2 , must have b_g rovibrational character and B_u rovibronic symmetry. Taking this into account, it is plausible that the perturbing state is one of the b_g symmetry members of the $\nu'_3 + 4\nu'_6$ pentad. The possible assignments are then either $\nu'_3 + \nu'_4 + 3\nu'_6$ or $\nu'_3 + 3\nu'_4 + \nu'_6$. More information is needed about the exact nature of the interactions of the levels that compose the $4\nu'_6$ pentad before the perturber can be definitively assigned. For example, rotational constants for the ν'_4 and $3\nu'_6$ states as well as those of the $4\nu'_6$ pentad in $^{13}\text{C}_2\text{H}_2$ would aid in determining the character of the perturbation. In $^{12}\text{C}_2\text{H}_2$ the rotational constants of those states have been determined [36] and are instrumental in understanding the role of the $4\nu'_6$ pentad in the dynamics of the \tilde{A} state.

3.4 $V_0^3K_0^1$ LIF Spectra

Figure 3-4 shows a portion of the LIF spectrum recorded for the $V_0^3K_0^1$ band. There are several unidentifiable lines in this portion of the spectrum. From the figure it is evident that the low-J lines in the Q branch are perturbed. It was impossible to determine their exact assignment without information from other K subbands. Hot-band transitions originating from $l=1$ levels in the ground electronic would terminate on the same parity levels as those in the Q branch. The Q branch of cold band transitions, originating from $l=0$ levels in the ground state which include R and P branch transitions that have e-parity, terminate on f-parity levels. Hot-band transitions originating from $l=1$ levels can have either e or f parity and the Q, P and R branches terminate on either e- or f-parity states depending on the parity of the $l=1$ ground state level. This allows for absolute rotational assignment of the observed perturbers of the low-J lines in the Q branch of the $V_0^3K_0^1$ band.

The perturbation is either due to interactions with the $4\nu_b$ pentad or interactions with a nearby triplet state. In $^{12}C_2H_2$, triplet perturbers and $4\nu_b$ perturbers have been identified in the Q branch of the $V_0^3K_0^1$ band. Fluorescence lifetime measurements would be able to distinguish between the two types of perturbers. Triplet states are long-lived in comparison to singlet states and, in the case of $^{12}C_2H_2$, the fluorescence decay from rovibrational levels in V^3K^1 , which are perturbed by triplet states, is on the order of microseconds, whereas the fluorescence decay from an unperturbed singlet state is on the order of 300 ns. However, the experiments performed here are done in a room temperature cell at a pressure of 200 mTorr. The fluorescence decays under these conditions exhibit collisionally shortened decay rates and it is impossible to determine an accurate collision-free lifetime. By lowering the pressure in the cell to 50 mTorr it would be possible to measure lifetimes as long as 600 ns. In order to measure lifetimes on the order of microseconds, it would be necessary to use a molecular beam rather than an ordinary absorption cell.

There are also several other perturbations evident in the spectrum. For example, the P(7) and R(5) lines, which both terminate on the same upper state rotational

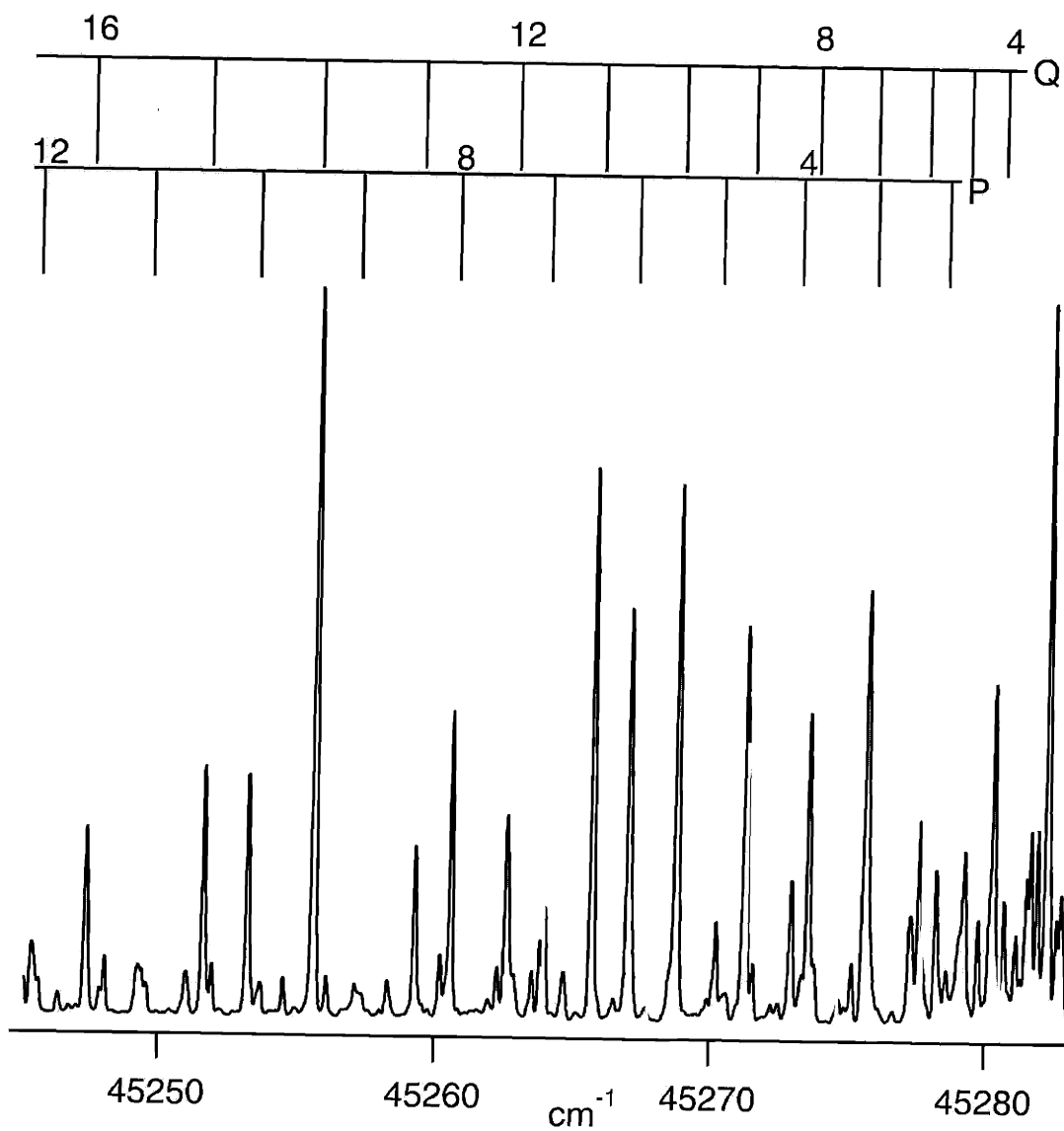


Figure 3-4: Laser Induced Fluorescence of the $V_0^3K_0^1$ band. The spectrum exhibits many perturbations. The lines Q(1) - Q(3), in particular, are extremely fractionated and it is difficult to assign them without performing a lifetime study or obtaining information from other vibrational bands.

level, consist of 3 resolved strong features. There are also two weak features slightly to the blue of P(5) and this pattern is replicated in R(3). Another perturbation is evident in P(9). The expected 10:6 intensity alternation dictates that P(9) should be weaker than P(10) or P(8), but the observed line strength is considerably weaker than expected. The P(9) line is so weak that it almost disappears. Lines terminating on higher lying even-J *e*-parity states, such as P(11), P(13) and P(15) are much stronger. Some of the unidentifiable lines may be attributed to hot-band transitions, triplet perturbers, or singlet perturbers. Since the extra lines could not be rotationally analyzed, it is presently impossible to determine their origin. The lines that could be identified and assigned to the $V_0^3K_0^1$ band were rotationally analyzed. The unperturbed lines were fit to Equations 2.3 and 2.4 and rotational constants were determined for the rovibronic levels of V^3K^1 .

The LIF spectrum was highly congested and Dispersed Fluorescence spectra from all the observed transitions in the R branch region of the spectrum were recorded in order to aid in assignment. The dispersed fluorescence experiments are described in Chapter 4. The low resolution dispersed fluorescence spectra recorded from different J-levels of the same vibronic transition should appear similar since they are described by the same set of Franck-Condon factors. DF spectra originating from different vibronic levels of the \tilde{A} state would of course have different Franck-Condon factors and as a result should look very different. By exploiting these Franck-Condon signatures, it was possible to separate all of the transitions in the R branch of the $V_0^3K_0^1$ band up to $J' \sim 23$ from transitions originating from a different upper state vibronic level. The use of the DF spectra greatly facilitated assignment of the returning high J-lines in the R branch. Figure 3-5 depicts most of the dispersed fluorescence patterns obtained for all observed transitions in the R branch region of the $V_0^3K_0^1$ band. In this figure the x axis is uncalibrated and is simply the pixel number on the intensified charge coupled device (ICCD). The grating position for all of these DF scans was centered at 300 nm. It is evident from the figure that transitions originating from rotational levels of V^3K^1 exhibit the same overall gross pattern in the dispersed fluorescence spectra. In other words, the interpolyad intensity patterns of vibrational levels of the

\tilde{X} state, are the same for transitions originating from the same \tilde{A} state vibrational band. If the transitions originated from different vibrational levels of the \tilde{A} state, the interpolyad intensity pattern observed in the DF spectrum for each transition would be different even though the intrapolyad intensity patterns would be similar, regardless of which vibrational band in the \tilde{A} state is excited. Moreover, several transitions were observed in the LIF spectrum and their DF spectra demonstrated that they do not belong to the V^3K^1 band. The vibronic character of these other levels has not been determined. The DF spectra of originating from these unknown upper state levels are shown in Figure 3-5.

Table 3.5 includes a list of all transitions assigned to the $V_0^3K_0^1$ band and the residuals of the fit to equations 2.3 and 2.4. Several perturbed lines were not used in the fit in order to obtain accurate rotational constants for the band and those lines are specified by an asterisk in the table. From the fit, the following molecular constants were determined: $T_e = 45282.92 \text{ pm } 0.35 \text{ cm}^{-1}$; $B = 1.06 \text{ pm } 0.005 \text{ cm}^{-1}$; $C = 0.967 \text{ pm } 0.005 \text{ cm}^{-1}$. The residuals (observed - calculated) are reported. The transitions were fit to within $<0.09 \text{ cm}^{-1}$. Considering that this spectrum is highly perturbed, the obtained rms error is perfectly reasonable.

Table 3.5: Assignment of Observed Rovibrational Transitions of the $V_0^3K_0^1$ band. Transitions are reported in cm^{-1} . The residuals reported are observed minus calculated values based on the least square fit to equations 2.3 and 2.4. The residuals are also reported in cm^{-1} . Transitions denoted with an * were not included in the fit to determine rotational constants.

$V_0^3K_0^1$							
J'	J''	Transition	Residual	J'	J''	Transition	Residual
19	20	45206.56	-0.037	9	9	45271.29	-0.002
18	19	45212.04	-0.036	3	4	45272.97	-0.024
17	18	45217.34	-0.036	8	8	45273.59	-0.035
16	17	45222.46	-0.021	7	7	45275.68	-0.012
14	15	45232.15	0.0046	2	3	45275.68	-0.033
19	19	45233.1	0.049	6	6	45277.61	0.11
13	14	45236.74	0.023	1	2	45278.22	-0.059
18	18	45238.18	0.052	5	5	45279.24 *	0.19
12	13	45241.1	-0.0016	4	4	45280.29	-0.057
17	17	45242.95	0.031	1	0	45284.89	-0.1

continued on next page

<i>continued from previous page</i>							
$V_0^3K_0^1$							
J'	J''	Transition	Residual	J'	J''	Transition	Residual
11	12	45245.31	-0.0053	24	23	45285.81 *	0.035
16	16	45247.33	-0.094	2	1	45287.08 *	0.16
10	11	45249.38	0.014	23	22	45287.97 *	0.17
15	15	45251.62	-0.035	3	2	45288.73	0.063
9	10	45253.22	0.0071	22	21	45289.62 *	0.006
14	14	45255.61	-0.0016	4	3	45290.28	0.018
8	9	45257.11 *	-0.17	21	20	45291.15 *	-0.072
13	13	45259.29	-0.00073	5	4	45291.7	0.008
7	8	45260.59	0.11	20	19	45292.71 *	0.084
12	12	45262.62	-0.068	6	5	45292.95 *	-0.007
6	7	45263.85 *	-0.0087	19	18	45293.9 *	0.063
11	11	45265.73	-0.099	18	17	45294.9	0.048
5	6	45267.06	-0.0084	8	7	45295.11	0.11
10	10	45268.79	0.1	9	8	45295.75	-0.018
4	5 *	45270.24	0.13	16	15	45296.35	0.029

3.5 Conclusion

In this chapter, LIF spectra of the $^{13}\text{C}_2\text{H}_2 \tilde{A}-\tilde{X} V_0^3K_0^1$ and $V_0^4K_0^1$ bands are reported. A rotational analysis of each band was performed. Additionally, both spectra exhibit several perturbations. In the spectrum of the $V_0^4K_0^1$ band, a B-type Coriolis perturber is observed. The vibrational identity of the perturber is uncertain. However, based on symmetry arguments and knowledge of perturbations of similar states in $^{12}\text{C}_2\text{H}_2$, it is reasonable to attribute the perturbation to $K=0$ levels of either $\nu_3 + \nu_4 + 3\nu_6$ or $\nu_3 + 3\nu_4 + \nu_6$.

In the case of the $V_0^3K_0^1$ band, the spectrum proved quite complicated to assign and deperturb. It is well known that the \tilde{A} state $3\nu_3$ level of acetylene is strongly mixed with singlet and triplet states. Assignment of several of the higher-J lines in the R branch was made possible by Dispersed Fluorescence spectra. The low-J levels in the Q branch are strongly fractionated and their dominant rovibronic character could not be determined.

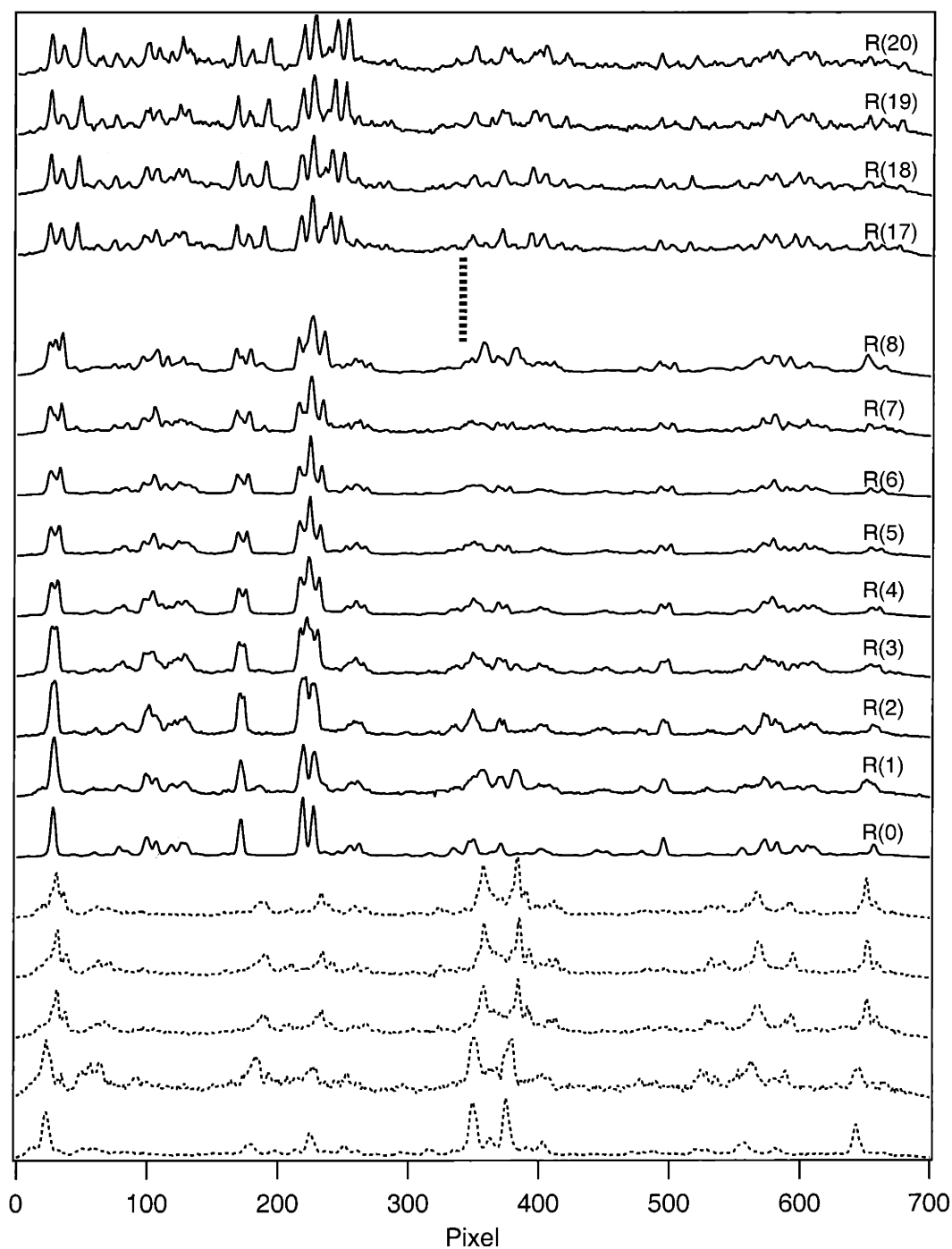


Figure 3-5: Dispersed fluorescence patterns originating from lines in the R branch region of the $V_0^3K_0^1$ band. It is easy to determine which transitions in the LIF spectrum originate from the same vibronic band. The solid curves correspond to DF spectra originating from rotational levels of the $V_0^3K_0^1$ band. The dotted lines are DF spectra originating from unknown rotational lines which do not belong to the $V_0^3K_0^1$ band.

Chapter 4

$\tilde{A} \ ^1A_u - \tilde{X} \ ^1\Sigma_g^+$ Dispersed Fluorescence Spectra of $^{13}\text{C}_2\text{H}_2$

Abstract

We have recorded dispersed fluorescence (DF) spectra (18 cm^{-1} resolution) from the $J_{K_a K_c} = 1_{10}$ rotational level of six vibrational levels in the S_1 ($\tilde{A} \ ^1A_u$) state of $^{13}\text{C}_2\text{H}_2$. Improvements in our methods of recording and calibrating DF spectra, that have enhanced the quality of our data sets, are briefly discussed. More than 50 fractionated bright state patterns associated with approximately conserved polyad quantum numbers have been extracted from our DF data sets using a spectroscopic pattern recognition technique, Extended Cross Correlation. These polyads extend to internal energies as high as 20,000 cm^{-1} above the zero-point vibration level. The polyad fractionation patterns observed at high energy are surprisingly simple relative to the corresponding patterns of $^{12}\text{C}_2\text{H}_2$. Comparison between the DF spectrum of $^{13}\text{C}_2\text{H}_2$ and $^{12}\text{C}_2\text{H}_2$ reveals slower intramolecular vibration redistribution in $^{13}\text{C}_2\text{H}_2$, particularly with nonzero quanta of CC stretch excitation. More than 15 patterns were extracted above the energy at which acetylene \leftrightarrow vinylidene isomerization is predicted to be energetically feasible ($\sim 15,200 \text{ cm}^{-1}$) and the dynamical information encoded in these patterns is addressed. In particular, we have analyzed a subset of the $^{13}\text{C}_2\text{H}_2$ polyads, the *pure bending polyads*, those with zero quanta of excitation in each of the stretch modes, [$N_s = v_1 + v_2 + v_3 = 0$]. The observed pure bending levels are reproduced to a root-mean-square error of $< 1.5 \text{ cm}^{-1}$ by two different effective Hamiltonian models: an 11 parameter normal-mode, and a 13 parameter local-mode model.

4.1 Introduction

Much effort has been invested in elucidating the short-time vibrational dynamics of the S_0 state of acetylene [7, 8, 9, 37, 11, 12, 13, 38], particularly because acetylene is one of the simplest systems capable of exhibiting bond-breaking isomerization. A set of 11 dynamically important anharmonic resonances governs the interactions among groups of nearly degenerate vibrational levels of the electronic ground state. This leads to a set of approximately conserved “polyad quantum numbers” for acetylene. Each polyad is uniquely defined by the quantum numbers $N_{\text{res}} = 5v_1 + 3v_2 + 5v_3 + v_4 + v_5$, $N_s = v_1 + v_2 + v_3$, $l = l_4 + l_5$, and the rigorously conserved quantum numbers, g/u symmetry, J , and parity. The polyad model for $^{12}\text{C}_2\text{H}_2$ is well established [11, 12, 13, 38].

There now exists a fairly complete understanding of the short time (~ 1 ps) acetylene bending dynamics at internal energy below $15,000\text{ cm}^{-1}$ [7, 8, 10]. The large-amplitude bending motions in acetylene have been intensely studied because they are expected to play an important role in promoting acetylene-to-vinylidene isomerization. The pure *cis* or *trans* bending normal-mode motions, by themselves, are not expected to lead to isomerization. However, local-bending motions, which have been demonstrated to be extremely stable at $\sim 15,000\text{ cm}^{-1}$ are closely linked to isomerization in acetylene [7, 8]. Numerous absorption, dispersed fluorescence (DF), and stimulated emission pumping (SEP) spectra have been recorded which probe $E_{\text{vib}} < 15,000\text{ cm}^{-1}$ but no spectroscopic signatures of acetylene \leftrightarrow vinylidene isomerization have yet been reported in frequency domain spectra, owing in part to the extreme complexity of these high energy spectra.

One predicted, but as yet unobserved, spectral signature of this isomerization process is spectrally resolved nuclear permutation tunneling splittings due to the exchange of the two hydrogen atoms between the two carbon atoms [19, 39]. Such splittings are unobservable in $^{12}\text{C}_2\text{H}_2$ because one component of each tunneling doublet has a nuclear spin statistical weight of zero. However in $^{13}\text{C}_2\text{H}_2$ this is not the case. Symmetrically ^{13}C substituted acetylene should exhibit nuclear permu-

tation tunneling splittings,[19, 39], thereby providing a way to observe directly the acetylene \leftrightarrow vinylidene isomerization dynamics. Therefore, we have begun a systematic spectroscopic study of $^{13}\text{C}_2\text{H}_2$.

Several absorption studies, which are sensitive primarily to CH stretch excitation, have been performed on $^{13}\text{C}_2\text{H}_2$ [40, 41, 42, 43, 44, 45, 1, 20]. The Dispersed Fluorescence (DF) spectra reported here, complement those previous studies because they sample levels which are highly excited in the *trans*-bend and CC-stretch modes which are Franck-Condon active normal-modes in the acetylene $\tilde{A}^1A_u-\tilde{X}^1\Sigma_g^+$ system. Within the Born-Openheimer approximation, the potential energy surfaces for $^{12}\text{C}_2\text{H}_2$ and $^{13}\text{C}_2\text{H}_2$ are identical, and due to the relatively small mass difference between ^{13}C and ^{12}C , the DF spectra and dynamics of $^{13}\text{C}_2\text{H}_2$ and $^{12}\text{C}_2\text{H}_2$ are expected to be quite similar. At low energy, ($E_{vib} < 10,000 \text{ cm}^{-1}$) the DF spectra of the two isotopomers are in fact nearly identical; the polyad patterns in $^{13}\text{C}_2\text{H}_2$ lie at slightly lower energy due to the $^{12}\text{C}-^{13}\text{C}$ isotope shift. However, at higher energy, close inspection of the bright state fractionation patterns (polyads) reveals a greater simplicity in the DF spectrum of $^{13}\text{C}_2\text{H}_2$ relative to that of $^{12}\text{C}_2\text{H}_2$. As a consequence of this greater regularity and simplicity, we believe that $^{13}\text{C}_2\text{H}_2$ will be a better choice than $^{12}\text{C}_2\text{H}_2$ for the study of acetylene vibrational dynamics above the threshold of isomerization. This unexpected simplicity is the focus of this paper. Section II contains a brief description of our methods for recording and calibrating DF spectra. In Section III we compare the vibrational dynamics of $^{13}\text{C}_2\text{H}_2$ and $^{12}\text{C}_2\text{H}_2$ as revealed by pattern-recognition analysis of their respective DF spectra. In Section IV we report the fitting of two effective Hamiltonian models (one using a local-mode basis set and the other a normal-mode basis set) to our data, and in Section V we summarize these results and discuss their implications for the study of acetylene vibrational dynamics.

4.2 Experimental Details

The DF spectra that sample the vibrational dynamics in the electronic ground state of $^{13}\text{C}_2\text{H}_2$ were recorded from several vibrational levels of the \tilde{A}^1A_u state. The data set

consists of DF spectra excited via the ${}^rQ_0(1)$ ($J'_{K_a, K_c} = 1_{1,0}$) lines of the $V_0^0K_0^1$ (origin band), $V_0^1K_0^1$, $2_0^1V_0^1K_0^1$, $V_0^2K_0^1$, $V_0^4K_0^1$, and $2_0^1V_0^2K_0^1$ vibrational bands. V represents the *trans*bending mode, V_3' in the \tilde{A} state and V_4'' in the \tilde{A} state, “2” represents the CC stretch, and K is the unsigned body-fixed projection of the total angular momentum. To our knowledge, no spectroscopic information has been published on the \tilde{A}^1A_u state of ${}^{13}\text{C}_2\text{H}_2$. Consequently, our first step was to map out the rovibronic levels in the \tilde{A}^1A_u state using Laser Induced Fluorescence (LIF) Spectroscopy. The results of the LIF experiments will not be discussed here since they are not directly relevant to the present study, but they will be addressed in a future article [46].

As discussed previously [47, 37], the ${}^rQ_0(1)$ line in several C_2H_2 $\tilde{A} \leftarrow \tilde{X}$ vibronic cold bands is chosen so as to minimize Coriolis effects and to simplify the rotational structure in the spectra. The DF spectra were recorded with 18 cm^{-1} resolution. The experimental methodology for recording these spectra has been reported previously [37] and is briefly reviewed here. The output of a XeCl excimer (Lambda-Physik LPX-210icc), 250mJ/pulse at 60 Hz, pumped Lambda-Physik FL2002 dye laser (10mJ/pulse), operated with Coumarin 440 or 450 dye, was frequency doubled to produce about 1 mJ/pulse of radiation tunable from 215–230nm with a spectral width $\leq 0.05\text{ cm}^{-1}$. The beam of fundamental radiation was separated from the doubled light and subsequently passed through a ${}^{130}\text{Te}_2$ ($\sim 500\text{ }^\circ\text{C}$) cell used for frequency calibration. The frequency doubled dye laser output was locked onto the ${}^rQ_0(1)$ line of each $\tilde{A} \leftarrow \tilde{X}$ vibronic band. The UV beam was passed through a static cell containing 1.0 Torr of ${}^{13}\text{C}_2\text{H}_2$ (MSD Isotopes, 98% pure) which was subject to several freeze-pump-thaw cycles before it was distilled into the sample cell using a pentane-liquid N_2 slurry ($-129.7\text{ }^\circ\text{C}$). Previously, DF spectra were recorded at higher gas pressures (typically 5 Torr). Here we have utilized a lower pressure to reduce the “quasi continuous baseline” and “extra features” observed in earlier DF studies of ${}^{12}\text{C}_2\text{H}_2$ which have been attributed to collisional energy transfer [14, 37]. These unwanted contributions were further reduced by gating only over the first 200 ns after the laser pulse, as opposed to $1\text{ }\mu\text{s}$, as had been done in previous DF studies. Consequently, we have virtually obviated the need for the baseline stripping algorithms

that we used to process $^{12}\text{C}_2\text{H}_2$ DF spectra [37], and have only performed minor baseline stripping of the DF spectra when necessary. The fluorescence was imaged onto the slit of a monochromator (Jobin-Yvon HR640mm, 1200 gr/mm grating) equipped with a Princeton Instruments intensified charge coupled device (ICCD), Model 1024-M059413, to record the dispersed fluorescence spectra. The entrance slit width of the monochromator was set to $\sim 100 \mu\text{m}$ and the grating was used in first order.

At each grating position, frequency calibration was performed using the emission from a series of atomic lamps (Fe, Kr, Ar, Xe, Hg, Ne) prior or subsequent to recording the acetylene fluorescence. Each DF segment (recorded at a particular grating angle) was recorded twice to permit the removal of spurious signals such as those due to cosmic rays. The grating positions were chosen such that each segment of spectrum overlapped with *at least half* of each adjacent segment. Previously, the DF segments were recorded such that the individual segments had minimal ($\leq 10\%$) overlap. That procedure enabled spectra to be recorded more rapidly, but made intensity calibration more difficult. Previously, in order to make meaningful comparisons between the intensities of peaks in adjacent segments, fluctuations in the laser power had to be monitored and accounted for in the concatenation of spectral segments. However, the current methodology permits superior intensity and frequency calibration, and improved signal to noise ratio. Intensity calibration is straightforward and virtually effortless due to the duplication of each segment of the spectrum. Direct comparison of the intensities of the replicated peaks in each segment eliminates the need to normalize each segment with respect to fluctuations in laser power. This is accomplished by creating a recursion map [5, 6] of the two frequency calibrated overlapping segments. (See Figure 4-1.) The intensity ratio of the segments is given by the slope of the line of the recursion map (the slope is generally close to 1) and least squares fitting of the recursion map slope is used to optimally scale the relative intensities of the segments.

Improvement of the intensity calibrations was not the only benefit from recording the segments in this 50% overlapped fashion. (See Figure 4-2). A trivial benefit is an improved signal to noise ratio, since fluorescence emission at each wavelength was recorded twice and could be averaged. Furthermore, each segment was frequency

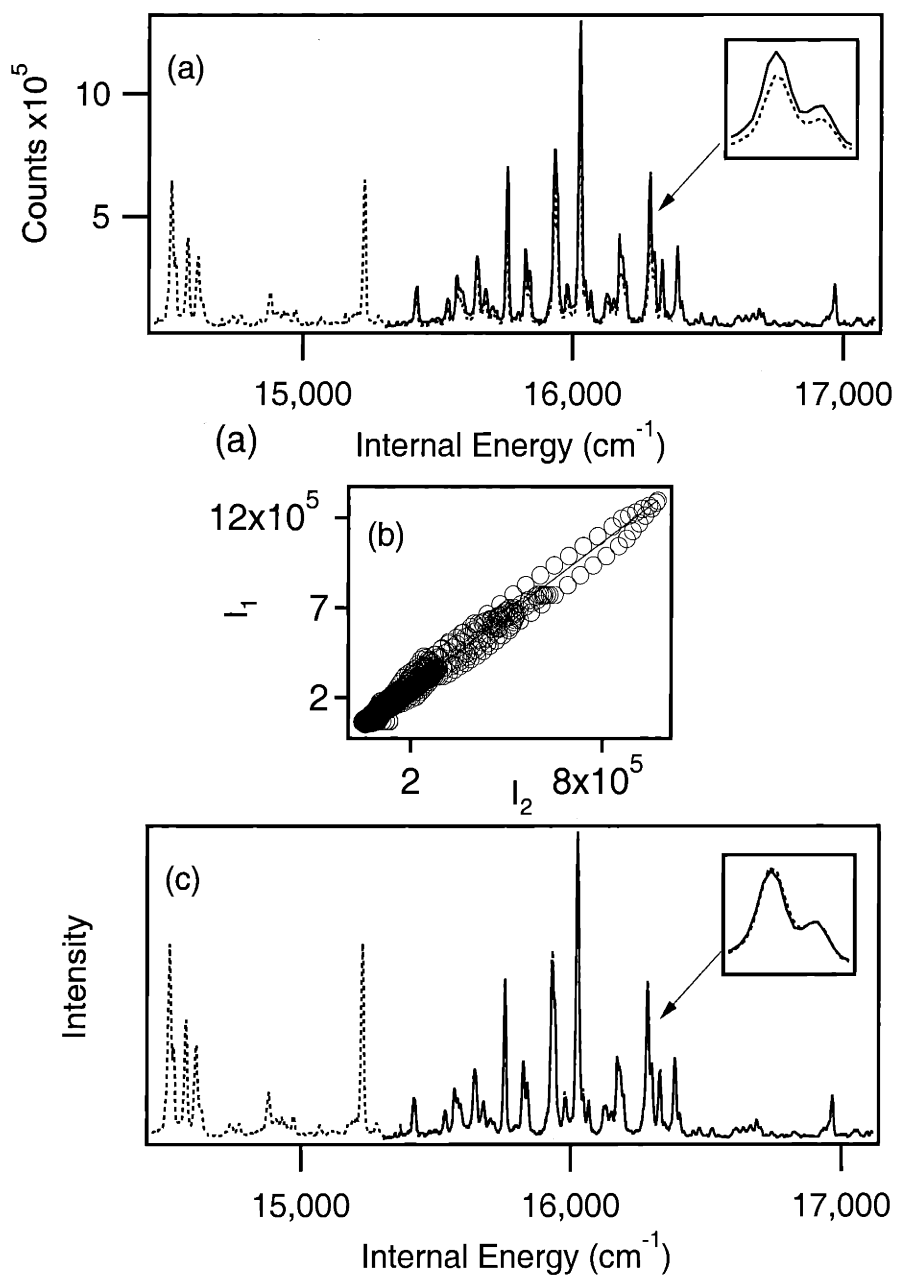


Figure 4-1: Panel (a) shows the unscaled raw spectra. Panel (b) is the recursion map of the overlapping portions of the frequency calibrated segments, where the intensity of one segment is plotted versus the intensity of the second. The intensity ratio of the segments is given by the slope of the line in the recursion map. Panel (c) depicts the intensity-scaled segments

calibrated independently. This eliminated gross calibration errors. Excess spectra (those portions of the segments which overlap by more than 50%) could be discarded, as illustrated in the top panel of Figure 4-2. Frequency calibration error is determined to be $\pm 0.93 \text{ cm}^{-1}$ (as determined by comparing the frequencies of lines in two independently recorded and calibrated segments). Additional details of our revised DF methodologies can be found in Ref. [14].

4.3 Results

The DF spectra excited via the $V_0^2K_0^1$, $2_0^1V_0^1K_0^1$, $2_0^1V_0^2K_0^1$ and $V_0^4K_0^1$ bands are shown in Figure 4-3. Spectra originating from the $V_0^0K_0^1$, $V_0^1K_0^1$, and $V_0^4K_0^1$ bands are not depicted here. The origin band DF spectrum is omitted since we were unable to record it with a signal to noise ratio comparable to the other bands. We recorded the $V_0^1K_0^1$ band DF spectrum only from $\sim 5,000$ to $18,000 \text{ cm}^{-1}$ to aid analysis of especially complex regions of the DF spectra where several patterns were strongly overlapped. In addition, the DF spectrum excited via the ${}^rQ_0(1)$ line of the $V_0^4K_0^1$ band exhibited the effect of an anharmonic perturbation in the \tilde{A} state and will be discussed later in this section. We achieved excellent signal to noise ratios in these spectra. For example, the spectrum from $V_0^2K_0^1$ band has a S/N ratio of 1000:1.

Figure 4-4 is a comparison of $^{12}\text{C}_2\text{H}_2$ and $^{13}\text{C}_2\text{H}_2$ DF spectra at low and high energy. As mentioned previously, at low vibrational energy the most intense features in the DF spectrum of $^{13}\text{C}_2\text{H}_2$ are shifted to slightly lower internal energy than the corresponding features of $^{12}\text{C}_2\text{H}_2$. This is predominantly due to the difference, $\Delta\omega_2 \approx 65 \text{ cm}^{-1}$, in the CC stretching frequency for the two isotopomers. Obviously, the relative shifts between the corresponding spectral features increase as the number of quanta of CC stretch increases. Neglecting this slight isotope shift, however, the patterns in the DF spectrum of $^{13}\text{C}_2\text{H}_2$ correspond one to one with those in $^{12}\text{C}_2\text{H}_2$.

At higher internal energy, contrasting behavior emerges. The $^{13}\text{C}_2\text{H}_2$ spectrum appears somewhat simpler (less fractionation) than the corresponding $^{12}\text{C}_2\text{H}_2$ spectrum, and this is indicative of slower IVR in $^{13}\text{C}_2\text{H}_2$. In order to examine this effect

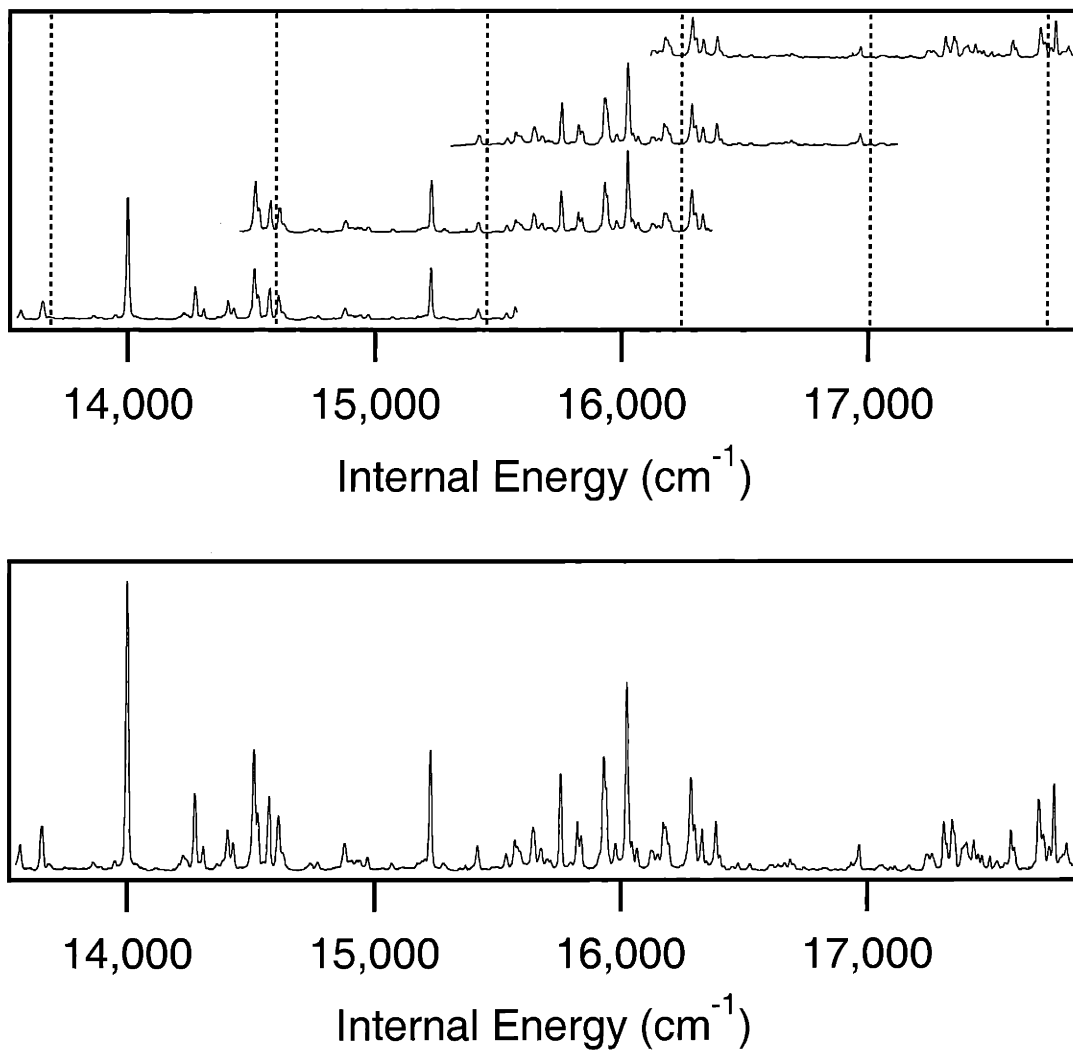


Figure 4-2: In the upper panel, 7 consecutive dispersed fluorescence segments are shown. Each segment overlaps with more than half of the adjacent segment. The bottom panel illustrates the result of the concatenation of the above segments.

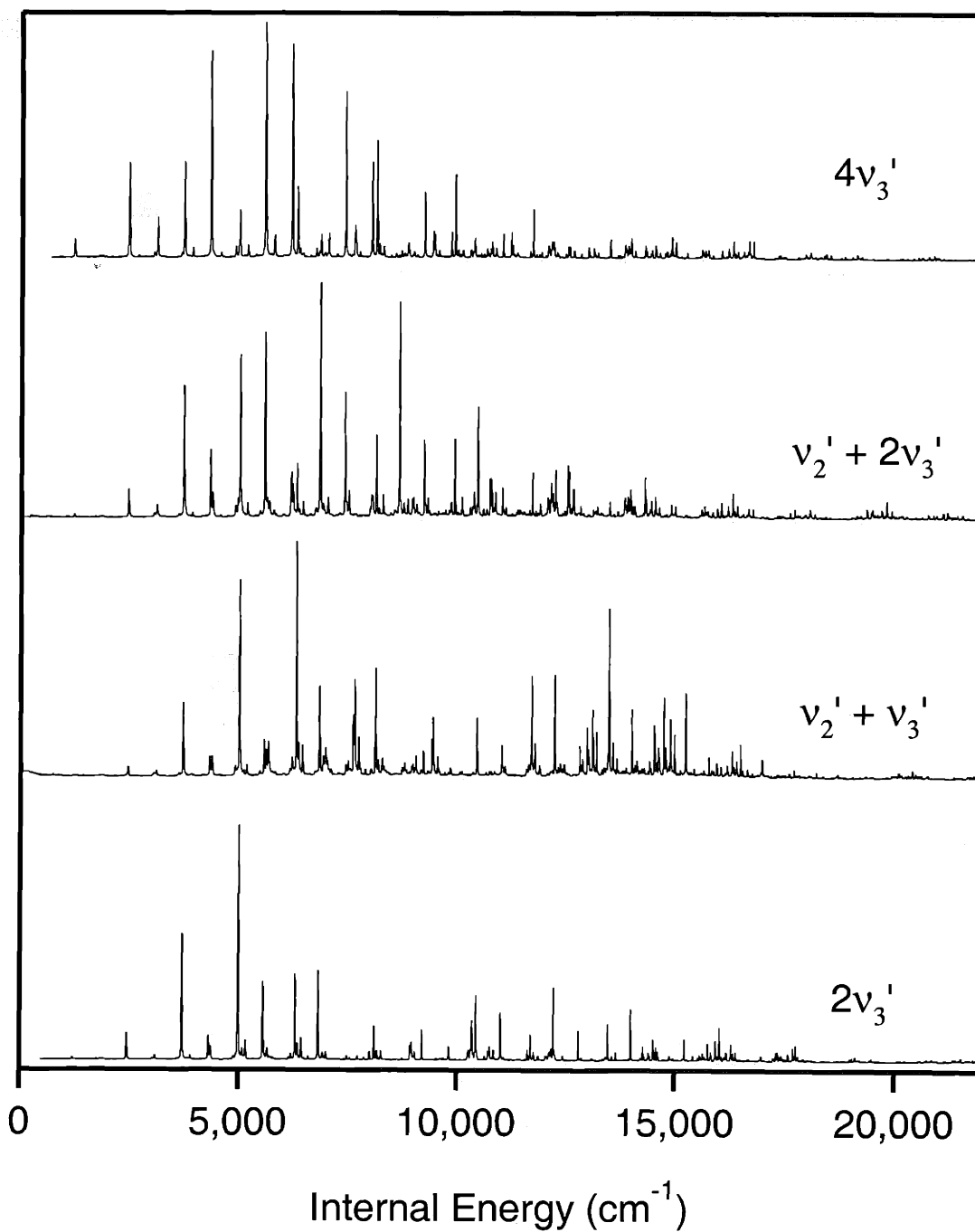


Figure 4-3: DF spectra excited via the $V_0^2K_0^1$, $2_0^1V_0^1K_0^1$, $2_0^1V_0^2K_0^1$, and $V_0^4K_0^1$ bands, which extend from 0 to 22,000 cm^{-1} of internal energy.

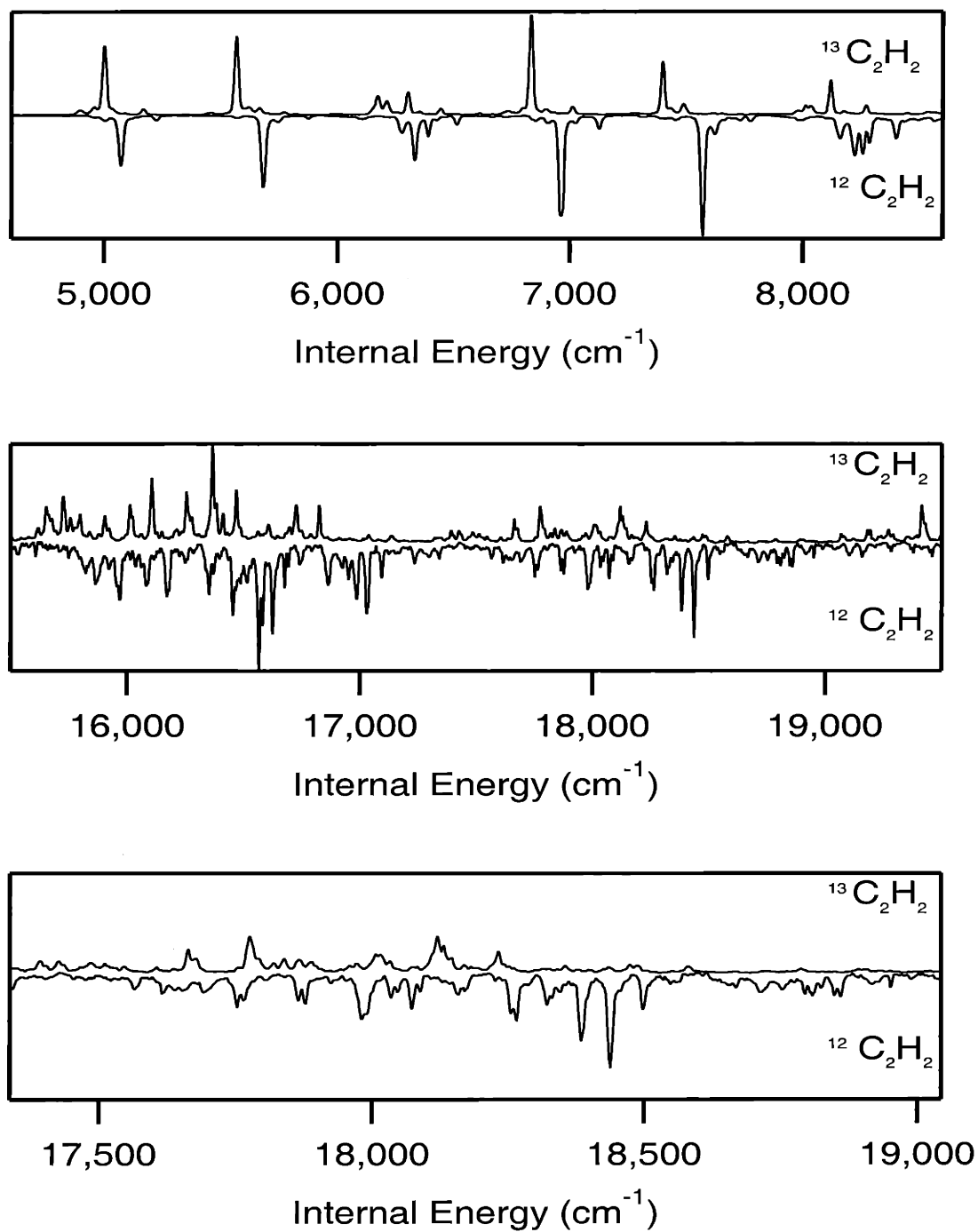


Figure 4-4: Comparison of the $^{12}\text{C}_2\text{H}_2$ versus $^{13}\text{C}_2\text{H}_2$ DF spectra at low and high energy. At low internal energy the spectra are quite similar but at high internal energy the $^{13}\text{C}_2\text{H}_2$ spectrum becomes obviously simpler.

more closely, the spectra have been processed using a spectral pattern recognition technique, Extended Cross Correlation, XCC,[5, 6] to extract the patterns associated with the approximately conserved polyad quantum numbers. We have extracted more than 50 distinct fractionation patterns from our DF data set. Figure 4-5, an “IVR map”, depicts some of these patterns arranged horizontally according to the number of quanta of *trans*-bend, v_4 , and vertically according to the number of quanta of CC-stretch, v_2 . With such a map, we can survey the systematic trends in the IVR as a function of increasing excitation in either of the two Franck-Condon bright modes.

Consistent with previous studies of $^{12}\text{C}_2\text{H}_2$, we find that the fractionation increases with increasing quanta of *trans*-bend for $v_4 \leq 14$ [9]. However, as the number of quanta of CC-stretch increases, the patterns change minimally. Specifically, the comparison of the fractionation patterns with $v_2 = 0$ and those with $v_2 = 1$ and 2 in Figure 4-5 shows that the polyad patterns are nearly independent of v_2 even at high internal energy. This simplicity can be attributed to the relative unimportance of the (3,245) stretch-bend resonance in $^{13}\text{C}_2\text{H}_2$ relative to $^{12}\text{C}_2\text{H}_2$. The (3,245) resonance is necessarily inoperative in $N_s = 0$ (pure bending polyads), but plays a critical role in the dynamics within $N_s \neq 0$ polyads in $^{12}\text{C}_2\text{H}_2$ [48, 9]. In $^{13}\text{C}_2\text{H}_2$ this resonance does not play such an important role because the energy difference, $\omega_3 - (\omega_2 + \omega_4 + \omega_5)$ is approximately 60 cm^{-1} in $^{13}\text{C}_2\text{H}_2$ whereas it is on the order of 2 cm^{-1} in $^{12}\text{C}_2\text{H}_2$. It is conceivable that the (3,245) resonance could turn on at higher energies. However, the effective mode frequencies and coupling matrix elements change in known ways, and it is straight forward to predict whether this stretch-bend resonance should begin to contribute to the IVR at high energy. The first (3,245) resonance relevant to the $(0, v_2, 0, v_4, 0)$ bright state IVR couples states $(0, (v_2 - 1), 1, (v_4 - 3)^1, 1^{-1})$ with $(0, v_2, 0, (v_4 - 2)^{+2}, 2^{-2})$ and $(0, v_2, 0, (v_4 - 2)^0, 2^0)$, which in turn are coupled to the $(0, v_2, 0, (v_4)^0, 0^0)$ bright state by Darling-Dennison resonances.

One way of understanding this interaction (at least qualitatively) is to investigate the semi-classical detuning of the zero-order frequencies of the modes in question. The classical frequencies can be computed from the effective Hamiltonian as the partial derivatives of the zero-order energies with respect to each of the quantum numbers.

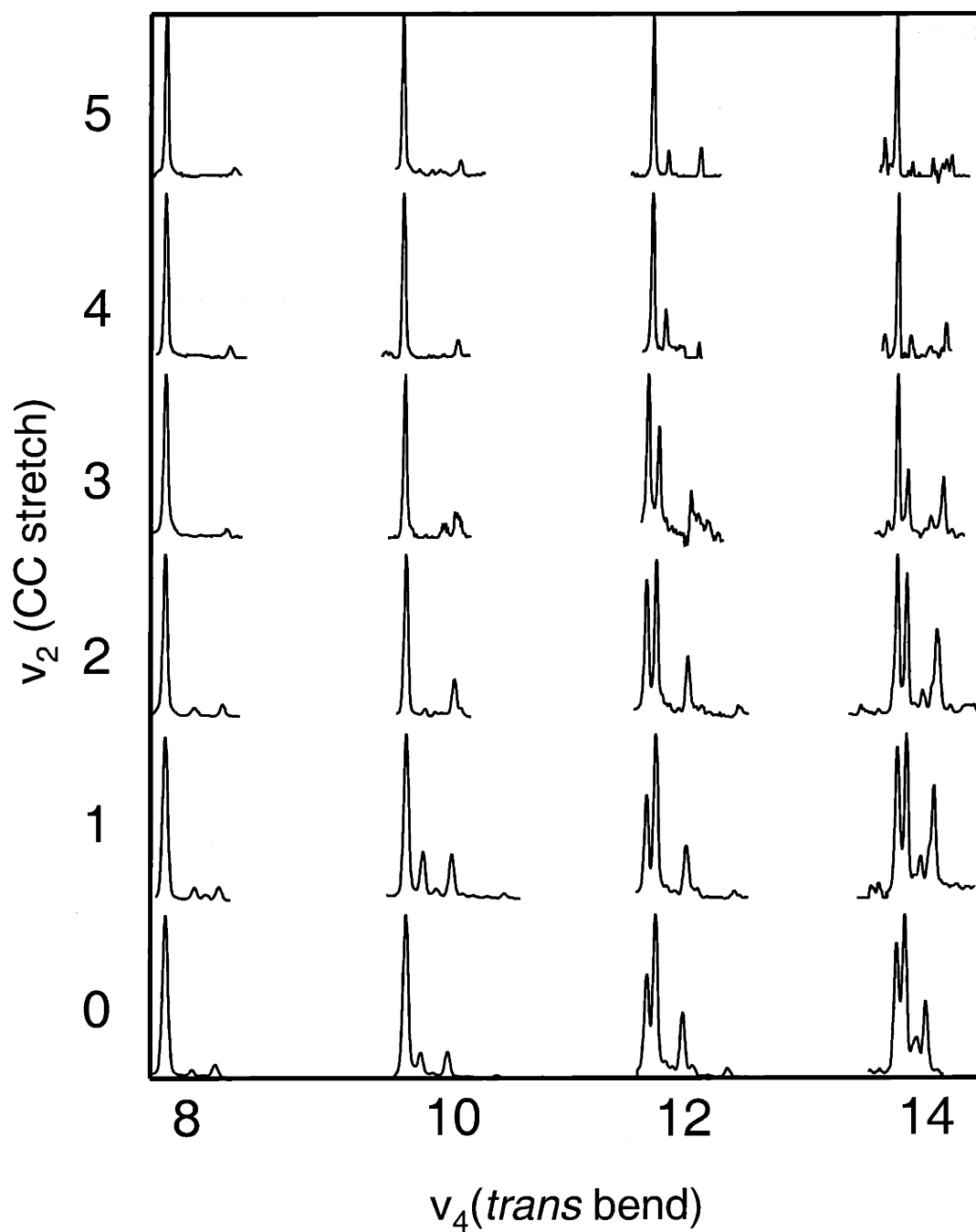


Figure 4-5: A sample of the extracted polyad patterns for $^{13}\text{C}_2\text{H}_2$ assembled into an IVR map. More than 50 distinct patterns have been extracted and identified. Here we show 24 of those patterns arranged according to the number of quanta of *trans*-bend, v_4 , and the number of quanta of CC-stretch, v_2 .

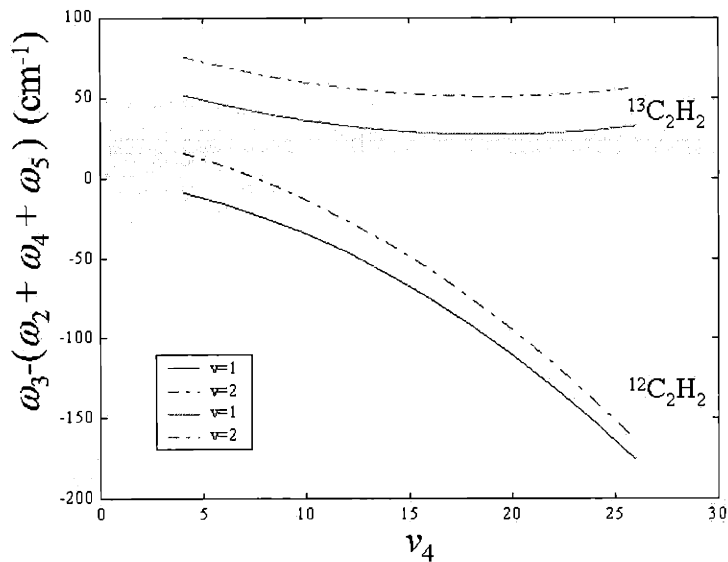


Figure 4-6: Classical mechanical zero-order frequency detuning for the (3,245) resonance in $^{13}\text{C}_2\text{H}_2$ and $^{12}\text{C}_2\text{H}_2$ calculated from our effective Hamiltonian model. $^{12}\text{C}_2\text{H}_2$ should be strongly influenced by the (3,245) resonance while $^{13}\text{C}_2\text{H}_2$ is not.

Figure 4-6 depicts the results of this calculation for both $^{13}\text{C}_2\text{H}_2$ and $^{12}\text{C}_2\text{H}_2$. The frequency detuning never crosses through zero as the number of quanta of *trans* bend increases in $^{13}\text{C}_2\text{H}_2$. However, this is not the case for $^{12}\text{C}_2\text{H}_2$. From Figure 4-6 it is obvious that the (3,245) resonance does not play as strong a role in $^{13}\text{C}_2\text{H}_2$ as compared to $^{12}\text{C}_2\text{H}_2$. Consequently, this resonance does not impact the IVR within the ≈ 0.3 ps short-time regime sampled by our spectra.

The polyad patterns extracted at high energy exhibit a beautiful simplicity. We have been able to extract at least 15 patterns at energies above the predicted zero-point-dressed energy of the acetylene \leftrightarrow vinylidene isomerization barrier [49]. These patterns were no more difficult to extract than those at low energy and, in general, they are similar in appearance to the fractionation patterns sampled at lower energy.

This is illustrated in Figure 4-7. The polyads $[N_{\text{res}}, N_s] = [20,0]$, $[23,1]$ and $[22,0]$ lie below the predicted zero-point isomerization energy but the other 5 polyads, $[26,2]$, $[25,1]$, $[28,2]$, $[24,0]$, and $[27,1]$, lie above it. The fractionation patterns of the 5 polyads which lie above the barrier are similar to those of the 3 polyads which lie below 15,000 cm^{-1} . (There is one spurious peak, indicated by an asterisk, in polyad $[25,1]$, which may belong to a different polyad but could not be removed by the XCC pattern recognition analysis.) These fractionated polyads consist predominantly of a three line fractionation pattern. Similar fractionation patterns have been identified previously in $^{12}\text{C}_2\text{H}_2$ and have been associated with local-mode behavior in the acetylene bend modes [8]. These patterns thus reveal nothing that could suggest isomerization on a 0.3 ps time scale.

4.3.1 V_0^4 band

The DF spectrum of the $V_0^4K_0^1$ band was excluded from the pattern recognition analysis of the $^{13}\text{C}_2\text{H}_2$ DF data set owing to a suspected perturbation of the $4V_3' K_a' = 1$ \tilde{A} state vibrational level. In Figure 4-8 the DF spectrum excited via the $V_0^4K_0^1$ band is compared with the pure bending bright state fractionation patterns extracted from the XCC analysis of $2_0^1V_0^1K_0^1$, $V_0^2K_0^1$, and $2_0^1V_0^2K_0^1$ vibrational band DF spectra. There is strong evidence for *two classes of bright states* in the $4V_3'$ DF spectrum. The single bright state expected in the DF spectrum is $(0, v_2, 0, v_4, 0)$. But states of the type $(0, v_2, 0, v_4 - 2, 2)$ appear to have their own intrinsic intensity in the $4V_3'$ DF spectra. The peak at $\sim 5010 \text{ cm}^{-1}$ is the $(0,0,0,8,0)$ bright state, weakly perturbed by at least two weak states that can be observed at $\sim 5090 \text{ cm}^{-1}$ and at $\sim 5170 \text{ cm}^{-1}$. However the nominal $(0,0,0,8,0)$ level at $\sim 5010 \text{ cm}^{-1}$ has nearly zero Franck-Condon intensity from the $4V_3', K_a' = 1$ vibrational level. The peak at $\sim 4975 \text{ cm}^{-1}$ in this spectrum arises from a different bright state, $(0,2,0,2,0)$. Despite the low FC intensity of the perturbed $(0,0,0,8,0)$ bright state in the $V_0^4K_0^1$ DF spectrum, the dominant perturbers of the bright state $[(0,0,0, 6^0, 2^0)$ and $(0,0,0, 6^{+2}, 2^{-2})]$ do have appreciable intensity. They could not have borrowed this intensity from the $(0,0,0,8,0)$ bright state because it had none to lend. The distortion in the fractionation patterns for other members

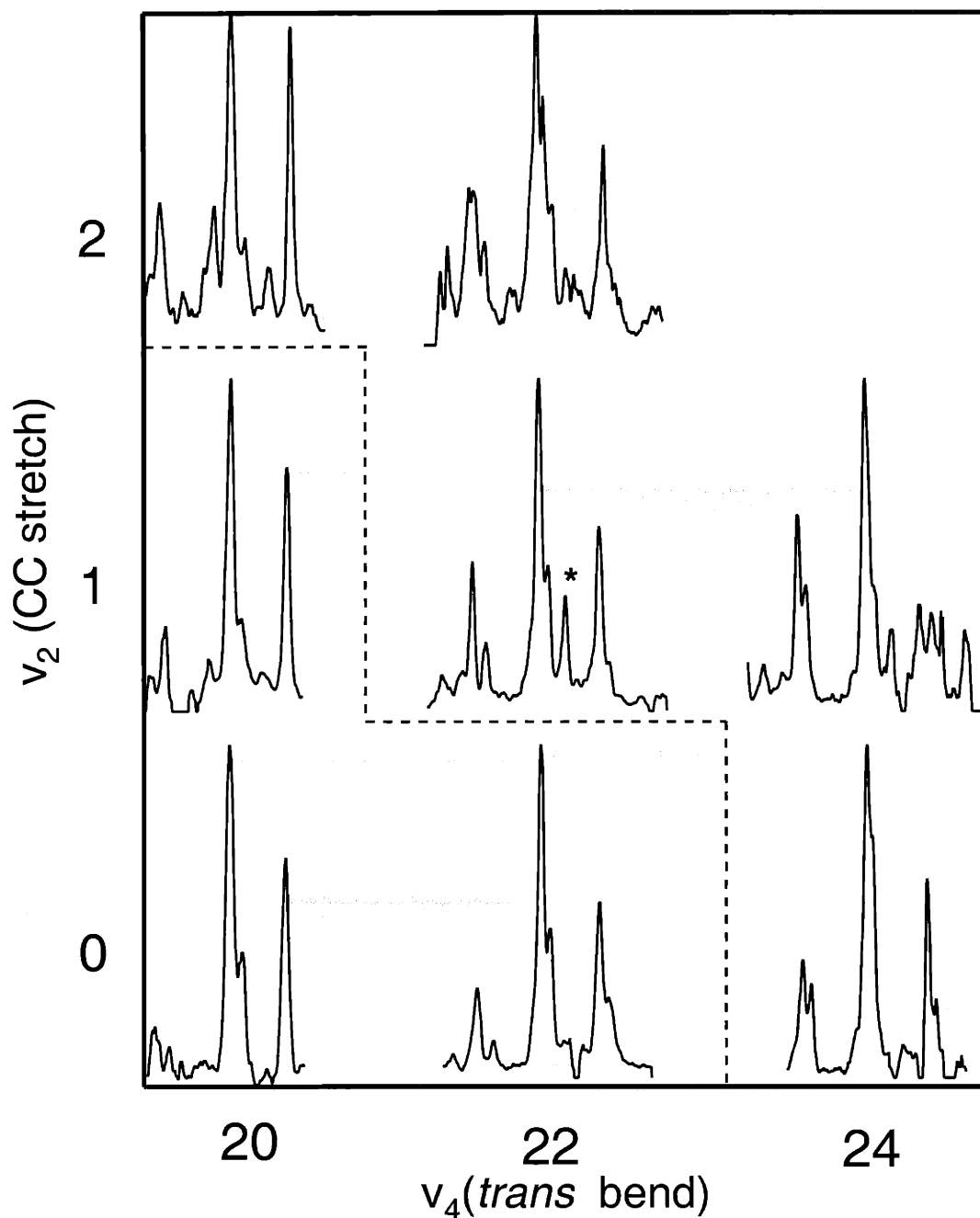


Figure 4-7: Extracted fractionation patterns above and below the lowest predicted zero-point dressed energy of the isomerization barrier. The polyads [20,0], [23,1], and [22,0] beneath the dashed line lie below the isomerization energy but the other 5 patterns above the dashed line lie above the isomerization barrier. Note the similarity in the fractionation patterns of the polyads. The spurious peak denoted with an asterisk in polyad [25,1] is attributed to a different polyad, but we were unable to disentangle the two polyads.

of the pure bending polyad progression, observed via the $V_0^4 K_0^1$ excitation, can also be attributed to an interference effect between the transition amplitude associated with the $(0, v_2, 0, v_4, 0)$ and $(0, v_2, 0, v_4 - 2, 2)$ bright states. Zero order $v_5'' \neq 0$ states are not expected to be bright in our dispersed fluorescence spectra because the *cis*-bend mode is Franck-Condon inactive. The only mechanism that could confer intrinsic brightness on $v_5'' \neq 0$ states in fluorescence from the \tilde{A} -state would require that the excited state wavefunction must have some *cis* bending character. The $4\nu_3', K_a' = 1$ level of the $\tilde{A}^1 A_u$ state could acquire *cis*-bend character through a perturbation by a state involving excitation in the ν_4' (torsion) and/or ν_6' (antisymmetric in-plane bend) modes, both of which correlate with the ground state *cis*-bend mode, ν_5'' . Anharmonic perturbations of this general type have been postulated to be responsible for the low-J perturbation of the $3\nu_3' K_a' = 1$ band in $^{12}\text{C}_2\text{H}_2$. These perturbations will be discussed in a future publication [46].

4.4 Effective Hamiltonian Models

4.4.1 Normal-Mode Fitting

Significant effort has been invested by several groups in developing effective Hamiltonian models for the $^{12}\text{C}_2\text{H}_2 \tilde{X}^1\Sigma_g^+$ state [9, 50, 12, 11]. Recently, Herman and coworkers have applied a similar model to $^{13}\text{C}_2\text{H}_2$ [1]. Their data set consists primarily of IR and Raman spectra, which, in the high energy regime, predominantly probe eigenstates with substantial CH stretch excitation. Our complementary DF data set yields information about high excitation in the *trans*-bend (up to at least $v_4'' = 24$) and CC stretch (up to $v_2'' = 7$) modes. As a preliminary step toward investigating the dynamics involved with isomerization, we have chosen to begin by fitting a subset of these polyads, the $N_s = 0$, pure bend polyads. In such a case, N_{res} simplifies to $N_{\text{res}} = v_4 + v_5 = N_b$, where N_b is the total number of bending quanta.

Most effective Hamiltonian models that have been used to fit acetylene vibrational levels have been expressed in terms of a normal-mode basis set. However, other classes

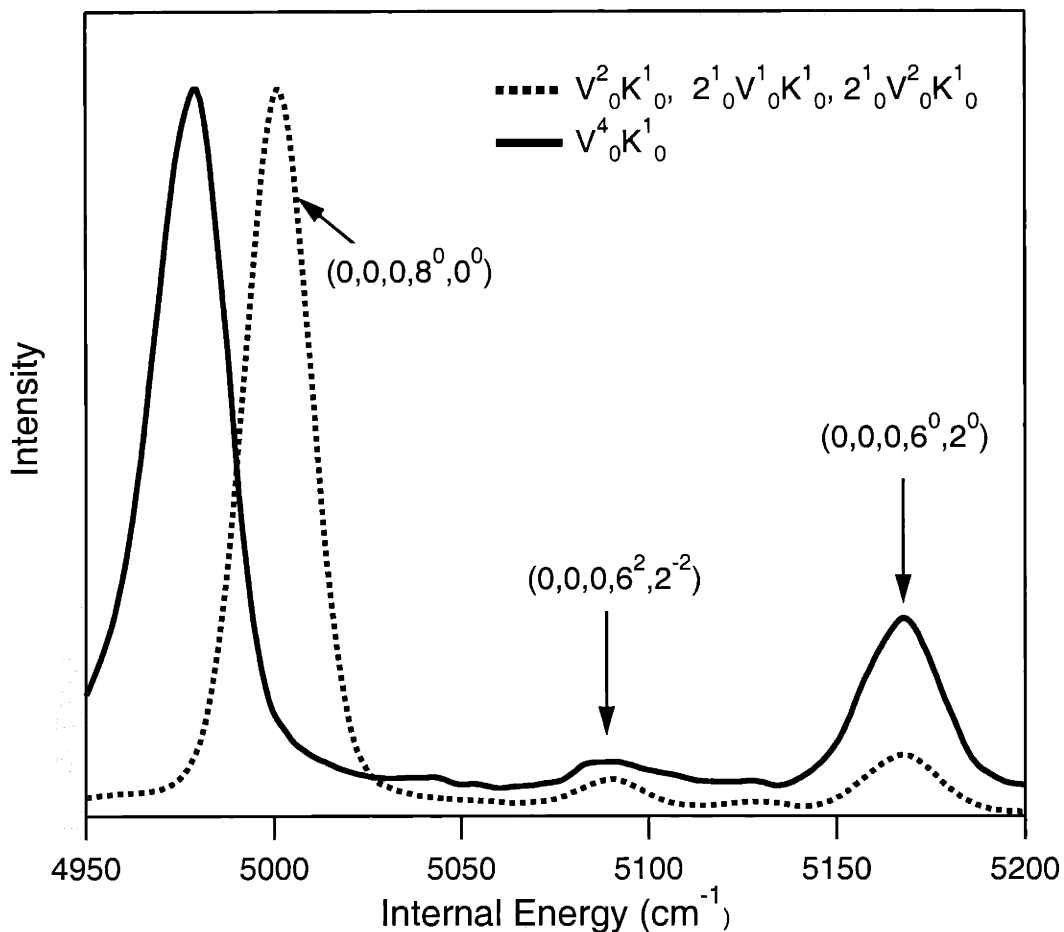


Figure 4-8: Comparison of the DF spectrum excited via the $V_0^4 K_0^1$ band with the pure bending bright state fractionation patterns extracted from the $2_0^1 V_0^1 K_0^1$, $V_0^2 K_0^1$, and $2_0^1 V_0^2 K_0^1$ vibrational band DF spectra. There is strong evidence for contributions from two classes of bright states in the figure. The usual bright state expected in the DF spectrum is $(0, v_2, 0, v_4, 0)$. Instead, states of the type $(0, v_2, 0, v_4 - 2, 2)$ appear in the $V_0^4 K_0^1$ DF spectra to have their own intrinsic intensity. This intensity in the $(0, v_2, 0, v_4 - 2, 2)$ bright state is present because of an anharmonic perturbation in the \bar{A} state.

of basis sets are possible. For example, systems with two coupled stretching modes (including acetylene) have been modelled using both normal-mode (symmetric and antisymmetric stretch) and local-mode (stretching of one of the two equivalent bonds) models [8, 51, 52, 53, 54, 55, 56, 57, 58]. Moreover, it has been demonstrated that the normal- and local-mode models are equivalent, at least order-by-order, and the parameters in the normal- and local-mode models can be related by so-called x-K relationships [53, 59, 60]. The acetylene bend modes can likewise be represented using either a normal- (*trans* and *cis* bend) or local- (two equivalent CCH bends) mode model [8, 51], and recently an explicit local-mode bending effective Hamiltonian has been developed for $^{12}\text{C}_2\text{H}_2$ [7]. Once again, the normal- and local-mode models are equivalent order-by-order, but the local-mode model provides a better *zero-order* representation of the bending quantum states/dynamics at high ($\sim 15,000 \text{ cm}^{-1}$) vibrational excitation, in the sense that most of the eigenstates can be assigned local-mode quantum numbers (the normal-mode representation is of course superior at low energies). Among the important implications of this finding is that there exists a class of highly excited (> 20 quanta) “local-bender” states which, in a classical sense, involve very large amplitude bending motions of a single hydrogen; in such a state, the molecule has a much larger probability of being located near the transition state for acetylene \leftrightarrow vinylidene isomerization than it does near the linear equilibrium geometry.

The data included in the fit are listed in Table 4.1. Note that we have adopted the notation used in reference [7]. The H_N^{eff} (normal-mode effective Hamiltonian) is similar to that used in previous studies of $^{12}\text{C}_2\text{H}_2$ [7]. The matrix elements for the effective Hamiltonian in the normal-mode basis are reported elsewhere [7, 12]. In our analysis, the IR and Raman data were weighted more heavily than the DF data, but not by the usual reciprocal squared uncertainty factor. Using the reciprocal-squared uncertainties as weights is most appropriate if the model being used can be expected to be essentially “perfect”, in the sense that all discrepancies between the predictions of the optimized model and the data would be attributable to measurement errors. That is clearly not the case here, due to the truncation of the Dunham expansion and

the omission of high-order resonances (which could lead to weak polyad breaking, for example). The weight values chosen, as well as other details of the fit methodology are explained in Ref. [8].

Table 4.1: Data included in the effective Hamiltonian fit. The vibrational energies in the lower section of the table are for the 31 pure-bending vibrational levels, observed by absorption spectroscopy, that were previously reported by Herman and coworkers[1]. The upper section of the table lists 30 pure-bending vibrational levels that were assigned by applying numerical pattern-recognition to our dispersed fluorescence data set. The columns N_b , l , and g/u specify the polyad and symmetry assignments of the vibrational levels included in the fit. For the $l = 0$ polyads, the parity of the vibrational wavefunctions is specified as a superscript; that is, “+” specifies a vibrational wavefunction of $\Sigma_{g/u}^+$ symmetry species, and “-” specifies $\Sigma_{g/u}^-$. The notations E_N^{calc} and E_C^{calc} refer to the normal-mode and local-mode fits respectively and $0^+/2$ designates an unresolved pair of $l = 0/l = 2$ eigenstates, the calculated energies of which were averaged.

N_b	l	g/u	$E^{obs}(\text{cm}^{-1})$	$E_N^{calc}(\text{cm}^{-1})$	$E_C^{calc}(\text{cm}^{-1})$
6	$0^+/2$	g	3718.21	3716.27	3716.70
6	0^+	g	3909.99	3906.97	3908.30
8	$0^+/2$	g	5001.06	5000.21	5001.75
8	0^+	g	5089.93	5089.83	5088.17
8	2	g	5127.97	5125.58	5125.73
8	0^+	g	5167.41	5165.90	5167.97
10	$0^+/2$	g	6303.19	6301.63	6304.57
10	$0^+/2$	g	6353.16	6353.12	6351.01
10	2	g	6393.80	6393.04	6393.55
10	$0^+/2$	g	6443.50	6440.95	6443.91
12	$0^+/2$	g	7611.04	7607.41	7609.74
12	$0^+/2$	g	7639.37	7607.41	7638.93
12	2	g	7671.36	7671.72	7673.00
12	$0^+/2$	g	7730.50	7727.46	7731.07
12	0^+	g	7762.76	7764.43	7762.54
14	0^+	g	8944.02	8941.95	8943.55
14	$0^+/2$	g	8970.78	8970.79	8969.33
14	$0^+/2$	g	9041.33	9042.54	9041.58
16	0^+	g	10361.1	10361.3	10361.2
18	$0^+/2$	g	11776.8	11778.8	11772.5
20	0^+	g	13099.9	13101.5	13101.1
20	$0^+/2$	g	13192.5	13194.6	13190.5
22	0^+	g	14407.8	14410.5	14410.6
22	$0^+/2$	g	14515.2	14514.7	14519.0

continued on next page

<i>continued from previous page</i>					
N_b	l	g/u	$E^{obs}(\text{cm}^{-1})$	$E_N^{calc}(\text{cm}^{-1})$	$E_L^{calc}(\text{cm}^{-1})$
22	0 ⁺	<i>g</i>	14613.1	14614.8	14611.0
24	0 ⁺	<i>g</i>	15825.9	15826.1	15827.7
24	2	<i>g</i>	15840.0	15838.6	15838.8
24	0 ⁺	<i>g</i>	15933.0	15933.1	15933.2
24	0 ⁺ /2	<i>g</i>	16033.8	16029.9	16032.9
24	2	<i>g</i>	16048.0	16047.6	16047.3
1	1	<i>g</i>	603.9	603.3	603.0
1	1	<i>u</i>	728.4	728.0	728.3
2	0 ⁺	<i>g</i>	1212.3	1211.8	1211.5
2	0 ⁺	<i>g</i>	1445.3	1444.9	1445.3
2	2	<i>g</i>	1215.5	1215.0	1214.7
2	2	<i>g</i>	1459.0	1458.7	1458.9
2	0 ⁺	<i>u</i>	1317.2	1316.6	1316.6
2	0 ⁻	<i>u</i>	1329.6	1328.5	1329.30
2	2	<i>u</i>	1336.7	1336.5	1336.5
3	1	<i>g</i>	1828.4	1828.5	1828.3
3	1	<i>g</i>	2036.4	2036.1	2036.1
3	1	<i>g</i>	2054.1	2053.5	2054.4
3	3	<i>g</i>	1834.8	1834.9	1834.9
3	3	<i>g</i>	2072.0	2072.5	2072.3
3	1	<i>u</i>	1921.3	1921.0	1921.0
3	1	<i>u</i>	1940.9	1940.5	1941.2
3	1	<i>u</i>	2164.7	2164.5	2164.7
3	3	<i>u</i>	1952.7	1953.2	1953.1
3	3	<i>u</i>	2192.1	2192.1	2192.0
4	0 ⁺	<i>g</i>	2448.7	2450.0	2449.9
4	0 ⁺	<i>g</i>	2626.4	2626.5	2626.3
4	0 ⁺	<i>g</i>	2872.8	2873.1	2873.0
4	0 ⁻	<i>g</i>	2639.5	2638.9	2639.7
4	2	<i>g</i>	2644.6	2645.4	2644.9
4	2	<i>g</i>	2886.5	2886.9	2886.6
4	0 ⁺	<i>u</i>	2531.6	2532.2	2531.8
4	0 ⁺	<i>u</i>	2743.4	2743.7	2743.4
4	2	<i>u</i>	2532.6	2532.9	2533.0
4	2	<i>u</i>	2758.7	2758.9	2758.6

One major difference of our H_N^{eff} fit model from previous $^{12}\text{C}_2\text{H}_2$ studies is that we have chosen to fit a smaller number of parameters. All sextic terms have been excluded except for y_{444} . By eliminating the diagonal anharmonicity terms, y_{445} , y_{455} , y_{555} , and higher order off diagonal terms, r_{445} , and r_{545} , we have reduced the number

of fit parameters to 11 in contrast with the 16 parameters used in the refinement of $H_{\mathcal{N}}^{eff}$ for $^{12}\text{C}_2\text{H}_2$ [7]. Our DF data set, which involves pure-bending bright states with $v_4' \leq 24$, is very sensitive to the y_{444} diagonal anharmonicity and for this reason it was included while the other y_{ijk} terms were held fixed at 0.0. Even with this reduction in the number of parameters, the model reproduced the observed “pure-bending” levels to within an RMS error of $\pm 1.33 \text{ cm}^{-1}$. Panels (a) and (b) of Figure 4-9 illustrate the results of this fit for polyads [12,0] and [24,0]. Our fit was able to reproduce fine details, such as the line at 7884 cm^{-1} .

Moreover, the fit worked equally well for polyads at high energy as it did for those at low energy. Note that the [24,0] polyad, which lies slightly above the energy for which isomerization is predicted to become energetically feasible, was retained in the fitted data set because it created no appreciable distortion of our $H_{\mathcal{N}}^{eff}$ fit results. It is important to note that the data in Table 4.1 were fit in a ‘boot-strapping’ manner [7]. Initially, the parameters were refined using only polyads at low energy. Subsequently, higher energy patterns were added one-by-one to the fit. The final results of our systematic refinement of the fit parameters are listed in Table 4.2. Constants not derived from our DF spectra (rotational constants, etc.), which were needed to define the $H_{\mathcal{N}}^{eff}$, were taken from reference [1].

4.4.2 Local-Mode Fitting

The local-mode fit was performed with exactly the same set of adjustable parameters used in previous studies of $^{12}\text{C}_2\text{H}_2$ [7]. For this study we used 13 parameters to perform the local-mode fit. The details of the $H_{\mathcal{L}}^{eff}$ have been discussed previously [7]. Because local-mode effective Hamiltonians, particularly for bend modes, remain less common than normal-mode models, we briefly review our notation and the terms in $H_{\mathcal{L}}^{eff}$. We designate the two equivalent 2D bend modes as “A” and “B”. For each local-bend, there is an identical Dunham-type expansion for the zero-order energies: $(\omega_A, x_{AA}, g_{AA}, y_{AAA} = \omega_B, x_{BB}, g_{BB}, y_{BBB})$. Cross-anharmonicities between the 2 local-bends are also included $(x_{AB}, g_{AB}, y_{AAB} = y_{ABB})$. The most important anharmonic resonance is the “1:1” resonance between the 2 local-bends, which is

Table 4.2: Parameters determined from a least-squares fit of the pure bending effective Hamiltonian, expressed in the *normal-mode basis set*, to the data set described in the text. Numbers in parentheses are 1σ uncertainties in the last digit (estimates obtained from diagonal elements of the covariance matrix). All parameters are in units of cm^{-1} .

Parameter	Fit Value (cm^{-1})
ω_4	598.921 (24)
ω_5	726.667 (23)
x_{44}	3.649 (6)
x_{45}	-1.756 (10)
x_{55}	-2.196 (5)
g_{44}	0.727 (22)
g_{45}	6.955 (30)
g_{55}	3.526 (20)
y_{444}	-0.0375 (28)
r_{45}	-5.986 (12)
s_{45}	-8.836 (24)

parameterized by λ [in the normal-mode picture, the 1:1 resonance is responsible for the difference in the *trans*- and *cis*- bend frequencies]. The strength of the 1:1 resonance also has a strong dependence on vibrational excitation, as represented by $\lambda_A = \lambda_B$ (linear dependence), $\lambda_{AA} = \lambda_{BB}$ (quadratic dependence), and λ_l (vibrational angular momentum dependence) parameters. Finally r_{AB} and s_{AB} parameterize the local-mode equivalent of the vibrational l-resonance and Darling-Dennison bend resonance, which exchange 2 quanta of excitation or vibrational angular momentum between the 2 local-bends.

Panels (c) and (d) of Figure 4-9 illustrate the results of our local-mode fit for polyads [12,0] and [24,0]. The parameters determined in this fit are found in Table 4.3. The pure-bend vibrational levels were fit to within an error of $\pm 1.22 \text{ cm}^{-1}$.

It is clear that both models do an excellent job of fitting the pure-bend polyads from Figure 4-9. The H_C^{eff} does a slightly better job of fitting our data (based on the RMS errors), but the normal-mode model contains 2 fewer parameters. These differences are minor, however, as might be expected given that the 2 models are equivalent, with the exception of the neglected sextic terms.

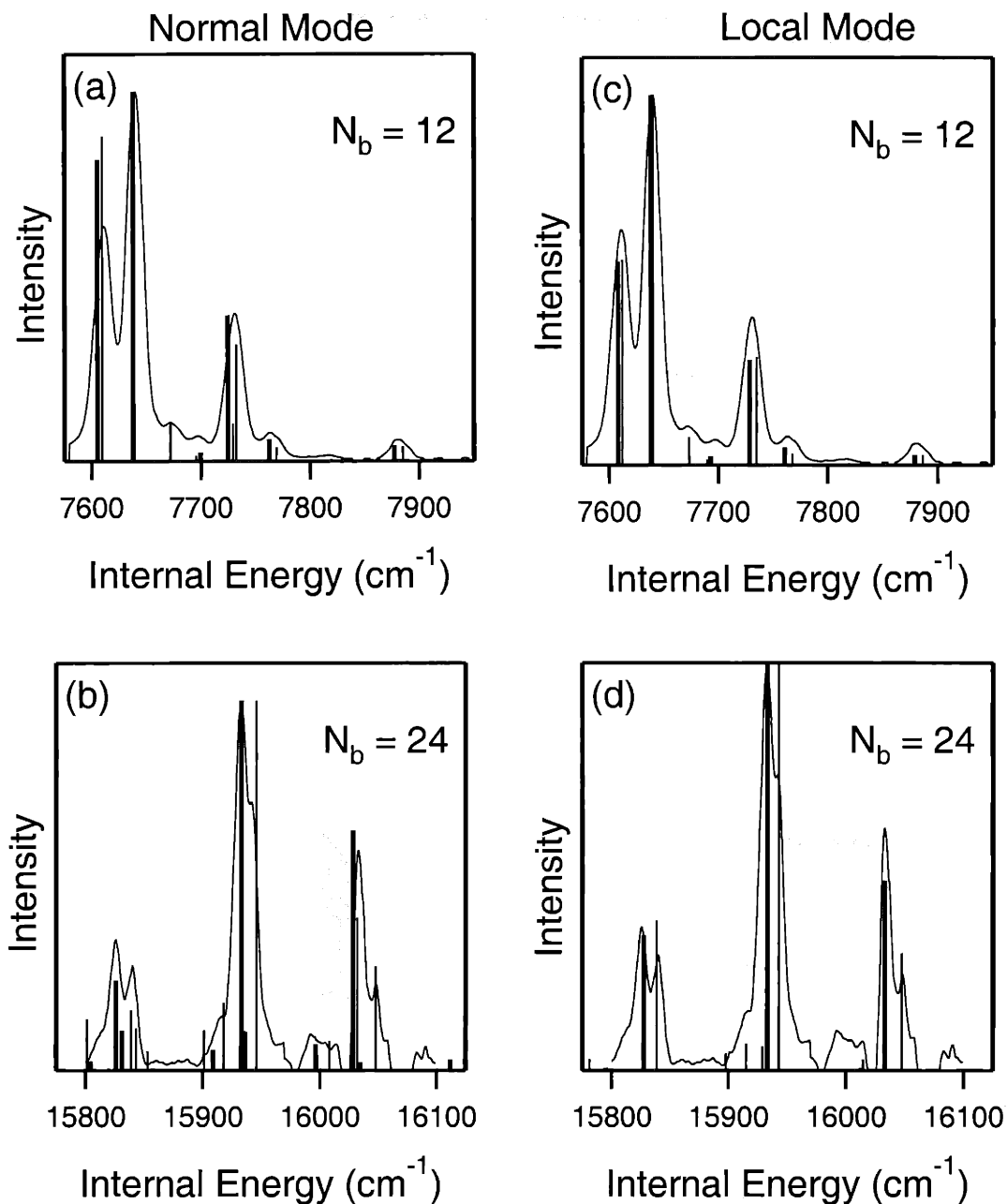


Figure 4-9: Panels (a) and (b) illustrate the results of the normal-mode fit for pure bend polyad fractionation patterns [12,0] and [24,0]. The fractionation patterns in the pure bend polyads were fit to an RMS error of ± 1.33 cm⁻¹. Panels (c) and (d) illustrate the results of the local-mode fit, and, in this case, the pure bend bright state fractionation patterns were fit to an RMS error of ± 1.22 cm⁻¹.

Table 4.3: Parameters determined from a least-squares fit of the pure-bending effective Hamiltonian, expressed in the *local-mode basis set*, to the data set described in the text. Numbers in parentheses are 1σ uncertainties in the last digit (estimates obtained from diagonal elements of the covariance matrix). All parameters are in units of cm^{-1} .

Parameter	Fit Value (cm^{-1})
$\omega_A = \omega_B$	662.139 (29)
$x_{AA} = x_{BB}$	-1.488 (15)
x_{AB}	1.850 (24)
$g_{AA} = g_{BB}$	5.026 (8)
g_{AB}	0.144 (17)
r_{AB}	3.669 (13)
s_{AB}	1.767 (19)
$y_{AAA} = y_{BBB}$	0 ¹
$y_{AAB} = y_{ABB}$	-0.0458 (11)
λ	-64.322 (37)
$\lambda_A = \lambda_B$	3.069 (10)
$\lambda_{AA} = \lambda_{BB}$	-0.0299 (4)
λ_l	-1.360 (7)

4.5 Conclusion

Despite the relatively small mass difference between ^{12}C and ^{13}C , the DF spectra of $^{13}\text{C}_2\text{H}_2$ exhibit a beautiful simplicity at high energy that is not seen in our previously reported $^{12}\text{C}_2\text{H}_2$ spectra. This is relevant to earlier SEP spectra recorded by Jonas [61]. SEP spectra of $^{13}\text{C}_2\text{H}_2$ around $15,000 \text{ cm}^{-1}$ were found to be considerably more sparse than comparable spectra of $^{12}\text{C}_2\text{H}_2$. The relative unimportance of the (3,245) stretch bend resonance in $^{13}\text{C}_2\text{H}_2$ versus $^{12}\text{C}_2\text{H}_2$ may account for the difference in the observed density of states.

The simplicity of the $^{13}\text{C}_2\text{H}_2$ DF spectra suggests that the least torturous path to insights into the unimolecular dynamics of acetylene at $E_{\text{vib}} > 15,000 \text{ cm}^{-1}$ will involve the $^{13}\text{C}_2\text{H}_2$ isotopomer. Careful analysis of the polyad fractionation patterns extracted from high resolution spectra should aid in elucidating the dynamics of the acetylene \leftrightarrow vinylidene isomerization process. To this end we have begun by modelling the pure bend polyads above $15,000 \text{ cm}^{-1}$. Efforts have been made to perform

a global fit to our entire DF data set, which covers polyads including up to 7 quanta of CC-stretching motion. At the threshold to isomerization, the local-bends will be especially sensitive to the onset of isomerization. Since we do not *directly* observe local-bending motion in our DF spectra, any effects of isomerization will at best be subtle. Taking this into consideration, it is understandable how the bright state fractionation patterns at $E_{vib} > 15,000 \text{ cm}^{-1}$ simply continue the trends in the bright state fractionation patterns observed at lower energy. Higher resolution studies, such as by SEP spectroscopy, may detect subtle changes in the spectrum as acetylene begins to be dynamically capable of isomerizing to vinylidene. Finally, this work provides guidance for future experiments aimed at obtaining direct spectroscopic evidence of isomerization. Through the careful selection of particular intermediate and final states, SEP spectra of $^{13}\text{C}_2\text{H}_2$ promise to reveal sample acetylene \leftrightarrow vinylidene isomerization, through both the manifestation of resolvable tunneling splittings and subtle changes in the polyad fractionation patterns, especially at the local-bend (low energy) extreme of each polyad.

Acknowledgments

We dedicate this paper to Professor Josef Plíva, whose insights and pioneering analyses built the foundation on which rest all insights into the dynamics of acetylene. This research has been supported by DOE Grant No. DE-FG0287ER13671. M.P.J. acknowledges support from the Department of the Army under a National Defense Science and Engineering Graduate Fellowship and from the Fannie and John Hertz Foundation. M.L.S. acknowledges AFSOR support from Grant No. AASERT-97-F49620-97-1-0384. The authors would like to thank Professor Michel Herman for a preprint of the article on $^{13}\text{C}_2\text{H}_2$ [1].

Chapter 5

Cavity Ring-Down Spectroscopy of $\tilde{A}^1A_u - \tilde{X}^1\Sigma_g^+$ Transition of $^{12}\text{C}_2\text{H}_2$: Determination of Absorption Cross Sections

5.1 Introduction

Cavity Ring-Down Spectroscopy, CRDS, is an ultra-sensitive, linear, absorption-based technique ideal for studying molecules that cannot be examined by either conventional absorption based methods or other widely used techniques such as Laser Induced Fluorescence (LIF), Resonance Enhanced Multiphoton Ionization (REMPI), or Stimulated Emission Pumping (SEP) [62, 63, 64]. The high sensitivity achieved in cavity Ring-Down experiments allows for the observation of very weak transitions, such as vibrational overtone transitions or nominally forbidden electronic transitions. Since CRDS is an absorption-based technique, it is possible to study molecules that do not fluoresce or cannot be conveniently or efficiently ionized such as radicals that dissociate too fast to be ionized. More importantly, CRDS can be used to extract quantitative information from CRD spectra, which accurately measure absorption

strengths (absorbance). If the concentration of a species is known, then CRDS can be used to extract absolute absorption coefficients. Or, if the absorption coefficient is known, then absolute concentrations of various species can be determined even in high pressure environments where collisions and chemiluminescence often interfere, such as flames and plasmas.

The ability to make sensitive quantitative absorption measurements makes CRDS extremely valuable. Typically, laser-based absorption experiments are degraded by excess noise, due to fluctuations in laser intensity, that prohibits one from attaining the shot noise limit.¹ For example, pulsed lasers typically exhibit pulse-to-pulse intensity fluctuations on the order of 10%. CRDS is immune to this noise because absorption in a CRD spectrum is a function of the Ring-Down rate of light in the cavity and is independent of the absolute intensity of the light impinging on the detector. Pulsed CRDS experiments routinely achieve minimum detectable absorption losses in the $10^{-6} - 10^{-10}\text{cm}^{-1}$ range and continuous wave CRDS experiments typically exhibit sensitivities on the order of $10^{-10} - 10^{-12}\text{cm}^{-1}$ [65]. CRDS outperforms other techniques employing either a multipass cell (sensitivity 10^{-6}cm^{-1}) or frequency modulation spectroscopy (sensitivity $10^{-6} - 10^{-8}\text{cm}^{-1}$) and in some cases it may even outperform techniques such as intracavity laser absorption spectroscopy (sensitivity $10^{-6} - 10^{-11}\text{cm}^{-1}$) [65].

We have chosen CRDS to study acetylene precisely because of its capability for ultra-sensitive and quantitative measurements. Ingold's and King's pioneering 1953 experiments were the first to provide absolute absorption strength measurements for the $\tilde{A} \ ^1A_u - \tilde{X} \ ^1\Sigma_g^+$ transition of acetylene. Using a discharge light source and a spectrograph equipped with photographic plates, they measured a series of bands in acetylene from 250-210 nm at gas pressures ranging up to 1.5 atm. Their work showed that the geometry of the upper electronic state was *trans*-bent which was the

¹The shot noise limit is the fundamental noise limit due to the interaction of a quantized light field with the electrons of the photodetector. The shot noise is proportional to the average photocurrent, and therefore proportional to the incident light field. The shot noise is given by: $(i_{shot})^2 = 2eBI_{dc}$ where e is the charge of an electron, B is the bandwidth of the detector, and I_{dc} is the average photocurrent.

first example of a complete rotational and vibrational analysis of a nonlinear↔linear electronic transition. Additionally, Ingold and King measured oscillator strengths for several bands by calculating the integrated intensity of each vibrational band. The intensity of a band is given by the total integrated absorption cross section of the band: $\alpha_v = \int \alpha_o dv$, which has units of cm^{-2} (if v is in units of cm^{-1}). The oscillator strength for a given band is then calculated using [3]:

$$f_v = \frac{mc^2}{\pi N e^2} \int \alpha_o dv \quad (5.1)$$

where m = mass of an electron, e = charge of an electron, c = speed of light, and N = molecules/ cm^3 in the vibrationless ground state. They identified a vibrational progression, which they referred to as the C series. Their C series is numbered 0 through 5 and corresponds to transitions from the vibrationless ground state to *trans* bending vibrations (0 through 5 quanta) in the upper electronic state. Values of α_v for this series were measured from several different spectrograms and were found to be consistent to within 15%. They then multiplied α_v by the appropriate constant factor of $4.78 \times 10^{-8} \text{ cm}^2$ for their experiments, to obtain f_v .

There are several motivations for remeasuring the absolute absorption strength of bands of the $\tilde{A} \ ^1A_u - \tilde{X} \ ^1\Sigma_g^+$ transition in acetylene via CRDS. First of all, in order to determine the electronic transition oscillator strength it is crucial to determine the oscillator strength for the origin band. Ingold and King were unable to measure the transition intensity for the origin band. It is necessary to determine this absolute absorption cross section as well as the cross section for several cold and hot-bands exciting exclusively the *trans*-bend in order to characterize how the transition moment depends on the *trans*-bending coordinate. At linear geometry, the $\tilde{A} - \tilde{X}$ electric dipole transition moment is zero by symmetry. A current major research effort in our group is the calculation of Franck-Condon factors for various transitions in the $\tilde{A} \ ^1A_u - \tilde{X} \ ^1\Sigma_g^+$ system of acetylene and its isotopomers. These calculations depend on accurately modelling the dependence of the electronic transition moment on the *trans*-bending displacement. The experimentally determined absolute absorption

strengths provide a valuable comparison for the calculated Franck-Condon factors and consequently a benchmark for determining the accuracy of the model used in those calculations.

Additionally, these experiments demonstrate that extremely sensitive absorption measurements can be performed in the ultraviolet region of the spectrum. To date, highly reflective mirrors, (mirrors with a reflectivity $> 99.5\%$) are not available for wavelengths shorter than 250 nm. As a result of the poor mirror reflectivity, the cavity lifetimes in the ultraviolet region are typically on the order of 1 microsecond, in contrast to the ≈ 100 microseconds achieved with mirrors operating in other spectral regions. In other words, the finesse, Q , of the cavity is lower in the ultraviolet and the laser beam experiences fewer round trips in the cavity. As a result it is difficult to achieve sensitivities comparable to those achieved in the visible or IR regions of the spectrum. Since the reflectivity of the mirrors in the UV is low we employ other methods to reduce the 'noise' in our measurements to obtain absorption sensitivities comparable to those reported in the visible and IR spectral regions. The CRDS scheme employed here minimizes 'noise' that results when the beam exiting the cavity translates across the nonuniform surface of the detector, thereby sampling regions of varying sensitivity. This noise appears as a modulation of the exponential decay and has been attributed to 'mode-beating'. The high sensitivity demonstrated in these CRDS experiments may be especially useful in future double resonance schemes for studying acetylene where low pressures are needed to prevent collisional depopulation.

5.2 History of CRDS

In the past decade Cavity Ring-Down Spectroscopy has become a widely used spectroscopic tool due to its experimental simplicity. CRDS originated from experiments in the 1980's aimed at measuring the properties of highly reflective mirrors, which were being developed for applications in high powered lasers, gyroscopes, and optical frequency standards [66, 67, 68, 65, 64]. The standard procedure was possible to determine the transmission of such mirrors with state-of-the-art power meters but

direct methods for determining their reflectivity and scattering/absorption losses did not exist. The first to propose to measure the decay rate of photons in an optical cavity was Herbelin [66] in 1980 and 5 years later this was achieved experimentally by Anderson [67].

In 1988, O'Keefe and Deacon [69] were the first to apply the Ring-Down methodology originally used for mirror reflectivity determination, as a spectroscopic tool in a pulsed cavity Ring-Down experiment. In their seminal paper on pulsed-CRDS, they reported absolute measurements of the doubly forbidden $b^1\Sigma_g^+ \rightarrow X^3\Sigma_g^+$ transition in molecular oxygen. In a static, 25 cm long gas cell, with $R > 99.5\%$ mirrors O'Keefe and Deacon [69] reported a sensitivity of $2 \times 10^{-8} \text{ cm}^{-1}$.

Since 1988, CRDS has gained widespread use in experimental Physical Chemistry. It is beyond the scope of this work to provide a detailed and comprehensive discussion of the variety of CRDS experiments performed over the past 13 years. Instead, it is best to briefly mention a few of the pioneering achievements made using CRDS. For a complete review of the state-of-art of CRDS experiments, the reader is referred to a paper by Scherer, Paul, O'Keefe, and Saykally [64] and the book edited by Busch et al [63], which contains articles written by the most prominent groups in the CRDS field.

In 1990, cavity Ring-Down spectroscopy was adapted by O'Keefe and the Saykally group at Berkeley for use in molecular beam studies of transition metal clusters [70]. They achieved a sensitivity on the order of 10^{-8} cm^{-1} for their studies of copper clusters produced in a laser vaporization supersonic expansion and they were able to perform rotational analysis of the observed transitions. Later work in that group extended CRDS to examine organic species and water clusters [71]. Lin and coworkers [72] were the first to demonstrate that CRDS could be used in kinetic studies. Such experiments in chemical kinetics are feasible when the rate processes are slower than the Ring-Down decay. Lin et al examined the formation of the phenyl radical by laser photolysis of nitrobenzene. Romanini and Lehmann [73] were the first to use CRDS to study the dynamics of highly excited vibrational states in small polyatomic molecules. Their work centered on overtone spectroscopy of HCN. They achieved a sensitivity

on the order of 10^{-10}cm^{-1} using a two-channel boxcar instead of by digitizing the waveform. In HCN, they observed Coriolis coupling and the Herman-Wallis² effect, which enabled them to improve upon the models describing the vibrational structure and electric dipole moment function of HCN at high energy [73, 74, 75, 76].

Numerous advances have emerged from Meijer's group in Nijmegen, who exploited short cavities in their pulsed CRDS experiments in the ultraviolet region. They studied such species as the OH radical [77], O₂ [78, 79], and were the first to use pulsed-CRDS for trace gas detection [80] in the uv region. They were the first to realize that non-exponential decays result if the laser linewidth is greater than the absorption linewidth. They also developed many other variations on pulsed CRDS, such as polarization dependent pulsed CRDS [81], Fourier transform CRDS [80], phase-shift pulsed CRDS [82].

Other important early contributors to the field of pulsed -CRDS include the Zare [83, 84] group at Stanford and Hodges, Looney, and van Zee [85] at the National Institute of Standards and Technology.

Continuous wave cavity Ring-Down spectroscopy, although more difficult to implement than pulsed CRDS, is also widely used. Meijer's group in Nijmegen successfully coupled cw laser light into a resonator and detected trace concentrations of various gas phase species [77, 78]. The Zare group at Stanford has also advanced the state of the cw - CRDS art, by using the Pound-Drever- Hall technique to lock the frequency of the laser to the Ring-Down cavity [86]. Using this technique, shot-noise limited sensitivities on the order of 10^{-8}cm^{-1} have been achieved. By combining heterodyne detection methods, such as frequency modulation spectroscopy, with cw-CRDS, the detection and resolution limits have been pushed even further, as will be discussed in chapter 6.

²In HCN, the Herman-Wallis effect accounts for an asymmetry in the line intensities for the P and R branches due to Coriolis coupling.

5.3 Theoretical Background: Two Distinct Viewpoints

The basic principles governing CRDS have been reviewed on many occasions and rigorous treatments can found in the works of Lehmann and Romanini [73] and Zalicki and Zare [87]. The pulsed UV-CRDS experiments in the Field group have also been described elsewhere [62] however, for the sake of completeness, a theoretical treatment of CRDS will be briefly reviewed here.

There are two distinct models that can be used to describe the interaction of a light pulse with a Ring-Down Cavity, RDC. The first model, referred to as the 'ping-pong' model by Zare [65], provides a rather simplistic yet useful description of CRDS, in which the pulse bounces between the cavity mirrors. On each bounce, a small fraction of the light is transmitted through the mirror out of the cavity. The second, more sophisticated approach takes into account the transfer function of the cavity and more accurately describes the interaction of light injected into the RDC. First let us consider the simplest case of a light pulse bouncing between two mirrors. The intensity of the pulse exiting the cavity on the n -th bounce, I_n , decays due to cavity losses and the overall envelope of the pulse exiting the cavity is an exponential decay. Each time the pulse encounters a mirror, it is attenuated due to the finite reflectivity of the mirror. However, there are several other loss mechanisms in the RDC. The pulse in the cavity experiences losses due to diffraction, Rayleigh scattering, and of course, from any absorbing medium in the cell. Consider the case where the laser pulse duration is shorter than the round trip time of the cavity. (This is a typical constraint for most naive treatments of pulsed CRDS experiments.) The round trip time of the Ring-Down cavity, RDC, is $t = 2L/c$ where c is the speed of light (2.99792458×10^8 m/s) and L is the cavity length. The output intensity I_{out} after n round trips is:

$$I_{out} = T^2(1 - \alpha L)^{2n+1}I_{in} \quad (5.2)$$

where, I_{in} is the initial pulse intensity, T is the transmission of each mirror, and αL

accounts for the total cavity losses. If the total cavity losses are small, $\alpha L \ll 1$, then equation 5.2 can be expanded and rewritten as

$$I_{out} = T^2 e^{-(2n+1)\alpha L} I_{in}. \quad (5.3)$$

The intensity of the first pulse exiting the cavity is simply $I_0 = T^2 e^{-\alpha L} I_{in}$. For the purpose of CRDS experiments, the absolute intensity is not important. Only the rate of change in intensity due to losses and absorptions is relevant. Consequently, the intensity of the first pulse exiting the cavity, I_0 , can be substituted into equation 5.3 and this result is rewritten to give:

$$\ln\left(\frac{I_{out}}{I_0}\right) = -(2n)\alpha L. \quad (5.4)$$

From this it is easy to see that a plot of the logarithm of $\frac{I_{out}}{I_0}$ vs n (or time) will yield the combined losses of the cavity. Recall that $\alpha = \alpha(\omega)_{abs} - \alpha_{cavity}$, where $\alpha(\omega)_{abs}$ is the frequency dependent loss due to an absorber in the cavity and α_{cavity} accounts for all other losses in the cavity that are not due to absorption. The loss described by α has units of cm^{-1} and $\alpha_{cavity} = \frac{1}{L}(T_{cav} + L_{cav})$ where T_{cav} and L_{cav} refers to the transmission and loss of the cavity respectively. When the round trip time is substituted back into Equations 5.4 we obtain:

$$\ln\left(\frac{I_{out}}{I_0}\right) = -n(\alpha(\omega)_{abs}ct + \alpha_{cavity}ct). \quad (5.5)$$

The Ring-Down signal has a first-order exponential decay envelope where the characteristic decay time, or Ring-Down time, τ , is given by $\frac{1}{\tau} = \alpha(\omega_{abs})c + \alpha_{cavity}c$. It is possible to determine the baseline, $\alpha_{cavity}c$ by measuring either the Ring-Down time with no sample in the cavity or by measuring the Ring-Down time in a region of the spectrum where the sample does not absorb. Experimentally it is not trivial to determine α_{cavity} . Since α_{cavity} is simply the loss present in an empty cavity, naively, one might assume that α_{cavity} could be independently measured, either before the sample is introduced to the cell or after the sample has been evacuated from the

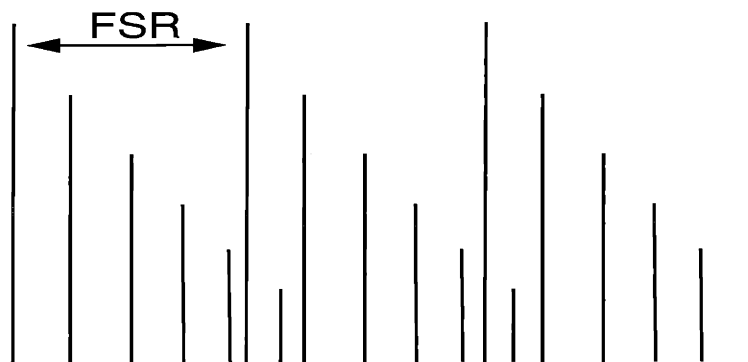


Figure 5-1: Mode structure of a resonator.

cavity. However, experimental difficulties preclude determination of the baseline in that manner. It was found that every time the pressure in the cell was drastically altered, by either adding or removing a sample, the baseline changed in an apparently random manner. This is due to the mechanical instability of the cavity. The random changes in baseline are due to infinitesimal motions of the mirrors in their mounts, which alters cavity alignment and therefore the Ring-Down time measured for the evacuated cavity. It is therefore necessary to determine the baseline while the sample is in the cavity. Since $\alpha(\omega)_{abs}$ is frequency dependent, the baseline can be determined by tuning slightly off resonance. However, care must also be taken not to tune too far off resonance, since the mirror reflectivity is wavelength dependent.

The ping-pong model described above provides an accurate basis for analysis of the spectrum obtained in a CRDS experiment, however, it does not accurately describe the interaction of the cavity with the laser pulse. In order to completely characterize this interaction, the transfer function of the RDC must be taken into account. The basic principle here is the fact that the cavity behaves as a Fabry-Perot etalon and is capable of supporting only certain frequencies of light, which are dependent on the specific modes of the cavity that are excited. The cavity modes are determined by the geometrical boundary conditions of the cavity. The transfer function of the RDC is a comb of Airy functions which appears as a series of repeating sharp resonances. This is illustrated by Figure 5-1. The spacing between identical resonances is determined

by the free spectral range, FSR, of the cavity. The FSR of a cavity is set by the cavity length, $FSR = c/2L$. The width of each resonance is determined by the FSR and the finesse, Q , of the cavity. The Q of a perfectly aligned cavity is primarily determined by the reflectivity of the cavity; the finesse increases as the reflectivity of the mirrors increases. The finesse of a cavity is given by the total loss of the cavity $Q_{cav} = \frac{2\pi}{\alpha 2L}$. The full width at half maximum of the cavity resonances is given by $\delta\nu = (FSR)/Q$, and from this relation, it is easy to see that as the finesse increases the cavity resonances narrow, thereby allowing less light to effectively couple into the cavity. If a very narrow laser frequency is needed for high resolution spectroscopy, use of a high finesse cavity is ideal for narrowing the frequency of a laser beam, as will be discussed in Chapter 6. Additionally, a higher RDC finesse results in longer Ring-Down times, thereby increasing the sensitivity of CRDS experiments. However, in some cases, higher finesse leads to other experimental difficulties that reduce the sensitivity. Less light is coupled into the cavity, and thus less light exits the cavity, necessitating the use of amplifiers which may increase the noise level. Ideally, a perfect amplifier would not add any noise above the shot noise limit, however this may not always be the case. The primary issues concerning additional technical noise, due to the use of an amplifier, deal with gain instability and nonlinearity of the amplification process.

Following the notation of Looney, Hodges, and van Zee in [88], the electric field of the light, \tilde{E} , at frequency ω , exiting the RDC using a field based description of the light and the RDC is given by a weighted sum of all the excited eigenmodes of the cavity [89]

$$\tilde{E}(x, y, L/2, \omega) = \sum_q \sum_{mn} C_{mn} \Psi_{mn} \tilde{e}_{qmn}(\omega) \quad (5.6)$$

where Ψ_{mn} refers to an eigenmode of the RDC, C_{mn} is a spatial overlap factor that accounts for the spatial coupling of the light into the cavity, and $\tilde{e}_{qmn}(\omega)$ is the spectrum of the mode leaving the cavity given by the product of the RDC response function, $\tilde{H}_{qmn}(\omega)$ and the incident field spectrum $\tilde{e}_i(\omega)$ [89]

$$\tilde{e}_{qmn}(\omega) = \tilde{H}_{qmn}(\omega) \tilde{e}_i(\omega). \quad (5.7)$$

Equation 5.6 gives the frequency dependent electric field exiting the cavity, but what is measured by a square law detector at the output of the RDC is actually the intensity of the field. The intensity of the field is found by spatial integration of the square of the Fourier transform of $\tilde{E}(x, y, L/2, \omega)$. The result, given by van Zee [89], is a complicated expression composed of two terms. The first term is a single summation over the longitudinal modes of the cavity which describes the exponential envelope of the decay. The second term resulting from the spatial integration of the square of the Fourier transform of $\tilde{E}(x, y, L/2, \omega)$ is a double summation which contains interference terms between the cavity modes. The interference terms have a cosine dependence on difference in frequencies for any two interacting modes. This accounts for the beating between these modes that results in a sinusoidal modulation of the exponential decay envelope. If only one longitudinal mode of the cavity is excited, the interference term disappears, however this single mode limit is usually not achieved in pulsed CRDS experiments. Typically, several longitudinal modes is excited and modulation of the exponential decay is observed. Whether a single mode or several modes of the RDC are excited depends on the cavity design and alignment, which will be discussed in the next section.

5.4 Brief Note on Cavity Design

In our experiments we utilize a symmetric resonator where the cavity is composed of two identical concave mirrors where the cavity length, L , is equivalent to $1.5R$, where R is the mirror radius of curvature. Figure 5-3 is a stability diagram for various types of resonators. For a symmetric resonator, the mirror curvatures are $R_1 = R_2 = R$ and the waist of the resonant Gaussian mode lies at the midpoint of the cavity, as shown in Figure 5-2. The beam waist, ω_0 , and end-mirror spot size, ω_1 , are given by Siegman [90] as:

$$\omega_0^2 = \frac{L\lambda}{\pi} \sqrt{\frac{1+g}{4(1-g)}} \quad \text{and} \quad \omega_1^2 = \omega_2^2 = \frac{L\lambda}{\pi} \sqrt{\frac{1}{4(1-g^2)}} \quad (5.8)$$

where $g_1=g_2=g=1 - L/R$.

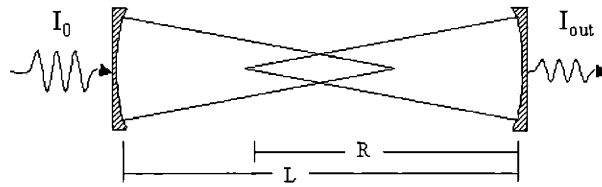


Figure 5-2: Symmetric Resonator where $R_1 = R_2 = R \geq L/2$.

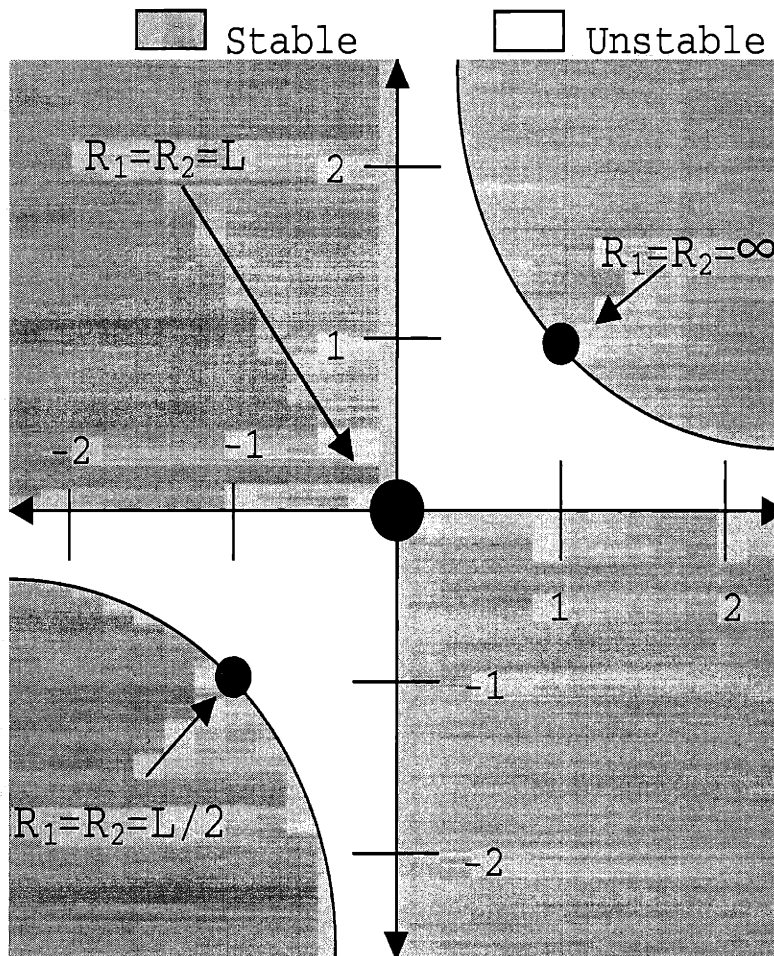


Figure 5-3: Stability diagram for various types of resonators.

In our experiments we use a symmetric resonator with $L=1.5R$. If the cavity is designed and aligned such that the constraint, $L=1.5R$, is exactly satisfied, then the pulse will exit the back mirror of the cavity in a repeating sequence of 3 stationary locations [62, 90]. The waveform observed from the detector will consist of 3 distinct groups of peaks, all with the same exponential decay constant but different initial intensities. This is illustrated in the top half of Figure 5-4. This is the mode-beating that is characteristic of the excitation of multiple longitudinal cavity modes, as discussed in the previous section. Each family of output beams experiences the same losses and therefore has the same decay constant, but the intensities are different because each spot samples a different region of the detector surface with nonuniform sensitivity. If the constraint that the cavity length is $1.5R$ is not met exactly, then many modes of the RDC are excited and the beam no longer exits the cavity in a repeating sequence of 3 stationary locations. The original 3 spots shift from one round trip to the next (pingpong model), resulting in the formation of Lissajous patterns of exit spots on the mirrors and detector. This results in a complicated seemingly random modulation of the Ring-Down signal, since the pulse is sweeping over the detector surface, sampling locations with varying quantum efficiency. The bottom panel in Figure 5-4 illustrates the signal observed from a cavity where the length is slightly offset from $1.5R$. One additional factor that can contribute to noise in the exponential decays, is associated with spatial mode-matching of the pulse to the TEM_{00} mode of the RDC. This is the C_{mn} term in equation 5.6. If the light is not spatially mode-matched to the cavity, some of it, and in the worst case, all of it is rejected from the cavity. This presents several problems. Firstly, if the beam is not spatially mode-matched, many modes of the cavity besides the TEM_{00} mode are excited and this leads to mode-beating. Also, if the pulse is not spatially filtered and matched to the cavity, the size of the beam waist on the exit (and entrance) mirror is modulated on every roundtrip and each of the 3 spots will have a different size on each pass through the cavity and therefore sample different amounts of the nonuniform surface of the detector. Consequently, the noise level increases. Finally, lack of spatial mode-matching results in a lower pulse power reaching the detector.

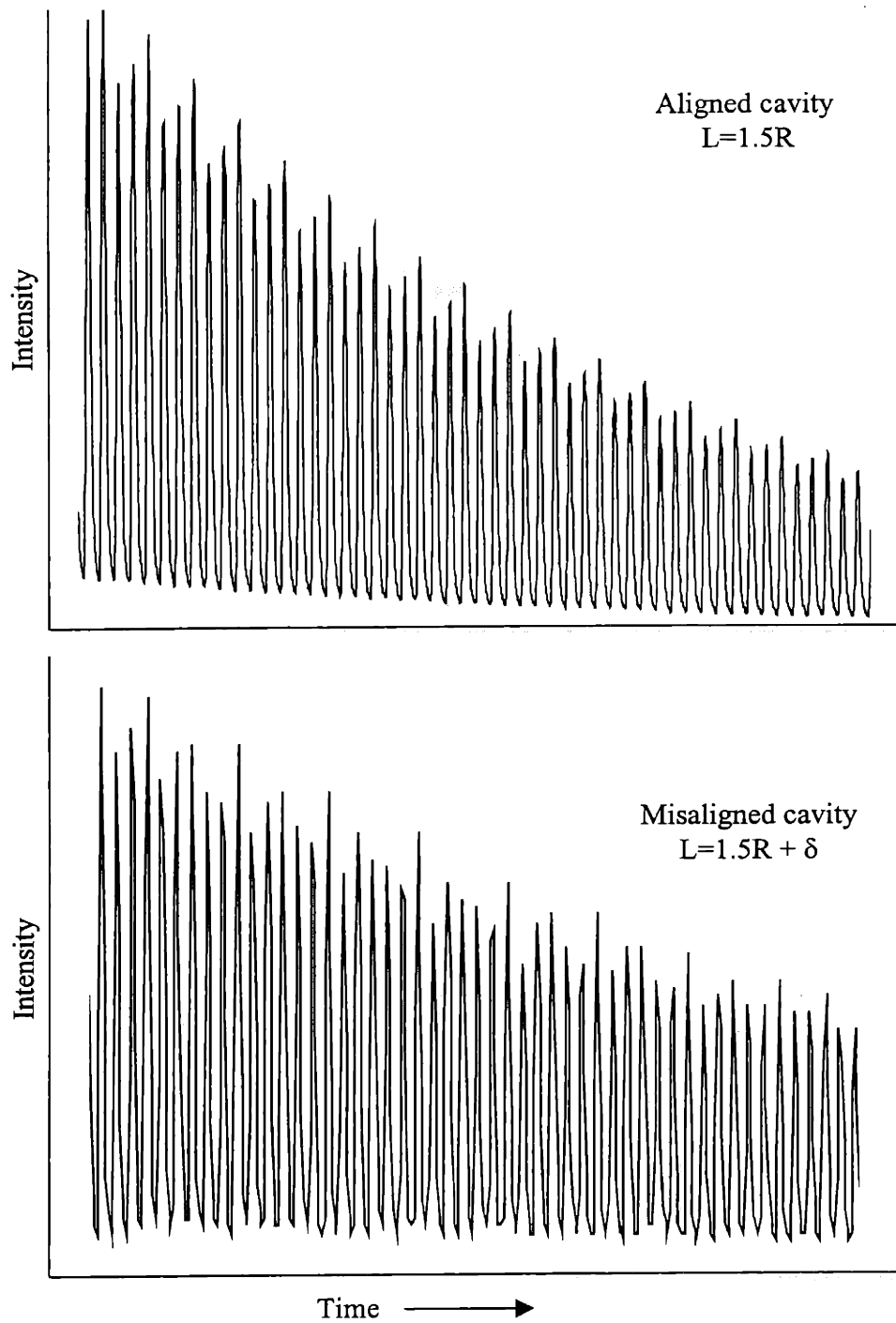


Figure 5-4: Ring-Down decays for a mode matched and incorrectly mode matched cavity. In the case of the mode matched cavity ($L=1.5R$), the pattern of 3 stationary exit spots results in 3 families of exponential decays with the same decay constant. For the case of the mismatched cavity the intensity pattern appears random and is a result of mode-beating.

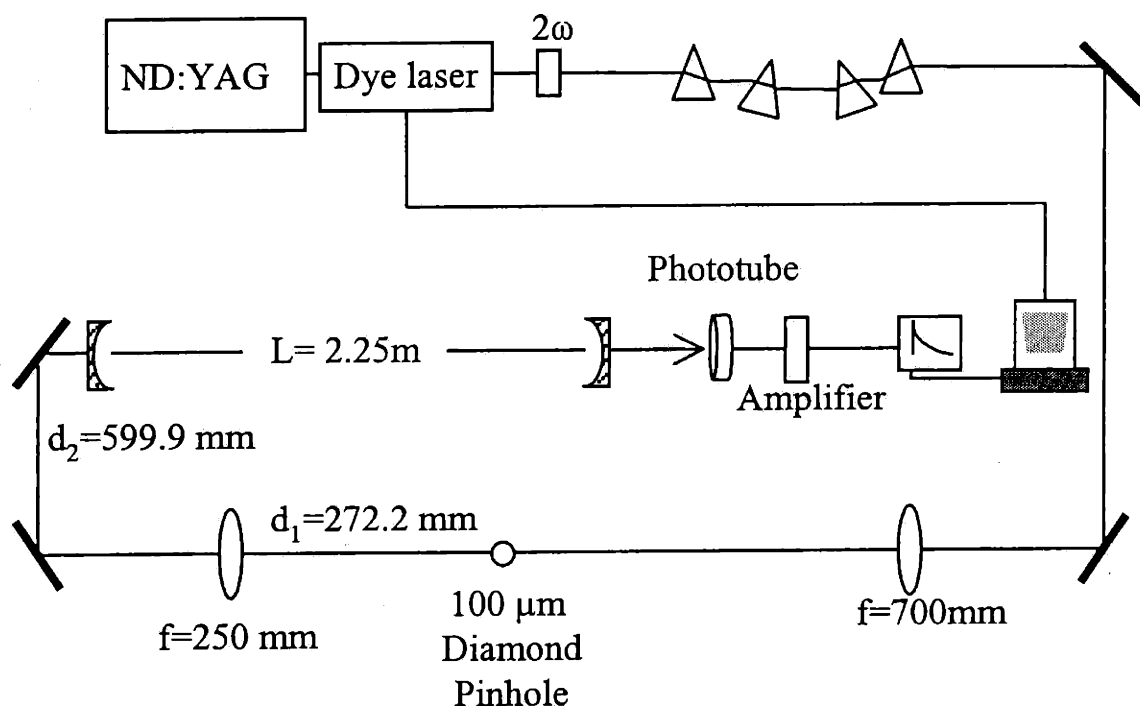


Figure 5-5: CRD spectrometer

In our experiments great care was taken to ensure that the RDC length was exactly $1.5R$ and that the pulse was spatially mode matched to the cavity. Moreover, the procedure used to determine the decay constants from the observed Ring-Down waveforms was designed to eliminate the noise associated with the mode beating that resulted from excitation of more than one longitudinal mode of the RDC. This was performed by determining the individual decay constants for each of the 3 families of peaks observed in the digitized waveform instead of just determining an averaged decay constant for the entire waveform. This will be discussed further in the next section.

5.5 CRDS Experimental Details

Figure 5-5 illustrates the cavity Ring-Down spectrometer. The output of a Spectra-Physics Quanta Ray DCR-3 ND:YAG laser operating at 10Hz was used to pump

a Lambda-Physik FL3002 dye laser, equipped with an intracavity etalon. The dye laser, operated with Coumarin 460 or 480 dye, was etalon scanned over a range of $\approx 10 \text{ cm}^{-1}$. Approximately 2.5 mJ of tunable radiation (450–490 nm) was produced with a spectral width $\leq 0.04 \text{ cm}^{-1}$. The dye laser was controlled remotely using a data acquisition program written in C++ by Dr. Sergey Panov. The output from the dye laser is frequency doubled using a β -BBO crystal with 15% conversion efficiency. The doubled output is separated from the fundamental frequency using four 60° S1-UV fused silica prisms. The four prisms are aligned so that the laser beam does not move as the laser is scanned over a large wavelength region. If only one prism were used to separate the fundamental radiation from the second harmonic, the beam direction would change constantly. By configuring the four prisms properly, the beam always travels along the same path, regardless of wavelength. This obviates the need to realign the cavity during a scan.

The laser beam is spatially matched to the cavity, using a series of lenses and a diamond pinhole. A 700 mm focal length lens is used to focus the beam onto a $100 \mu\text{m}$ pinhole that spatially filters the beam and produces a Gaussian beam shape. Next, a second lens (focal length 250mm) is used to mode match the laser pulse to the RDC. The lens and pinhole must be placed a specific distance away from the entrance mirror of the cavity in order to couple the light into the RDC most efficiently. The distances between the pinhole and the cavity and the lens and the cavity are calculated using the matrix formalism for optics, using a program provided by Dr. Alexander Kachanov. The details of this can be found in references [91, 62]. The lens is placed 599.9 mm in front of the entrance mirror of the RDC and the pinhole is located 872.6 mm in front of the entrance mirror. The cavity consists of 2 identical, highly reflective mirrors with a radius of curvature, $R = 1500 \text{ mm}$, manufactured by VLOC optics. For these experiments 2 different sets of RDC mirrors are used, depending on the wavelength needed. The first set of mirrors is coated with peak reflectivity centered at 240 nm, and the second set at 230 nm. The mirror coatings are highly reflective for wavelengths within $\pm 5 \text{ nm}$ of the center wavelength. The mirrors are secured in aluminum holders which are mounted into standard 1 inch diameter mirror

mounts. The exit mirror and detector are both mounted on one translation stage so that the cavity length can be properly adjusted. The mirror holders terminate in an approximately 2 inch long 0.5 inch diameter tube. The ends of these holders can be then connected, using standard UltraTorr fittings, to a 6 in long, 1/5 in diameter stainless steel bellows and then to a 0.5 in diameter stainless steel tube. The cavity is completely enclosed and sealed so that it can be evacuated and the sample gas introduced.

The RDC cavity is first aligned open to air, without the bellows and stainless steel cell. Once this is done, the absorption cell is installed along with the bellows, while monitoring the Ring-Down waveform to ensure that the cavity remains aligned. The cavity length and mirror alignment are then readjusted to obtain the 3 groups of peaks, each series with the same decay constant. The pressure in the cell must be changed slowly while evacuating or filling the RDC with sample gas. The mirrors may move slightly and the cavity length and alignment must be reset. Great care must be taken when making any adjustments. If the length of the RDC or the alignment changes too much, the Ring-Down signal will disappear and then it becomes virtually impossible to align RDC.

Acetylene (Matheson) is subject to several freeze-pump-thaw cycles to remove impurities. As mentioned in previous chapters, acetylene is packaged with acetone. In order to freeze the acetone and prevent it from entering the cell, a pentane-liquid N₂ slurry (-129.7 °C) is used. Approximately 8 Torr of acetylene is used in the cell. The pressure is measured using a MKS Baratron (Model 626A).

Since the finesse of the RDC in the ultraviolet region of the cavity is low, more light exits the cavity than in typical ring down experiments performed in the visible region of the spectrum. Consequently, a biplanar phototube (Hamamatsu, model R1193U-02) serves as the detector instead of a standard photomultiplier tube. The biplanar phototube permits a higher cathode current and as a result shot noise limited performance can be achieved. The output of the phototube is sent to a variable-gain low-noise current amplifier (Femto, model DLPCA-200). The output of the amplifier is sent to an oscilloscope (Lecroy, Model 3430A), which is capable of a collecting 200k

samples at a digitizing rate of 1Gs/s when all four channels are coupled. A back reflection from one of the prisms is directed onto a photodiode and the output of the photodiode is used to trigger the oscilloscope. The oscilloscope is controlled remotely using the same suite of programs that control the scanning of the dye laser.

At each frequency of the dye laser, the oscilloscope averages the Ring-Down waveform for 20 shots and the laser is scanned in steps of 0.052 cm^{-1} . For higher resolution scans the laser is scanned in steps of 0.019 cm^{-1} and 200 shots are averaged. The averaged waveform is immediately fit using a computer program written by Dr. Sergey Panov to obtain a decay constant [91]. The laser pulse duration is $\approx 5\text{ ns}$ and the cavity round trip time is 15 ns. The use of a fast detector, amplifier, and oscilloscope enables us to resolve each individual Ring-Down peak. Each peak in the waveform is fit, not just the overall envelope of the decay. For each one of the 3 groups of peaks, the peak heights and baselines are determined and fit using a routine based on the Savitsky-Golay algorithm [62, 91]. The baseline for the ring down decay is determined by assuming that it passes through the calculated minima (baseline) for each Ring-Down peak. Baseline subtraction is performed and the resulting peak heights are sorted into 3 families of curves. Each of these curves is then subject to a weighted least squares fitting routine to extract the Ring-Down time for each. By fitting the individual peaks in order to determine the decay constant, it is possible to eliminate some of the noise due to mode beating in the RDC. Of course, not all the mode beating noise can be removed in this way since the cavity is never perfectly aligned and the exit spots do move slightly on the detector's surface and the spot sizes do not remain perfectly constant. Once the waveform is fit, the dye laser is instructed to move to a new position and a new Ring-Down waveform is collected and fit.

5.6 CRDS Results

CRDS spectra were recorded for the $V_0^0K_0^1$, $V_0^1K_0^1$, $V_1^2K_1^0$, and $2_0^1V_0^1K_0^1$ band in the $^{12}\text{C}_2\text{H}_2 \tilde{A} \leftarrow \tilde{X}$ electronic transition. Figure 5-6 illustrates the raw spectrum obtained from a CRDS experiment. The decay constant is plotted versus wavelength. All

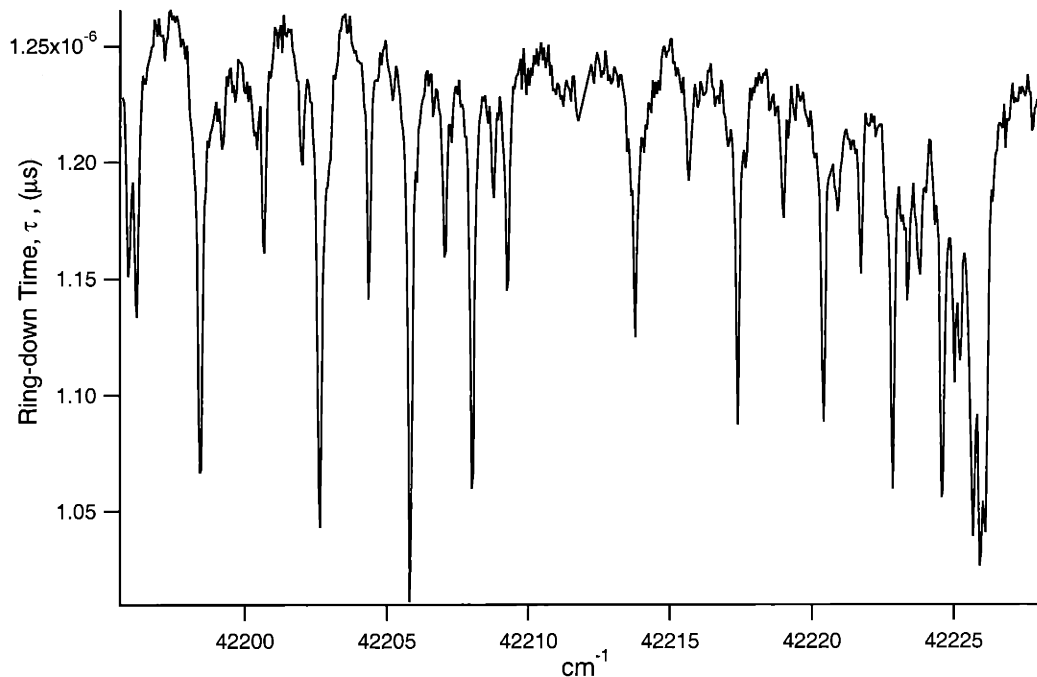


Figure 5-6: Raw CRD spectrum. Ring-Down time, versus frequency.

of these transitions in acetylene are well known and can be used to calibrate the frequency of the spectrum.

The absorption strength, $\alpha(\omega)$ is $1/c\tau - \alpha_{cavity}$, where α_{cavity} is the baseline determined from off resonance or empty cavity losses. For the spectra shown here, the baseline, α_{cavity} is determined from the off resonance Ring-Down decay times and is simply subtracted from the spectrum. In Figure 5-7, the observed intensities are given in terms of $\alpha(\omega)$ instead of τ as seen in the raw spectrum shown in 5-6. The observed transitions and their assignments are listed in Table 5.1. All of these transitions have been observed before [29, 3]. However, the intensity of the origin band has never been reported. The peak intensities, $\alpha(\omega)$, are given as well as the absolute peak intensity $\sigma(\omega)$, where $\sigma(\omega) = 1/N \alpha(\omega)$. N is the number of molecules per unit area and has units of $cm^{-3}mol^1$.

Shown in Figures 5-9, 5-8, 5-10, and 5-11 are the spectra taken for additional bands in the $\tilde{A}^1A_u - \tilde{X}^1\Sigma_g^+$ transition. The assignments and line intensities are given

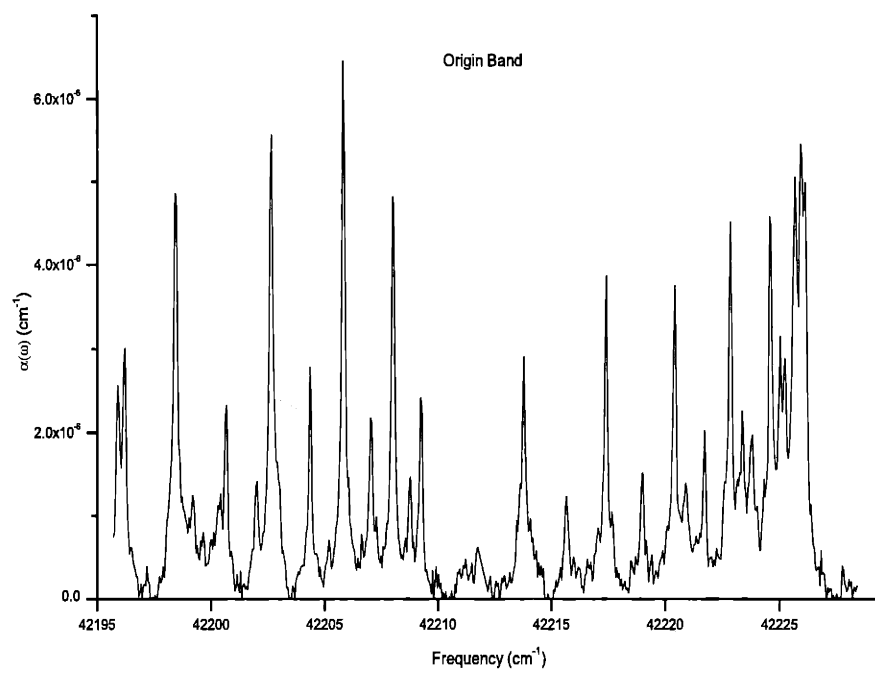


Figure 5-7: Absorption Spectrum of the Origin band. Pressure = 8.6 Torr

in Tables 5.2, 5.3, 5.4 and 5.5.

Table 5.1: Assignment of observed Rovibrational Transitions of $V_0^0K_0^1$ at 8.6 Torr. The peak intensities, $\alpha(\omega)$, are reported in cm^{-1} and the absolute intensities of each line, $\sigma(\omega)$, are given in cm^2/mol . Transitions that are blended are indicated with an *.

Band	(J')	K_a	K_c	(J'')	l	Transition (cm^{-1})	$\alpha(\omega)$ (cm^{-1})	$\sigma(\omega)$ (cm^2/mol)
$V_0^0K_0^1$	10	1	10	10	0	42195.90	2.25E-06	4.82
$V_0^0K_0^1$	4	1	3	5	0	42196.19	2.76E-06	5.91
$V_0^0K_0^1$	9	1	9	9	0	42198.42	4.75E-06	10.17
$V_0^0K_0^1$	3	1	2	4	0	42199.11	8.04E-07	1.72
$V_0^0K_0^1$	8	1	8	8	0	42200.66	2.13E-06	4.56
$V_0^0K_0^1$	2	1	1	3	0	42201.99	1.22E-06	2.60
$V_0^0K_0^1$	7	1	7	7	0	42202.63	5.50E-06	11.77
$V_0^0K_0^1$	6	1	6	6	0	42204.36	2.53E-06	5.42
$V_0^0K_0^1$	5	1	5	5	0	42205.82	6.18E-06	13.22
$V_0^0K_0^1$	4	1	4	4	0	42207.05	1.79E-06	3.84
$V_0^0K_0^1$	3	1	3	3	0	42208.02	4.79E-06	10.26
$V_0^0K_0^1$	2	1	2	2	0	42208.76	1.08E-06	2.31
$V_0^0K_0^1$	1	1	1	1	0	42209.25	2.33E-06	4.99
$V_0^0K_0^1$	1	1	0	1	0	42211.75	7.08E-07	1.52
$V_0^0K_0^1$	2	1	1	1	0	42213.76	2.27E-06	4.86
$V_0^0K_0^1$	3	1	2	2	0	42215.70	7.52E-07	1.61
$V_0^0K_0^1$	4	1	3	3	0	42217.39	3.32E-06	7.10
$V_0^0K_0^1$	5	1	4	4	0	42218.99	1.28E-06	2.73
$V_0^0K_0^1$	6	1	5	5	0	42220.41	3.18E-06	6.81
$V_0^0K_0^1$	7	1	6	6	0	42221.72	1.50E-06	3.20
$V_0^0K_0^1$	8	1	7	7	0	42222.84	3.91E-06	8.36
$V_0^0K_0^1$	20	1	19	19	0	42223.36	1.41E-06	3.02
$V_0^0K_0^1$	9	1	8	8	0	42223.79	1.27E-06	2.71
$V_0^0K_0^1$	10	1	9	9	0	42224.59	4.31E-06	9.23
$V_0^0K_0^1$	11	1	10	10	0	* 42225.23	1.81E-06	3.88
$V_0^0K_0^1$	12	1	11	11	0	42225.65	3.88E-06	8.30
$V_0^0K_0^1$	14	1	13	13	0	* 42226.02	4.75E-06	10.17

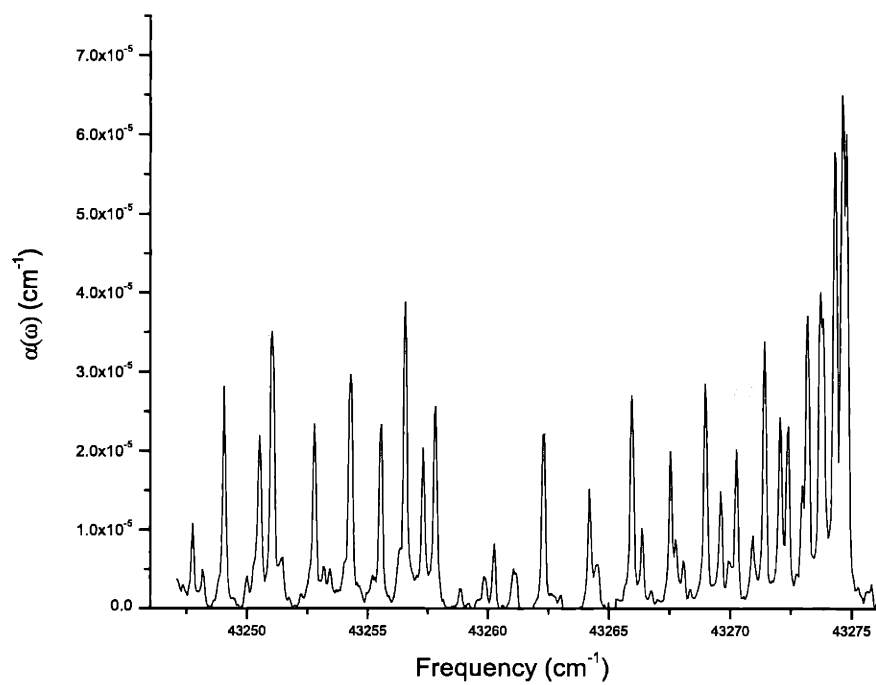


Figure 5-8: Absorption Spectrum of the $V_0^1 K_0^1$ transition. The pressure in the cell was 7 Torr.

Table 5.2: Assignment of observed Rovibrational Transitions of $V_0^1K_0^1$ band. The peak intensities, $\alpha(\omega)$, are reported in cm^{-1} and the absolute intensities of each line, $\sigma(\omega)$, are given in cm^2/mol . The spectra were recorded with 7 Torr of acetylene.

Band	(J')	K_a	K_c	(J'')	l	Transition (cm^{-1})	$\alpha(\omega)$ (cm^{-1})	$\sigma(\omega)$ (cm^2/mol)
$V_0^1K_0^1$	3	1	2	4	0	43247.75	1.89E-05	49.57
$V_0^1K_0^1$	8	1	8	8	0	43249.06	2.72E-05	71.64
$V_0^1K_0^1$	2	1	1	3	0	43250.52	2.11E-05	55.58
$V_0^1K_0^1$	7	1	7	7	0	43251.05	3.55E-05	93.39
$V_0^1K_0^1$	6	1	6	6	0	43252.80	2.29E-05	60.16
$V_0^1K_0^1$	1	1	0	2	0	43253.20	5.16E-06	13.55
$V_0^1K_0^1$	5	1	5	5	0	43254.29	3.07E-05	80.73
$V_0^1K_0^1$	4	1	4	4	0	43255.55	2.36E-05	62.17
$V_0^1K_0^1$	3	1	3	3	0	43256.56	3.95E-05	103.74
$V_0^1K_0^1$	2	1	2	2	0	43257.31	1.90E-05	49.88
$V_0^1K_0^1$	1	1	1	1	0	43257.81	2.54E-05	66.89
$V_0^1K_0^1$	1	1	0	0	0	43260.25	7.36E-06	19.35
$V_0^1K_0^1$	2	1	1	1	0	43262.30	2.27E-05	59.65
$V_0^1K_0^1$	3	1	2	2	0	43264.21	2.91E-05	76.42
$V_0^1K_0^1$	4	1	3	3	0	43265.95	2.63E-05	69.16
$V_0^1K_0^1$	24	1	24	23	0	43266.38	9.19E-06	24.16
$V_0^1K_0^1$	5	1	4	4	0	43267.55	1.85E-05	48.60
$V_0^1K_0^1$	6	1	5	5	0	43268.98	2.80E-05	73.71
$V_0^1K_0^1$	22	1	21	21	0	43269.98	4.25E-06	11.18
$V_0^1K_0^1$	7	1	6	6	0	43270.25	1.90E-05	49.87
$V_0^1K_0^1$	21	1	20	20	0	43270.92	7.26E-06	19.08
$V_0^1K_0^1$	8	1	7	7	0	43271.41	3.29E-05	86.50
$V_0^1K_0^1$	20	1	19	19	0	43272.05	2.36E-05	62.16
$V_0^1K_0^1$	9	1	8	8	0	43272.37	2.14E-05	56.37
$V_0^1K_0^1$	10	1	9	9	0	43273.17	3.64E-05	95.66
$V_0^1K_0^1$	11	1	10	10	0	* 43273.76	3.78E-05	99.28
$V_0^1K_0^1$	12	1	11	11	0	43274.31	5.82E-05	153.00
$V_0^1K_0^1$	13	1	12	12	0	* 43274.69	6.18E-05	162.53

Table 5.3: Assignment of observed Rovibrational Transitions of $2_0^1V_0^0 K_0^1$ band recorded at 7 Torr. Several other vibrational bands observed in this spectral region are also listed. The peak intensities, $\alpha(\omega)$, are reported in cm^{-1} and the absolute intensities of each line, $\sigma(\omega)$, are given in cm^2/mol .

Band	(J')	K_a	K_c	(J'')	l	Transition (cm^{-1})	$\alpha(\omega)$ (cm^{-1})	$\sigma(\omega)$ (cm^2/mol)
$V_1^2K_0^1$	19	0	1	20	1	43573.24	8.41E-06	22.11
<i>continued on next page</i>								

<i>continued from previous page</i>						Transition	$\alpha(\omega)$	$\sigma(\omega)$
Band	(J')	K_a	K_c	(J'')	l	(cm^{-1})	(cm^{-1})	(cm^2/mol)
$2_0^0V_0^0K_0^0$	9	0	9	9	0	43573.50	1.01E-06	2.66
$2_0^1V_0^0K_0^1$	12	1	12	12	0	43575.74	3.24E-06	8.52
$2_0^1V_0^0K_0^1$	6	1	5	7	0	43576.22	3.09E-06	8.12
$V_1^2K_1^0$	27	0	27	27	1	43576.47	4.68E-06	12.30
$2_0^0V_0^0K_0^1$	7	0	7	7	0	43578.25	1.46E-06	3.84
$2_0^1V_0^0K_0^1$	11	1	11	11	0	43578.90	5.09E-06	13.38
$2_0^1V_0^0K_0^1$	5	1	4	6	0	43579.57	6.26E-06	16.46
$V_1^2K_1^1$	27	1	27	27	1	43579.72	6.01E-06	15.80
$V_1^2K_1^0$	18	0	18	19	1	43580.14	3.08E-06	8.10
$2_0^1V_0^0K_0^1$ *	10	1	10	10	0	43581.83	1.68E-06	4.42
$2_0^1V_0^0K_0^1$ *	4	1	3	5	0	43581.83	1.68E-06	4.42
$V_1^2K_1^2$	27	2	25	28	1	43582.85	3.86E-06	10.15
$V_1^2K_1^0$	26	0	26	26	1	43583.28	2.53E-06	6.65
$2_0^1V_0^0K_0^1$	9	1	9	9	0	43584.33	2.87E-06	7.55
$2_0^1V_0^0K_0^1$ *	8	1	8	8	0	43586.78	3.65E-06	9.60
$V_1^2K_1^0$ *	17	0	17	18	1	43586.79		
$V_1^2K_1^1$ *	26	1	26	26	1	43586.79		
$2_0^1V_0^0K_0^1$ *	7	1	7	7	0	43588.87	5.13E-06	13.49
$2_0^1V_0^0K_0^1$ *	2	1	1	3	0	43588.87		
$V_1^2K_1^0$	25	0	25	25	1	43589.77	6.84E-06	17.98
$2_0^1V_0^0K_0^1$	6	1	6	6	0	43590.87	1.32E-06	3.47
$2_0^1V_0^0K_0^1$	5	1	5	5	0	43592.36	3.97E-06	10.44
$V_1^2K_1^0$	16	0	16	17	1	43593.18	6.71E-06	17.64
$2_0^1V_0^0K_0^1$	4	1	4	4	0	43593.67		
$V_1^2K_1^1$	25	1	25	25	1	43593.81	1.13E-05	29.71
$2_0^1V_0^0K_0^1$	3	1	3	3	0	43594.68	5.42E-06	14.25
$2_0^1V_0^0K_0^1$	2	1	2	2	0	43595.46	1.51E-06	3.97
$2_0^1V_0^0K_0^1$ *	1	1	1	1	0	43595.97	6.78E-06	17.83
$V_1^2K_1^0$ *	24	0	24	24	1	43595.97	6.78E-06	17.83
$V_1^2K_1^2$	25	2	23	26	1	43596.76	5.30E-06	13.93
$V_1^2K_1^0$	15	0	15	16	1	43599.32	9.92E-06	26.08
$2_0^1V_0^0K_0^1$ *	2	1	1	1	0	43600.44	6.01E-06	15.80
$V_1^2K_1^1$ *	24	1	24	24	1	43600.44	6.01E-06	15.80
$V_1^2K_1^0$	23	0	23	23	1	43601.90	7.60E-06	19.98
$V_1^2K_1^2$	24	2	22	25	1	43603.50	2.51E-06	6.60
$2_0^1V_0^0K_0^1$	4	1	3	3	0	43603.99	2.87E-06	7.55
$V_1^2K_1^0$	14	0	14	15	1	43605.10	9.18E-06	24.13
$2_0^1V_0^0K_0^1$	6	1	5	5	0	43606.71	1.32E-05	34.70
$V_1^2K_1^0$	22	0	22	22	1	43607.41	8.11E-06	21.32
$2_0^1V_0^0K_0^1$	7	1	6	6	0	43608.06	3.82E-06	10.04
$2_0^1V_0^0K_0^1$	6	1	7	7	0	43608.94	4.60E-06	12.09

continued on next page

<i>continued from previous page</i>						Transition	$\alpha(\omega)$	$\sigma(\omega)$
Band	(J')	K_a	K_c	(J'')	1	(cm^{-1})	(cm^{-1})	(cm^2/mol)
$2_0^1V_0^0K_0^1$	9	1	8	8	0	43609.76	2.78E-06	7.31
$V_1^2K_1^2$	23	2	21	24	1	43610.13	9.22E-06	24.24
$2_0^1V_0^0K_0^1$ *	10	1	9	9	0	43610.62	1.14E-05	29.97
$V_1^2K_1^0$ *	13	0	13	14	1	43610.62	1.14E-05	29.97
$V_1^2K_1^0$	13	0	13	14	1	43612.82	1.13E-05	29.71
$2_0^1V_0^0K_1^0$	21	0	21	21	1	43612.82	1.13E-05	29.71

Table 5.4: Assignment of the observed Rovibrational Transitions in the region of 43020 - 43076 cm^{-1} . The peak intensities, $\alpha(\omega)$, are reported in cm^{-1} and the absolute intensities of each line, $\sigma(\omega)$, are given in cm^2/mol . Overlapped lines are denoted by an * and the same peak intensity is reported for each line.

Band	(J')	K_a	K_c	(J'')	1	Transition	$\alpha(\omega)$	$\sigma(\omega)$
						(cm^{-1})	(cm^{-1})	(cm^2/mol)
$V_2^2K_2^0$	15	0	15	15	2	43020.95	1.13E-05	29.71
$V_2^2K_2^{1*}$	17	1	17	17	2	43021.43	2.11E-05	55.47
$V_2^2K_0^{0*}$	14	0	14	14	0	43021.43	2.11E-05	55.47
$V_2^2K_0^1$	16	1	16	16	0	43022.50	4.25E-06	11.17
$2_1^1V_0^0K_1^{2*}$	2	2	1	1	1	43024.09	2.03E-05	53.37
$2_1^1V_0^0K_1^{2*}$	2	2	0	1	1	43024.09	2.03E-05	53.37
$V_2^2K_0^{1*}$	10	1	9	11	0	43024.09	2.03E-05	53.37
$V_2^2K_0^0$	13	0	13	13	0	43024.75	6.47E-06	17.01
$V_2^2K_2^1$	9	1	9	10	2	43025.27	8.48E-06	22.29
$2_1^1V_0^0K_1^{2*}$	3	2	2	2	1	43025.76	8.22E-06	21.61
$2_1^1V_0^0K_1^{2*}$	3	2	1	2	1	43025.76	8.22E-06	21.61
$V_2^2K_2^{1*}$	16	1	16	16	2	43025.76	8.22E-06	21.61
$V_2^2K_0^{1*}$	15	1	15	15	0	43026.87	1.45E-05	38.12
$2_1^1V_0^0K_1^{2*}$	4	2	3	3	1	43027.24	1.13E-05	29.71
$2_1^1V_0^0K_1^{2*}$	4	2	2	3	1	43027.24	1.13E-05	29.71
$V_2^2K_2^{0*}$	13	0	13	13	2	43027.24	1.13E-05	29.71
$V_2^2K_0^1$	9	1	8	10	0	43028.11	1.08E-05	28.39
$2_1^1V_0^0K_1^{2*}$	5	2	4	4	1	43028.54	4.22E-06	11.09
$2_1^1V_0^0K_1^{2*}$	5	2	3	4	1	43028.54	4.22E-06	11.09
$2_1^1V_0^0K_1^{2*}$	6	2	5	5	1	43029.71	1.36E-05	35.76
$2_1^1V_0^0K_1^{2*}$	6	2	4	5	1	43029.71	1.36E-05	35.76
$V_2^2K_2^{1*}$	15	1	15	15	2	43029.81	2.86E-05	75.19
$V_2^2K_2^{1*}$	8	1	8	9	2	43029.81	2.86E-05	75.19
$2_1^1V_0^0K_1^{2*}$	7	2	6	6	1	43030.36	7.23E-06	19.01
$2_1^1V_0^0K_1^{2*}$	7	2	5	6	1	43030.36	7.23E-06	19.01
$V_2^2K_0^0$	11	0	11	11	0	43030.43	9.35E-06	24.58

continued on next page

<i>continued from previous page</i>						Transition	$\alpha(\omega)$	$\sigma(\omega)$
Band	(J')	K_a	K_c	(J'')	1	(cm^{-1})	(cm^{-1})	(cm^2/mol)
$2_1^1 V_0^0 K_1^{2*}$	8	2	7	7	1	43030.92	1.09E-05	28.66
$2_1^1 V_0^0 K_1^{2*}$	8	2	6	7	1	43030.92	1.09E-05	28.66
$V_2^2 K_0^{1*}$	14	1	14	14	0	43030.92	1.09E-05	28.66
$2_1^1 V_0^0 K_1^{2*}$	9	2	8	8	1	43031.45	1.07E-05	28.13
$2_1^1 V_0^0 K_1^{2*}$	9	2	7	8	1	43031.45	1.07E-05	28.13
$2_1^1 V_0^0 K_1^{2*}$	10	2	9	9	1	43031.78	1.65E-05	43.38
$V_2^2 K_0^1$	8	1	7	9	0	43031.90	2.50E-05	65.73
$V_2^2 K_2^0$	11	0	11	11	2	43032.62	1.05E-05	27.61
$V_2^2 K_0^0$	10	0	10	10	0	43033.05	1.17E-05	30.76
$V_2^2 K_2^1$	14	1	14	14	2	43033.70	1.67E-05	43.91
$V_2^2 K_2^1$	7	1	7	8	2	43034.40	1.79E-05	47.06
$V_2^2 K_0^1$	13	1	13	13	0	43034.75	2.34E-05	61.52
$V_2^2 K_0^0$	9	0	9	9	0	43035.20	9.45E-06	24.84
$V_2^2 K_0^1$	7	1	6	8	0	43035.59	1.48E-05	38.91
$V_2^2 K_2^{0*}$	9	0	9	9	2	43037.27	3.36E-05	88.34
$V_2^2 K_0^{0*}$	8	0	8	8	0	43037.27	3.36E-05	88.34
$V_2^2 K_0^1$	12	1	12	12	0	43038.30	1.08E-05	28.39
$V_2^2 K_2^1$	6	1	6	7	2	43038.62	1.37E-05	36.02
$V_2^2 K_0^{1*}$	6	1	5	7	0	43039.08	3.64E-05	95.70
$V_2^2 K_0^{0*}$	7	0	7	7	0	43039.08	3.64E-05	95.70
$V_2^2 K_2^1$	12	1	12	12	2	43040.56	2.29E-05	60.21
$V_2^2 K_0^1$	11	1	11	11	0	43041.49	2.78E-05	73.09
$V_2^2 K_2^{1*}$	5	1	5	6	2	43042.47	1.92E-05	50.48
$V_2^2 K_0^{1*}$	5	1	4	6	0	43042.47	1.92E-05	50.48
$V_2^2 K_2^{1*}$	11	1	11	11	2	43043.62	3.22E-05	84.66
$V_2^2 K_0^{0*}$	3	0	3	3	0	43043.62	3.22E-05	84.66
$V_2^2 K_0^1$	10	1	10	10	0	43044.46	2.09E-05	54.95
$V_2^2 K_0^1$	4	1	3	5	0	43045.58	2.47E-05	64.94
$V_2^2 K_2^1$	4	1	4	5	2	43046.15	1.83E-05	48.11
$V_2^2 K_2^1$	10	1	10	10	2	43046.44	2.31E-05	60.73
$V_2^2 K_0^1$	9	1	9	9	0	43047.15	3.59E-05	94.38
$V_2^2 K_0^1$	3	1	2	4	0	43048.55	1.91E-05	50.21
$V_2^2 K_2^1$	9	1	9	9	2	43048.99	4.09E-05	107.53
$V_2^2 K_0^{1*}$	8	1	8	9	0	43049.52	3.33E-05	87.55
$V_2^2 K_2^{1*}$	3	1	3	4	2	43049.52	3.33E-05	87.55
$V_2^2 K_0^{1*}$	2	1	1	3	0	43051.31	3.35E-05	88.07
$V_2^2 K_2^{1*}$	8	1	8	8	2	43051.31	3.35E-05	88.07
$V_2^2 K_0^1$	7	1	7	7	0	43051.61	5.10E-05	134.08
$V_2^2 K_2^1$	2	1	2	3	2	43052.63	1.12E-05	29.4454
$V_2^2 K_0^{1*}$	6	1	6	6	0	43053.40	8.32E-05	218.737
$V_2^2 K_2^{1*}$	7	1	7	7	2	43053.40	8.32E-05	218.74

continued on next page

continued from previous page

Band	(J')	K_a	K_c	(J'')	l	Transition (cm^{-1})	$\alpha(\omega)$ (cm^{-1})	$\sigma(\omega)$ (cm^2/mol)
$V_2^2 K_0^1$	1	1	0	2	0	43054.03	7.74E-06	20.35
$V_2^2 K_0^{1*}$	5	1	5	5	0	43055.03	9.22E-05	242.40
$V_2^2 K_2^{1*}$	6	1	6	6	2	43055.03	9.22E-05	242.40
$V_2^2 K_2^1$	1	1	1	2	2	43055.56	3.00E-05	78.87
$V_2^2 K_0^1$	4	1	4	4	0	43056.33	3.44E-05	90.44
$V_2^2 K_2^1$	5	1	5	5	2	43056.66	4.06E-05	106.74
$V_2^2 K_0^1$	3	1	3	3	0	43057.34	6.84E-05	179.83
$V_2^2 K_0^{1*}$	2	1	2	2	0	43058.19	3.51E-05	92.28
$V_2^2 K_2^{1*}$	4	1	4	4	2	43058.19	3.51E-05	92.28
$V_2^2 K_0^1$	1	1	1	1	0	43058.67	3.30E-05	86.76
$V_2^2 K_0^{1*}$	26	1	25	25	0	43058.95	4.81E-05	126.46
$V_2^2 K_2^{1*}$	3	1	3	3	2	43058.95	4.81E-05	126.46
$V_2^2 K_2^1$	2	1	2	2	2	43059.61	5.07E-06	13.33
$V_2^2 K_0^1$	1	1	0	0	0	43061.17	5.65E-06	14.8542
$V_2^2 K_0^1$	25	1	24	24	0	43061.50	3.57E-06	9.39
$V_2^2 K_0^2$	19	2	17	19	0	43062.64	4.48E-06	11.78
$V_2^2 K_0^1$	2	1	1	1	0	43063.19	2.25E-05	59.15
$V_2^2 K_0^1$	24	1	24	23	0	43063.74	9.76E-06	25.6596
$V_2^2 K_0^1$	3	1	2	2	0	43065.07	1.18E-05	31.0228
$V_2^2 K_0^1$	23	1	22	22	0	43065.82	5.02E-06	13.1979
$V_2^2 K_0^1$	4	1	3	3	0	43066.79	3.03E-05	79.6603
$V_2^2 K_0^1$	22	1	21	21	0	43067.58	1.57E-05	41.2761
$V_2^2 K_0^1$	5	1	4	4	0	43068.39	1.90E-05	49.952
$V_2^2 K_0^1$	21	1	20	20	0	43069.29	1.55E-05	40.7503
$V_2^2 K_0^1$	6	1	5	5	0	43069.78	2.68E-05	70.4586
$V_2^2 K_0^2$	17	2	15	17	0	43070.06	1.85E-05	48.6375
$V_2^2 K_0^1$	20	1	19	19	0	43070.68	2.00E-05	52.5811
$V_2^2 K_0^1$	7	1	6	6	0	43071.03	1.83E-05	48.1117
$V_2^2 K_0^1$	9	1	8	8	0	43072.90	3.04E-05	79.9232
$V_2^2 K_0^1$	10	1	9	9	0	43073.70	4.25E-05	111.735
$V_2^2 K_0^1$	11	1	10	10	0	43074.22	4.02E-05	105.688
$V_2^2 K_0^1$	12	1	11	11	0	43074.71	5.68E-05	149.33
$V_2^2 K_0^3$	20	3	17	21	0	43076.23	3.97E-06	10.4373
$V_2^2 K_0^2$	15	2	13	15	0	43076.58	3.99E-06	10.4899

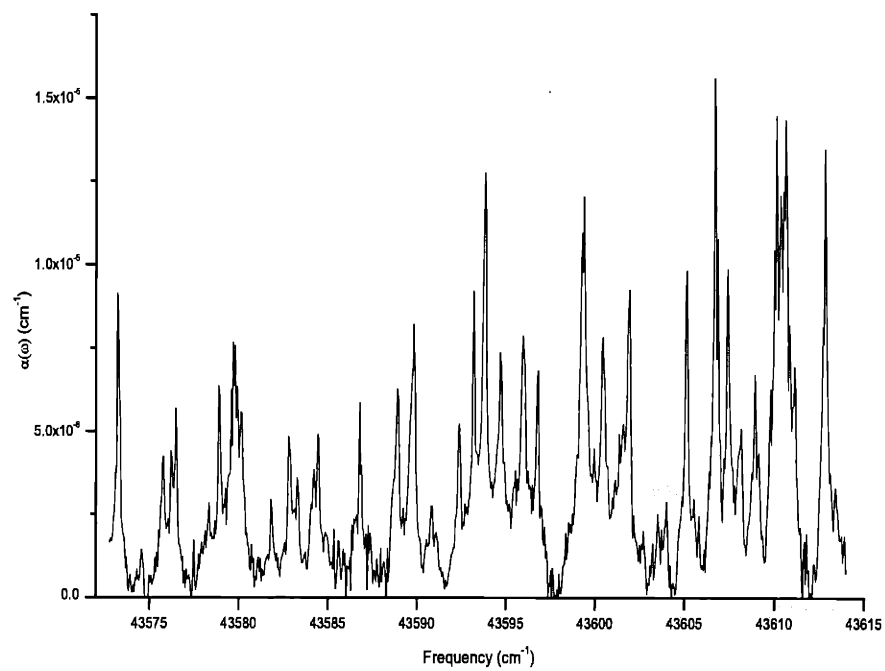


Figure 5-9: Absorption Spectrum of the $2_0^1 V_0^0 K_0^1$ transition recorded at 7 Torr.

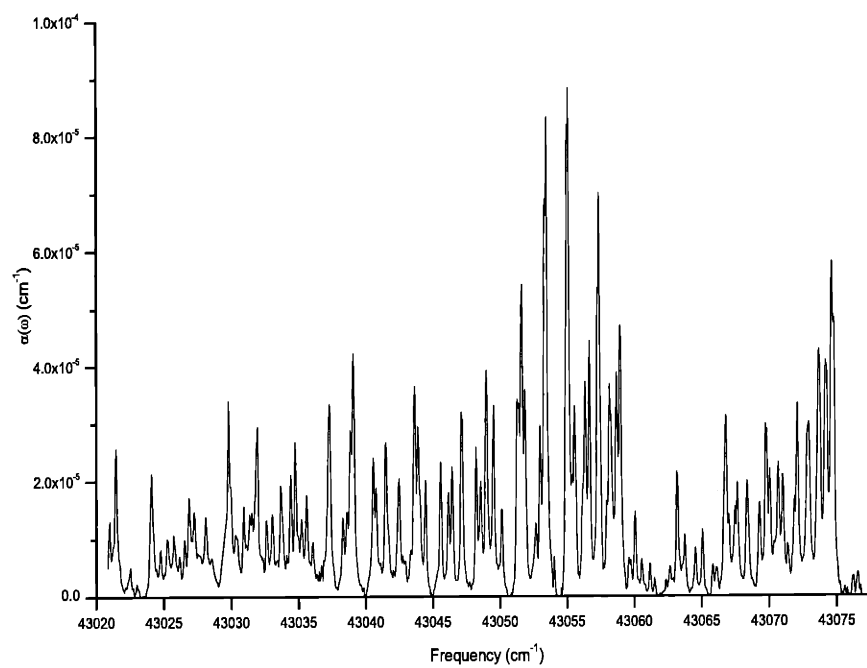


Figure 5-10: CRD spectrum of Rovibrational Transitions in the region of 43020 - 43076 cm^{-1} .

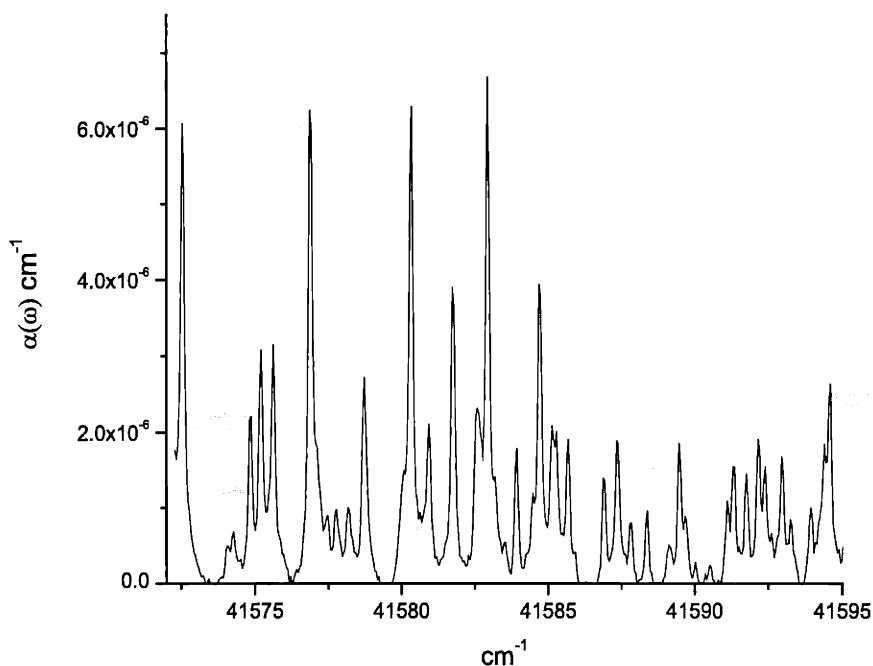


Figure 5-11: Absorption Spectrum of the $V_1^0 K_1^0$ transition.

Table 5.5: Assignment of the observed Rovibrational Transitions of the $V_1^0 K_1^0$ transition. Other rovibrational transitions observed in this region are also reported. The peak intensities, $\alpha(\omega)$, are reported in cm^{-1} and the absolute intensities of each line, $\sigma(\omega)$, are given in cm^2/mol . Overlapped lines are denoted by an * and the same peak intensity is reported for each line.

Band	(J')	K_a	K_c	(J'')	l	Transition (cm^{-1})	$\alpha(\omega)$ (cm^{-1})	$\sigma(\omega)$ (cm^2/mol)
$V_1^0 K_1^0$	11	0	11	11	1	41572.54011	6.03E-06	15.8532
$V_3^1 K_3^{4*}$	15	4	11	15	3	41574.05748	4.01E-07	1.05425
$V_3^1 K_3^{4*}$	15	4	12	15	3	41574.05748	4.01E-07	1.05425
$V_1^0 K_1^0$	10	0	10	10	1	41574.84728	2.27E-06	5.96795
$V_1^0 K_1^0$	3	0	3	4	1	41575.20664	3.00E-06	7.88716
$V_1^0 K_1^1$	13	1	13	13	1	41575.62298	3.00E-06	7.88716
$V_1^0 K_1^{0*}$	9	0	9	9	1	41576.88781	6.50E-06	17.0889
$V_3^1 K_3^{4*}$	14	4	10	14	3	41576.88781	6.50E-06	17.0889
$V_3^1 K_3^{4*}$	14	4	11	14	3	41576.88781	6.50E-06	17.0889
$V_1^0 K_1^{0*}$	8	0	8	8	1	41578.72889	2.70E-06	7.09845
$V_1^0 K_1^{1*}$	12	1	12	12	1	41578.72889	2.70E-06	7.09845
$V_1^0 K_1^{0*}$	7	0	7	7	1	41580.31765	6.27E-06	16.4842

continued on next page

continued from previous page

Band	(J')	K_a	K_c	(J'')	1	Transition (cm^{-1})	$\alpha(\omega)$ (cm^{-1})	$\sigma(\omega)$ (cm^2/mol)
$V_3^1 K_3^{4*}$	13	4	9	13	3	41580.31765	6.27E-06	16.4842
$V_3^1 K_3^{4*}$	13	4	10	13	3	41580.31765	6.27E-06	16.4842
$V_1^0 K_1^0$	1	0	1	2	1	41580.92545	1.96E-06	5.15295
$V_1^0 K_1^{0*}$	6	0	6	6	1	41581.75115	4.15E-06	10.9106
$V_1^0 K_1^{1*}$	11	1	11	11	1	41581.75115	4.15E-06	10.9106
$V_3^1 K_3^{4*}$	12	4	8	12	3	41582.59074	2.18E-06	5.73134
$V_3^1 K_3^{4*}$	12	4	9	12	3	41582.59074	2.18E-06	5.73134
$V_1^0 K_1^0$	5	0	5	5	1	41582.93254	6.45E-06	16.9574
$V_1^0 K_1^0$	4	0	4	4	1	41583.9174	1.78E-06	4.67972
$V_1^0 K_1^{0*}$	3	0	3	3	1	41584.70605	3.98E-06	10.4636
$V_1^0 K_1^{1*}$	10	1	10	10	1	41584.70605	3.98E-06	10.4636
$V_1^0 K_1^{0*}$	2	0	2	2	1	41585.20472	1.97E-06	5.17924
$V_3^1 K_3^{4*}$	11	4	7	11	3	41585.20472	1.97E-06	5.17924
$V_3^1 K_3^{4*}$	11	4	8	11	3	41585.20472	1.97E-06	5.17924
$V_1^0 K_1^0$	1	0	1	1	1	41585.67673	1.79E-06	4.70601
$V_1^0 K_1^{1*}$	9	1	9	9	1	41586.90743	1.56E-06	4.10132
$V_3^1 K_3^{4*}$	10	4	6	10	3	41587.36398	1.98E-06	5.20553
$V_3^1 K_3^{4*}$	10	4	7	10	3	41587.36398	1.98E-06	5.20553
$V_1^0 K_1^0$	19	0	19	18	1	41588.35504	1.09E-05	28.6567
$V_3^1 K_3^{4*}$	9	4	5	9	3	41589.47771	1.83E-06	4.81117
$V_3^1 K_3^{4*}$	9	4	6	9	3	41589.47771	1.83E-06	4.81117
$V_3^1 K_3^{4*}$	8	4	4	8	3	41591.31921	1.57E-06	4.12761
$V_3^1 K_3^{4*}$	8	4	5	8	3	41591.31921	1.57E-06	4.12761
$V_1^0 K_1^0$	17	0	17	16	1	41592.15677	1.76E-06	4.62714
$V_1^0 K_1^{0*}$	4	0	4	3	1	41592.95744	1.56E-06	4.10132
$V_3^1 K_3^{4*}$	7	4	3	7	3	41592.95744	1.56E-06	4.10132
$V_3^1 K_3^{4*}$	7	4	4	7	3	41592.95744	1.56E-06	4.10132
$V_1^0 K_1^{0*}$	5	0	5	4	1	41594.51606	2.18E-06	5.73134
$V_3^1 K_3^{4*}$	6	4	2	6	3	41594.51606	2.18E-06	5.73134
$V_3^1 K_3^{4*}$	6	4	3	6	3	41594.51606	2.18E-06	5.73134
$V_1^0 K_1^0$	15	0	15	14	1	41595.23013	1.94E-06	5.10036
$V_1^0 K_1^{0*}$	6	0	6	5	1	41595.64745	1.93E-06	5.07407
$V_3^1 K_3^{4*}$	5	4	1	5	3	41595.64745	1.93E-06	5.07407
$V_1^0 K_1^0$	7	0	7	6	1	41596.58646	3.10E-06	8.15007

5.7 Determination of Oscillator Strengths

From the absorption loss, (ω) , it is straightforward to calculate the oscillator strength, f , for a given vibrational band. The measured absorption, $\alpha(\omega)$, determined in a

CRD spectrum is a function of the number of molecules per unit volume, N, that the laser beam intercepts. The absorption cross section on the other hand is a molecular property and is independent of the number of molecules. The molar absorption cross section, $\sigma(\omega)$ is given by:

$$\sigma(\omega) = \frac{1}{N}\alpha(\omega) \quad (5.9)$$

and the integrated cross section for a particular rovibrational line is determined from the integrated absorption:

$$\sigma_{jk}^i = \int \sigma(\omega)d\omega = \frac{1}{N} \int \alpha(\omega)d\omega \quad (5.10)$$

The molar absorption cross section $\sigma(\omega)$ has units of cm^2mol^{-1} , $\alpha(\omega)$ has units of cm^{-1} and the integrated absorption cross section, $\int \sigma(\omega)d\omega$, has units of cm^1mol^{-1} and $\int \alpha(\omega)d\omega$ has units of cm^{-2} . N is the number of molecules (in moles) per unit volume and has units of $cm^{-3}mol^1$. The value of N is determined from the experimental conditions using the following:

$$N = \frac{P(Torr)Loschmidt(molecules/cm^3Torr)}{Avagadro(molecules/mole)} \quad (5.11)$$

$$Avagadro = 6.0221367 \times 10^{23} \text{ molecules/mole}$$

$$P = \text{Pressure Torr}$$

$$Loschmidt = 2.68719 \times 10^{19} \times \frac{273.15}{T} \times \frac{1}{760} \text{ molecules } cm^{-3}Torr^{-1}$$

The Loschmidt number is the number of molecules at 0 degrees and 1 atm .

By taking into account the Hönl-London factor and population of the initial state for a particular rovibrational transition, the total integrated absorption cross section for a vibrational band, $\sigma(\omega)_{band}^i$ can be determined:

$$\sigma_{band}^i = \frac{\sigma_{jk}^i}{Hönl - LondonFactor \times PopulationFactor \times IsotopeFactor} \quad (5.12)$$

where, $\sigma_{band}^i > \sigma(\omega)_{jk}^i$.

For a perpendicular transition the Hönl-London factors, S_{jk} for P, Q and R branch transition are:[92]

$$\text{P branch: } S_{jk} = \frac{2(J-1 \mp K)(J \mp K)}{J(2J+1)} \quad (5.13)$$

$$\text{Q branch: } S_{jk} = \frac{2(J+1 \pm K)(J \mp K)}{J(J+1)} \quad (5.14)$$

$$\text{R branch: } S_{jk} = \frac{2(J+2 \pm K)(J+1 \pm K)}{(J+1)(2J+1)} \quad (5.15)$$

The above equations must be normalized. Recall that for P, Q, R lines of a particular J, $\sum S_{jk} = 1$. However, if we sum over the S_{jk} terms in equation 5.13, 5.14, 5.15 for a particular J, $\sum S_{jk} = 4$ and consequently equations 5.13, 5.14, 5.15 must be normalized by dividing each S_{jk} by 4 in order to obtain the correct factor relating the integrated line intensity to the integrated band intensity.

The isotope factor is simply 1 for the case of a pure sample. The population factor, P, accounts for the density of molecules thermally excited into particular rovibronic levels in the ground state and is related to the partition function for a particular level at a certain temperature:

$$P = \frac{(2I+1)(2J+1)\exp^{-\frac{Bhc}{kT}J(J+1)}}{Q_{vib}Q_{rot}} \quad (5.16)$$

and the rotational and vibrational partition functions are calculated from:

$$Q_{rot,nuc} = \sum_{J_{even}} (2J+1)\exp\left(-\frac{Bhc}{kT}J(J+1)\right) + 3 \sum_{J_{odd}} (2J+1)\exp\left(-\frac{Bhc}{kT}J(J+1)\right) \quad (5.17)$$

$$Q_{rot,nuc} = 2\left(\frac{kT}{hcB} + \frac{1}{3} + \frac{1}{15}\frac{hcB}{kT} + \frac{4}{315}\left(\frac{hcB}{kT}\right)^2 + \dots\right) \quad (5.18)$$

$$Q_{vib} = (1 - \exp^{-\omega_1 hc/kT})^{-d_1} (1 - \exp^{-\omega_2 hc/kT})^{-d_2} (1 - \exp^{-\omega_3 hc/kT})^{-d_3} \dots \quad (5.19)$$

where D_i is the degeneracy of a vibrational level. In order to simplify the calculation note that $\omega_i hc/kT = 1.439\omega_i/T$.

Finally the unitless oscillator strength can be determined by substituting equation 5.12 into equation 5.1 to obtain

$$f_v = \frac{mc^2}{\pi e^2} \sigma(\omega)_{band}^i \quad (5.20)$$

$$f_v = 1.128 \times 10^{12} (\text{molecule/cm}) \times \sigma(\omega)_{band}^i (\text{cm/molecule}) \quad (5.21)$$

or

$$f_v = 1.8732 \times 10^{-12} (\text{mol/cm}) \times \sigma(\omega)_{band}^i (\text{cm/mol}). \quad (5.22)$$

Take for example Q(1) of $V_0^1 K_0^1$. In Table 5.2 the absorption strength, $\alpha(\omega)$ is $2.54 \times 10^{-5} \text{ cm}^{-1}$ and the molar absorption cross section, $\sigma(\omega)$, is reported to be $66.89 \text{ cm}^2 \text{ mol}^{-1}$. Before we can calculate the oscillator strength, we need to determine the integrated cross-section. The lineshape of each transition is assumed to be Doppler broadened (inhomogeneous lineshape). The full width half maximum of the line for an inhomogeneously broadened Doppler lineshape is given by:

$$\Delta v_{FWHM}^D = 7.162 \times 10^{-7} v_0 \sqrt{\frac{T}{M}} \quad (5.23)$$

where v_0 is the frequency at line center in unit of cm^{-1} and T is the temperature in Kelvin, and M is the molecular mass in atomic mass units. For Q(1) in the $V_0^1 K_0^1$ band v_0 is 43257.81 cm^{-1} and $\Delta v_{FWHM}^D = 0.103 \text{ cm}^{-1}$. Pressure broadening can be neglected since, for acetylene, the pressure broadening rate is approximately 10 MHz/Torr. For sample pressures on the order of 10 Torr, used in these experiments, this corresponds to a pressure broadening of 100 MHz or 0.003 cm^{-1} , which is clearly negligible with respect to the Doppler width.

Additionally, the linewidth of the doubled output of the laser (0.06 cm^{-1} in the uv) is smaller than Δv_{FWHM}^D and therefore it is reasonable to assume that the observed transitions have an inhomogeneously broadened Doppler lineshape. The integrated absorption cross section can be determined from absorption cross-section at line cen-

ter, $\sigma(0)$, by using the normalized lineshape function $g(v - v_0)$ evaluated at linecenter $g(0)$. The normalized Doppler lineshape [93] is given by:

$$g(v - v_0) = \frac{2}{v_{FWHM}^D} \sqrt{\frac{\ln 2}{\pi}} \exp^{-4 \ln 2 ((v - v_0)/v_{FWHM}^D)^2}. \quad (5.24)$$

Therefore, the integrated cross section is simply:

$$\sigma_{jk}^i = \frac{v_{FWHM}^D}{2} \sqrt{\frac{\pi}{\ln 2}} \sigma(\omega)_{jk}. \quad (5.25)$$

For Q(1) of $V_0^1 K_0^1$ equation 5.25 results in:

$$\sigma_{jk}^i = 7.33 \text{ cm/mol (or } 1.218 \times 10^{-23} \text{ cm/molecule)}.$$

The Hönl-London factor for a Q(1) line can be calculated from equation 5.14 and is determined to be: $S_{jk} = 2$. Recall, that this factor must be normalized such that the sum over S_{jk} terms obtained in from equation 5.13, 5.14, 5.15 for a particular J, $\sum S_{jk} = 1$. For Q(1), this results in a normalized $S'_{jk} = 1/2$.

The population factor for Q(1) is straightforward to determine from equations 5.16, 5.18, and 5.19. For Q(1) of $V_0^1 K_0^1$, $I = 1$, $J = 1$, the population factor, P_{vJ} is 2.049×10^{-2} .

Now using equation 5.22, the oscillator strength for the $V_0^1 K_0^1$ band is $f_v = 1.35 \times 10^{-9}$. Ingold and King [3], determined f_v for the same band to be 4.2×10^{-8} .

The above calculation can be repeated for all the observed transitions. For the Q(1) line of the origin band, $V_0^0 K_0^1$, $f_v = 9.80 \times 10^{-11}$. This is 14 times weaker than the oscillator strength for the $V_0^1 K_0^1$ band.

An average of the oscillator strengths determined for 28 lines measured in the $V_0^1 K_0^1$ band for the low resolution scans yields $f_v = 1.53 \times 10^{-9} \pm 9.80 \times 10^{-10}$. It is puzzling that the 1σ uncertainty in this measurement is $\sim 70\%$. Similarly, an average of the oscillator strength determined for 27 lines measured in the $V_0^0 K_0^1$ transitions yields $f_v = 7.81 \times 10^{-11} \pm 1.70 \times 10^{-11}$. There is a large variance in the determination of f_v from the rotational lines of the low resolution scans. This discrepancy is due to the large step size used in the low resolution scans. The observed rovibrational

transitions were not sufficiently sampled in the low resolution scans, and as a result the band oscillator strengths calculated from each individual rotational line varied.

The minimum detectable absorption sensitivity of the CRD measurement can be calculated using:

$$\frac{d\tau}{\tau} = \frac{d\alpha}{\alpha} \quad (5.26)$$

where, in this case, $d\tau$ is the rms noise of the CRD scan and τ is the intensity of the absorption feature. For the Q(1) line of $V_0^1K_0^1$, $d\sigma = 3 \times 10^{-9}$ s, $\sigma = 3.3 \times 10^{-7}$ s, and $\alpha = 2.54 \times 10^{-5}$ cm⁻¹. This results in a minimum absorption sensitivity of 2×10^{-7} cm⁻¹. This sensitivity is an order of magnitude worse than the sensitivity previously reported for uv cavity Ring-Down measurements performed in this group on O₂ [62, 91]. The reflectivity of the mirrors may have degraded once the highly reflective mirror surface came into contact with acetylene. Additionally, the reflectivity of the mirrors is highly dependent on wavelength. The highly reflective coating on the cavity mirrors is centered at a particular wavelength and the reflectivity falls off rapidly with wavelength. For the observed transitions in the $V_0^1K_0^1$ band, between 231.1 nm and 231.2 nm, the cavity Ring-Down mirrors used had maximum reflectivity at 230 nm. The observations were made at least 1 nm away from the center wavelength of the mirror coatings. Consequently, at these wavelengths, the cavity had a lower finesse, resulting in a poorer minimum absorption sensitivity. Finally, if the cavity is evacuated too quickly after being open to air, various contaminants such as water or pump oil may deposit on the mirrors and degrade the mirror reflectivity [73].

5.8 Conclusion

Intensities of several rovibrational lines of the $\tilde{A}^1A_u-\tilde{X}^1\Sigma_g^+$ band were measured using Cavity Ring-Down Spectroscopy. For the $V_0^1K_0^1$ transition, the oscillator strength, f_v , was determined to be 1.9×10^{-9} . Similarly, the oscillator strength for the $V_0^0K_0^1$ band was determined to be 9.80×10^{-11} based on the measurement of the Q(1) transition. The intensity ratio of the $V_0^1K_0^1$ to $V_0^0K_0^1$ band is 14. This value is slightly smaller than the calculated ratio of Franck-Condon factors of 16 reported by Watson [94]

The oscillator strengths were determined assuming a Doppler limited lineshape for each transition. The integrated intensities may in fact be much smaller than calculated. The linewidth of a frequency doubled FL3002 Lambda Physik dye laser is observed to be 0.06 cm^{-1} . However, in reality the linewidth may be slightly larger. Recall that the Doppler FWHM is 0.1 cm^{-1} . Consequently, in order to accurately calculate the integrated line intensity any broadening due to the spectral width of the uv pulse should be taken into account.

Additionally, technical noise may be an important factor. Shown in Figures 5-12 and 5-13 is a comparison of the CRD spectrum of the $V_0^1 K_0^1$ transition observed at high resolution (200 shot average, 0.019 cm^{-1} step size) and at lower resolution $V_0^1 K_0^1$ (20 shot average, 0.052 cm^{-1} step size). Note that the spectra shown in Figures 5-7, 5-9, 5-8, 5-10, and 5-11 and the cross sections listed in Tables 5.1, 5.2, and 5.3, 5.4 and 5.5 were all measured with the 20 shot average, 0.052 cm^{-1} step size. Due to time constraints, high resolution scans were only recorded over a few rotational lines in each band. From the spectra shown in Figures 5-12 and 5-13, it is evident that there is at least a 20% difference in the measured intensities of the same line between the high resolution and low resolution scans. The high resolution scans exhibit a larger change in ring-down time than the low resolution scans resulting in larger absorption cross sections for the high resolution data. This is very troublesome. Table 5.6 is a comparison of the absorption intensities, $\alpha(\omega)$, and calculated band oscillator strengths, f_v , for several rotational lines of the $V_0^1 K_0^1$ transition measured at low and high resolution. A comparison for the origin band transitions reveals a similar discrepancy between the high resolution and low resolution results [91]. The oscillator strength for the $V_0^1 K_1^0$ band, determined from the transitions observed in the high resolution scan, are a factor of 20 smaller than the value reported by Ingold and King [3].

There are several possible sources of error which may account for the difference in absorption measurements for high resolutions and low resolution scans as well as for the difference in the oscillator strength determined here and the value reported by Ingold and King [3]. The discrepancy between the high resolution and low resolution

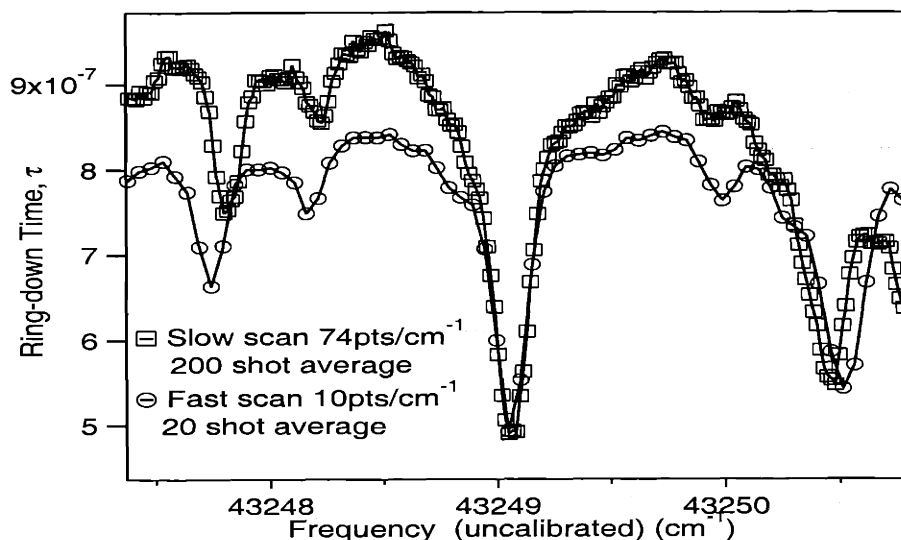


Figure 5-12: Absorption Spectrum of the $V_0^1 K_0^1$ transition near Q(8). For the high resolution scans the change in ring-down time for a particular absorption feature is much larger than the change in ring-down times observed for the low resolution scans. Consequently, the measured absorption cross section for the high resolution scans is larger.

Table 5.6: Absorption strength, $\alpha(\omega)$, and Band oscillator strengths, f_v , for several rotational lines of the $V_0^1 K_0^1$ transition measured at low and high resolution.

Transition	$\alpha(\omega)$ cm $^{-1}$ (high res.)	f_v (high res.)	$\alpha(\omega)$ cm $^{-1}$ (low res.)	f_v (low res.)
Q(1)	3.52E-05	1.77E-09	2.54E-05	1.28E-09
Q(2)	2.63E-05	2.42E-09	1.90E-05	1.75E-09
Q(3)	6.56E-05	1.49E-09	3.95E-05	8.98E-10
Q(4)	2.78E-05	1.55E-09	2.36E-05	1.32E-09
P(3)	2.51E-05	2.00E-09	2.11E-05	1.68E-09
Q(8)	3.31E-05	1.32E-09	2.72E-05	1.08E-09

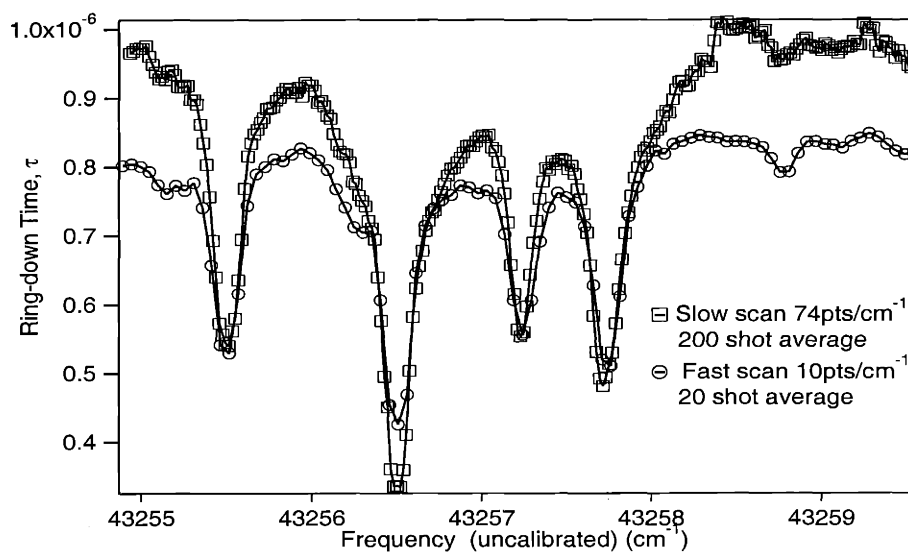


Figure 5-13: Absorption Spectrum of the $V_0^1 K_0^1$ transition near Q(1), Q(2), and Q(3). For the high resolution scans the change in ring-down time for a particular absorption feature is much larger than the change in ring-down times observed for the low resolution scans. Consequently, the measured absorption cross section for the high resolution scans is larger.

scans is primarily due to the sampling rate. The step size for the low resolution scans is too large. As a result, the transitions in the low resolution scans are undersampled and the measured absorption cross section are too low.

One source of error that plagues pulsed-CRDS experiments could be Amplified Stimulated Emission, ASE, from the dye laser. According to Romanini and Lehmann [73], ASE can degrade the accuracy and reproducibility of the absolute absorption intensity. ASE is random and constantly changing and it can contribute to overall Ring-Down decay if it is injected into the cavity. However, it is not absorbed by any molecules in the cell and as a result measurements of the absorption intensity are compromised. Romanini and Lehmann [73] took great care to minimize ASE using a Brillouin Scattering setup. In the CRD setup described here, recall that the output of the dye laser was frequency doubled using a β -BBO crystal. ASE is not efficiently frequency doubled and consequently it should not be a problem in these experiments.

Additionally, in order to correctly determine the absorption cross section from CRD measurements, the linewidth of cavity modes in relation to the molecular linewidth and the laser linewidth must be considered. In these experiments, the linewidth of the cavity modes in relation to the molecular linewidth and laser linewidth is not a possible source of error. However, it is worth discussing why this the case. Lehmann et al [75], van Zee et al [88] and Zare et al [87] have rigorously formulated the CRD output signal for the possible cases relating the linewidth and spacing of the cavity modes, the linewidth of the molecular transitions, and the laser linewidth. In order to obtain accurate absorption intensities it is necessary that the FSR of the cavity is smaller than the FWHM of the molecular resonance. Additionally, the linewidth of the molecular resonance must be broader than the linewidth of the light in the cavity. In these experiments, it was assumed that multiple longitudinal and transverse modes of the cavity were excited even though care was taken to mode match the laser beam to the cavity to avoid noise due to mode beating as described in Section 5.3. The FWHM Doppler width for acetylene transitions observed in the UV region is $\sim 0.1 \text{ cm}^{-1}$. The FSR of the 2.25 m cavity is 66MHz or rather 0.0022 cm^{-1} . This guarantees that at least 45 ring-down cavity modes will fall under the full

Doppler profile. There are clearly enough cavity modes to sample the entire Doppler broadened absorption line, therefore the measured absorption intensities should be unaffected by the ring-down cavity mode spacing.

One final source of error is concerned with the relationship of the laser linewidth to the linewidth of the molecular resonance in CRD experiments. If the laser linewidth is comparable to the Doppler linewidth then the Ring-Down time is overestimated by fitting the Ring-Down decay to a simple exponential decay. This results in a smaller absorption coefficient than the true absorption coefficient. In order to determine whether this is actually a source of error in the experiments described here, additional experiments need to be performed in which the molecular transitions are pressure broadened so their linewidths are much greater than that of the laser pulse.

To obtain accurate absorption coefficients from the CRD experiment two things must be changed. First, the molecular line must be broadened such that it is broader than the laser cavity FSR. Finally, the laser must be pressure scanned. Recall that the laser is etalon scanned, a continuous pressure scan would eliminate any errors resulting from undersampling.

Chapter 6

Noise Immune Cavity Enhanced Optical Heterodyne Molecular Spectroscopy of $^{13}\text{C}_2\text{H}_2$ and H_2O

6.1 Introduction

There has been considerable interest in using molecular overtone transitions in the visible and near-ir regions of the spectrum as optical frequency standards [95]. The natural linewidths of these transitions are typically in the kHz range and the wide wavelength range and abundance of such transitions makes them quite appealing for laser stabilization. However, molecular overtone transitions are typically weak and it is therefore quite challenging to exploit them by any direct absorption technique. Ultrasensitive, high resolution methods, such as frequency modulation spectroscopy (FM) or cavity Ring-Down, are needed.

Noise Immune Cavity Enhanced - Optical Heterodyne Molecular Spectroscopy, NICE-OHMS is the most sensitive method known for studying weak molecular overtone transitions at sub-Doppler resolution [96]. NICE-OHMS is ideal for studying extremely weak overtone transitions because it combines cavity enhancement, frequency modulation spectroscopy (FM), and saturation spectroscopy to achieve high sensitiv-

ity and high resolution. A high finesse cavity increases the effective absorption path length by a factor of $(2 \times \text{Finesse} / \pi)$; thereby increasing the sensitivity by the same amount. Moreover, by matching the FM modulation frequency of the rf sidebands to the free-spectral-range (FSR) of the cavity, the noise level is further reduced. In cavity-enhanced, optical heterodyne spectroscopy, residual fluctuations in laser power and frequency affect the amplitude and phase of the carrier and sidebands transmitted through the cavity. If the carrier and rf sidebands are transmitted by different cavity modes, the FM null is destroyed and added noise is introduced. However, by exactly matching the sideband rf frequency to the cavity-free-spectral range, or an integer multiple of the FSR, the carrier and sidebands will experience the same variations in intensity and phase, thereby maintaining the FM null in the absence of a molecular transition. Previous NICE-OHMS experiments on high overtones of acetylene have demonstrated integrated absorption sensitivities on the order of $5 \times 10^{-14} \text{cm}^{-1}$; far exceeding the sensitivity of either FM or cavity ringdown [96]. Sasada and coworkers reported a NICE-OHMS sensitivity of $9.5 \times 10^{-11} \text{cm}^{-1}$ at a time constant of 1.25 s, for their investigations of $2\nu_3$ vibrational overtone band of methane. Recent studies on the weak magnetic dipole transitions of the $b^1\Sigma_g^+(v' = 0) \leftarrow X^3\Sigma_g^-(v'' = 0)$ band of O_2 have demonstrated minimum detectable absorption coefficient of $6.9 \times 10^{-11} \text{cm}^{-1} \text{Hz}^{-1/2}$ [97].

High sensitivity is not the only benefit of NICE-OHMS. By saturating the transition of interest, sub-Doppler resolution is achieved. Normally sub-Doppler resolution is quite difficult to achieve in view of the extremely small transition moments for molecular overtone transitions. Consider, for example, typical electric dipole transition moments for acetylene. The transition moments are on the order of 1 mD for the $3 \leftarrow 0$ quantum transition of the antisymmetric CH stretching mode, but for the $5 \leftarrow 0$, the transition moment is on the order $100 \mu\text{D}$. The use of a build-up cavity often makes it possible to saturate weak overtone transitions. The actual power inside the cavity is several orders of magnitude greater than that incident on the cavity; consequently saturating overtone transitions with 4 or 5 quanta of CH stretching motion becomes trivial. The sub-Doppler resolution thus obtained is valuable for metrology

purposes. For example Ye et al. have demonstrated 70 kHz linewidths for rotational levels in the (0,1,3,0,0) overtone in C₂HD [98].

The goal of the experiments described here is to resolve the nuclear permutation splittings in isotopically substituted acetylene, ¹³C₂H₂, to gain a better understanding of the vinylidene↔acetylene isomerization process in the electronic ground state. It is thought that the zero-point dressed barrier to isomerization lies near 15,600 cm⁻¹[49]. As a result, in order to observe nuclear permutation splittings, transitions near or high above 15,600 cm⁻¹ must be accessed. Specifically, we are investigating high overtones of ¹³C₂H₂ around 18,000 cm⁻¹. Typically, it is difficult to access high overtones of acetylene in absorption since these transitions are extremely weak. For example, the band $\nu_1 + 5\nu_3$ at 18,430.2 cm⁻¹ has a dipole moment on the order of 35 μ Debye [99]. Additionally, the permutation tunneling splittings should be extremely small since the CH stretching motion (which is the primary motion excited in acetylene overtone spectroscopy) does not couple strongly to the isomerization coordinate [20]. Consequently, a high resolution, ultrasensitive technique such as Noise Immune Cavity Enhanced Optical Heterodyne Molecular Spectroscopy, NICE-OHMS, is necessary.

Due to experimental constraints, a double resonance scheme was designed to excite overtones near 18,000 cm⁻¹. All of this work was performed over a two year period utilizing the NICE-OHM spectrometer in John Hall's laboratory at JILA/University of Colorado. The spectrometer operated in the spectral region of 730-830 nm. In order to gain access to overtones which were energetically above the calculated isomerization barrier, a second excitation was necessary. Moreover, a double resonance excitation scheme was chosen such that bending vibrations, which increase the coupling to the isomerization coordinate, are excited. In this double resonance scheme a DFB diode laser operating near 1.5 μ m is used to saturate a rotational line in the ($v'_1, v'_2, v'_3, v'_4, v'_5$) \leftarrow ($v''_1, v''_2, v''_3, v''_4, v''_5$) = (1,1,0,1,1) \leftarrow (0,0,0,0,0) transition in acetylene. A Ti:Sapphire laser operating near 790nm or 830nm is then scanned in attempts to access either the (4,1,1,1⁺,1⁻) or the (2,1,3,1⁺,1⁻) overtone. The NICE-OHMS detection takes place on this second step, where the frequency stabilized Ti:Sapphire laser is locked to the high finesse cavity.

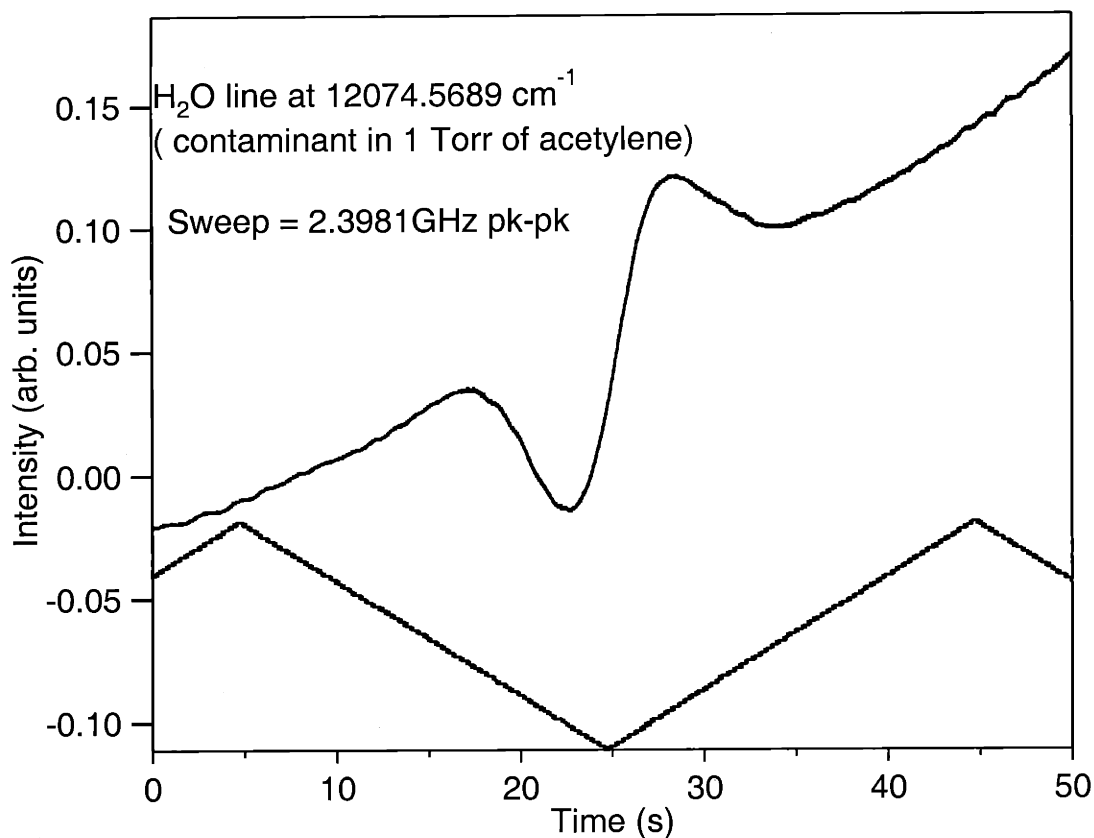


Figure 6-1: Trace amount of water vapor detected in 1 Torr of $^{13}\text{C}_2\text{H}_2$. The dispersion line shape maps out the Doppler profile of the transition centered at 12,074.5689 cm^{-1} . The signal from the sweep wave applied to the voltage driver of the PZT serves to roughly calibrate the scan, where the peak to peak range of the sweep wave corresponds to tuning the laser frequency a distance of 2.3981 GHz.

One serendipitous outcome of these experiments was the detection of H_2O vapor as a contaminant in the $^{13}\text{C}_2\text{H}_2$ sample. The observation of water transitions in the 800 nm region allowed us to characterize the operation of the NICE-OHMS spectrometer since there were no one photon acetylene transitions in this spectral region. Illustrated in Figure 6-1 is the initial serendipitous observation of trace amounts of water vapor in what was thought to be a pure sample of $^{13}\text{C}_2\text{H}_2$ at 1 Torr. The dispersion line maps out the Doppler profile of the line at 12,074.5689 cm^{-1} . Several laser scans had to be concatenated in order to map out the entire transition because the cavity can only be scanned 1 to 1.5 GHz. The signal from the sweep wave applied to the voltage driver of the PZT serves to roughly calibrate the scan, where the peak to

peak range of the sweep wave corresponds to tuning the laser frequency a distance of 2.3981 GHz. Several measurements were made on various transitions in water and a pressure broadening study was performed on one of the lines.

We have investigated several $\Delta K_a = 0$ transitions of the (ν_1, ν_2, ν_3) (211) \leftarrow (000) band of water using NICE-OHMS. Specifically, over 40 transitions terminating on rovibrational levels extending from $J' = 0$ to $J' = 6$ for various combinations of K'_a, K'_c in the upper state were examined.

The experiments performed on the transitions in water will be described first and are intended as a tool for introducing the principles and capabilities of NICE-OHMS. The later half of this chapter will focus on the double resonance NICE-OHMS experiments on $^{13}\text{C}_2\text{H}_2$.

6.2 Experimental Setup: Initial One-Photon Experiments on H_2O and $^{13}\text{C}_2\text{H}_2$

The NICE-OHMS setup has been described previously,[95] but I will briefly review it here. Figure 6-2 depicts the experimental setup of our spectrometer. An argon ion laser pumped, JILA-designed Ti:Sapphire laser provides tunable radiation from approximately 730 nm to 830 nm. Intensity stabilization of the Ti:Sapphire laser is accomplished using an acousto-optic modulator(AOM) at the output of the laser. The AOM also serves as an optical isolator. The Ti:Sapphire laser is frequency stabilized by locking it to a high finesse cavity (finesse $\sim 16,400$). The laser-cavity lock is accomplished in reflection using the Pound-Drever-Hall method [100]. An LiTaO_3 electro-optic modulator, EOM1, imposes 4 MHz sidebands on the carrier frequency. Phase sensitive demodulation of the beat at, $\delta = 4$ MHz, observed in reflection provides the necessary error signal for locking to the cavity. Note the reflected beam from the cavity is obtained by using a polarizing beam splitter, PBS, and a 1/4 waveplate in front of the Ring-Down cavity as shown in Figure 6-2. Frequency corrections to the Ti:Sapphire laser output are provided by several different mechanisms. Amplified and

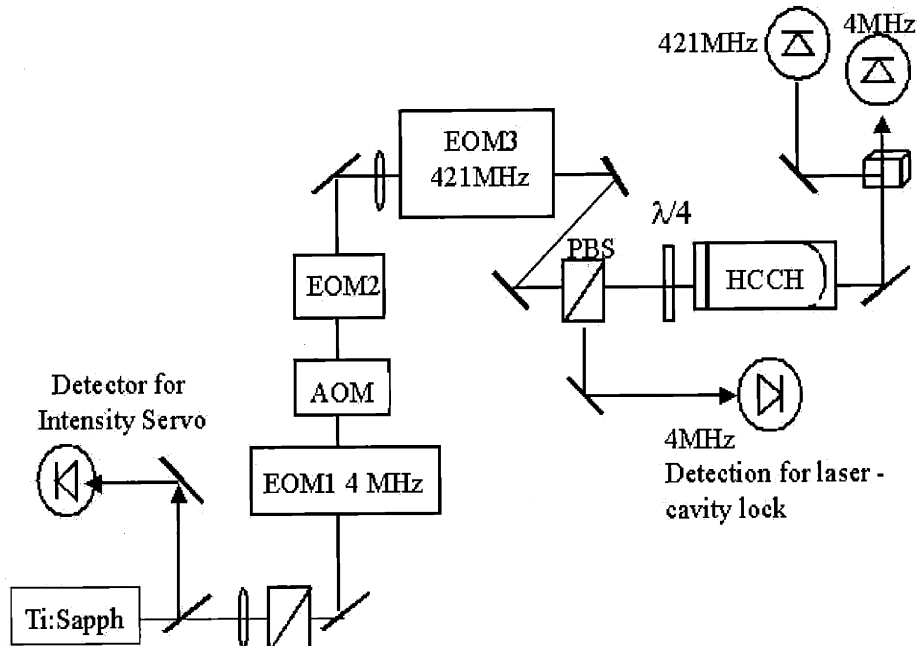


Figure 6-2: Experimental setup of the NICE-OHMS Spectrometer.

filtered correction signals are sent to the laser cavity piezoelectric transducer (PZT), which corrects for large deviations in frequency, and to EOM2 and the AOM in Fig. 6-2, which function together as an external frequency stabilizer system to correct for smaller deviations [101].

The high finesse cavity, to which the Ti:Sapphire laser is locked, consists of a Zerodur cylinder with two (re-entrant) mirrors attached. The re-entrant mirrors allow for transmission of the incident beam through the back face of the mirror. The input mirror is flat while the output mirror is concave ($R = 60$ cm). The output mirror is mounted on a PZT, not shown in the figure, such that the cavity length and, consequently the laser frequency, can be tuned. In addition, this PZT allows us to dither the cavity length.

The finesse of the empty cavity was initially determined by the cavity Ring-Down method. The laser frequency was quickly scanned over a cavity resonance and the transmitted light intensity was recorded on a digital oscilloscope. The finesse is then determined from the Ring-Down decay time. For the cavity used in these experiments the finesse was measured to be 16,400. Shown in Figure 6-3 is the Ring-Down decay

measurement. Note that Ring-Down decays are evident for the carrier laser frequency, ω_0 , as well as for the $\omega_0 \pm 4MHz$ sidebands imposed on the carrier frequency, which serve to lock the laser to the cavity using the Pound-Drever-Hall method.

A third EOM imposes 421.196 MHz sidebands on the carrier. This frequency corresponds to the free spectral range, FSR of the cavity. An exact match between the cavity FSR and the rf modulation frequency is essential to maintain the noise immune property of our spectrometer. In order to scan the laser over a few gigahertz, the length of the high finesse cavity must be scanned. Consequently, the FSR changes continuously throughout a scan. In order to maintain the noise immunity of the spectrometer, the frequency imposed on the carrier by EOM3, must be actively tracked to the value of the FSR. The experimental setup for tracking the sideband frequency, Δ , to the FSR is shown in Figure 6-4. The drive frequency for EOM3 is produced by 2 signal sources, a fixed frequency synthesizer and a tunable, low-phase-noise voltage controlled crystal oscillator, VCXO. The frequency of the VCXO and the fixed frequency synthesizer are summed, filtered, and amplified before being input to EOM3. Generating the drive frequency for EOM3, Δ , in this way enables us to servo control the frequency of the VCXO as the cavity length is scanned so that the rf modulation frequency used to produce the sidebands is constantly matched to the FSR of the cavity. This tracking of Δ to the FSR is accomplished by dithering the output of the fixed rf synthesizer at a frequency, ω . By dithering the output of the fixed rf synthesizer instead of the VCXO, the modulation remains constant as the VCXO is tuned and a better modulation quality is obtained.[99] In these experiments, the dither frequency ω , was kept low, such that a single photodiode could be used to detect the modulation at both ω and δ in reflection. Phase sensitive detection, using light reflected from the input mirror of the cavity produces an error signal at 51 kHz for the VCXO servo loop. The error signal produced is shown in the left panel of Figure 6-5. By measuring the VCXO frequency on a frequency counter, the change in the FSR of the cavity as it is scanned is determined. The VCXO frequency for a scan is shown in Figure 6-6. A frequency offset of 150 MHz has been subtracted. The cavity is scanned approximately 70 MHz, and the rms frequency noise is 125 Hz.

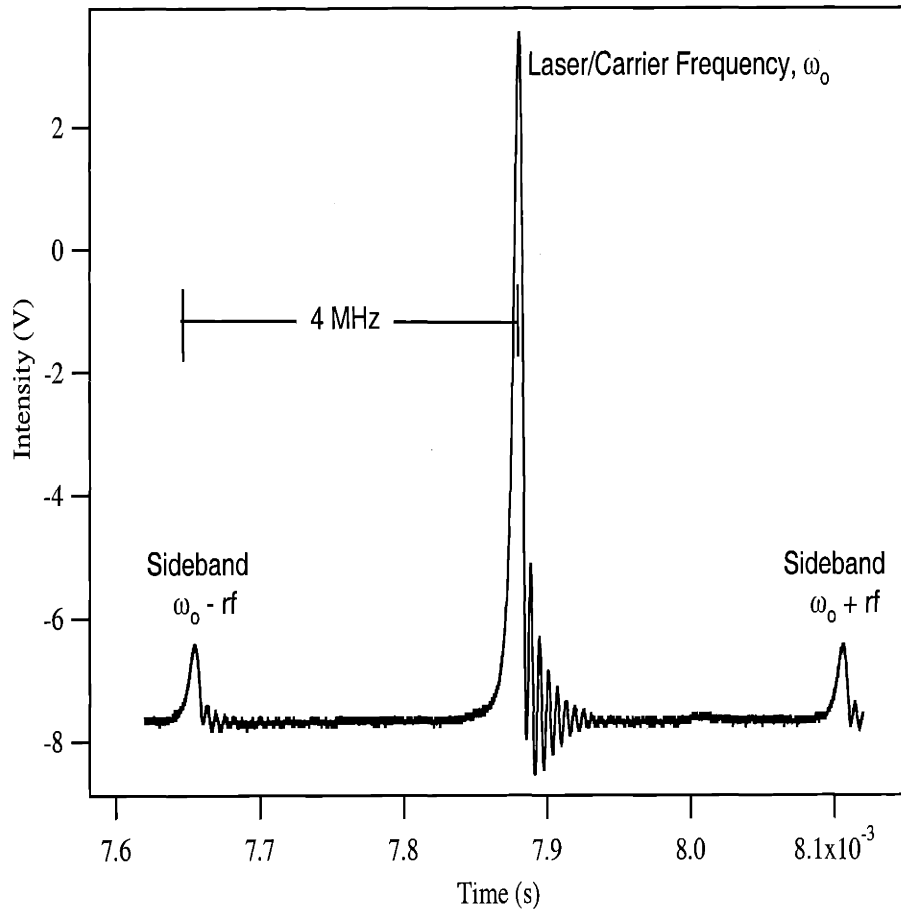


Figure 6-3: Measurement of finesse of the NICE-OHMS spectrometer using the cavity Ring-Down method. Ring-Down decays are evident for the center laser frequency, ω_0 , and the 4 MHz rf sidebands, $\omega_0 \pm rf$, which were imposed on the carrier frequency for Pound-Drever-Hall locking of the laser to the high finesse cavity.

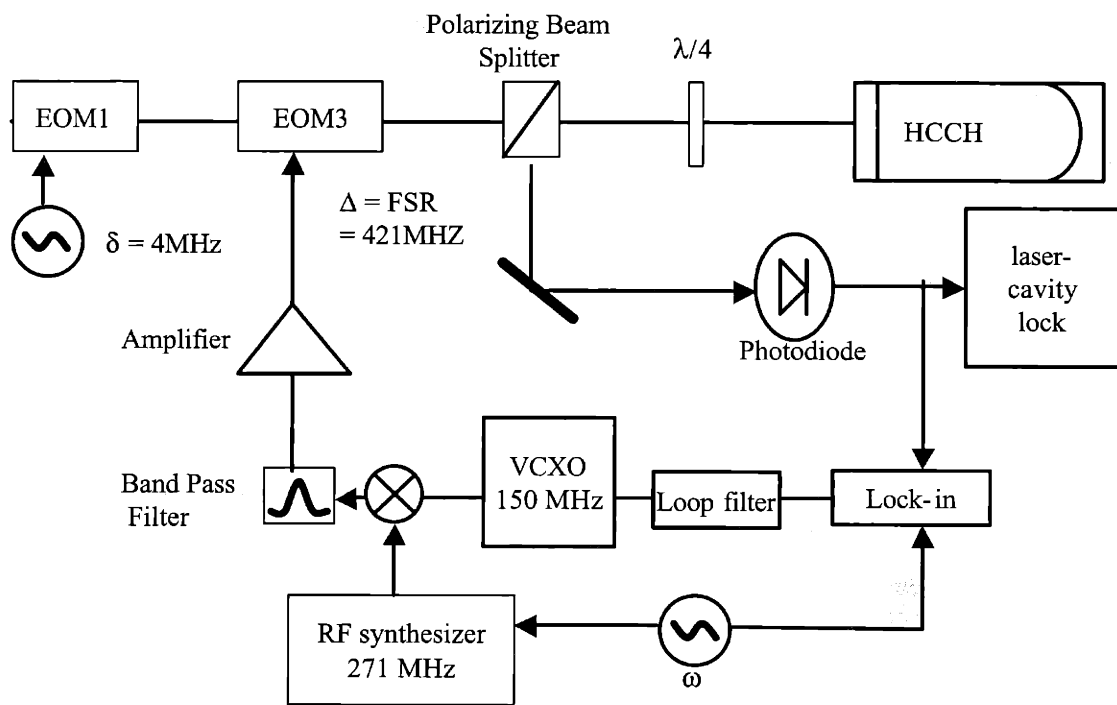


Figure 6-4: VCXO servo used for tracking the 421 MHz sidebands to the free spectral range of the cavity.

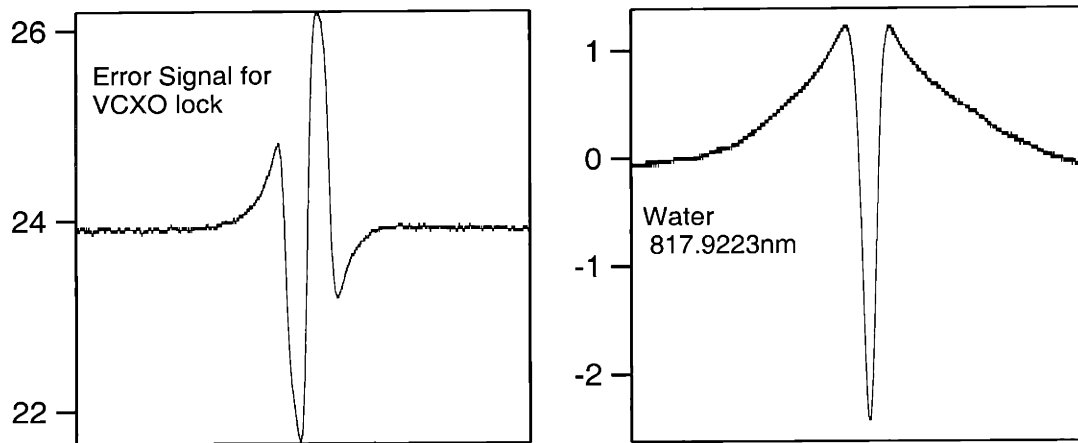


Figure 6-5: The error signal produced for tracking the FM sidebands Δ to the cavity FSR as the laser is scanned over a rovibrational transition in water is shown in the left panel. Shown on the right, is the saturated absorption NICE-OHMS signal for a transition in water observed at 817.9223 nm.

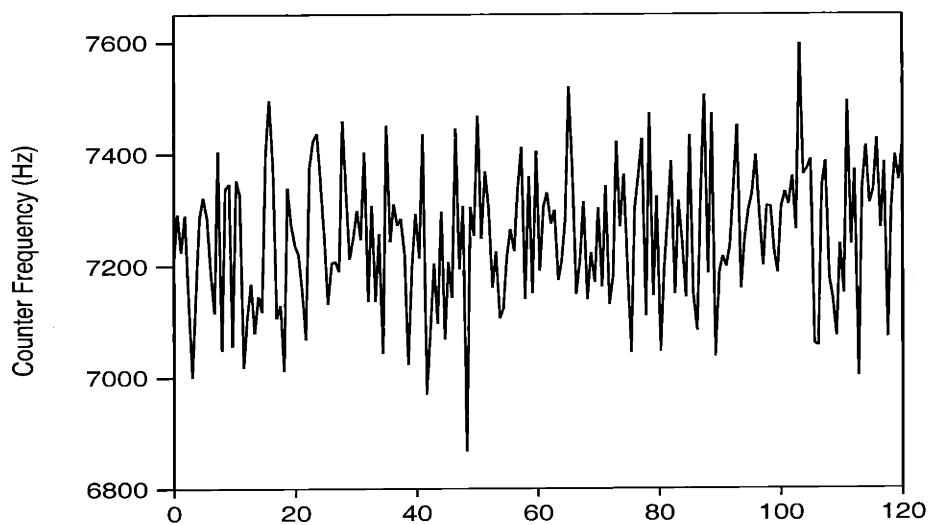


Figure 6-6: VCXO frequency. The cavity is scanned approximately 70 MHz, and the rms noise is 125 Hz. Note that a frequency offset of 150MHz has been subtracted.

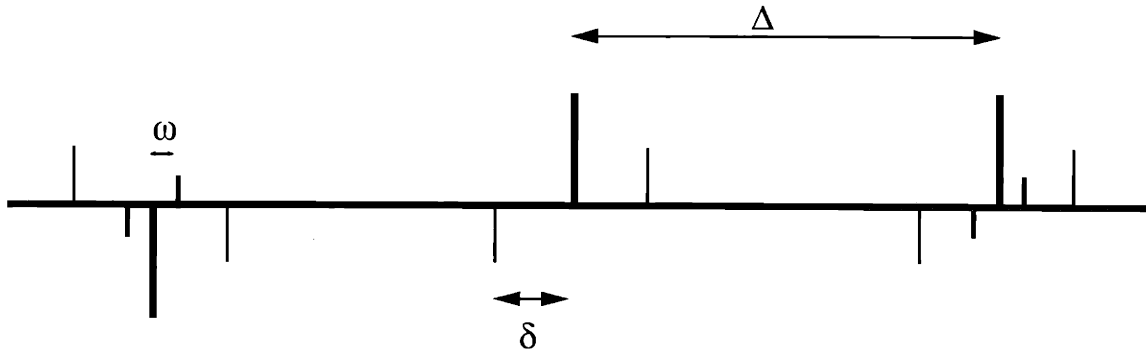


Figure 6-7: FM modulation of the incident laser beam. Modulation at $\delta = 4\text{MHz}$ is used to lock the laser frequency to the high finesse cavity. Modulation at $\Delta = 421\text{MHz}$ is used to generate the NICE-OHMS signal, and modulation at $\omega = 51\text{kHz}$ is used to actively lock Δ to the FSR of the cavity.

Since the laser is locked to the cavity, simple demodulation at Δ always yields a null signal unless there is an absorber in the cavity. Consequently, a second modulation is necessary to obtain information about the match between the cavity FSR and the sideband frequency, δ . Figure 6-7 illustrates the 3 different modulations of the incident laser beam. The modulation at δ is used to track the laser frequency to the high finesse cavity. Phase sensitive demodulation at Δ generates the NICE-OHMS signal, and the modulation at ω is used to actively track Δ to the FSR of the cavity as the cavity and therefore the laser is scanned. This triple modulation scheme is the same approach as described by Ye et al.[96, 99, 95, 98]. Another approach to obtaining information about the match between the cavity FSR and the sideband frequency, δ was developed by DeVoe and Brewer[102]. They detected the reflected signal from the cavity at the difference frequency of the two modulations, Δ and δ as shown in Figure 6-4.

The beam transmitted through the cavity is steered onto a detector resonant at 421 MHz. The absorption signal is derived from the rf output of this detector. This signal is amplified, bandpass filtered, and then demodulated using a double balanced mixer. This demodulated rf signal is then sent to a lock-in amplifier referenced to the dither on the cavity PZT. This dither aids in reducing noise and any dc

offsets. The PZT was typically dithered at 800Hz with an amplitude of approximately 400kHz. The dither amplitude was determined by beating the Ti:Sapphire laser, which is locked to the cavity, against a second JILA-designed Ti:Sapphire laser. Care was taken to ensure that the dither amplitude was smaller than the FWHM of the molecular transition in order to prevent the amplitude of the dither from broadening our saturated absorption line shapes. Shown in Figure 6-8 is an example of the broadening of the saturated absorption signal that results from a too large dither amplitude. The solid curve illustrates the saturated absorption for a H₂O (14 mTorr) absorption at 12,226.1 cm⁻¹. The dither amplitude of the PZT of the high finesse cavity was in this case approximately 2.2 MHz. The dotted curve shows the result for the same conditions except that the dither amplitude was 1 MHz. A 1 MHz dither is still larger than acceptable. If we assume that the pressure broadening rate for acetylene is roughly 10 MHz/Torr then a typical 50 mTorr sample has a pressure broadened linewidth of 500 kHz. The dither amplitude of the PZT was routinely kept at 150 MHz. Additionally, by fitting the lineshape appropriately, any broadening effects due to the dither amplitude may be removed. This is discussed in Section 6.3.

The absolute frequency of our spectrometer was measured using a home-built wavemeter. The wavemeter was calibrated to ± 5 MHz using a Ti:Sapphire laser locked on the ⁸⁵Rb 2-photon transition at 778.10542 nm. Variations of the index of refraction in air due to changes in wavelength, temperature, and pressure, were then accounted for using the equations given in reference [103] to get accurate readings of the Ti:Sapphire laser wavelength [103].

6.2.1 Comparison of NICE-OHMS Signal for Different Demodulation Schemes

As was described earlier, the NICE-OHMS signal was obtained by demodulating the signal at $\Delta = 421$ MHz recorded in transmission. However, it is possible to obtain NICE-OHMS signal in reflection as well. Additionally, it is thought that demodulation

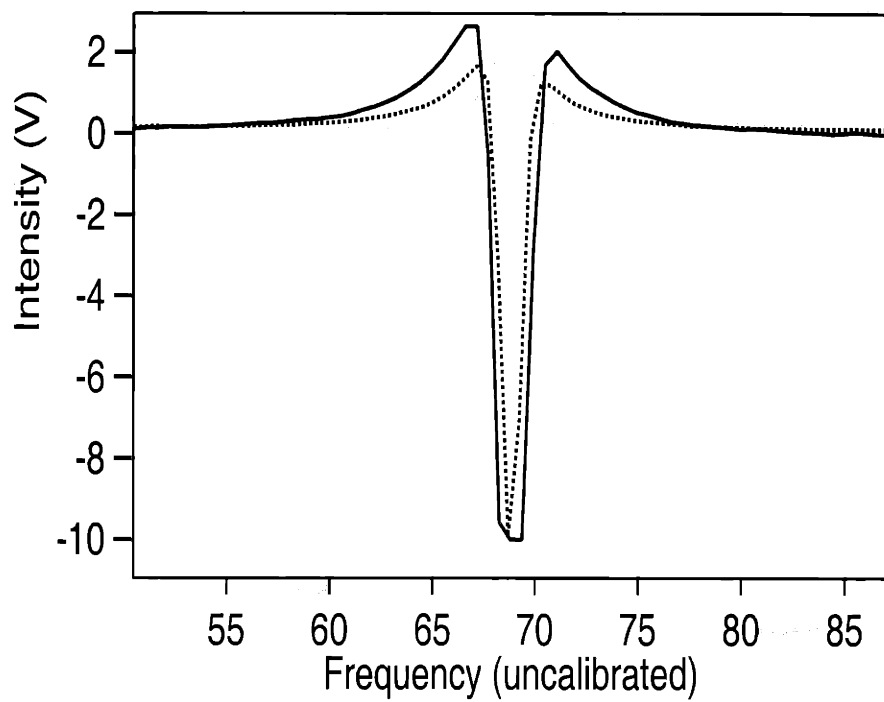


Figure 6-8: Comparison of saturated absorption NICE-OHMS lineshapes for a H_2O absorption at $12,226.1 \text{ cm}^{-1}$ at 14 mTorr. Solid curve shows the signal for a 2.2 MHz dither amplitude on the cavity PZT and the dotted curve shows the signal for a 1 MHz dither amplitude.

in reflection at the sum or difference frequency $\Delta \pm \delta$ may lead to a lower noise level [99, 102].

Shown in Figure 6-9 are NICE-OHMS signals recorded for several different demodulation schemes. The inset in each panel is an expanded view illustrating the noise level. In each scan of the transition at 817.922 nm, the saturated absorption signal was obtained using a sample pressure of 50 mtorr of H₂O. Shown in panel a) is the result for demodulation at 417 MHz in reflection. Shown in panel b) is the result for demodulation at 421 MHz in reflection. Shown in panel c) is the NICE-OHMS signal obtained in transmission for demodulation at 421MHz and finally shown in panel d) is the dc transmission.

In Panel a) the signal obtained for demodulation at 417 MHz is shown. The 417 MHz reference signal that was fed into the double balanced mixer was obtained by generating the sum and difference frequencies of 421 MHz and 4 MHz in a coupler. The output was filtered to remove the sum frequency, 425 MHz, and then amplified. The peak to peak signal is 6.5 V and the standard deviation of the noise level is 0.05 V. This corresponds to a signal to noise ratio, S/N of 127 with a 30 ms integration time. For a cavity finesse of 16,000, the noise equivalent sensitivity is 4.7×10^{-11} . The shot-noise limited minimum noise-equivalent detection sensitivity at a 1 s integration time is given by:[99]

$$\alpha_{min} = \frac{\pi}{finesse} \sqrt{\frac{eB}{I_{dc}}} \frac{1}{J_0 J_1} \quad (6.1)$$

where J_0 and J_1 are the Bessel functions which describe the frequency modulation intensity of the carrier and the sidebands generated by EOM3, e is the charge of an electron, B is the detection bandwidth, and I_{dc} is the photocurrent generated by the detector. The shot-noise limit for 60 μ W incident on the reflection detector is 5×10^{-13} .

In Panel b, the signal obtained for demodulation at 421 MHz in reflection is shown. The peak-to-peak signal is 3.5 V and the standard deviation of the noise level is 0.024 V. This corresponds to a signal to noise ratio, S/N of 147 with a 30 ms integration time. The noise equivalent sensitivity is 4.1×10^{-11} . This is slightly better than the

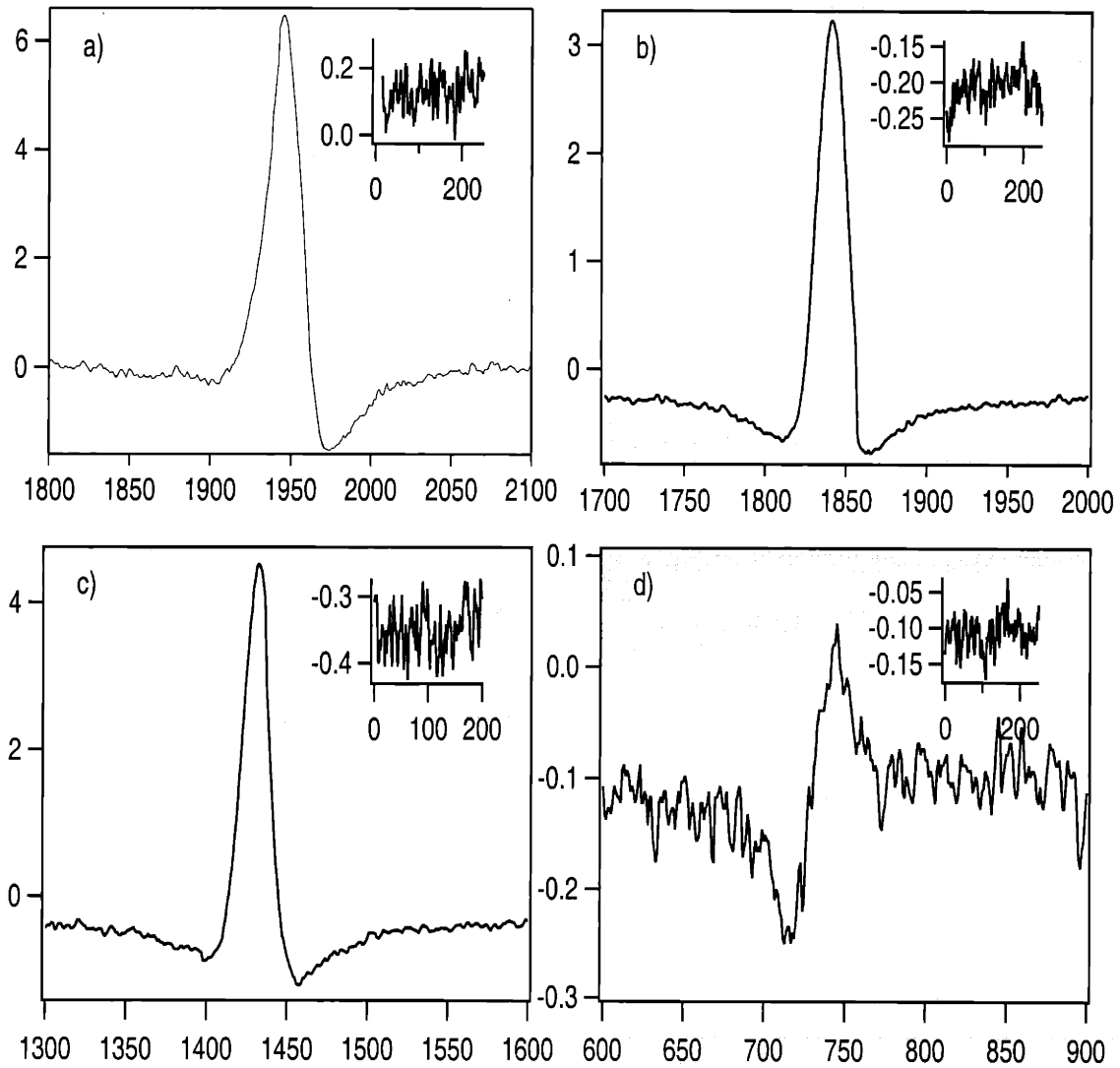


Figure 6-9: Panel a) is the result for demodulation at 417 MHz in reflection. Panel b) is the result for demodulation at 421 MHz in reflection. Panel c) is the NICE-OHMS signal obtained in transmission for demodulation at 421 MHz and panel d) is the dc transmission. The insets in each panel are an expanded view of the noise level.

result obtained for demodulation at the 417 MHz difference frequency.

In Panel c), a NICE-OHMS signal detected in transmission and demodulated at 421 MHz is shown. The S/N ratio is 143 and the noise equivalent sensitivity is 4.1×10^{-11} . The power of the light transmitted by the cavity is much smaller than the power of the reflected light. Consequently, the noise-equivalent sensitivity (shot-noise limit) is lower. In other words, the fundamental limit for the minimum detectable absorption loss is lower and the measurement is more sensitive. In this case, the noise-equivalent sensitivity for the transmitted light is 2×10^{-11} .

Finally in Panel d) of Figure 6-9 the dc cavity dither detection is shown. Instead of demodulating the rf signal output of a detector viewing the transmitted or reflected light, the direct dc signal of a detector viewing the transmitted light is sent to a lock-in amplifier. The lock-in amplifier is referenced to the dither frequency on the PZT. Note that in all the other cases, the demodulated rf signal was also sent to the lock-in. From the figure, it is clear that the NICE-OHMS method is far superior to simple dc cavity dither detection for which the S/N is only 9.

In both instances where the detection was done in reflection, the experimentally obtained noise-equivalent sensitivity was at least 100 times worse than the minimum noise-equivalent sensitivity. However, it has been proposed that heterodyne detection done in reflection should be better at achieving the shot noise limit [99]. There are several reasons why the noise level is much higher than expected when molecular signals are detected in reflection. In transmission the cavity serves to spatially mode clean and match the local oscillator signal. In reflection, this is not the case. The perfect mode of the reflected light can be altered by any EOMs and AOMs in the optical path, thus generating amplitude noise. Moreover, this amplitude noise of the spatial mode of the reflected beam can be time-dependent. Additionally, any pointing instability of the incident beam will increase the noise level. In order to achieve shot-noise limited detection sensitivities using detection methods in reflection, Ye has suggested that a second optical cavity should be placed before the high finesse cavity to spatially filter and stabilize the direction of the incident beam.[99]

6.3 One Photon H₂O Results

Noise Immune Cavity Enhanced - Optical Heterodyne Molecular Spectroscopy has been used to investigate (211)-(000) vibrational transition of water vapor. To my knowledge this is the first sub-Doppler resolution, precision measurement of the water transitions in the 800-830 nm region using ultrasensitive detection methods. I have measured more than 40 rotational-vibration transitions in this region of the spectrum. The line positions and derived molecular constants are reported. In addition, I have measured the pressure broadening rate for the $J'_{K_a, K_c} \leftarrow J''_{K_a, K_c} = 4_{0,4} \leftarrow 3_{0,3}$ transition at 12,226.101 cm⁻¹ of the (211)-(000) transition and those results will also be discussed. The results presented here measure the transitions to ± 5 MHz absolute accuracy.

Using the NICE-OHMS method, we recorded saturation dips for over 40 absorption lines in the (211) \leftarrow (000) band. Figure 6-10 illustrates one of the recorded saturation dips for the $J'_{K_a, K_c} \leftarrow J''_{K_a, K_c} = 4_{0,4} \leftarrow 3_{0,3}$ transition at 12226.1 cm⁻¹. The H₂O pressure was approximately 20 mTorr. Note that the lineshape is the second derivative of an absorption lineshape. FM demodulation results in a dispersion curve. Recall that this signal is then fed to a lock-in amplifier referenced to a low frequency dither on the cavity PZT. The final optimized signal is a second derivative of the absorption profile. The actual sign of the lineshape can either be positive or negative depending on the phase of the lock-in amplifier. There is a slight asymmetry in our experimental line shapes. We believe this is due to residual amplitude modulation.

Enhanced sensitivity is a key advantage of NICE-OHMS. The S/N for this scan is 1120 at a 1 s integration time. For comparison, the DC transmission signal was also recorded using lock-in detection, where the reference was again the dither on the cavity. From Figure 6-10 it is obvious that the DC S/N is inferior to that of the NICE-OHMS signal. In the case of the DC signal, the S/N is only 50 at a 1s integration time. From this DC signal we can easily determine the number density of saturated molecules. First, the original signal size must be determined based on the

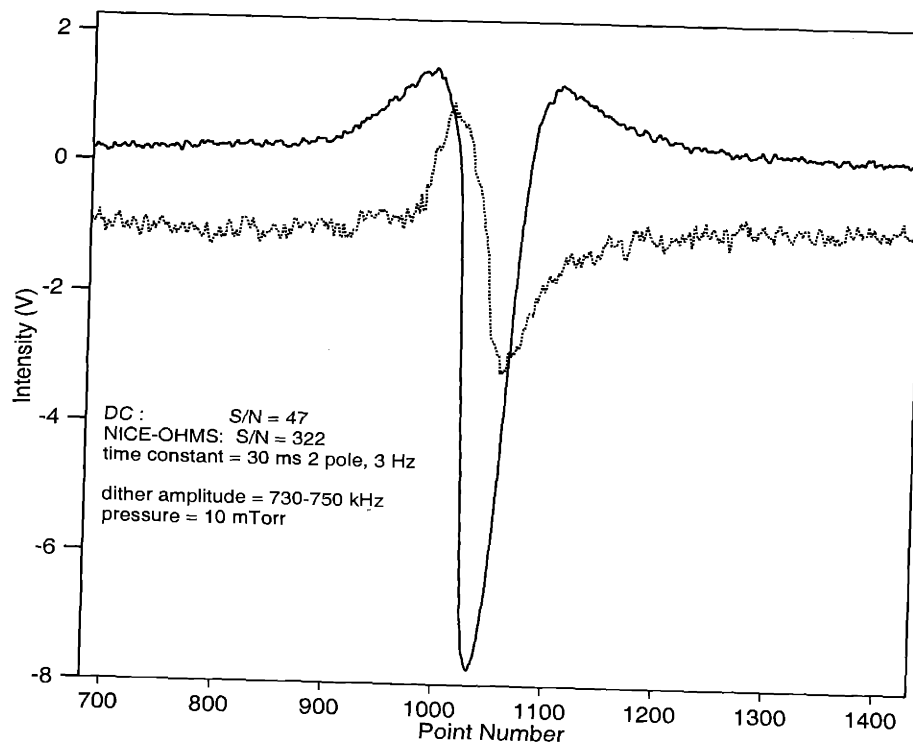


Figure 6-10: $J'_{K_a, K_c} \leftarrow J''_{K_a, K_c} = 4_{0,4} \leftarrow 3_{0,3}$ transition at 12226.1 cm^{-1} . Solid line: NICE-OHMS signal at 10 mTorr. Dotted line: DC detection.

parameters set on the lock-in amplifier. For a Lorentzian peak, the true signal size is given by:[99]

$$\text{Lorentzian Peak} = \frac{\sqrt{2}}{\text{ScaleFactor} = 0.98} V_{pk-pk} \frac{\text{Sensitivity}}{\text{FullScale}} \quad (6.2)$$

where, V_{pk-pk} is the peak-to-peak amplitude of the DC signal, the sensitivity of the lock-in amplifier is 50 mV and has a full scale value of 10 V. The scale factor is determined from the Wahlquist correction factor [104] which accounts for the dither amplitude of the PZT. In this case, the scale factor is ≈ 0.96 .

This corresponds to an original signal size of ≈ 3 mV. The single-pass integrated saturated absorption α_{sat} , is given by:[99]

$$\frac{\alpha_0 - 2\alpha_{sat}}{\alpha_0} = \sqrt{\frac{P_{dc}}{P_{sat}}} \quad (6.3)$$

where, α_0 is simply $2\pi/\text{finesse}$, P_{dc} is the transmitted intensity (13 V for this measurement) and P_{sat} is calculated from equation 6.2 to be 3 mV. The single-pass integrated saturated absorption α_{sat} , was determined to be 23×10^{-9} .

The noise equivalent sensitivity for both the DC and NICE-OHMS experiments shown in Figure 6-10 can now be determined from α_{sat} . The noise equivalent sensitivity is simply $\alpha_{sat}/\text{signal-to-noise ratio}$. For the NICE-OHMS signal this corresponds to a noise equivalent sensitivity of 2×10^{-11} . This is only slightly inferior to the estimated shot noise limit, for this particular scan, which was calculated to be 1.7×10^{-11} .

The measured rotational transitions in the (211) \leftarrow (000) band are listed in Table 6.1. The last column reports the difference between the transitions measured in this study and previous experiments. Typically, the NICE-OHMS transitions are found to be 45 ± 10 MHz to the red of the previous reported data.

We have also performed a least squares fit of the vibration-rotation energy levels using Watson's[35] A-reduced form of the asymmetric rotor Hamiltonian. Watson's Hamiltonian is expressed in the form of a power series that can conveniently be extended to arbitrarily high order [105]. The matrix is composed of $\Delta K = 0$ and

$\Delta K = \pm 2$ terms. The constant terms in Eqn. 6.5 are the quartic distortion coefficients while those in Eqns. 6.6 and 6.7 are the sextic and eighth-order distortion coefficients, respectively.

$$H = \frac{1}{2}(B + C)J^2 + [A - \frac{1}{2}(B + C)](J_z^2 - bJ_-^2) \quad (6.4)$$

$$H^4 = -\Delta_J J^4 - \Delta_{JK} J^2 J_z^2 - \Delta_K J_z^4 - 2\delta_J J^2 J_-^2 - \delta_K (J_z^2 J_-^2 + J_-^2 J_z^2) \quad (6.5)$$

$$H^6 = H_J J^6 + H_{JK} J^4 J_z^2 + H_{KJ} J^2 J_z^4 + H_K J_z^6 + 2h_J^4 J_-^2 + h_{JK} J^2 (J_z^2 J_-^2 + J_-^2 J_z^2) + h_K (J_z^4 J_-^2 + J_-^2 J_z^4) \quad (6.6)$$

$$H^8 = L_J J^8 + L_{JK} J^6 J_z^2 + L_{JK} J^4 J_z^4 + L_{KKJ} J^2 J_z^6 + L_K J_z^8 + 2l_J J^6 J_-^2 + l_{JK} J^4 (J_z^2 J_-^2 + J_-^2 J_z^2) + l_{KJ} J^2 (J_z^4 J_-^2 + J_-^2 J_z^4) + l_K (J_z^6 J_-^2 + J_-^2 J_z^6) \quad (6.7)$$

where,

$$b = (C - B/2A - B - C) \quad (6.8)$$

and,

$$J_{\pm}^2 = (J_x^2 - J_y^2). \quad (6.9)$$

The (000) ground state vibration-rotation energy level parameters were held fixed at the values given in reference [105] and the upper state parameters were allowed to vary. Unfortunately, the residuals for the fit were larger than the experimental error in determining the frequencies of the transitions. The transitions were measured to within 5 MHz, but the residual of the theoretical fit were considerably larger and the fit was able to reproduce some of the transitions only to within 0.01 cm^{-1} . Consequently,

the results of the fit have been omitted from this discussion.

However, it is important to understand why the fit performed so poorly. The 211 state is a member of the $3\nu + \delta$ polyad [106] and interacts with the (310), (112), (013), (230), (131), (032) and (051) states. In particular, it is known that the (211) level is strongly perturbed by the nearby (310) level via a B-type Coriolis interaction. The (211) and (310) states lie only 12 cm^{-1} apart and strong mixing occurs for each J. In order to accurately determine the rotational constants, this interaction must be accounted for. Flaud and coworkers [106] simultaneously fit over 500 rovibrational energy levels in these states and determined a set of 104 vibrational energies, rotational, resonance, and centrifugal distortion constants for the $3\nu + \delta$ polyad by taking into account the anharmonic and coriolis perturbations coupling the vibrational levels. Only when all of these perturbations are taken into account can the (211) state be accurately modelled.

Table 6.1: Transitions observed in the NICE-OHMS experiment. The differences between our measurements and those of Toth [2] are listed in column 4.

J K_a K_c (211)	J K_a K_c (000)	NICE-OHMS (cm^{-1})	Difference (MHz)
3 3 1	4 3 2	12052.81751	-99.3
0 0 0	1 0 1	12127.45925	-125
5 3 3	5 3 2	12136.51655	-064.9
6 4 2	6 4 3	12140.50725	-184
5 4 2	5 4 1	12144.79311	-189
6 5 1	6 5 2	12144.8609	-109
5 4 1	5 4 2	12145.27694	-166
1 1 1	1 1 0	12145.44256	-183
5 3 2	5 3 3	12146.62122	-137
2 2 1	2 2 0	12149.2005	-160
4 4 1	4 4 0	12149.72991	-149
4 4 0	4 4 0	12149.78755	-194
5 5 0	5 5 1	12150.2492	-270
5 5 1	5 5 0	12150.2492	-270
3 3 0	3 3 1	12150.3331	-150
2 2 0	2 2 1	12151.82247	-103
6 6 1	6 6 0	12155.52529	-71
6 6 0	6 6 1	12155.52529	-71
1 1 0	1 1 1	12156.20719	-0.111

continued on next page

<i>continued from previous page</i>				
J K _a K _c (211)	J K _a K _c (000)	NICE-OHMS (cm ⁻¹)	Difference (MHz)	
1 0 1	0 0 0	12173.76331	-109	
2 1 2	1 1 1	12190.74187	-163	
2 0 2	1 0 1	12195.18902	-158	
2 1 1	1 1 0	12202.0266	-180	
3 1 3	2 1 2	12207.74998	-172	
3 0 3	2 0 2	12212.06837	-173	
3 2 2	2 2 1	12218.8282	-144	
4 1 4	3 1 3	12223.00342	-78	
3 2 1	2 2 0	12223.83829	-181	
3 1 2	2 1 1	12224.68079	-91	
4 0 4	3 0 3	12226.09959	-161	
5 1 5	4 1 4	12236.559	-130	
4 2 3	3 2 2	12237.46464	-146	
5 0 5	4 0 4	12238.31124	-126	
4 3 2	3 3 1	12243.53595	-125	
4 1 3	3 1 2	12244.71738	-132	
4 3 1	3 3 0	12244.78621	-89.1	
4 2 2	3 2 1	12248.01782	-168	
6 1 6	5 1 5	12248.57778	-112	
6 0 6	5 0 5	12249.3885	-120	
5 2 4	4 2 3	12254.51644	-121	
5 1 4	4 1 3	12260.9938	-130	
6 2 5	5 2 4	12267.04329	529	
5 2 3	4 2 2	12270.81262	-108	
6 1 5	5 1 4	12278.71896	-124	
6 3 4	5 3 3	12280.43701	-119	
6 3 3	5 3 2	12289.13026	-124	
6 2 4	5 2 3	12291.04483	-117	

We have also performed a preliminary study of pressure broadening of the $J'_{K_a, K_c} \leftarrow J''_{K_a, K_c} = 4_{0,4} \leftarrow 3_{0,3}$ transition at 12226.1 cm⁻¹. The results of this are shown in Figure 6-12. In order to determine the FWHM of the lineshape accurately at each pressure, the NICE-OHMS lineshape was fit to a second derivative of a Lorentzian taking into account the effect of broadening due to the dither amplitude of the end mirror of the high finesse cavity. The fit is based on Wahlquist's modulation broadening formalism. Following the notation given in reference [99], the molecular dispersion lineshape has the form:

$$\text{Lineshape}_{disp} \propto \frac{\xi\Gamma}{\Gamma^2 + \xi^2}, \quad (6.10)$$

where ξ is the frequency detuning and Γ is the HWHM. However, the modulation amplitude of the dither on the cavity end mirror, H_ω , needs to be accounted for. For this, we need to first define the following parameters [99]:

$$\begin{aligned} a &= \frac{\xi}{H_\omega} \quad b = \frac{\Gamma}{H_\omega} \\ \rho &= 1 + a^2 + b^2, \\ \sigma &= \sqrt{\rho^2 - 4a^2}, \text{ and} \\ \Lambda &= \rho + \sigma. \end{aligned} \quad (6.11)$$

The lineshape after signal recovery from the lock-in amplifier is given by:

$$\text{Signal} = b \cdot \left[2 - \frac{\sqrt{\Lambda^2 - 2\Lambda}}{\sigma} \right]. \quad (6.12)$$

In Figure 6-11 is shown a calibrated scan for the transition at 12226.1 cm^{-1} . The results of the fit to the lineshape are shown in addition to the residuals between the fit and experimental data. To determine a pressure broadening rate for the $J'_{K_a, K_c} \rightarrow J''_{K_a, K_c} = 4_{0,4} \rightarrow 3_{0,3}$ transition, we recorded and fit the lineshapes for this transition at several different pressures. From this, the pressure broadening rate is determined to be $12.2 \pm 0.6 \text{ MHz/Torr}$. This is slightly lower than the average pressure broadening coefficients determined from other rovibrational transitions in this band. An average self broadened rate of 18 MHz/Torr at 296 K for rotational lines in the (211) band has been reported [107]. The pressure gauge, Hastings Instruments, Model 2000, which was used to measure the pressure of water vapor in the cell, has an accuracy of 15% and this may account for the difference in the pressure broadening coefficients.

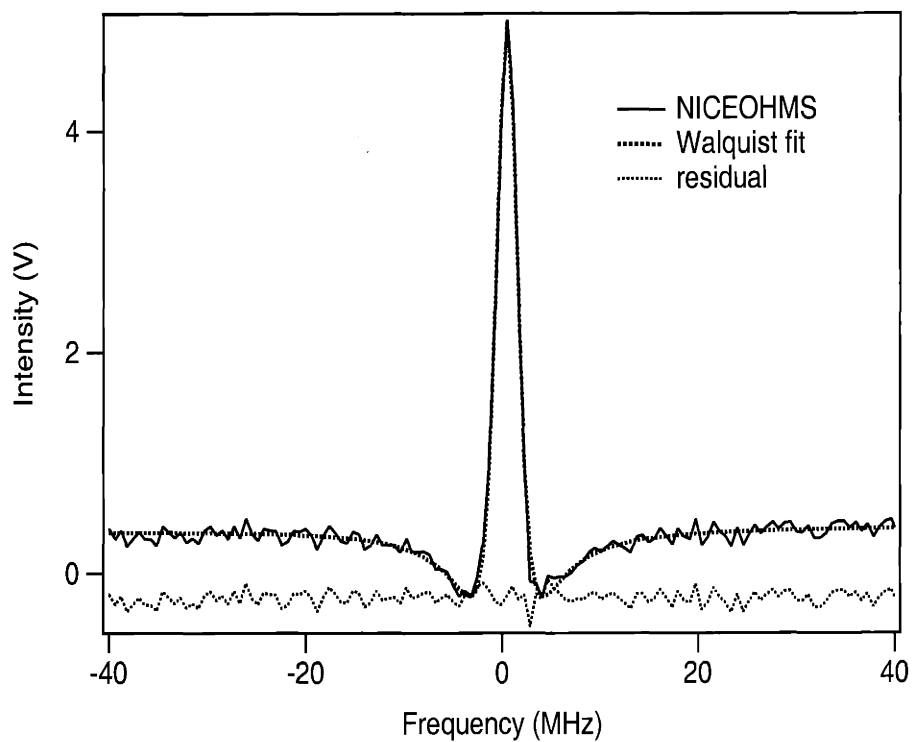


Figure 6-11: Frequency scan of the H_2O resonance at 817.922 nm and the theoretical fit based on Wahlquist's modulation broadening formalism. Fit residuals are shown in the lower curve.

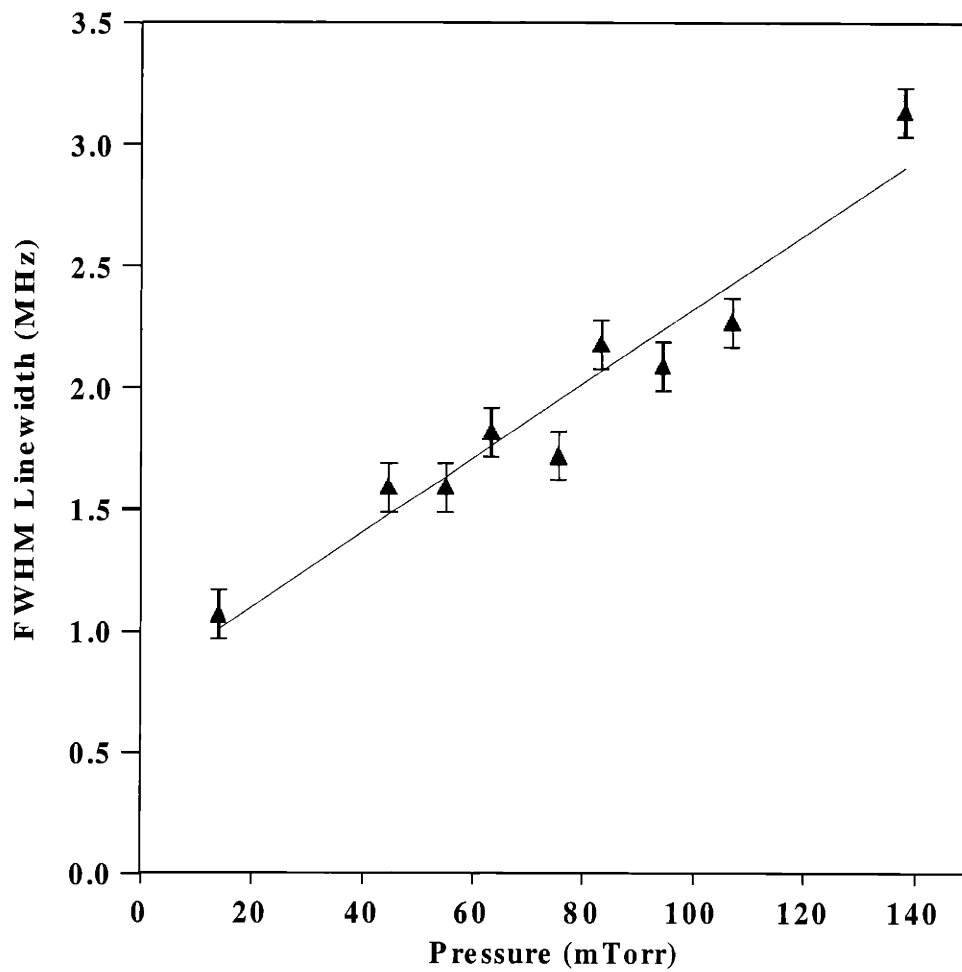


Figure 6-12: Pressure study of the absorption line at $12,226.101 \text{ cm}^{-1}$. The pressure broadening rate is determined to be 12 MHz/Torr .

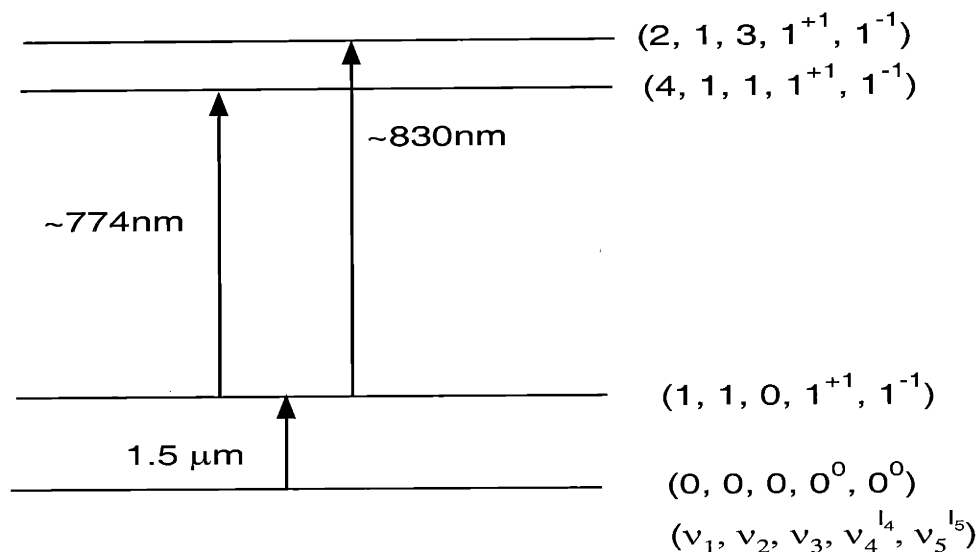


Figure 6-13: A diode laser at $1.5 \mu\text{m}$ is used to excite the $(1,1,0,1^{+1},1^{-1})$ overtone which is resonant with $(1,0,1,0,0)$ level. A Ti:Sapphire laser is used to access rotational levels in either the $(2,1,3,1^{+1},1^{-1})$ or $(4,1,1,1^{+1},1^{-1})$ vibrational levels.

6.4 Double Resonance NICE-OHMS of Acetylene

As described earlier, the primary objective of the NICE-OHMS experiments was to observe nuclear permutation tunneling splittings in $^{13}\text{C}_2\text{H}_2$. The NICE-OHM spectrometer could only access transitions in the region of $12,100 - 13,700 \text{ cm}^{-1}$. Consequently, in order to access transitions in the $18,000 \text{ cm}^{-1}$ region of the spectrum, a double resonance scheme was necessary. Diagramed in Figure 6-13 is the double resonance NICE-OHMS scheme. A diode laser at 1.5μ is used to excite the $(1,1,0,1^{+1},1^{-1})$ overtone which is resonant with $(1,1,1,0,0)$ level. The second step requires the use of a Ti:Sapphire laser to access rotational levels in either the $(2,1,3,1^{+1},1^{-1})$ or $(4,1,1,1^{+1},1^{-1})$ vibrational level. When these experiments were initially performed the energies of the $(2,1,3,1^{+1},1^{-1})$ and $(4,1,1,1^{+1},1^{-1})$ levels were not experimentally known. Using the effective Hamiltonian model discussed in Chapter 4 the energies of rotational levels in each band were estimated. Using our double resonance NICE-OHMS technique, described in the following section, we then searched for the $(4,1,1,1^{+1},1^{-1})$ level based on the calculated line positions. Unfortunately, this

level was never found.

A second collaboration with Kevin Lehmann and Giacinto Scoles at Princeton proved to be quite fruitful in pinpointing the positions of several rovibrational levels. In the experiments performed at Princeton, we were able to locate the position of the $(2,1,3,1^{+1},1^{-1})$ level and look for nuclear permutation tunneling splittings. Although permutation doublets were not observed within the 15 MHz resolution of these experiments, an enhanced understanding of the acetylene \leftrightarrow vinylidene isomerization coordinate was gained. The experiments performed at Princeton will be discussed briefly in Section 6.6.

6.5 Double Resonance NICE-OHMS Experimental Details

The experimental details for the double-resonance experiment are similar to those described in Section 6.2. The NICE-OHMS spectrometer described earlier is used to detect rovibrational lines in the $(4,1,1,1^{+1},1^{-1}) \leftarrow (1,1,0,1^{+1},1^{-1})$ or the $(2,1,3,1^{+1},1^{-1}) \leftarrow (1,1,0,1^{+1},1^{-1})$ transition of $^{13}\text{C}_2\text{H}_2$. The Ti:Sapphire laser operating near 790nm or 830nm is locked to a high finesse cavity which is used to tune the laser continuously over 1.2 GHz. The Ti:Sapphire laser is not a commercial system and the electronics controlling the internal etalon and Mach-Zender interferometer must be manually adjusted, and the laser must be locked to the cavity before each 1.2 GHz segment could be scanned. As a result, it took several days to search a 1 cm^{-1} region of the spectrum for rovibrational transitions.

The $^{13}\text{C}_2\text{H}_2$, obtained from Cambridge Isotopes, was 99.98% pure. It was subject to several freeze-pump-thaw cycles before use in the high finesse cavity.

The first attempt at double resonance NICE-OHMS was to locate rotational lines of the $(4,1,1,1^{+1},1^{-1})$ level. A DFB (distributed feedback) diode laser (Ortel Corp., Model 1710) was used to excite rotational lines in the $(1,1,0,1^{+1},1^{-1}) \leftarrow (0,0,0,0,0)$ transition. A DFB diode laser was chosen because of its widespread availability,

relatively low cost, and ease of use. The diode laser was mounted in a 15 pin Butterfly mount (Newport, Model 744) which was adapted for use with the current controller (ILX Lightwave, Model LDX-3620) and temperature controller (ILX Lightwave, Model LDT-510B) by the electronics shop at JILA. The DFB laser output was delivered via a fiber pigtail. It was found that the output of the fiber optic pigtail diverged greatly. To compensate for this divergence, a fiber optic mounted collimating lens was coupled to the end of the fiber pigtail of the DFB diode laser. After collimation, the radiation of the diode laser was directed along the same optical path as the Ti:Sapphire laser. Note that the two beams were overlapped after EOM3, thus the DFB diode laser did not pass through any of the acousto-optic or electro-optic modulators. The high finesse cavity was transparent to 1540 nm light. Approximately 10-15 mW of 1540 nm radiation was incident on the cavity and $\approx 4-5$ mW was transmitted through the cavity.

The Ortel diode laser output was 30 mW centered at 1540 nm and could be frequency tuned using the temperature or current controller. At the time of this experiment, diode lasers with higher output powers were not available. Additionally, the DFB laser was hand selected to ensure that the center wavelength was suitable since the laser could only be tuned $\approx \pm 0.5$ nm. With a center frequency of 1540 nm only high-J P lines in the $(1,1,0,1^{+1},1^{-1}) \leftarrow (0,0,0,0,0)$ transition could be accessed. DFB diodes were not commercially available in spectral region of 1530 nm, which corresponds to low-J rotational lines in this vibrational band. Using the current controller, the wavelength of the diode was adjustable at a rate of 0.1nm/°C. The operating temperature of the diode had to be kept below 50 °C and above 0 °C to prevent damage. Small adjustments of the current (± 10 mA) were performed to make fine adjustments to the wavelength of the diode laser without reducing the output power. The diode laser could be tuned ≈ 100 MHz/mA.

The wavelength of the Ortel diode laser was determined by frequency doubling its output using a periodically poled lithium niobate (PPLN) crystal and beating the second harmonic of this with the Ti:Sapphire laser. A wavemeter operating in the 1550 nm spectral region was not readily available and therefore a less expensive

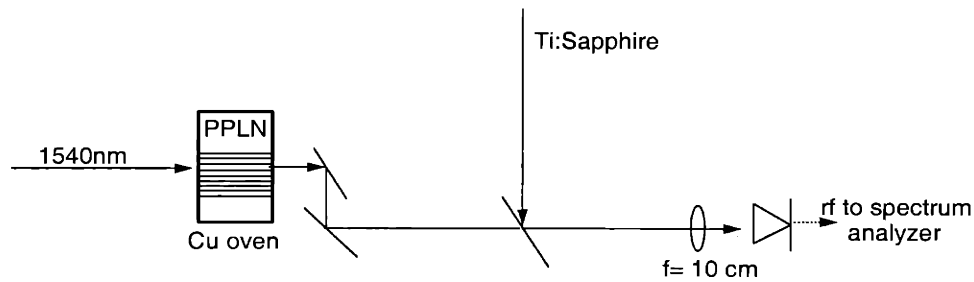


Figure 6-14: Wavelength measurement of DFB diode laser from Ortel.

alternative for determining the wavelength was implemented. The PPLN crystal (Crystal Technology, Inc.) was 19 mm long x 11 mm wide x 0.5 mm thick and had 10 different domains (or stripes) ranging from 18.6 μm to 20.4 μm . Each domain is capable of frequency doubling a different wavelength region. In order to achieve phase matching at a particular wavelength, the correct domain had to be used at the correct temperature. For doubling wavelengths near 1540 nm, the PPLN crystal was placed in a copper oven, which was resistively heated to 53 $^{\circ}\text{C}$. Approximately 10 mW of vertically polarized light from the DFB diode laser was focused onto the 18.6 μm grating of the PPLN crystal. Care had to be taken to properly focus the 1540 nm light through the length of the crystal to ensure that all of it remained within the 18.6 μm domain. In Figure 6-14, the experimental setup for determining the frequency of the Ortel diode is illustrated. Approximately 1.6 μW of second harmonic light was generated using the PPLN crystal. The second harmonic light was then focused on a heterodyne detector along with the output of the Ti:Sapphire laser. The beat note was observed using a rf spectrum analyzer.

The beat note exhibited a comb of frequencies with a 42 MHz spacing. This corresponded to the length of the fiber collimator. Apparently, feedback from the lens in the collimator caused the DFB diode to lase at several frequencies, generating the 42 MHz comb observed in the beat note. This problem was solved by replacing the 2 meter long fiber optic collimator with a microscope objective in order to collimate the output of the diode laser in free space.

An example of the observed beat note between the second harmonic of the DFB

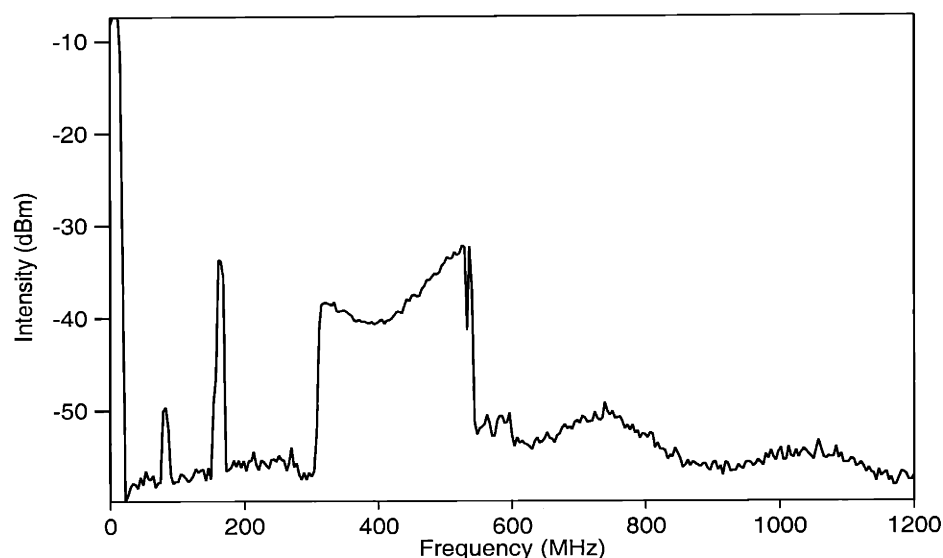


Figure 6-15: Beat note between the frequency doubled output of the DFB diode laser and the Ti:Sapphire laser at 769.41 nm. The signals at 80 and 160 MHz are due to the acousto-optic modulation of the Ti:Sapphire laser beam. The signal at 400 MHz is 200 MHz wide and is due to the drift of the DFB diode laser, which has an instantaneous linewidth of 3 MHz.

diode laser and the Ti:Sapphire laser is shown in Figure 6-15. The diode laser was roughly centered on the P(14) transition at 1537.96nm (the temperature controller was set to 7.5 °C). The signals at 80 and 160 MHz are due to the acousto-optic modulation of the Ti:Sapphire laser beam. The signal at 400 MHz is 200 MHz wide and is due to the drift of the DFB diode laser which has a linewidth of 3 MHz. The frequency of the Ti:Sapphire laser was 769.41 nm. From Figure 6-15 it is clear that the observed beat note was not stable. The frequency of the DFB diode laser drifted continuously over a range of approximately 200 MHz. In order to observe any NICE-OHMS signal during the second step of the double resonance experiment, it is necessary that the DFB diode laser be stable and consistently excite the same velocity group. Otherwise, it is possible that as the second laser, (Ti:Sapphire) is scanned slowly, the diode laser may move off of resonance and consequently, no NICE-OHMS signal will be observed.

To ensure that the DFB diode excites the same velocity group as the Ti:Sapphire

laser is tuned, the diode laser is locked to the molecular resonance. The output of the Ortel DFB diode was tuned to the P(16) rotational line of the $(1,1,0,1^{+1},1^{-1}) \leftarrow (0,0,0,0,0)$ transition. The current source of the diode laser was slowly dithered over the top of the molecular resonance. The output of a detector monitoring the absorption was sent to a lock-in amplifier. The signal from the lock-in amplifier was sent to a JILA designed loop filter that supplied a dc correction voltage. This correction voltage was then fed into the ILX Lightwave the current supply for the diode.

Once the diode laser was stabilized on a molecular resonance, the Ti:Sapphire laser was scanned near 12074.5 cm^{-1} . Unfortunately, no double resonance signal due to absorption of second photon was observed. The second photon should have accessed the $(4,1,1,1^{+1},1^{-1})$ level in $^{13}\text{C}_2\text{H}_2$. Recall that this level has never been observed and its energy was predicted based on the results in Chapter 4. It is possible that the calculated energy of this band is incorrect. Experiments performed at Princeton, in an attempt to locate this level were also unsuccessful. A 60 cm^{-1} region was searched and the $(4,1,1,1^{+1},1^{-1})$ level was not found.

However, the experiments performed at Princeton did locate a different level that belongs to the same polyad. Transitions were observed that terminated on low-J rotational levels in the $(2,1,3,1^{+1},1^{-1})$ band. Oddly, the location of this band was successfully predicted by the Hamiltonian in Chapter 4, even though it failed to accurately predict the location of the $(4,1,1,1^{+1},1^{-1})$ level.

A second attempt was made to observe double resonance NICE-OHMS signal due to excitation of the $(2,1,3,1^{+1},1^{-1})$ level. The set-up described above was used. The diode was locked on a high J line of the transition and the Ti:Sapphire laser was scanned several wavenumbers in the vicinity of high-J lines in the $(2,1,3,1^{+1},1^{-1})$ level. Nothing was seen. In the Princeton studies, only a few low-J lines were observed and based on their rotational analysis, which did not include centrifugal distortion constants, the locations of the higher-J levels were predicted. Since the double resonance NICE-OHMS experiments were limited in their ability to scan quickly, only a small wavenumber region was searched and no transitions were found. It is entirely possible that in order to accurately determine the location of high-J lines, the centrifugal dis-

tortions constants are need. Moreover, in the Princeton experiments which sampled low-J lines, a perturbation was found. It is conceivable that this perturbation, or an other Coriolis interaction causes the high-J lines of the $(2,1,3,1^{+1},1^{-1})$ level to shift in energy and become weaker in intensity.

The final attempt to observe double resonance NICE-OHMS signal due to excitation of the $(2,1,3,1^{+1},1^{-1})$ level required the use of a different diode laser. The goal of this final attempt was to exactly reproduce the exact experiments performed at Princeton. This required some drastic changes to the experimental setup. Several narrow bandwidth diode lasers were obtained on loan from ILX Lightwave. These diode lasers were centered near 1530 nm, consequently low-J lines in the transition could be accessed. However, the PPLN crystal could not be used at 1530 nm. In order to determine the wavelength accurately, a wavemeter operating in the IR region was constructed. The details of the wavemeter construction are lengthy and will not be reviewed here.

All of the diodes had a maximum output of 3 mW. An Erbium doped fiber amplifier was constructed courtesy of Dr. David Jones which was able to amplify the 3mW output of the diode laser to 50 mW. A diode laser which was already mounted in a housing with a grating and the necessary thermoelectric coolers was selected for use. The previously described current and temperature controllers were used to operate the diode. The frequency of the diode laser was stabilized by locking the diode laser to the molecular resonance under study. A second sample cell was placed after the high finesse cavity, contained 500 mTorr of $^{13}\text{C}_2\text{H}_2$. The absorption of the 1.5 μm radiation passing through this cell was monitored and used for locking the diode laser. For these experiments, we choose the R(1) or R(2) line of the $(1,1,0,1^{+1},1^{-1}) \leftarrow (0,0,0,0,0)$ transition and used a sample pressure of 50 mTorr in the high finesse cavity.

Over time, the finesse of the cavity had degraded to 2,000. Consequently, another cavity was built using the same zerodur rod. The cavity mirrors were standard 'super' mirrors from Newport Corporation. The input mirror was flat and the end mirror had a 1 m radius of curvature. Recall that the previous end mirror had a 60 cm radius

of curvature. As a result, the lens used to mode match the Ti:Sapphire beam to the high finesse cavity had to be adjusted. The finesse of this cavity was determined to be 34,200. The finesse was measured by determining the width of a cavity resonance. The FWHM of the cavity resonance was 0.0123 MHz and the FSR of the cavity was 420.857 MHz. This corresponds to a finesse of 34,200. Previously, the finesse of the original cavity was measured using the cavity Ring-Down method. Using that method, it was found that the finesse of every cavity built was always 16,000. But when determining the finesse by measuring the FWHM of the resonance, the finesse of the original cavity which had degraded over time, was determined to be on the order of 2,000. From this it is clear that all of our measurements of the cavity finesse based on the cavity Ring-Down method were incorrect. Those measurements were limited by the time response of the detector.

Nevertheless, even though all of these improvements were made, no double resonance NICE-OHMS signal was observed when the Ti:Sapphire laser was scanned $\pm 0.5 \text{ cm}^{-1}$.

6.6 Double Resonance NICE-OHMS of Acetylene Results and Discussion

Neither the $(4,1,1,1^{+1},1^{-1})$ nor the $(2,1,3,1^{+1},1^{-1})$ vibrational levels were located using Noise Immune Cavity Enhanced Optical Heterodyne Detection. This null result is very puzzling. Figure 6-16 is an example of a 1 photon transition in $^{13}\text{C}_2\text{H}_2$ at 793.3677 nm with a sample pressure of 50 mTorr using the final cavity which had a reliably measured finesse of $34,000 \text{ cm}^{-1}$. In this figure the (10300) vibrational level is excited. The signal-to-noise ratio is 660. In this scan the noise level is set by the digitization noise of the 16 bit data acquisition board. The signal to noise ratio for this scan might actually be much higher. For the DC scan, the S/N ratio is 170.

There are several possible explanations for the failure to observe double-resonance NICE-OHMS signals and the inability to reproduce the results of the Princeton ex-

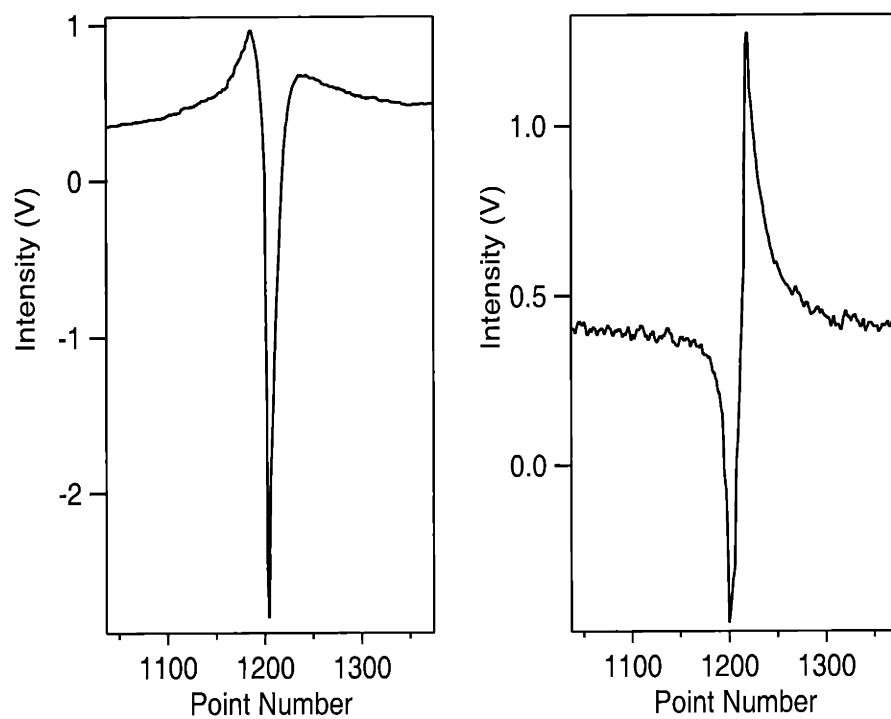


Figure 6-16: Comparison of NICE-OHMS and DC absorption signals using a cavity with a finesse of 32,000. Left: One photon NICE-OHMS signal of $^{13}\text{C}_2\text{H}_2$ at 793.3677nm. Right: DC signal

periments [20]. First and foremost, the $(4,1,1,1^{+1},1^{-1})$ state was not seen in either experiment, which leads us to conclude that the calculation of its vibrational energy was incorrect. It is possible that this level is strongly perturbed and its energy was shifted from that predicted by the model in Chapter 4 or that it may have been too weak to be observed.

The oscillator strength for the $(2,1,3,1^{+1},1^{-1}) \leftarrow (1,1,0,1^{+1},1^{-1})$ transition should be comparable to that of the $(1,0,3,0,0) \leftarrow (0,0,0,0,0)$ transition shown in Figure 6-16, since both transitions involve a change in 4 quanta of CH stretching motion. With the enhanced sensitivity of the 34,000 finesse cavity, it would be easy to detect a NICE-OHMS signal at least 100 times weaker than the shown in Figure 6-16. It is puzzling that the transition into the $(2,1,3,1^{+1},1^{-1})$ state was not observed. There are several possible explanations that may account for this. First, although extreme care was taken to ensure that the beams of the diode laser and Ti:Sapphire laser overlapped in the cavity, it is possible that overlap of the two beams was not ideal. In such a case, only a small fraction of the molecules or possibly none of the molecules that would have been excited into the $(1,1,0,1^{+1},1^{-1})$ level, were interrogated by the Ti:Sapphire laser beam. Additionally, it is possible that we were unable to excite sufficient population into the $(1,1,0,1^{+1},1^{-1})$ level. Assuming the cell pressure is in the free flight regime, it should only take ≈ 25 mW to completely saturate a rotational transition in the $(1,1,0,1^{+1},1^{-1}) \leftarrow (0,0,0,0,0)$ band. However, at sample pressures on the order of 20-50 mTorr, considerably more power is needed to saturate the transition. In fact, for a sample pressure of 50 mTorr, 790 mW are required to promote 50% of the population into the $(1,1,0,1^{+1},1^{-1})$ level. With the amplified diode output of 50 mW, at most 3% of the lower state population is transferred into the $(1,1,0,1^{+1},1^{-1})$ state. This is just at the limit of the detection sensitivity of the NICE-OHMS spectrometer when a 34,000 finesse cavity is used. Nonetheless, a weak NICE-OHMS signal should have been seen, providing the diode laser beam and the Ti:Sapphire laser beam were entirely overlapped.

6.7 Conclusion

Due to time constraints, the double resonance NICE-OHMS experiments were halted. With more time several improvements could have been made. The performance of the erbium doped fiber amplifier used to amplify the output of the diode laser could have been enhanced by altering the 'home built' amplifier to produce output powers on the order of 100mW. Additionally, commercial systems, although expensive, are now available which routinely produce amplified output powers on the order of 500 mW to 10W. A fiber amplifier with an output on the order of 1W would easily have saturated the transition and a double resonance NICE-OHMS signal should have been observed.

A cavity could also be designed with 3 mirrors which is resonant in both the 1.5 μm and 800nm spectral regions. One end mirror would have to be highly reflective at both frequencies, the second mirror would have to be highly reflective at 800 nm and highly transmissive at 1.5 μm and the final end mirror would have to be highly reflective at 1.5 μm and transmissive at 800 nm. Intracavity powers on the order of Watts for both 1.5 μm and 800nm would be achievable.

Although any one of these experimental enhancements would allow for the observation of transitions into the $(2,1,3,1^{+1},1^{-1})$ state, it is not certain that nuclear permutation tunneling splittings would be observed. The double resonance NICE-OHMS experiments have a resolution limited by the transit time of the molecule in the beam. For acetylene, this is on the order of 300 kHz. (The laser linewidth is determined by the cavity finesse, which for a finesse of 34,000, would be 12 kHz FWHM). The experiments performed at Princeton did not resolve nuclear permutation tunneling splittings within their 15 MHz resolution. It is possible that nuclear permutation tunneling splittings could be resolved using the NICE-OHMS technique, which has a factor of 50 better resolution.

However, the states that are predominantly characterized by CH stretching motion (such as the $(2,1,3,1^{+1},1^{-1})$ level) are not strongly coupled to the isomerization coordinate, which is essentially a local bend [20]. In order to gain information about

states that are strongly coupled to the isomerization coordinate, other techniques such as Stimulated Emission Pumping, SEP, are needed. High overtone experiments on the \tilde{X} state primarily excite states with CH stretch motion and only a few (1-2) quanta of bending motion. Consequently, the levels sampled in overtone experiments may not show any evidence of nuclear permutation tunneling splittings.

For example, the eigenstate observed in the Princeton experiments, at 18,580 cm^{-1} is predominantly composed of the $(2,1,3,1^{+1},1^{-1})$ basis state. The character of this basis state is distributed over 100 eigenstates. The basis states of the $[N_{res}, N_s] = [30,6]$ polyad that involve the maximal bending excitation are $(0,6,0,12^0,0^0)$ and $(0,6,0,0^0,12^0)$. The squared overlaps of the $(0,6,0,12^0,0^0)$ and $(0,6,0,0^0,12^0)$ basis states with the eigenstate are only 0.1% and 0.1×10^{-6} % respectively. The eigenstate observed in the Princeton experiments has little bending character. However, if the resolution of the experiment is sufficient, the observation of nuclear permutation tunneling splittings is possible.

To determine theoretically the magnitude of the tunneling splittings, a procedure such as the one outlined in Yongqin Chen's dissertation [39] may be used. Two Hamiltonians must be constructed twice. The first Hamiltonian is exactly the one described in Chapter 4, H_{eff}^{ace} . The second effective Hamiltonian is the same as the first except it includes a vinylidene level basis state, $H_{eff}^{ace+vinyl}$. The eigenstates of $H_{eff}^{ace+vinyl}$ are bounded by the eigenstates of the first Hamiltonian, H_{eff}^{ace} . In other words, they must occur between the original locations of the eigenstates of H_{eff}^{ace} . Since the degeneracy of the rotational levels is broken due to interactions with vinylidene, there will be 2 eigenstates of $H_{eff}^{ace+vinyl}$ between adjacent eigenstates of H_{eff}^{ace} .

The H_{eff}^{ace} matrix must be diagonalized then the $H_{eff}^{ace+vinyl}$ is constructed by adding one additional vinylidene level. The $H_{eff}^{ace+vinyl}$ can then be transformed back to the original basis by augmenting the original transformation with an additional row and column vector representing the vinylidene basis state. This transformed matrix can now be diagonalized and compared to the original eigenstates of H_{eff}^{ace} . To date this calculation has not been performed. The results of this calculation would be highly beneficial in identifying target levels for overtone and SEP experiments.

Consider, the observed eigenstate at 18580 cm^{-1} if perturbed by vinylidene may only shift 10 cm^{-1} since it is bounded by levels at 18570 cm^{-1} and 18590 cm^{-1} . However, recall that the Princeton experiments had a resolution of 15 MHz , and no splittings were observed. If there exists a vinylidene level which is at least 100 cm^{-1} away from the observed state at 18580 , the coupling matrix element would have to be on the order of 0.05 cm^{-1} in order for tunneling splittings to be observed. However, the level at 18560 has very little bending character, so it is conceivable that the vinylidene level would have to lie much closer to the acetylene level in order to observe a permutation doublet. At this juncture, no theoretical predictions for the either the magnitude of the nuclear permutation tunneling splittings, or the coupling matrix elements between acetylene and vinylidene vibrational levels for the observed eigenstate at 18580 cm^{-1} has been made. Schork and Koeppel have theoretically studied acetylene-vinylidene isomerization dynamics and determined the optimized geometries and energetics for vinylidene, acetylene and the transition state. They concluded that the lifetime of vinylidene is mode-specific, where vinylidene excited states such as the CH rocking mode, have a faster rate of isomerization than the vibronic ground state of vinylidene. In conclusion, a calculation determining the tunneling splittings for various levels in the region of the isomerization barrier, and above which examines the mode specificity of the isomerization process would be exceedingly valuable in guiding current experimental efforts aimed at directly observing spectroscopic signatures of acetylene \leftrightarrow vinylidene isomerization.

Chapter 7

Conclusion

The projects described in this thesis laid the foundation for understanding how large amplitude vibrational motions, which lead to bond breaking isomerization, are encoded in frequency domain spectra. Unfortunately, nuclear permutation tunneling splittings which are indicative of the acetylene \leftrightarrow vinylidene isomerization process, were not observable using direct absorption methods such as the NICE-OHMS technique outlined in Chapter 6 or the optothermal double resonance experiments performed at Princeton discussed in Chapters 6 and 4.1.

The results of the high resolution absorption experiments [20] confirm that local bender eigenstates, which are localized along the isomerization coordinate, are not strongly coupled to the rest of phase space. Consequently, experiments must be designed which directly interrogate these levels in order to observe acetylene \leftrightarrow vinylidene isomerization. The Laser Induced Fluorescence and Dispersed Fluorescence studies of $^{13}\text{C}_2\text{H}_2$ described in Chapters 2-1, 3, and 4 are essential steps in mapping out the spectroscopy and dynamics in both the ground electronic state and the first excited singlet state so that 'transition state spectroscopy' can be performed.

A preliminary attempt was made at observing nuclear permutation tunneling splitting in $^{13}\text{C}_2\text{H}_2$ using SEP. In those experiments, no evidence of tunneling doublets was observed. However, it is worth describing those experiments in the hope that future work will focus on SEP experiments of $^{13}\text{C}_2\text{H}_2$ where specific perturbation facilitated 'local bender plucks' are employed in order to observe nuclear permutation tunneling

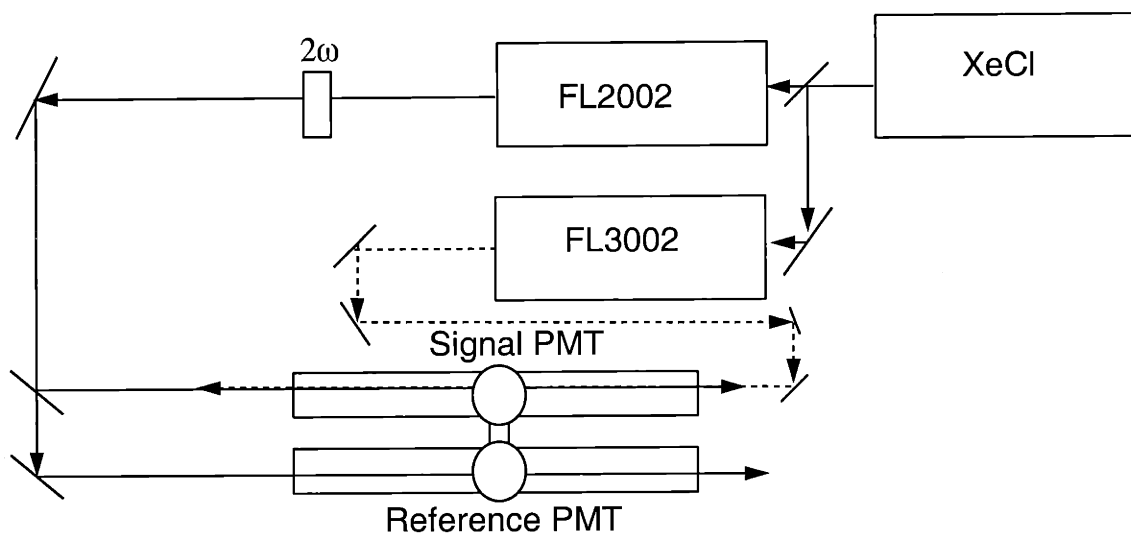


Figure 7-1: SEP experimental setup.

doublets.

Additionally, current research focused on understanding IVR in the \tilde{A} state via hot-band transitions will briefly be discussed.

7.1 Stimulated Emission Pumping Experiments

Preliminary Stimulated Emission Pumping Experiments were performed on $^{13}\text{C}_2\text{H}_2$. The experimental details of the SEP experiments are similar to those described by Moss et al [108] and will be briefly reviewed here for the sake of completeness. Illustrated in Figure 7-1 is the experimental setup for the SEP experiment.

A XeCl excimer laser (Lambda-Physik LPX-210icc) operating at 20 Hz and 330 mJ/pulse is used to pump two dye lasers. The first dye laser, which excited the 'pump transition' in SEP experiments, was a Lambda-Physik FL2002 dye laser, equipped with an intracavity etalon. Coumarin 440 or 450 dye was used and an output power of 10 mJ/pulse was obtained. In order to obtain tunable UV radiation (215–240 nm), the output of the dye laser was subsequently frequency doubled using a β -BBO crystal with a 10% conversion efficiency. The UV radiation was produced with a

spectral width $\leq 0.05 \text{ cm}^{-1}$. The UV radiation was sent through both arms of the SEP cell depicted in Figure 7-1. The UV radiation was tuned to either the ${}^rQ_0(1)$ or the ${}^rQ_0(3) V_0^2K_0^1$ transition in the state of ${}^{13}\text{C}_2\text{H}_2$.

A Lambda-Physik FL3002 dye laser, equipped with an intracavity etalon, operating with Coumarin 440 was used to stimulate the 'dump transition'. The fundamental radiation was used to transfer population from the $J' = 1$ or $J' = 3$ $2\nu_3$ rovibrational levels in the \tilde{A} state to rovibrational levels in the \tilde{X} state. The dye laser was pressure tuned over a range of $\approx 10 \text{ cm}^{-1}$ during each scan by varying the pressure of N_2 from vacuum to 1 atm. Frequency calibration was performed using a portion of the fundamental radiation from the dye laser, which was sent through a quartz ${}^{130}\text{Te}_2$ cell that was heated to either ($\sim 500 \text{ }^\circ\text{C}$) or ($\sim 650 \text{ }^\circ\text{C}$). Spectra were calibrated to an accuracy of 0.02 cm^{-1} .

As shown in Figure 7-1, the SEP cell has 2 arms. The UV radiation was sent through both arms of the SEP cell. The 440 nm output of the FL3002 dye laser is focused to a diameter less than 1 mm and counterpropagated with the 220 nm radiation in the signal arm. Fluorescence in each arm of the cell is detected perpendicular to the direction of the laser propagation using a Hamamatsu R331 photomultiplier tube. A Schott filter (UG11) is placed in front of the photomultiplier to reduce scattered light from the laser. The signals from the photomultipliers were each sent to a boxcar integrator (Stanford Research Systems SRS 250), gated to accept signal in the 0-100 ns interval after the laser pulse and averaged over 30 shots. The signal was normalized by ensuring that the fluorescence detected from each arm of the cell was the same when only the UV radiation was directed into the cell. The outputs of both boxcars were digitized and fluorescence dips were recorded using LabVIEW data acquisition software.

The SEP cell was filled with 200 mTorr of ${}^{13}\text{C}_2\text{H}_2$ (MSD Isotopes, 98% pure) which was subjected to several freeze-pump-thaw cycles before it was distilled into the sample cell. Details of this process can be found in Chapters 4 and 2-1.

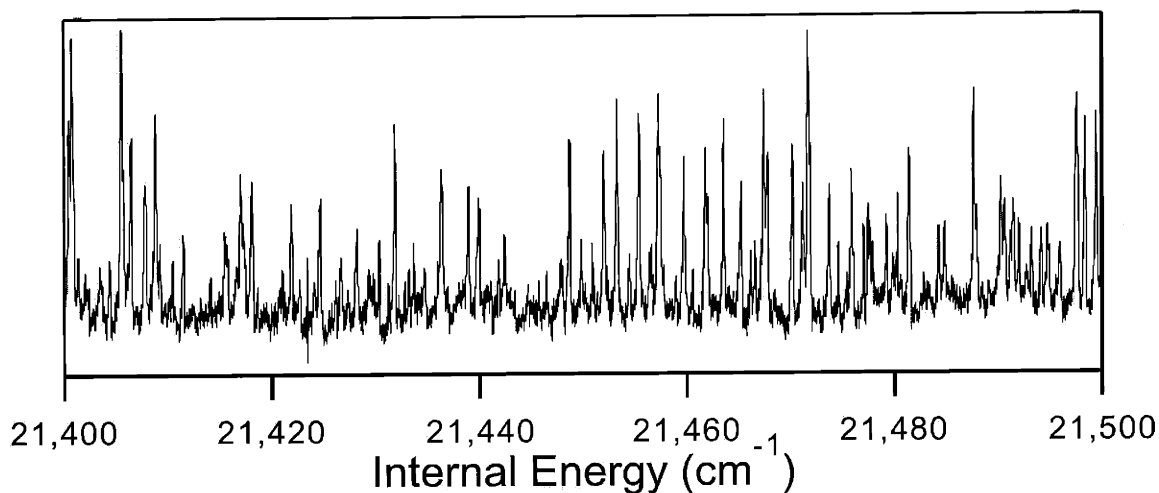


Figure 7-2: Portion of the SEP spectrum of $^{13}\text{C}_2\text{H}_2$ near $E_{vib} = 21,400 \text{ cm}^{-1}$. The $J' = 1$ of the V^2K^1 level was used as an intermediate state. No nuclear permutation tunneling doublets were observed.

7.1.1 Results of Preliminary Stimulated Emission Pumping Experiments

A portion of an SEP spectrum is shown in Figure 7-2. This spectrum was obtained using $J' = 1$ of the V^2K^1 level as an intermediate state and covers the region of internal energy from $21,400 \text{ cm}^{-1}$ to $21,500$. Several spectra were recorded using the Q(1) and Q(3) rotational lines.¹ These spectra spanned several hundred cm^{-1} of internal energy in the ground state near $21,500 \text{ cm}^{-1}$. No permutation tunneling doublets were identified in this region. Note that these experiments sampled an energy region at least $6,000 \text{ cm}^{-1}$ above the zero-point-dressed barrier for acetylene \leftrightarrow vinylidene isomerization. The absence of resolvable nuclear permutation tunneling splittings, after performing a *trans*-bend 'pluck' of eigenstates $6,000 \text{ cm}^{-1}$ above the zero-point dressed barrier, confirms that the isomerization coordinate is highly localized and in order to gain access to acetylene \leftrightarrow vinylidene isomerization states on the \tilde{A} state surface, a 'local bender pluck' is necessary.

¹In some instances Q(2), Q(4), Q(5), and Q(7) lines were used as intermediated levels.

7.2 Current Work: Hot-band Experiments

In order to determine A-rotational constants and the magnitudes of a-type Coriolis interactions one must measure the energy spacing between rotational manifolds of different K'_a quantum numbers. Additionally, rotational assignments of Q branch transitions of the type $K'_a = 1 \leftarrow l' = 0$ and $K'_a = 0 \leftarrow l' = 1$ (as those discussed in Chapters 2-1 and 3) cannot be confirmed due to the absence of combination differences. Information concerning other K'_a subbands would aid in assignment and resolve any ambiguities.

The rovibrational bands presented in this thesis primarily have $K'_a = 1$. Recall that the electronic ground state, \tilde{X} , is linear while the \tilde{A} state is bent. Consequently, only $\Delta K'_a = \pm 1$ transitions can occur between a linear ground state and a bent excited state. Laser Induced Fluorescence experiments of cold bands in acetylene, such as the ones described in Chapters 2-1 and 3, originate from $l' = 0$ levels and the selection rules for a linear to bent transition require that $\Delta K_a = \pm 1$. Consequently only $K'_a = 1$ levels are sampled.² In order to sample $K'_a = 0, 2$ levels, hot-band transitions originating from one quantum of ν_4' with $l' = 1$ must be excited. Likewise, hot-band transitions originating from two quanta of ν_4' with $l' = 0$ and 2 terminate on $K'_a = 1$ and 3 levels in the \tilde{A} state. Unfortunately, hot-band transitions are typically 10 to 100 times weaker than the cold band transitions observed in LIF or CRD spectra. Additionally, the hot-bands in acetylene are typically overlapped with cold band transitions and are obscured by them making it difficult to rotationally assign them.

Recently, experiments designed to disentangle hot-band transitions from the cold band transitions have proved to be successful. These experiments interrogate $K'_a = 0, 2$ subbands instead of the usual $K'_a = 1$ levels. Two LIF spectra were recorded simultaneously using the SEP cell described earlier. One arm of the cell was cooled to $\sim -100^\circ\text{C}$ while the other arm was heated to $\sim 50^\circ\text{C}$. The rotational transitions which belong to the hot-band should gain intensity as the temperature is increased.

² $K'_a = 0, 2$ levels gain intensity via axis-switching and may also be observed under special circumstances

The intensity ratio of the cold band transition to hot-band transitions will depend on the temperature of the cell. Extended Cross Correlation analysis, similar to the analysis used on the DF spectra, can be used to disentangle the hot-band and cold band transitions. Shown in the top panel of Figure 7-3 is an LIF scan near 45,000 cm^{-1} simultaneously recorded at two different temperatures. The middle graph in this figure is a recursion map similar to the one shown in Chapter 4. The slopes of the lines in the recursion map can be used to disentangle the hot-band transitions from the cold bands. Illustrated in the bottom panel in Figure 7-3 is the result of this extended cross correlation analysis. The hot-band transitions were successfully separated from the cold band transitions.

The results of these experiments are currently being analyzed. The information about additional K'_a subbands is useful in the assignment of transitions observed in Soji Tsuchiya's [36] group at Japan Women's University and recent work by Fleming Crim and coworkers. From the determination of energy spacing between different K'_a manifolds it is possible to obtain A-rotational constants and information concerning a-type Coriolis interactions which will aid in assignment of unknown transitions. In order to understand IVR in the \tilde{A} state, it is necessary to understand the interactions of the $4v'_{bend}$ perturber with other levels as well as the interactions amongst the levels composing the $4v'_{bend}$ polyad. This requires information about several K'_a subbands. Once IVR (more specifically the $4v'_{bend}$ perturbation) of the \tilde{A} state is well understood, we can attempt 'perturbation facilitated local bender plucks' of $^{13}\text{C}_2\text{H}_2$ states primarily localized along the acetylene \leftrightarrow vinylidene isomerization coordinate on the \tilde{X} surface such plucks will reveal nuclear permutation tunneling splittings in SEP experiments.

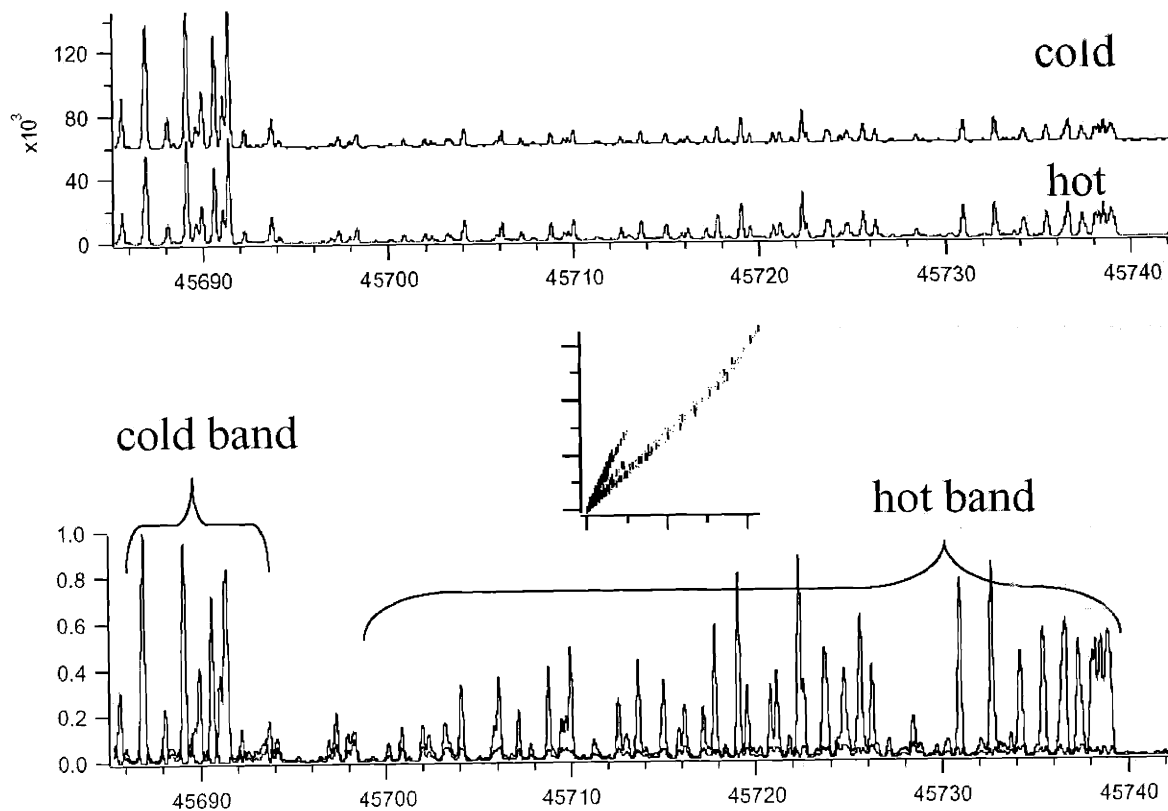


Figure 7-3: Preliminary results of hot-band Experiments implementing eXtended Cross Correlation to disentangle hot-band transitions from cold band transitions. Spectra taken at simultaneously at two different temperatures are shown in the upper panel. The middle diagram is a recursion map used for disentangling the spectra. The disentangled hot-band and cold-band spectra are shown in the bottom panel. Courtesy of Zicheng Duan.

Bibliography

- [1] G. Di Lonardo, L. Fusina, E. Venuti, J. W. C. Johns, M. I. El Idrissi and J. Liévin and M. Herman, *J. Chem. Phys.* **111**, 1 (1999).
- [2] R. A. Toth, *J. Mol. Spec.* **166**, 176 (1994).
- [3] C. K. Ingold and G. W. King, *J. Chem. Soc.* 2702 (1953).
- [4] K. K. Innes, *J. Chem. Phys.* **22**, 863 (1954).
- [5] M. P. Jacobson, S. L. Coy, and R. W. Field, *J. Chem. Phys.* **107**, 8349 (1997).
- [6] S. L. Coy, M. P. Jacobson, and R. W. Field, *J. Chem. Phys.* **107**, 8357 (1997).
- [7] M. P. Jacobson, J. P. O'Brien, R. J. Silbey, and R. W. Field, *J. Chem. Phys.* **109**, 121 (1998).
- [8] M. P. Jacobson, R. J. Silbey, and R. W. Field, *J. Chem. Phys.* **110**, 845 (1999).
- [9] M. P. Jacobson, J. P. O'Brien, and R. W. Field, *J. Chem. Phys.* **109**, 3831 (1998).
- [10] M. P. Jacobson, C. Jung, H. S. Taylor, and R. W. Field, *J. Chem. Phys.* **111**, 600 (1999).
- [11] M. Abbouti Temsamani and M. Herman, *J. Chem. Phys.* **102**, 6371 (1995).
- [12] M. Abbouti Temsamani, M. Herman, S. A. B. Solina, J. P. O'Brien and R. W. Field, *J. Chem. Phys.* **105**, 11357 (1996).
- [13] M. Abbouti Temsamani and M. Herman, *J. Chem. Phys.* **105**, 1355 (1996).
- [14] M. P. Jacobson, Ph.D. thesis, Massachusetts Institute of Technology, 1999.
- [15] Y. Osamura, H. F. Schaefer III, S. K. Gray, and W. H. Miller, *J. Am. Chem. Soc.* **103**, 1904 (1981).
- [16] T. Carrington, Jr., L. M. Hubbard, H. F. Schaefer III, and W. H. Miller, *J. Chem. Phys.* **80**, 4347 (1984).
- [17] M. M. Gallo, T. P. Hamilton, and H. F. Schaefer III, *J. Am. Chem. Soc.* **112**, 8714 (1990).

- [18] J. Lundberg, Ph.D. thesis, Massachusetts Institute of Technology, 1992.
- [19] J. K. Lundberg, in *Molecular Dynamics and Spectroscopy by Stimulated Emission Pumping*, edited by H.-L. Dai and R. W. Field (World Scientific, Singapore, 1995), p. 791.
- [20] H. K. Srivastava, A. Conjusteau, H. Mabuchi, A. Callegari, K.K. Lehmann, G. Scoles, M. L. Silva and R. W. Field, *J. Chem. Phys.* **113**, 7376 (2000).
- [21] R. W. F. M. L. Silva, R. Jongma and A. M. Wodtke, *Ann. Rev. Phys. Chem.* **52**, 811 (2001).
- [22] G. J. Scherer, Y. Chen, R. L. Redington, J. L. Kinsey and R. W. Field, *J. Chem. Phys.* **85**, 6315 (1986).
- [23] A. L. Utz, J. D. Tobiasson, E. Carrasquillo, L. J. Sanders and F. F. Crim, *J. Chem. Phys.* **98**, 2742 (1993).
- [24] M. P. Jacobson and R. W. Field, *J. Phys. Chem. A* **104**, 3073 (2000).
- [25] K. L. Cunningham, Ph.D. thesis, Massachusetts Institute of Technology, 2000.
- [26] S. A. Altunata, Ph.D. thesis, Massachusetts Institute of Technology, 2001.
- [27] J. P. O'Brien, Ph.D. thesis, Massachusetts Institute of Technology, 1997.
- [28] J. L. K. E. Abramson, C. Kittrell and R. W. Field, *J. Chem. Phys.* **76**, 2293 (1982).
- [29] J. T. Hougen and J. K. G. Watson, *Can. J. Phys.* **43**, 298 (1965).
- [30] G. Di Lonardo, P. Ferracuti, L. Fusina, E. Venuti, J. W. C. Johns, M. I. El Idrissi and J. Liévin and M. Herman, *J. Mol. Spec.* **161**, 466 (1993).
- [31] N. Ochi and S. Tsuchiya, *Chem. Phys.* **152**, 319 (1991).
- [32] N. Ochi and S. Tsuchiya, *Chem. Phys. Lett.* **140**, 20 (1987).
- [33] J. H. M. Drabbels and W. L. Meerts, *J. Chem. Phys.* **100**, 165 (1994).
- [34] J. T. Hougen and J. K. G. Watson, *Can. J. Phys.* **43**, 298 (1965).
- [35] J. K. G. Watson, *J. Chem. Phys.* **46**, 1935 (1967).
- [36] M. Mizoguchi, N. Yamakita, S. Tsuchiya, A. Iwasaki, K. Hoshina, K. Yamouchi, *J. Phys. Chem.* **104**, 10212 (2000).
- [37] J. P. O'Brien, M. P. Jacobson, J. J. Sokol, S. L. Coy and R. W. Field, *J. Chem. Phys.* **108**, 7100 (1998).
- [38] M. I. El Idrissi, J. Liévin, A. Campargue and M. Herman, *J. Chem. Phys.* **110**, 2074 (1999).

- [39] Y. Chen, Ph.D. thesis, Massachusetts Institute of Technology, 1988.
- [40] R. R. Hall, Ph.D. thesis, Rice University, 1984.
- [41] G. J. Scherer, K. K. Lehmann and W. Klemperer, *J. Chem. Phys.* **78**, 2817 (1983).
- [42] G. Di Lonardo, P. Feracuti, L. Fusina, E. Venuti and J. W. C. Johns, *J. Mol. Spec.* **161**, 466 (1993).
- [43] G. Di Lonardo, P. Feracuti, L. Fusina and E. Venuti, *J. Mol. Spec.* **164**, 219 (1994).
- [44] M. Becucci, E. Castellucci, L. Fusina, G. Di Lonardo and H. W. Schrötter, *J. Raman Spec.* **29**, 237 (1998).
- [45] J. Hietanen, V. M. Horneman and J. Kauppinen, *Mol. Phys.* **59**, 587 (1986).
- [46] M. L. Silva, M. P. Jacobson, Z. Duan and R. W. Field, manuscript in preparation.
- [47] S. A. B. Solina, J. P. O'Brien, R. W. Field, and W. F. Polik, *J. Phys. Chem.* **100**, 7797 (1996).
- [48] K. Yamanouchi, N. Ikeda, S. Tsuchiya, D. M. Jonas, J. K. Lundberg, G. W. Adamson and R. W. Field, *J. Chem. Phys.* **95**, 6330 (1991).
- [49] J. F. Stanton and J. Gauss, *J. Chem. Phys.* **110**, 1831 (1999).
- [50] J. Plíva, *J. Mol. Spec.* **44**, 165 (1982).
- [51] K. K. Lehmann, *J. Chem. Phys.* **84**, 6524 (1986).
- [52] J. E. Baggott, *Mol. Phys.* **65**, 739 (1988).
- [53] K. K. Lehmann, *J. Chem. Phys.* **96**, 8117 (1992).
- [54] M. E. Kellman, *J. Chem. Phys.* **83**, 3843 (1985).
- [55] M. S. Child and R. T. Lawton, *Faraday Discuss.* **71**, 273 (1981).
- [56] A. B. McCoy and E. L. Sibert III, *J. Chem. Phys.* **105**, 459 (1996).
- [57] E. L. Sibert III and A. B. McCoy, *J. Chem. Phys.* **105**, 469 (1996).
- [58] G. M. Schmid, S. Coy, R. W. Field, and R. J. Silbey, *Chem. Phys. Lett.* **219**, 331 (1994).
- [59] I. M. Mills and A. G. Robiette, *Mol. Phys.* **56**, 743 (1985).
- [60] I. M. Mills and F. J. Mompean, *Chem. Phys. Lett.* **124**, 425 (1986).

- [61] D. M. Jonas, Ph.D. thesis, Massachusetts Institute of Technology, 1992.
- [62] I. Dubinsky, Ph.D. thesis, Massachusetts Institute of Technology, 2001.
- [63] *Cavity Ringdown Spectroscopy: An Ultratrace-Absorption Measurement Technique*, edited by K. W. Busch and M. A. Busch (American Chemical Society, Washington, DC, 1999), p. 106.
- [64] J. J. Scherer, J. B. Paul, A. O'Keefe and R. J. Saykally, *Chem. Rev.* **97**, 25 (1997).
- [65] B. A. Paldus and R. N. Zare, in *Cavity Ringdown Spectroscopy: An Ultratrace-Absorption Measurement Technique*, edited by K. W. Busch and M. A. Busch (American Chemical Society, Washington, DC, 1999), p. 49.
- [66] J. M. Herbelin and J. A. McKay, *Appl. Opt.* **20**, 3341 (1981).
- [67] D. Z. Anderson, J. C. Frisch and C. S. Masser, *Appl. Opt.* **23**, 1238 (1984).
- [68] K. W. Busch and M. A. Busch, in *Cavity Ringdown Spectroscopy: An Ultratrace-Absorption Measurement Technique*, edited by K. W. Busch and M. A. Busch (American Chemical Society, Washington, DC, 1999), p. 7.
- [69] A. O'Keefe and D. A. G. Deacon, *Rev. Sci. Inst.* **59**, 2544 (1988).
- [70] A. O'Keefe, J. J. Scherer, A. L. Cooksy, R. Sheeks, J. Heath and R. J. Saykally, *Chem. Phys. Lett.* **172**, 214 (1990).
- [71] J. B. Paul, C. P. Collier, R. J. Saykally, J. J. Scherer and A. O'Keefe, *J. Phys. Chem. A* **101**, 5211 (1997).
- [72] T. Yu and M. C. Lin, *J. Am. Chem. Soc.* **115**, 4371 (1993).
- [73] D. Romanini and K. K. Lehmann, *J. Chem. Phys.* **99**, 6287 (1993).
- [74] D. Romanini and K. K. Lehmann, *J. Chem. Phys.* **102**, 633 (1995).
- [75] D. Romanini and K. K. Lehmann, *J. Chem. Phys.* **105**, 10263 (1996).
- [76] D. Romanini and K. K. Lehmann, *J. Chem. Phys.* **105**, 81 (1996).
- [77] T. G. Slanger, D. L. Heutis, P. C. Cosby, H. Naus and G. Meijer, *J. Chem. Phys.* **105**, 9393 (1996).
- [78] M. G. H. Bogaarts and G. Meijer, *J. Chem. Phys.* **102**, 5269 (1995).
- [79] R. T. Jongma, M. G. H. Bogaarts, I. Holleman and G. Meijer, *Rev. Sci. Inst.* **66**, 2821 (1995).
- [80] R. Engeln and G. Meijer, *Rev. Sci. Inst.* **67**, 2708 (1996).

- [81] R. Engeln, G. Bierden, E. v. d. Berg and G. Meijer, *J. Chem. Phys.* **107**, 4458 (1997).
- [82] R. Engeln and G. Meijer, *Chem. Phys. Lett.* **262**, 105 (1996).
- [83] P. Zalicki, Y. Ma, R. N. Zare, E. H. Wahl, J. R. Dadamio, T. G. Owano and C. H. Kruger, *Chem. Phys. Lett.* **234**, 269 (1995).
- [84] P. Zalicki, Y. Ma, R. N. Zare, E. H. Wahl, T. G. Owano and C. H. Kruger, *Appl. Phys. Lett.* **67**, 144 (1995).
- [85] J. T. Hodges, J. P. Looney and Roger D. van Zee, *Appl. Opt.* **35**, 4112 (1996).
- [86] B. A. Paldus, C. C. Harb, B. Wilke, J. Xie, J. S. Harris and R. N. Zare, *J. Appl. Phys.* **83**, 3991 (1998).
- [87] P. Zalicki and R. N. Zare, *J. Chem. Phys.* **102**, 2708 (1995).
- [88] J. P. Looney, J. T. Hodges and R. D. van Zee, in *Cavity Ringdown Spectroscopy: An Ultratrace-Absorption Measurement Technique*, edited by K. W. Busch and M. A. Busch (American Chemical Society, Washington, DC, 1999), p. 93.
- [89] J. P. Looney, J. T. Hodges and R. D. van Zee, *J. Chem. Phys.* **105**, 10278 (1996).
- [90] A. E. Siegman, *Lasers* (University Science Books, Mill Valley, CA, 1986).
- [91] L. M. Ruslen, Ph.D. thesis, Massachusetts Institute of Technology, 2001.
- [92] G. Herzberg, *Molecular Spectra and Molecular Structure II. Infrared and Raman Spectra of Polyatomic Molecules* (D. Van Nostrand Company, Inc., Princeton, NJ, 1945).
- [93] A. E. Bernath, *Spectra of Atoms and Molecules* (Oxford University Press, England, 1995).
- [94] J. K. G. Watson, *J. Mol. Spec.* **207**, 276 (2001).
- [95] J. Y. L.-S. Ma, P. Dubé and J. L. Hall, *J. Opt. Soc. Am. B* **16**, 2255 (1999).
- [96] L.-S. M. J. Ye and J. L. Hall, *J. Opt. Soc. Am. B* **15**, 6 (1998).
- [97] R. W. F. L. Gianfrani and L. Hollberg, *Opt. Soc. Am. B* **16**, 2247 (1999).
- [98] L.-S. M. J. Ye and J. L. Hall, *Opt. Lett.* **21**, 1000 (1996).
- [99] J. Ye, Ph.D. thesis, University of Colorado, 1997.
- [100] R. W. P. Drever, J. L. Hall, F. V. Kowalski, J. Hough, G. M. Ford, A. J. Munley and W. Ward, *Appl. Phys. B* **31**, 97 (1983).

- [101] J. Y. L.-S. Ma, P. Dubé and J. L. Hall, Quantum Electronics and Laser Science Conference **16**, 18 (1995).
- [102] R. G. DeVoe and R. G. Brewer, Phys. Rev. A **30**, 2827 (1984).
- [103] B. Edlen, Metrologia **2**, 71 (1966).
- [104] H. Wahlquist, J. Chem. Phys. **35**, 1708 (1961).
- [105] J. K. Messer and F. C. D. Lucia, J. Mol. Spec. **105**, 139 (1984).
- [106] J. M. Flaud, C. Camy-Peyret, A. Bykov, O. Naumenko, T. Petrova, A. Scherbakov and L. Sinitza, J. Mol. Spec. **183**, 300 (1997).
- [107] J. L. Steven Alder-Golden and N. Goldstein, J. Quant. Spectrosc. Radiat. Transfer **48**, 527 (1992).
- [108] D. B. Moss, M. P. Jacobson, R. Z. Duan, J. P. O'Brien and R. W. Field, J. Mol. Spec. **265**, 199 (2000).

Curriculum Vitae

BIRTH DATE: September 11, 1974.

EDUCATION: Brown University, Sc.B. *magna cum laude with Honors* (1996); Massachusetts Institute Of Technology, Ph.D. expected October 2001.

AWARDS AND HONORARY SOCIETIES: National Research Council Postdoctoral Fellow 2001; Honorable Mention, National Science Foundation fellowship, 1996,1997; Senior Research Award, Chemistry Department, Brown University, 1996; Sigma Xi.

PUBLICATIONS AND PRESENTATIONS:

Michelle L. Silva, Rienk Jongma, Robert W. Field, Alec M. Wodtke, "The Dynamics of 'Stretched Molecules': Experimental Studies of Highly Vibrationally Excited Molecules with Stimulated Emission Pumping", *Annu. Rev. Phys. Chem.* 52, 811-852 (2001).

H. K. Srivastava, A. Conjusteau, H. Mabuchi, A. Callegari, K.K. Lehmann, G. Scoles, M. L. Silva, and R. W. Field, "Rovibrational spectroscopy of the $v=6$ manifold in $^{12}\text{C}_2\text{H}_2$ and $^{13}\text{C}_2\text{H}_2$ ", *Journal of Chemical Physics*, 113, 7376, (2000).

Michelle L. Silva, Matthew P. Jacobson, Zicheng Duan, and Robert W. Field, "Anomalous Simplicity of the Dispersed Fluorescence Spectrum of $^{13}\text{C}_2\text{H}_2$ " presented at European Congress on Molecular Spectroscopy, August 2000. Coimbra, Portugal, accepted in *Journal of Molecular Structure*, 565- 566, 87 (2001).

Michelle L. Silva, "Cavity Ring-Down Spectroscopy of the A-X Transition in Acetylene", invited talk, University of New Hampshire, September 2001.

Michelle L. Silva, "Acetylene the Road to Isomerization", invited talk, Brown University, April 2001.

Michelle L. Silva, Robert W. Field, L.-S. Ma , Jun Ye and John L. Hall "Precision Measurement of the (211) Band of H_2O using Noise-Immune Cavity-Enhanced Optical Heterodyne Molecular Spectroscopy" presented at Conference on Lasers and Electro-optics/Quantum Electronics and Laser Science (CLEO/QELS '00), San Francisco, May 2000.

Michelle L. Silva, Matthew P. Jacobson, Zicheng Duan, and Robert W. Field, "Dispersed Fluorescence Spectra of $^{13}\text{C}_2\text{H}_2$ from the \tilde{A}^1A_u State" presented at 54th Ohio State University International Symposium on Molecular Spectroscopy, Ohio, June 1999.